UNIVERSITÉ PIERRE ET MARIE CURIE
École Doctorale 517 : Particules, Noyaux, Cosmos

Development and Characterization of Micro-Pattern Gas Detectors for Intense Beams of Hadrons

Maxence Vandenbroucke

TECHNISCHE UNIVERSITÄT MÜNCHEN
Physik-Department E18

UNIVERSITÉ PIERRE ET MARIE CURIE
École Doctorale 517 : Particules, Noyaux, Cosmos

TECHNISCHE UNIVERSITÄT MÜNCHEN
Physik-Department E18

Thèse en cotutelle entre / Doppelpromotion zwichen / Jointly supervised PhD between
L'UNIVERSITÉ PIERRE ET MARIE CURIE and TECHNISCHE UNIVERSITÄT MÜNCHEN

Spécialité / Fachrichtung / Subject
Physique des Particules / Teilchenphysik / Particle Physics

Development and Characterization of Micro-Pattern Gas Detectors for Intense Beams of Hadrons

Présentée par / Dissertation von / Presented by

M. Maxence VANDENBROUCKE

Pour obtenir le diplôme de / Zur Erlangung des akademischen Grades / To obtain the dual degree of
Docteur de l'Université Pierre et Marie Curie
and Doktor der Naturwissenschaften

Soutenue le 02 juillet 2012 devant le jury composé de:
Die Doktorprüfung fand am 2. Juli 2012 statt. Mitglieder der Prüfungskommission:
Defended the 2nd of July 2012 in front of the jury composed by:

Mme. Silvia DALLA TORRE	(rapporteur / Prüfer / referee)
M. Werner RIEGLER	(rapporteur / Prüfer / referee)
M. Walter F. HENNING	(rapporteur / Prüfer / referee)
M. Stephan PAUL	(rapporteur / Prüfer / referee)
M. Pascal VINCENT	(président / Vorsitzender / president)
M. Bernhard KETZER	(directeur de thèse / Betreuer / thesis supervisor)
M. Damien NEYRET	(directeur de thèse / Betreuer / thesis supervisor)

À mes parents.

Acknowledgments

First I would like to express my gratitude to Pascal Vincent who accepted to be the president of my jury. He is at the origin of this jointly supervised PhD, and, moreover, of my interest in the field of particle detectors back when I was following his lectures.

I am very grateful to Prof. Stephan Paul for accepting to be a member of my jury and the chairman for Technische Universität München. It was an honor and pleasure to work in his very dynamic group lead by his enthusiasm.

I am thankful to Silvia Dalla Torre for accepting to be an important part of my jury thanks to her involvement and expertise in the field of MPGD. I would like to extend my gratitude to Prof. Walter Henning for the interest and curiosity that he has shown in my work while reviewing it. My sincerest thanks go to Werner Riegler who dedicated some of his precious time and his immense knowledge on detectors and their history to give me valuable suggestions and relevant remarks.

The work presented here has been elaborated with a jointly supervised thesis agreement, which gave me the great chance of having not one, but two amazing supervisors.

Damien Neyret who introduced me to the wonderful world of research and gave me the taste of experimental physics. With his patience and kindness, he lead my work with Micromegas detectors (and more!) in all their aspects, from their assembly to their use in the COMPASS experiment. I am very grateful for his immensely important support, always with a smile, both on technical and administrative matters; thank you so much for all your precious and enjoyable time.

It has been a privilege to start my PhD with Bernhard Ketzer. With his inspiring motivation, he taught me more rigorous manners of being an experimental physicist. He also gave me the opportunity to present my work in several international conferences. I am deeply grateful for his guidance, his involvement on my work, and the time he dedicated to answer my numerous questions with his immense knowledge of experimental physics.

A thesis is before all the work of a team, in my case two teams.

In Munich, I am very grateful to Karin Frank who helped me so much with all my paper-work and everything else that allowed me to survive.

I am deeply thankful to Igor Konorov who was always willing to teach me the mysteries of electronics, reconstruction algorithms, and table tennis. A significant part of this work has been elaborated thanks to the numerous enjoyable discussions with Igor.

I also learned a lot from more experienced PhD students at TUM: in particular Christian Höppner with whom I had my first experience with the GEM-TPC. I thank Sebastian Neubert and Florian Haas for sharing with me a part of their wisdom. I will always be indebted to Sebastian Uhl who helped me progressing with all of my technical difficulties, in particular with DATE, thanks to his immense technical knowledge and know-how; I hope you also enjoyed helping me, even during Sundays.

I would like to thank all the young people at E18 and everybody who had to endure my annoying

French accent, starting with my fast-spreading office mate and friend Sverre Dørheim, Felix Böhmer with whom I will never forget Miami, Stefan Huber always around, Alexander Austregesilo, Markus Ball, Stefanie Grabmüller, Markus Krämer, Alexander Mann, Thiemo Nagel and Johannes Rauch. I will not forget about our colleagues from the universe cluster lead by the charismatic Laura Fabbietti, Martin Berger, Jia-Chii Berger-Chen, Francesco Cusanno, Robert Münzer, and also the people from Bonn where we had our first test beam David Kaiser, Theresa Negini, Roman Schmitz and Alexander Winnebeck.

At Saclay my first thought goes to Fabienne Kunne who welcomed me with her great carefulness. I would like to thank Yan Bedfer who is always a great source of wisdom, I wish I could have learned more from Yan and the other members of the team: mon parrain Etienne Burtin, Nicole d'Hose, Claude Marchand, and Stephane Platchkov.

I am thankful to the SPhN staff: Michel Garçon and the secretaries Danielle Coret and Isabelle Richard who kept their calm in front of my administrative mess.

A particular thank to the CLAS12 team, in particular Sébastien Procureur who agreed to correct a great deal of this manuscript with his rigorous eye and who was always available to answer my questions about Micromegas and his older detectors.

People from SEDI without whom no Micromegas would ever have been build correctly, Philippe Abbon, Marc Anfreville, Stephan Aune, and Michel Boyer. A particular thanks to Eric Delagnes, the designer of the AFTER chip who happily accepted to answer my user-like questions. I am grateful to Ioanis Giomataris, in particular for his help on the Wikipedia article. I would like also to thank Fabrice Gautheron for the long chats at CERN.

And of course the young (and less young) people who shared my time at Saclay and the short daily coffee break: Stefano Panebianco who dissipated my doubts before joining Saclay a while ago, even if he might have forgotten that discussion. It has been also a great pleasure to meet Luigi Capozza, always willing to answer my naive interrogations with his great scientific and linguistic culture. P.A.M. Guichon always ready to test the law of nature with golf balls. The "thésards", Florian Thibaud who helped me process the latest data presented here, I'm sure he'll finish my TODO list, Vincent Andrieux, keep fitting!, Florent Robinet my first office mate, Gabriel Charles, Nour Makke, Lucie Grente, Marie Boer and her infinite chatting capability, and all the other that I have forgotten.

A special thanks to Rob Veenhof from CERN for the passionate discussions about gas processes and his help with the MAGBOLTZ simulations.

Lastly and most importantly, my friends and family. To all people who visited me in Munich, the <|, Evy und Yves, and all the people who recognize themselves. My brothers and their family for being there, and of course my parents without whom none of these long studies, where I met my passion, would have been possible.

Abstract

Since the invention of Multi-Wire Proportional Chambers (MWPC) in 1968, gaseous detectors have transformed the field of high-energy physics experiments. The performances of MWPCs have greatly improved the precision of measurements up to a particle rate of 10^4 Hz/mm^2, which is the limit for wire detectors. To overcome this limitation, new concepts of gaseous detectors, the *Micro-Pattern Gas Detectors*, appeared in the late 90's. Nowadays, a renewed interest in these technologies is brought about by the design of the next generation of experiments. Specifically GEM and Micromegas tracking detectors have proved to reach spatial resolutions better than 100 μm and time resolutions below 10 ns at a rate above 10^6 Hz/mm^2. This work is dedicated to the development of these concepts and to the design and characterization of new detectors.

The first part of this thesis reports on the development of a Time Projection Chamber (TPC) for high rate environments. Traditionally read out by wire-chambers, these detectors suffer from the space charge created by back-drifting ions. This implies the use of an ion gate that limits the rate to ~ 1 kHz. Thanks to their intrinsic ion back-flow suppression, GEMs have been considered to operate TPCs in an un-gated mode. A prototype with 7 cm drift length and hexagonal pad readout has been assembled and connected to the low noise AFTER front-end electronic readout dedicated to MPGDs. The chamber has been commissioned with an external tracking telescope using an electron beam at the ELSA facility. A second test beam period for precision measurements using high-energy muons has demonstrated the great performances of the GEM-TPC.

The second part of this dissertation describes the development of the next generation of Micromegas for the future COMPASS-II experiment. The new Pixel Micromegas will have to sustain a hadron beam of 5×10^6 Hz/mm^2. Tests with current COMPASS Micromegas detectors have shown their limitations in term of maximal particle rate and discharge probabilities. A factor 10 to 100 in discharge rate reduction is required. This triggered a R&D project that concluded on the selection of GEM pre-amplification and buried resistors structure as realistic options. Both these technologies have been tested with 40×40 cm^2 prototypes, read by the fast APV25 front-end electronics, in COMPASS environment; promising results on efficiency, spatial and time residuals are reported.

Résumé

Depuis l'invention de la chambre proportionnelle multifilaire en 1968, les détecteurs gazeux ont transformés les expériences de physique des hautes énergies. Les performances des chambres à fils ont beaucoup amélioré la précision des mesures jusqu'à ce que le flux de particules atteigne 10^4 Hz/mm^2, la limite pour les détecteurs à lecture par fil. Pour dépasser cette limite, de nouveaux concepts de détecteurs gazeux sont apparus dans les années 1990, les Détecteurs Gazeux à Micro Motifs ou MPGD pour "Micro-Pattern Gas Detectors" en anglais. Avec l'avènement d'une nouvelle génération d'expériences, ces technologies connaissent un regain d'intérêt. En particulier les détecteurs GEM et Micromegas ont prouvé qu'ils pouvaient atteindre une résolution spatiale meilleure que 100 µm, une résolution temporelle de 10 ns à un flux de particules supérieur à 10^6 Hz/mm^2. Cette thèse est consacrée au développement, à la conception et à la caractérisation de ces détecteurs.

La première partie de cette thèse porte sur le développement d'une chambre à projection temporelle, TPC pour "Time Projection Chamber" en anglais, destinée aux haut flux de particules. Traditionnellement lue par des chambres à fils, ces détecteurs sont limités par la charge d'espace crée par les ions qui remontent dans le volume de dérive. Il est donc nécessaire de neutraliser ces ions à l'aide d'une grille dont l'utilisation limite la fréquence de déclenchement à ~ 1 kHz. Grâce à leur suppression intrinsèque des ions, une lecture à base de GEM est envisagée pour lire une TPC sans avoir à recourir à une grille. Un prototype de 7 cm d'espace de dérive équipé de pads hexagonaux a été assemblé à Munich. Munie de l'électronique AFTER dédié aux MPGDs, le détecteur a été testé à l'aide du faisceau d'électrons de l'accélérateur ELSA à Bonn, en Allemagne. Une seconde période de test à l'aide de muons de haute énergie a permis de démontrer les bonnes performances de la GEM-TPC.

La seconde partie de cette thèse décrit le développement de la prochaine génération de détecteurs Micromegas pour l'expérience COMPASS-II. Les nouveaux Pixels Micromegas devront supporter un flux de hadrons de 5×10^6 Hz/mm^2. Des tests avec les détecteurs actuels ont montré leur limitation en termes de flux de particules et de probabilité de décharge. Une réduction de cette probabilité d'un facteur de 10 à 100 est nécessaire. Ceci est à l'origine d'un programme de R&D qui a conduit à deux solutions : la pré-amplification par feuille de GEM et la protection des pistes par une structure resistive à base de résistances enterrées. Chacune de ces technologies a été testées avec des prototypes de 40×40 cm^2, lus par l'électronique APV dans l'environnement de l'expérience COMPASS. Des résultats prometteurs en terme d'efficacité, de résolutions spatiale et temporelle sont présentés.

Zusammenfassung

Seit der Entwicklung des Vieldrahtproportionalzählers “MWPC” im Jahr 1968 haben Gasdetektoren Experimente in der Hochenergiephysik verändert. Das Auflösungsvermögen von MWPCs, und die Möglichkeit bei hohen Teilchenraten von bis zu 10^4 Hz/mm^2 zu messen, haben die Genauigkeit der Experimente stark verbessert. Um die prinzipielle Limitierung der Teilchenrate zu überwinden, wurde Ende der 1990er Jahre ein neues Konzept für Gasdetektoren entwickelt, das auf mikroskopisch kleinen Strukturen basiert (Micro-Pattern Gas Detectors, MPGDs). Inzwischen tritt diese Technologie durch die Erfordernisse neuer Experimente immer weiter in den Vordergrund. Insbesondere Gaselektronenvervielfacher (Gas Electron Multiplier, GEM) und Micromegas-Detektoren (Micro Mesh Gaseous detectors) haben ihre Qualitäten als Spurdetektoren mit Ortsauflösungen um 100 μm und Zeitauflösungen besser als 10 ns bei Raten um 10^6 Hz/mm^2 bereits unter Beweis gestellt. Diese Arbeit widmet sich der Weiterentwicklung dieser Konzepte und der Entwicklung und Charakterisierung darauf basierender Detektoren.

Im ersten Teil der Arbeit wird die Entwicklung einer Zeitprojektionskammer (Time Projection Chamber, TPC) für hohe Teilchenraten beschrieben. Traditionell werden solche Detektoren mit Drahtkammern ausgelesen, wobei Ionen, die entlang der elektrischen Feldlinien aus der Verstärkungsebene in das Driftvolumen gelangen, das elektrische Feld lokal verzerren können. Deshalb werden die Ionen normalerweise von einer zusätzlichen Ebene von Drähten, die sich zwischen Anode und Driftvolumen befindet, neutralisiert. Dieses "Gating" limitiert die erlaubte Ausleserate auf ~ 1 kHz. Da in GEMs dieser Ionenrückfluß intrinsisch unterdrückt ist, sollte es möglich sein eine TPC mit GEM Verstärkung ohne "Gating" zu betreiben. Ein Prototyp mit 7 cm Driftlänge und einer hexagonalen Auslesestruktur wurde gebaut, und mit einer auf dem AFTER Chip basierenden Ausleseelektronik verbunden. Dieser Chip wurde spezifisch für die Erfordernisse von MPGDs entwickelt, im Rahmen dieser Arbeit wurde die Elektronik charakterisiert und ihre Eignung unter besonderer Berücksichtigung des erforderlichen niedrigen elektronischen Rauschens festgestellt. Der Prototyp wurde mit einem externen Teleskop aus Spurdetektoren an der Elektronen-Stretcher-Anlage (ELSA, Bonn) aufgebaut, wo mit einem Elektronenstrahl gemessen wurde. Ein zweiter Test wurde im hochenergetischen Myonen-strahl des COMPASS Experiments (CERN) gemacht. In beiden Fällen wird die erstklassige Qualität der GEM TPC gezeigt.

Im zweiten Teil dieser Dissertation wird die Entwicklung der nächsten Generation von Micromegas-Detektoren für das COMPASS-II Experiment beschrieben. Die neuen Micromegas-Detektoren müssen auch bei Raten von 5×10^6 Hz/mm^2 in einem Hadronenstrahl funktionieren. Die bisherigen COMPASS Micromegas sind durch die maximale Teilchenrate und die Entladungswahrscheinlichkeit beschränkt, die Entladungsrate muss um einen Faktor 10 bis 100 verringert werden. In einem Forschungs- und Entwicklungsprojekt wurde die Benutzung einer einzelnen GEM als Vorverstärker, sowie von "buried resistors" zwischen der Auslesestruktur und der Ausleseelektronik als erfolgversprechend herausgearbeitet. Beide Vorschläge wurden mit einem 40×40 cm^2 Prototypen in COMPASS getestet. Die Detektoren wurden mit einer APV25-basierten Elektronik ausgelesen, vielversprechende Ergebnisse bezüglich der Effizienz, und der Orts- und Zeitauflösung werden gezeigt.

Contents

Chapter 1

Introduction

More than 50 years after the first gaseous detector of E. Rutherford and H. Geiger, G. Charpak invented in 1959 the Multi-Wire Proportional Chamber. Its parallel electronic readout allowed to record data for computerized offline analysis. Previous methods based on the visual analysis of photographs required a consequent manpower for a very low event rate. The MWPCs revolutionized the field of high-energy physics, leading to large size experiments that opened the door to precision measurement and complex analysis. From the reconstructed position of particles in different detector planes that are immersed in a magnetic field, one can reconstruct the kinematic of the reaction.

In the mid 90's, it appeared that the limited rate capabilities of the MWPCs could not fulfill the conditions foreseen at the future LHC. The radial field geometry around wires coupled with the slow drifting ions limits the rate to several kHz before the ion density renders the detector inefficient. This drove R&D in the field of tracking detectors that led to the development of the Micro Strip Gas Chamber (MSGC). These detectors suffered from ageing and the development continued. It led to the discovery, almost simultaneously, in 1996, of the Micro-Mesh Gaseous Structure and Gaseous Electron Multiplier concepts. Together with the MSGC and other similar technologies, they have been later regrouped under the name MPGD for Micro-Pattern Gas Detector. A year later, COMPASS, for COmmon Muon Proton Apparatus for Structure and Spectroscopy, a fixed target experiment using the intense muon and hadron beams of the SPS was approved to study the spin structure of the nucleon and the hadron spectroscopy. This experiment required a high resolution with large acceptance spectrometer. The area between 2.5 to 20 cm from the beam center, downstream of the target, required detectors with a high rate capability, a good spatial resolution, and low material budget. The latter could only be matched by gaseous detectors whereas the most accurate ones, drift chamber and MWPC, could not fulfill the requirement in term of spatial resolution nor stand the expected particle flux. New technologies had to be invented and MPGDs have been considered for the first time as a realistic option. Since then, COMPASS has been at the leading edge of MPGDs and has demonstrated their great performances. As the next generation of experiments like COMPASS-II, LHC upgrades and future colliders, are being designed, a growing interest is put on MPGDs. In 2008 the R&D collaboration RD51 is created at CERN to regroup the efforts in MPGD research. As a result new promising technologies are being developed and the work presented here is a part of this effort.

This work aims at the development and characterization of MPGDs for high flux environment of hadrons, which are highly ionizing particles. This thesis is jointly supervised by the CEA Saclay, where most of the Micromegas technology was developed, and the E18 group of TUM, where the triple-GEM detectors of COMPASS were developed. Through the study of a Time Projection Chamber read by GEMs at E18 and a highly segmented Micromegas detector at Saclay, the characteristics and performances of MPGDs are explored.

The first chapter begins with the history and knowledge needed to understand MPGDs. A specific emphasis is put on the front-end readout electronics since they are an important part of the apparatus performances. At last the limitations of MPGDs are identified as a guideline for optimization.

A domain where electron amplification with MWPCs is a particular drawback concerns their use in Time Projection Chambers. Until recently, the large gaseous volume could only be read by wires that introduce a large quantity of ions requiring their suppression with an ion gate. The latter drastically limits the rate of such a detector to ~ 1 kHz. The intrinsic ion back-flow suppression, high-rate capabilities and large cluster size, make GEM detectors an ideal candidate for the amplification. Chap. 3 to 6 report on the full characterization of a GEM-TPC starting with the integration of a low noise front-end electronics dedicated to MPGDs. Chap. 5 develops the optimization of the reconstruction algorithms that, like the electronics, directly affect the detector performances. Through the results of two test beam periods, the characterization of a $10 \times 10\,\mathrm{cm}^2$ active area triple GEM prototype is reported in Chap. 6.

The second part of the thesis is dedicated to the development of the next generation of Micromegas detectors for the future COMPASS-II experiment. The foreseen increase of the beam intensity in addition to the activation of the central part of the detector requires a hadron rate capability up to $50\,\mathrm{MHz/cm}^2$. Tests with present COMPASS Micromegas chambers in a highly intense muon and hadron beams have shown the need to decrease the electronics occupancy by improving the segmentation of the readout electrodes. Hadrons are highly interacting particles which induce a discharge between the readout electrodes and the micro-mesh. This causes several micro seconds of dead time and ageing issues. A stable operation for COMPASS-II requires a discharge rate reduction from 10 to 100 that imposes to rethink the Micromegas concept. A dozen of dedicated prototypes have been built to test discharge rate reduction technologies. Chap. 8 describes the complete study of these detectors: from their assembly to their characterization during two test beam campaigns. Two promising solutions arise from this R&D: buried resistors and pre-amplification with a GEM foil. The latter combines the advantages of both Micromegas and GEM technologies and have been closely studied with simulations at the microscopic level as described in Chap. 9. Finally resistive and GEM pre-amplification solutions have been tested with $40\times40\,\mathrm{cm}^2$ prototypes in the COMPASS environment, Chap. 10 reports on the measurement of their performances.

Chapter 2

The Micro-Pattern Gas Detectors

Through an historical introduction followed by the review of the existing technologies and a compendium of the knowledge involved in the field of MPGDs, a picture of the state of the art is drawn around what constitutes the object of this work. A particular emphasis is put on signal processing and electronics. The limitations of these detectors are explored to serve as a guideline for innovative solutions that will push the performances of MPGDs .

2.1 Introduction to MPGDs

From the beginning of the XX$^{\text{th}}$ century, wire detectors have been used to detect ionizing particles. The history of gaseous detectors follows the miniaturization allowed by technological advances aiming at the reduction of the gap between the cathode and the electrode(s). Micro-Pattern Gas Detectors, or *MPGD*, are the latest development of this research.

This chapter will define, describe and explain the nature and the operation of MPGDs. First the general context will be given by a historical overview followed by the presentation of nowadays existing MPGDs. Then, details on gaseous processes and dedicated electronics will be given to show how to operate such a detector. Physical and electronics limitations will conclude this overview before continuing on the development and characterization of different types of MPGDs that is the core work of this thesis.

2.1.1 History: from Wire Counter to MPGDs

The history of gaseous detectors started more than 100 years ago in 1908 when Rutherford (shown in Fig. 2.1) and Geiger [1] invented the single wire proportional counter to detect newly discovered alpha particles. They learned how to operate this detector that consists of a wire in a gaseous volume closed by a cylindrical conductor. Depending on the potential difference that they applied between the wire and the cylinder, they discovered different working modes. At voltage of a few hundreds of volts, the output signal is rising with the high-voltage for a constant energy deposit, this is the proportional counter. With even higher voltages rendered possible by technological advances, the proportionality is lost, this is the Geiger-Mueller counter first described in 1928 [2]. It can be considered as the ancestor of all modern gaseous detectors and its particular discharge sound, caused by the discharge between the wire and the cylinder for each impinging particle, accompanied every measurement of radioactivity in the common culture.

In the 60's, large experiments at accelerators started using spark chambers invented in 1959. A high voltage pulse applied between stacks of electrodes induces a trail of sparks along the particle trajectory. The trail of sparks was recorded on photographic and early TV video cameras. This method

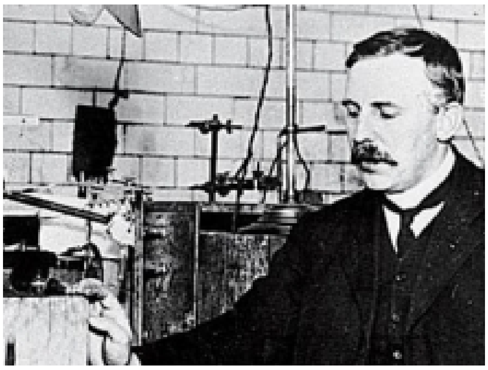

Figure 2.1: E. Rutherford, the father of gas detectors.

severely limits rate and the offline analysis by optical inspection is quite slow. A tremendous manpower was needed to produce results based on few events. For example, the E1A experiment at Fermi National Accelerator Laboratory used less than 60 polaroid pictures of sparks chambers to confirm the existence of neutral current [3]. Rare event physics pushed the development of electronic readout for sparks chambers. The most advanced system, using an array of wires, appeared in 1962 and was able to reach rates of tens of hertz [4]. Nevertheless it was still not a sufficient rate and it became the major limitation of experiments.

The revolution came in 1968 when Georges Charpak put together his experience with wire readout and gas detector, and invented, at CERN, the Multi Wire Proportional Chamber (MWPC), see Fig. 2.2. The MWPC was the first large array of sensitive elements with a fully parallel readout. The possibility of covering large areas at a moderate cost, low mass budget with great resolution modified the way particle physics experiments were done. Charpak obtained the Nobel Prize in 1992 for his “invention and development of particle detectors, in particular the multiwire proportional chamber” [4]. Several improvements of the MWPC such as: Drift Chamber, Multi-Drift Module, JET Chamber, Time Projection Chamber, Time Expansion Chamber, Multi-Step Chamber and many others, gradually replaced the original concept making use of different geometries and gas properties. By using the drift time in the gas volume, the drift chambers lowered by a factor of 5 the resolution of MWPC down to 100 µm. Nevertheless due to electrostatic repulsion, the maximal stable granularity for large detectors was reached at 2 mm, limiting spatial resolution. The radial electric field configuration of wires, not efficient for fast ion evacuation, limited the rate of MWPC. In addition complex gas mixtures, in particular Charpak’s so called “Magic gas” (mixture of argon, isobutane and CF_3Br), which have shown great gain performance, deposed chemical residue on wires, causing severe ageing issues. The last major drawback of the MWPC was its bad two-tracks resolving capabilities.

To overcome these issues, a gaseous detector without wire was invented in 1988, the Micro-Strip Gas Chamber (MSGC). Making use of photolithography on large insulating surfaces, the path of ions has been reduced to a hundred microns, enhancing by 2 orders of magnitude the maximal rate achievable by MWPC [5] and reducing the electrode granularity by a factor of 20. Unfortunately MSGCs have shown a slow degradation of gain over time under irradiation (due to polymerization of its materials), a high sensitivity to pollutants and also suffered from destructive discharges that melt the thin metal readout strips. In 1993, the Micro-Gap Chamber (MGC) [6] reduced the path for ion collection to 2 µm pushing the maximal rate achievable in gaseous detectors by another order of magnitude. Nevertheless, these detectors with a glass substrate were difficult to produce, expensive, limited in size and had a large material budget compared to other gaseous detectors.

Motivated by the challenging high luminosity foreseen at the future Large Hadron Collider at CERN,

Figure 2.2: G. Charpak, F. Sauli and J.C. Santiard at CERN with one of the first large MWPC prototypes.

several groups worked in the mid 90's on innovating geometries for gaseous detectors. In 1996 at Saclay, G. Charpak and I. Giomataris invented the Micro-Mesh Gaseous Structure (MicroMeGas[1]) [7], and the same year at CERN, F. Sauli designed the Gas Electron Multiplier (GEM) [8]. These technologies constitute the main core of what will be called the Micro-Pattern Gas Detectors (MPGD).

Since 1999, both Micromegas and GEM-based detectors have been extensively used at the SPS experiment COMPASS where, among other places, these technologies are in a continuous development. In 2008 the R&D group RD51 was created at CERN regrouping the efforts in MPGD research [9]; the work presented here started the same year.

In 2009, the CERN periodic magazine described "The continuing rise of micropattern detectors" [10] in particle physics showing the growing interest for these large size, low cost, low mass and fast detectors issued from more than 40 years of development after the MWPC. The constructive competition between "Micromegans" and "GEM-lovers" has encouraged the quest for the best of both technologies [4], leading to several new MPGD concepts that are described in Sec. 2.1.2.

Through the construction, development, characterization and simulation of new MPGD such as a GEM-TPC, a pixelized Micromegas, Micromegas with GEM pre-amplification and resistive Micromegas detectors, this thesis is taking a part in this effort on improving and pushing the performance of particle detectors that has started more than 100 years ago.

2.1.2 Overview of MPGD Technologies

Several geometries where used to achieve high gain and fast gaseous detectors. High gain is obtained by concentrating electric field lines in a small volume. Fast detectors have a short anode/cathode distance. With these two ideas in mind, new concepts have emerged following technical advances. After wire detectors, the MSGC and MGC used integrated circuit technology to etch thin anodes on glass substrate but have proven to be fragile. Then the genealogy of MPGDs divides in two main branches: Micromegas and GEM. Most of the efforts in the gaseous detector community were directed on the improvement of both technologies, giving birth to independent concepts. Meanwhile MSGC-like detectors continued to be explored especially in Asia with the MicroPIC detectors. A short description of these concepts gives here an overall view of the evolution of MPGDs.

---

[1] The historical writing of the Micro-Mesh Gaseous Structure is "MicroMeGas" whereas the simpler writing form "Micromegas" has been used in this text for a better readability.

MSGC (1988) The Micro Strip Gas Chamber, the close ancestor of MPGD, is the first gaseous detector that used photolithography to etch, on an insulator substrate, 200 µm pitch aluminum strips, see Fig. 2.3. Following the Drift Chamber concept, ions only have to drift 100 µm enabling a maximum particle rate (before a gain decrease) of 10^6 Hz/mm^2 compared to the 10^4 Hz/mm^2 of wire chambers. However the MSGC suffered from ageing issues and sensitivity to destructive discharges that kept them away from a wide use in particle physics. A MSGC tracker has been proposed for the Compact Muon Solenoid (CMS) experiment that reached a ~ 30 µm spatial resolution and stands a rate of 1 MHz/mm^2 [12] whereas the silicon detectors based solution has been preferred.

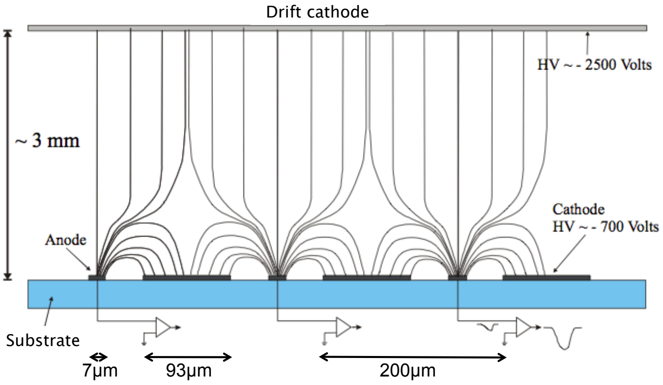

Figure 2.3: Field configuration of a MSGC [11]. Ion path from anode to cathode is reduced to 100 µm.

MGC (1993) The Micro Gap Chamber is an optimized version of a MSGC where the anode strip is situated on the cathode, shortening the ion drift distance to 2 µm as shown in Fig. 2.4. These detectors reach a 10 ns time resolution and an energy resolution of 14% (FWHM). It could stand a rate of 9×10^6 Hz/mm^2. These good performances made it an alternative between the precise, but small and expensive, solid-state detectors and the large and cheap wire chambers with moderate performances. Nevertheless the complexity of the process and the difficulty of fabrication of the glass substrate limited the size and possible utilizations of such a detector.

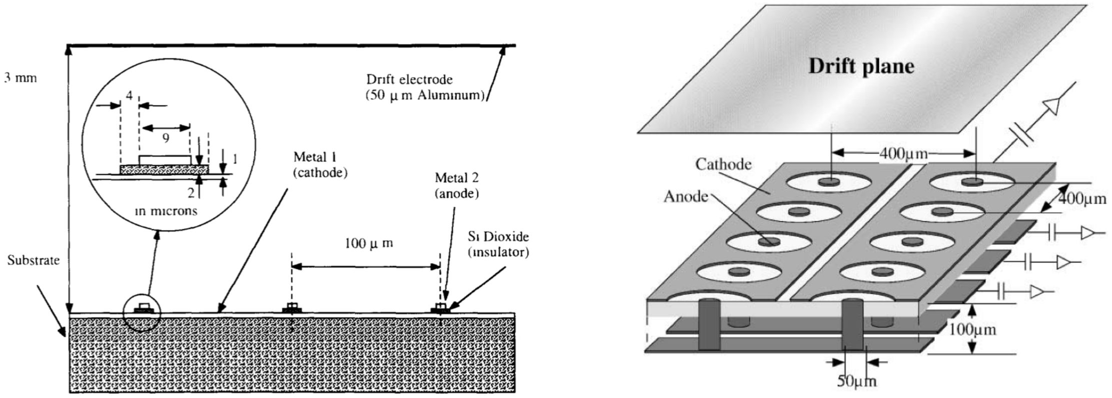

Figure 2.4: [Left] MGC schematic side view [6]. Anode wires are deposited on the top of a cathode to reduce the ion path to 2 µm. [Right] Schematic structure of a Micro Pixel Chamber [13].

***µ*PIC** (2001) The Micro Pixel Chamber (Micro PIC) is a MPGD using the Micro Dot Chamber [14] (MDC) pattern printed on a PCB. The idea is to use a small anode shaped as a dot instead of a strip.

The 100 μm circular gap around the dot shaped anode is used for amplification. By using signals of the anode and the cathode this detector provides signals on 2 dimensions using only a single stage monolithic detector. When the MDC is printed on silicon, it suffers from field distortion from the underneath anode wires. That is why this design must be printed on PCB. Unfortunately this promising detector suffers from discharges and has not been proven to be stable with gain above 10^3. A variation of this design with a Micromegas pre-amplification, the Micro-Mesh Micro-Pixel Chamber (M^3-PIC) [15] reaches a gain of 2×10^4 but loses all the advantages of a monolithic PCB with a 2 dimensional readout.

Micromegas (1996) By studying the reduction of the amplification gap of a parallel plate chamber, it appeared that small gaps have many advantages such as a high gain and fast ion collection. Using a metallic micro-mesh, a gas volume is separated in a sensitive volume, the *drift volume*, and an amplification volume. Primary charges are deposited in the drift volume so that they can drift, following the electric field, to the amplification gap, see Fig. 2.5. The high field in this second region, from 10 to 50 kV/cm, allows amplification with electron avalanche that induces a large signal on readout electrodes.

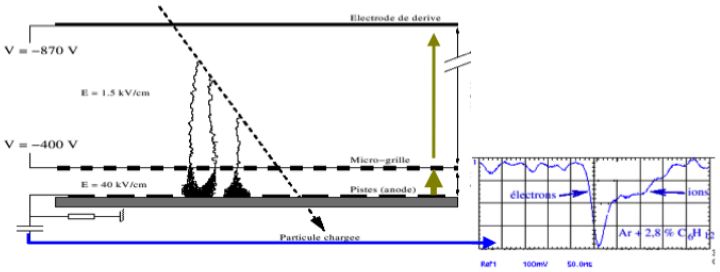

Figure 2.5: The Micromegas detector principle and the signal induced on the readout strips. A particle ionizes gas atoms, produces electrons drifting towards the amplification and induction gap, which is separated from the drift gap by a metallic micro-mesh. Between the micro-mesh and the readout strips, an intense electric field amplifies the primary electrons to induce the characteristic Micromegas signal on the readout strips. A more detailed description can be found in Chap. 7.

Fishing lines were first used to hold the micro grid at a tenth of a millimeter, and then came etched pillars on printed circuits to reduce dead areas and improve the flatness of the electrode. Since 2001, the Micromegas detectors have been successfully operated in COMPASS at rates up to 450 kHz/mm^2. The simple concept and field configuration make the Micromegas the simplest MPGD whereas it still suffers from discharges between the micro-mesh and the readout electrodes. This detector will be extensively discussed in this thesis, in particular in Chap. 7.

Bulk Micromegas (2006) By using simple PCB technologies, the micro-mesh has been integrated directly into the PCB, with the readout, as schematically shown in Fig. 2.6. This technique allows a good precision in the mechanical holding of the micro-mesh, in particular for nonar plan detector where the conservation of the amplification gap dimension is a challenge. The bulk technology [16] opens the possibility of industrial production of Micromegas with the standard PCB industry. Bulk detectors are very robust and are much easier to handle than GEM foils or thin micro-meshes. On the other hand, mechanical constraints at the production level still impose rather thick micro-meshes (18 μm diameter). That implies a larger material budget for bulk Micromegas detectors compared to standard ones, see Chap. 10 for an example at COMPASS. In 2008, 9 m^2 of bulk Micromegas detectors have been produced for the near detector of the T2K experiment [17].

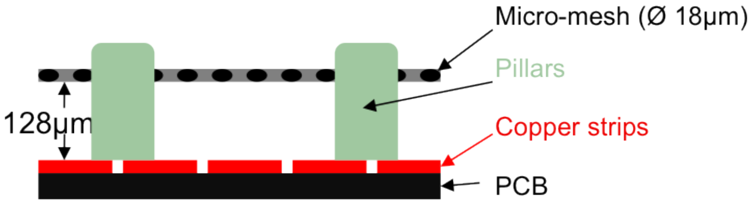

Figure 2.6: Principle of the bulk Micromegas. The woven micro-mesh, after lamination, is embedded into insulator pillars on the readout PCB. See also Fig. 2.7.

Resistive Micromegas (2002) The main issue with classic Micromegas detectors is the formation of discharges between the micro-mesh and the read-out electrodes, see Sec. 2.6.2 for details on discharges. The deposition of a resistive layer on the readout strips reduces the amplitude of discharges from several hundred of volts to less than one volt. When a discharge is forming in the amplification gap, the resistive layer potential reaches quickly the micro-mesh one and the discharge is quenched, see Fig. 2.7. There are several different resistive architectures, 3 of them are described and characterized in Chap. 8. In combination with the bulk technology, resistive Micromegas are one-stage amplification monolithic detectors that show virtually no discharge. This is a very promising technology even if its performances have not been completely investigated at the time of these lines are written. Ongoing R&D, described in Chap. 8, have shown promising results. The hope is to use it in experiments like COMPASS in 2012.

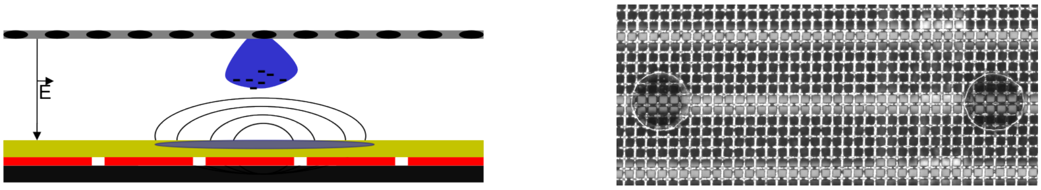

Figure 2.7: [Left] Principle of a simple resistive Micromegas. A resistive layer (in yellow) is deposited on the readout electrode. When a discharge (electron cloud in blue) starts from the micro-mesh, the resistive layer charges and creates an electric field that quenches the discharge. [Right] Photography of a detail of an active area of a restive bulk Micromegas. Two pillars, in transparent coverlay, hold the metallic micro-mesh. Underneath the mesh, dark zones are resistive pads connected on top of copper strips at a pitch of 400 µm.

Ingrid or integrated Micromegas (2007) Using a CMOS pixelized readout, Ingrid detectors integrates a Micromegas gaseous amplification stage in silicon using the Microelectromechanical systems (MEMS) production technologies, see Fig. 2.8. The Gridpix detector reaches a resolution of 4 µm (RMS), 50% efficiency with single electron extraction at a gain of 6×10^4. These hybrid MPGD/MEMS chips open new fields of application of gaseous detectors as CMOS-like sensors such as far UV camera or directional detectors for astrophysics.

GEM (1996) Another way of concentrating electric field lines in order to provide gaseous amplification is to use holes etched in an insulating material, as the Gaseous Electron Multiplier (GEM). In a GEM detector, and this is the main difference with Micromegas, the amplification stage is independent of the induction gap. This provides a great flexibility in terms of geometry and field configuration, but introduces mechanical complexity. A standard GEM foil is a 50 µm thick polyimide foil where a difference of potential is applied via two thin copper layers. The holes have a double conical

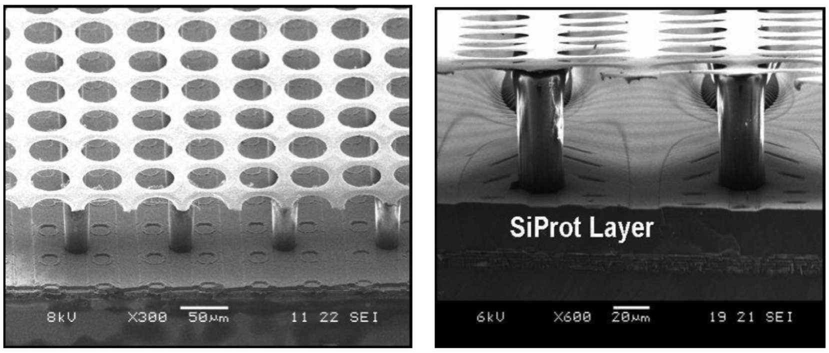

Figure 2.8: [Left] Scanning Electron Microscopy (SEM) image of the “InGrid” detector: a Timepix chip, resistive silicon-nitride (Si_3N_4) protection layer and insulating SU-8 pillars supporting a perforated aluminum grid of ∼ 1 µm. [Right] Photo of the “InGrid” structure with 7 µm Si_3N_4 protection layer [18].

shape with a 70 µm outer diameter and 50 µm inner rim diameter, see Fig. 2.9. There are a hundred of holes per mm on a standard GEM foil. Such an amplification stage can provide a stable gain of a few tens and therefore is usually used in a 3 layers stack. These triple GEM detectors have been extensively used in COMPASS since 2001 and in other experiments. A more detailed description with characterization is given later in Chap. 3.

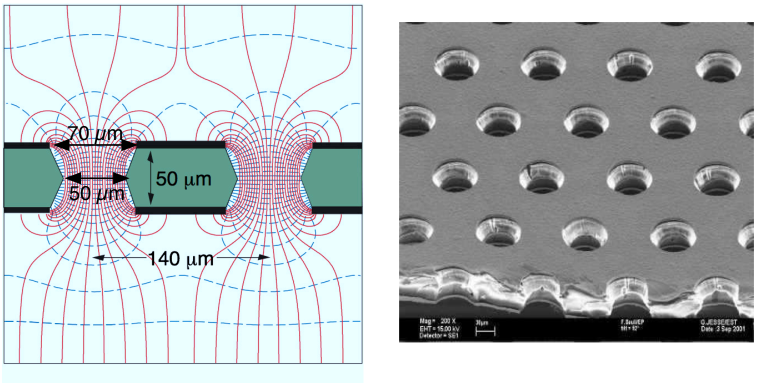

Figure 2.9: [Left] Electric field configuration of a GEM foil. [Right] Photography of a standard GEM foil, holes are spaced by 140 µm on the 50 µm thick polyimide foil [19].

MHSP (2000) The Micro-Hole and Strip-Plate is a GEM-like detector where the readout strip are printed on the bottom on the last foil on the stack, see Fig. 2.10. The readout strip follows the same pattern than a MSGC, it optimizes ion collection and lowers the ion backflow (as defined in Sec. 2.7) from a few percent for a standard GEM, to 0.1% and provides a two-stage amplification on a single foil.

THGEM (2004) The THick GEM detector is a GEM-like detector that uses a standard PCB instead of a kapton foil. With the increase of the hole size the performances are degraded but this detector is much easier to handle and a lot cheaper. Gains of 10^5 have been reached with a double THGEM with a high dependence on the space between the edge of the hole and the copper layer, the rim, see

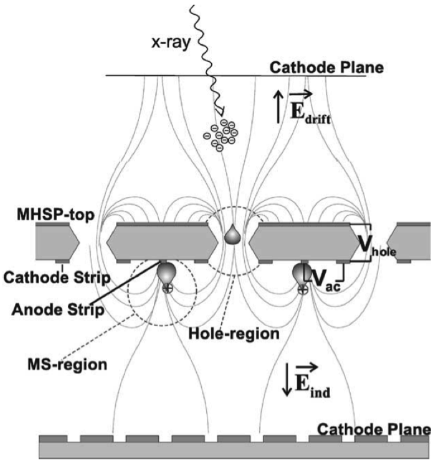

Figure 2.10: MHSP schematic diagram and its operating principle [20]. Charges deposited above the MHSP by radiation, *e.g.* an X-ray photon, are focused into a hole and multiplied as in a GEM. Avalanche electrons are transported toward the anode strips and multiplied in a second avalanche process. A part of the avalanche ions are collected at the cathode plane localized below the MHSP.

Fig. 2.11. Its successful operation in several noble gases at cryogenic conditions (notably LAr) was recently demonstrated [22]. THGEM are considered to be used as photon detector for Cherenkov imaging applications [21].

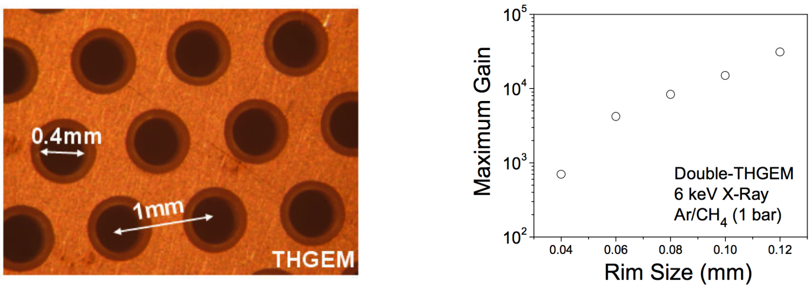

Figure 2.11: [Left] Photograph of a typical THGEM electrode; the hole diameter is 0.4 mm with a 0.1 mm etched rim, at a 1 mm pitch. The thickness of the PCB is 0.5 mm [Right] Maximum attainable gain versus rim size (same geometry as on [Left]). [21].

RETGEM (2007) To increase the maximum gain reachable with a THGEM detector, the REsisTive GEM makes use of a resistive layer to avoid discharges [23], it can operate at gains as high as THGEM while offering the advantage of being fully spark protected. Another variation of THGEM is the Strip Resistive Thick GEM (S-RETGEM), a photosensitive gaseous detector, which has been developed for an early forest fire detection system [24].

This catalogue of technologies shows the recent and constant progresses that have been achieved in the field and its variety. It is very likely that the next generation of experiments will use MPGDs. Other types of detectors, such as silicon based or RPCs have shown their limit in terms of radiation hardness, material thickness and rate capabilities in LHC experiments. Further development are of course necessary to bring MPGDs to their maximum potential.

To help understand these technologies, we will describe the processes and principles that are implicated in their operation after a short overview in Sec. 2.2.

2.2 Basic Principles of MPGDs

To explain how a gaseous detector works, we describe here the different steps from the interaction of particles with the detector to the final digital physics information. Fig. 2.12 summarizes the various steps of the treatment of the information from the creation of the signal inside the detector to the offline reconstruction of the position of the impact of the particle.

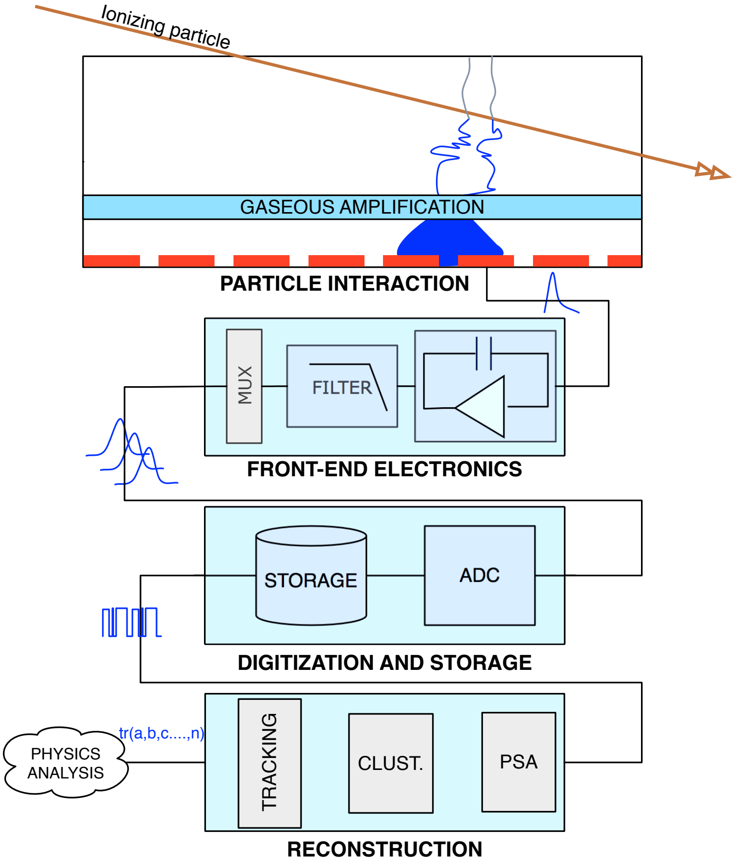

Figure 2.12: Schematic block view of the treatment of a signal from a MPGD. It shows the basic steps from the particle ionization to the reconstructed track of a particle. The first stage represents the interaction with an ionizing particle, the drift of two primary electrons, their amplification and the signal induction on the readout electrodes. The second stage symbolizes the analog electronics that amplifies and shapes signals for the third stage where they are digitized and stored. The last stage consists of an algorithm that converts the stored signals into useful information.

These processes will be described in the following sections : First gaseous interactions with the particle are describe in Sec. 2.3, then electronic amplification, filtering and digitization in Sec. 2.4.1. This description will be concluded by the overview of reconstruction algorithms in Sec. 2.5. To complete this general picture of the functioning of MPGDs, their limitations are explored in Sec. 2.6.

2.3 From Primary Ionization to Electrical Signal

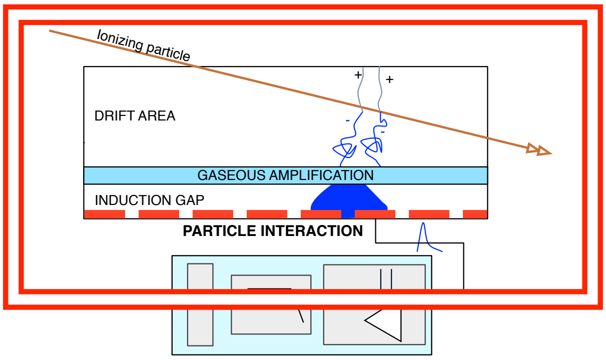

Figure 2.13: Drift of primary electrons and formation of an electrical signal on the detector electrodes.

The following developments are mainly based on wider and more general text books [25], [26] and [5].

2.3.1 Physics of Ionization

Gaseous detectors detect particles by locating the ionization that has been created in the active gas volume. The impinging particle interacts by inelastic collisions that either ionize or excite gas atoms. Ionization creates directly free electron/ion pairs. Excitation is followed by a de-excitation. In the *Penning effect*, the excited atom is in a metastable state and de-excites by emitting a photon that can interact with another atom, creating a resonance, or leave the active volume of the detector. In the *Jesse effect*, the excited atom ionizes an atom or molecule of another specie (the quencher) that has an ionization potential lower than the excitation energy of the first specie (generally a noble gas) [25].

The average number of primary pairs created by the interaction between the ionizing particle and the gas atoms is $< N_P >$. The actual number follows a Poisson distribution, proportional to $\exp(-< N_P >)$. As a result, the number of primaries does not fluctuate extensively for $< N_P >$ over 10. For instance, for particles at the minimum of ionization (MIP) in a gas mixture of $\mathrm{Ne/C_2H_6/CF_4}$ at 80/10/10, $< N_p >= 18.7\ \mathrm{cm}^{-1}$. In that case, there is about a 0.5% probability for a primary ionization to contain less than 9 pairs.

The primary electrons usually have enough energy to ionize again the gas and to create secondary charges. The total number of created charges, N_T, is the sum of primary and secondary charges. N_T a few times larger than N_P, see Tab. 2.1.

The probability of a released electron to have an energy E or higher follows an approximate $1/E^2$ dependence (Rutherford law). It leads eventually to an energetic electron (delta electron) that will travel and ionize atoms leaving a trail of several hundreds of microns, decreasing the spatial resolution of the reconstructed particle position.

For a given gas mixture, one can estimate the average number of total electrons by using the mean energy $< \mathrm{w_{mix}} >$ needed to created a pair for a given gas with:

$$< w_{mix} >= \sum_{i=1}^{n} w_i \tag{2.1}$$

where n is the number of gaseous species and w_i its average energy required to produce one electron-ion pair in the gas specie i. Tab. 2.1 gives the w_i of the most common gases used in gaseous detectors.

Gas	Z	A	Density	E_x (eV)	E_i (eV)	w_i (eV)	$[dE/dx]_{mip}$ (keV/cm)
He	2.0	2.0	0.178	19.8	24.5	41	0.32
Ar	18.0	39.9	1.782	11.6	15.7	26	2.44
Ne	10	20.2	0.90	16.6	21.56	36.3	1.56
Xe	54	131.3	5.86	8.4	12.1	22	6.76
CF_4	42	88	3.93	12.5	15.9	54	7
CO_2	22	44	1.98	5.2	13.7	33	3.01
CH_4	10	16	0.71	9.8	15.2	28	1.48
C_2H_6	18	30	1.34	8.7	11.7	27	1.15
iC_4H_{10}	34	58	2.59	6.5	10.6	23	5.93

Gas	N_P (cm^{-1})	N_T (cm^{-1})	Radiation Length (m)	Ion	Mobility (cm^2/V.sec)
He	4.2	8	745	-	-
Ar	23	94	110	Ar^+	1.00
Ne	12	43	345	-	-
Xe	44	307	15	-	-
CF_4	51	100	92.4	$iC_4H_{10}^+$	1.00
CO_2	35.5	91	183	CO_2^+	1.09
CH_4	25	53	646	Ar^+	1.87
C_2H_6	41	111	340	$C_2H_6^+$	1.23
iC_4H_{10}	84	195	169	$iC_4H_{10}^+$	0.614

Table 2.1: Physical Properties of gases at 20 °C and 760 Torr [27]

2.3.2 Drift, Transport and Diffusion in Gas

The created charges drift from the ionization zone toward the electrodes following the electric field $\vec{E}$. The electron velocity v, and its mean value, the drift velocity $< v >$, heavily depend on the mean time τ between two collisions with the gas atoms. This depends on the scattering cross-section, which is an emergent property of the molecular/atomic structure. Therefore the drift velocity is highly dependent on the nature of the gas but can be appreciated with a simple collision model :
the number of collisions dn is

$$\mathrm{dn} = \frac{\mathrm{d}x}{v\tau} \tag{2.2}$$

Between two collisions, the electron motion follows:

$$\mathrm{m}\frac{\mathrm{d}v}{\mathrm{d}t} = \mathrm{q_e E} \tag{2.3}$$

that gives in function of time:

$$x(t) = \frac{1}{2}\frac{\mathrm{q_e}}{\mathrm{m}}\mathrm{E}\cdot t^2 + t\cdot v_0 + x_0 \tag{2.4}$$

With v_0 and x_0 constants. The time between two collisions is determined by the probability, dP, of 0 collision between 0 and t, and exactly 1 collision between t and $t + \mathrm{d}t$

$$\mathrm{dP} = \frac{1}{\tau}\exp(-t/\tau)\mathrm{d}t \tag{2.5}$$

So the average displacement is:

$$<x>=\int_0^\infty \frac{1}{2}\frac{\mathrm{q_e}}{\mathrm{m}}\mathrm{E}t^2\mathrm{d}t=\frac{\mathrm{q_e}}{\mathrm{m}}\mathrm{E}\tau^2 \tag{2.6}$$

that gives the drift velocity for a given gas :

$$<v>=\frac{<x>}{\tau}=\frac{\mathrm{q_e}}{\mathrm{m}}\mathrm{E}\tau=\mu\mathrm{E} \tag{2.7}$$

where μ is the electron mobility (that also depends on E).

The mobility of ions, μ^+ is typically 10^3 times lower than the one of electrons. This causes the formation of space charge and limits the gain at high rate. This effect motivates the reduction of the distance between anode and cathode, which is the base principle of MPGD, see Sec. 2.6.

As the electron cloud drifts toward the anode, it diffuses in the gas following a Gaussian shape in all directions[2]. Its spherical spread (of radius r) scales with the square root of time (or distance) from the ionization point:

$$\sigma(r)=\sqrt{6\mathrm{D}t} \tag{2.8}$$

with D is the diffusion coefficient, a property of the gas.
Polyatomic gases are used in addition to noble gases for several reasons. Due to their large inelastic cross-section, they absorb the energy from the drifting electron and, in most of the gases, bring it to the Ramsauer-Townsend minimum. By using a polyatomic gas, such as CO_2, CH_4 or CF_4, one can achieve large drift velocities, and reduce diffusion near the thermal limit [26]:

$$\mathrm{D}=\frac{\mathrm{kT}\mu}{\mathrm{e}} \tag{2.9}$$

The Tab. 2.1 shows for instance that the velocity of the ions Ar^+ is greater in CH_4 than in pure Ar.
Another way to the reduce diffusion is to apply a longitudinal magnetic field. Through the Lorentz force, electrons are focused between collisions modifying the diffusion.
Another advantage of adding polyatomic gases is that they absorb UV light emitted by the excited noble gas atoms, which is largely involved in sparks formation (especially in the streamer mechanism, see Sec. 2.6).

Electronegative molecules, such as H_2O, CO_2 or CF_4, can capture electrons. The capture mechanism depends on the electric field and strongly on the gas mixture because of the three-body electron attachment [28]. A 0.1% addition of O_2 in an Ar/CO_2 mixture increases the electron capture by a factor 20, lowering the gain and decreasing the efficiency for long drift distances. This is why a special care of the gas system is required for the Ar/CO_2 GEM-TPC.

2.3.3 Electron Amplification in Intense Electric Field: the Avalanche Mechanism

When electrons from the primary ionizations gain enough kinetic energy between collisions to ionize gas atoms, a chain reaction called avalanche is formed.
The number of new electrons extracted $d\mathrm{n}$ within a distance $\mathrm{d}x$ is:

$$d\mathrm{n}=\alpha_{\mathrm{T}}dx \tag{2.10}$$

---

[2] There may be anisotropies in certain gases under the influence of an electric field

with α_T the first Townsend coefficient which is the inverse of the mean free path for ionization, λ: $\alpha_T = 1/\lambda$. λ decreases when the electric field increases. From Eq. 2.10 we have, for a path length within the amplification gap of a parallel plate detector (uniform electric field):

$$n = n_0 \cdot e^{\alpha_T x} \tag{2.11}$$

n_0 is the number of electrons arriving in the amplification gap; so the gain G is defined as

$$\mathrm{G} = \frac{n}{n_0} = e^{\alpha_T x} \tag{2.12}$$

An empirical maximum of the gain has been observed for parallel plate detectors and is known as the Raether limit at $G \approx 10^8$ [29]. Beyond the Raether limit, the avalanche process diverges and a discharge is formed. The exponential shape of the newly created electrons form a liquid-drop shape avalanche, with the head composed of electrons and the slower ions trailing, see Fig. 2.14.

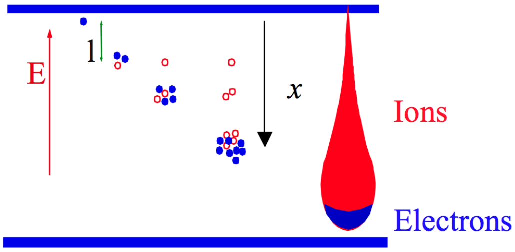

Figure 2.14: Charge multiplication in a uniform field. $l = \lambda$ is the mean free path for ionization [19].

α_T has been extensively studied for wire counters and depends on the gas, its pressure and the electric field. An early description from Rose and Korff is given for example:

$$\frac{\alpha_T}{P} = A e^{-B/PE} \tag{2.13}$$

with P the gas pressure and A, B constants that depend on gas parameters [30].
The number of created electrons follows a Furry distribution at low gain and a Polya distribution at high gain (as for the single photon response of a photo-multiplier) [31].

2.3.4 Induction and Signal Formation on the Readout Electrode, Ramo's Theorem

The formation of the current pulse on the readout electrode, often called "charge collection", begins when a charge moves in between the electrodes (and not when electrons arrive on strips as the term "collection" suggests), inducing a current on neighboring conductors. The shape of the signal depends on the number of charges, their position and their path in the detector.
S. Ramo gives a method [32] for computing the instantaneous current in neighboring conductors by a given specified field. This field is called *weighting field* and is calculated by computing the electric field created by the conductor, for which we want to compute the induced current, at a given potential (usually 1 V) and all other conductors grounded. The weighting field can be different from the electric field. The general case of the current $\mathrm{i_A}$ induced by a charge q on a conductor (see *1* in Fig. 2.15) is:

$$\mathrm{i_A} = \frac{\partial \mathrm{Q_A}}{\partial t} = \mathrm{q}\frac{\partial \mathrm{V_e}}{\partial t} = \mathrm{q}\frac{\partial \mathrm{V_e}}{\partial x}\frac{\partial x}{\partial t} = \mathrm{q} \cdot v_x \frac{\partial \mathrm{V_e}}{\partial x} \tag{2.14}$$

where v_x is the charge velocity and $\partial \mathrm{V_e}/\partial x$ is the weighting field. This method is extensively used in GARFIELD [33], the well-known electromagnetic field computing software.

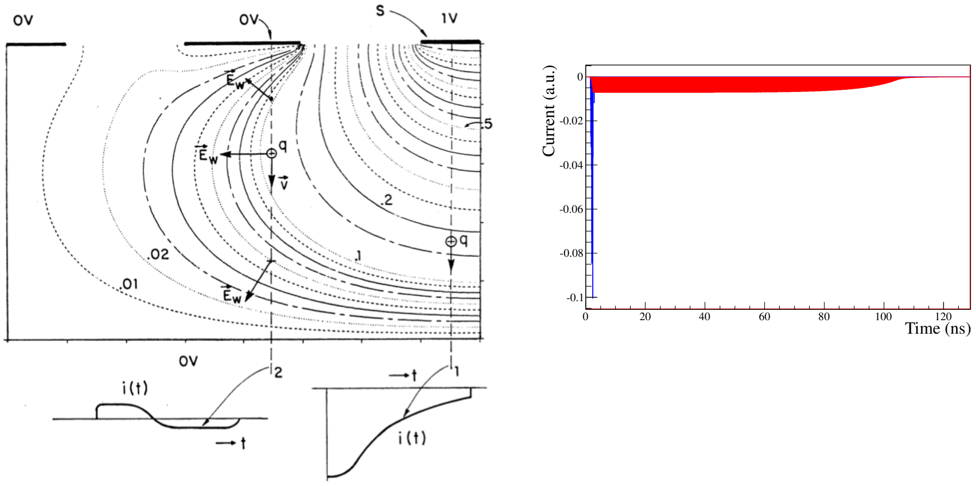

Figure 2.15: Left: The induced signals on strip by two charges using the weighting field $\vec{E}_w$ of the right strip at 1 V [5]. Right: Garfield simulation of an induction signal in a Micromegas strip detector, see Chap. 9. Blue represents the part of the signal induced by electron, red by ions.

Example of Ramo's theorem

1. **Parallel plate geometry:** Two charges, an electron and an ion are created in the middle of two parallel electrodes separated by a distance d, at potential V_b. The electric field E and the weighting field E_w (when a 1 V potential is applied) are:

$$E = \frac{V_b}{d} \text{ and } E_w = \frac{1}{d} \tag{2.15}$$

And the charge velocities v are

$$v_{e^-} = \mu_{e^-} \cdot E = \mu_{e^-} \frac{V_b}{d} \text{ and } v_{I^+} = \mu_{I^+} \cdot E = \mu_{I^+} \frac{V_b}{d} \tag{2.16}$$

Then the induced currents are

$$i_{e^-} = q_{e^-} \cdot v_{e^-} E_w = q_{e^-} \mu_{e^-} \frac{V_b}{d} \frac{1}{d} = q_{e^-} \mu_{e^-} \cdot \frac{V_b}{d^2} \tag{2.17}$$

$$i_{I^+} = q_{I^+} \cdot v_{I^+} E_w = q_{I^+} \mu_{I^+} \frac{V_b}{d} \frac{1}{d} = q_{I^+} \mu_{I^+} \cdot \frac{V_b}{d^2} \tag{2.18}$$

Since the charges are moving in opposite directions along x, the charges inducted by the electron Q_e and by the ion Q_i are:

$$Q_{e^-} = q_{e^-} \cdot \mu_{e^-} \cdot \frac{V_b}{d^2} \cdot \frac{x d}{\mu_{e^-} \cdot V_b} = q_{e^-} \cdot \frac{x}{d} \tag{2.19}$$

$$Q_{I^+} = q_{I^+} \cdot \mu_{I^+} \cdot \frac{V_b}{d^2} \cdot \frac{d(d - x)}{\mu_{I^+} \cdot V_b} = q_{I^+} \cdot (1 - \frac{x}{d}) \tag{2.20}$$

From the middle of the detector $x = d/2$ and we have:

$$Q_{I^+} = Q_{e^-} = \frac{q_{e^-}}{2} \tag{2.21}$$

In general the contribution of electrons and ions are not equal as in Eq. 2.21. For example in a Micromegas detector, that has a geometry close to the previous example, the avalanche mechanism creates the major part of the charges close to the readout electrodes. The fast electrons reach almost instantaneously the grounded electrode creating a very fast signal of ~ 10 ps whereas the main part of the signal comes from the ions slow drifting from the readout to the micro-mesh. A GARFIELD simulation [33] of a COMPASS detector shows the shape of the signal in Fig. 2.15

2. **Strip detector:** A charge is released in the same situation as in the previous parallel plate detector but the electrodes are segmented in strips. As previously the charge induces a current on the k^{th} strip on which it has been released but it also affects the $k+1^{\text{th}}$ strip. The weighting field change of sign along the charge path for these strips. Then the charge induces a bipolar signal that has an integral of zero, so that no energy is transferred.

3. **Pixel detector:** The same mechanism produces a signal on a pixel but the weighting field is more concentrated near the pixel. When the charge is in the induction gap, it only sees a small fraction of the pixel weighting field and the signal amplitude induced on the pixel is lower than for a strip in the same configuration.

The "physical" part of the detection ends here, the next section will treat the process of the signal produced by the mechanisms that have been described.

2.4 Front-End Electronics and Reconstruction

The electronics of a detector and the reconstruction algorithms might appear only remotely connected to a pure discussion on detector. Whereas in modern experiments, these technical issues are probably the most time consuming work of an experimental physicist. Even if the electronics is not a part of the detector itself, it deeply defines the detector capabilities.
The electronics of a gaseous detector is usually divided in two. An analog part close to the detector, called the Front-End Electronics (FEE), which pre-amplifies, shapes and bufferizes the analog signals. The second part, the digital electronics, controls, samples and transmits the information of the FEE. This architecture allows to cover the time latency between the event and the recording signal without making an extensive use of digital electronics, which is expensive, and power consuming. When the performances of a detector are considered, it is in reality the performances of a detector apparatus, including electronics and reconstruction algorithms.

In the next sections, the different parts of the detector apparatus are reviewed: the front-end analog electronics, the digitization of the signals and the reconstruction algorithms. Possible reconstruction errors and noise consideration are given in Sec. 2.6.

This section and the following are based on more general texts [34], [26], [35] and [36].

2.4.1 From Signals to Data; Front-End Electronics for MPGDs

Although there is a large variety of analog signal processing architectures, it is possible to enhance several general principles such as pre-amplification, shaping and digitization. Here we will mostly focus on tracking detectors and we will illustrate the discussion with the electronic circuits used in this thesis: the SFE16 [37], the APV25 [38] and the AFTER [39]. After their induction, electronic signals are recorded for offline analysis. The steps sketched in Fig. 2.16 are detailed in the next sections.

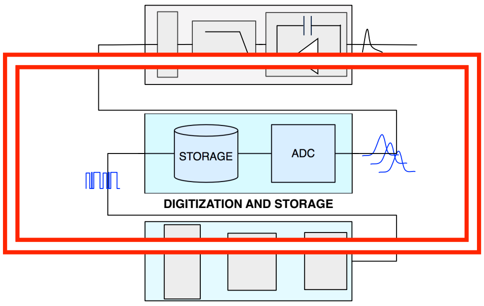

Figure 2.16: The electronics block schematics, from detectors signals to digital information.

The complex optimization of the FEE is made by tuning different, and often contradictory, parameters, such as: signal to noise ratio (SNR), detector capacitance, high integration, low material budget, linearity with signal amplitude, discharge resistance, radiation hardness, bandwidth, low power consumption, price per channel...
Here we will mainly focus on the qualities that have an impact on the overall detector efficiency and the SNR.

2.4.2 Overview of Analog Front-End Readout Electronics for MPGDs

Fig. 2.17 shows the main blocks of the analog part of a FEE that will be discussed in the next section. Directly at the output of the detector there is the protection circuit that avoids the destruction of the

ASIC in case of a discharge at the readout electrodes. Then, usually in a dedicated ASIC, there is a pre-amplification stage consisting of Charge Sensitive Amplifier (CSA), then several filters for Pole Zero Cancelation (PZC) and pulse shaping. Filtered signals are stored in a memory to cover the trigger latency (time between the detector records the passage of particle and the reception of the trigger signal). A description of these parts follows from Sec. 2.4.2.1 to Sec. 2.4.3.1. The use of analog circuit can be bypassed by direct digitization whereas it requires one high-speed ADC per detector channel.

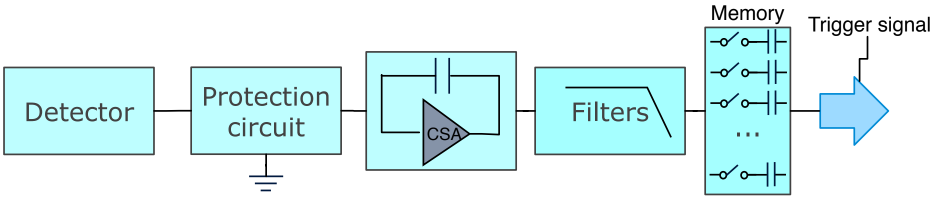

Figure 2.17: Front-end electronics chain from detector to digitization.

2.4.2.1 Electronics Protection Circuit

To avoid being damaged or deprogrammed, the FE chip has to be protected from large currents coming from the detector electrodes. Fig. 2.18 shows the protection circuits used for Micromegas and GEM detectors. For GEM detectors, the chip is protected by diodes that ground every signal above the minimum forward bias of the diodes. A capacitor of ten times the strip capacitance is used for AC coupling and to isolate from the leakage current of the diodes. This capacitor also affects the detector signals by lowering their amplitude by 10% [40]. With Micromegas detectors, it is needed to have a fast recovery of the more frequent discharges. To avoid draining all the charges of the micro-mesh, the readout electrode is not grounded via the two diodes, but reaches the micro-mesh voltage thanks to a large resistor. A large capacitor provides the AC coupling and diodes protect the ASIC from voltage spikes. The resistor introduces more electronic noise than in the GEM case. However it provides a fast recovery of a few milli-seconds after a discharge.

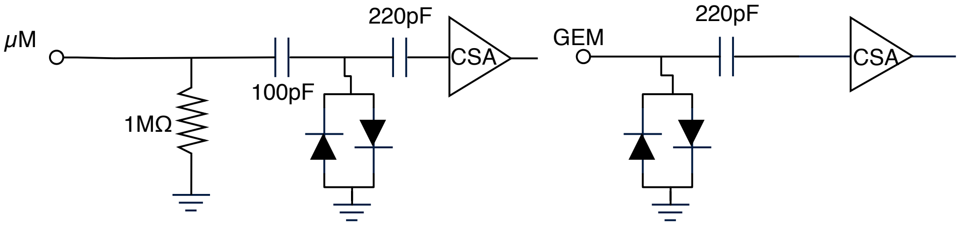

Figure 2.18: Protection circuit of front-end for Micromegas [Left] and GEM [Right].

2.4.2.2 Amplification and Charge Sensitive Amplifier

With a gaseous detector, the quantity to be measured is the total charge deposited by the impinging particle. That is why the signal needs to be integrated in the pre-amplification stage. This is done by a Charge Sensitive Amplifier, CSA, which integrates signals on the feedback capacitor C_f as shown in Fig. 2.19. The amplifier has to be the as close as possible to the detector to avoid picking up electromagnetic noise on long wires that also increase the detector capacitance.

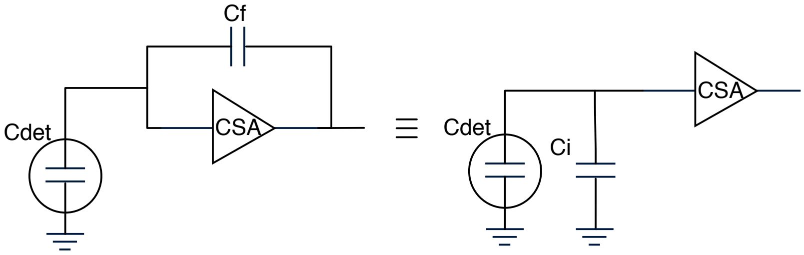

Figure 2.19: [Left] A simple Charge Sensitive Amplifier. [Right] The equivalent circuit of the CSA with the input capacitor C_i as defined in Eq. 2.24.

The energy deposited by the incident particle is proportional to the integration of the current pulse:

$$E \propto Q_i = \int i_s(t)dt \tag{2.22}$$

where $i_s(t)$ is the detector signal that lasts hundred of nanoseconds. The gain of the CSA is set by the well controlled value of C_f where the accumulated charge is:

$$Q_f = C_f \cdot v_f = C_f \cdot (A_D + 1) \cdot v_i \tag{2.23}$$

with A_D the open loop gain of the amplifier. Since no current can flow through the amplifier, all the charge Q_i charges C_f so $Q_i = Q_f$. Then the equivalent capacitor at the entry of the amplifier is:

$$C_i = Q_i / v_i = C_f \cdot (A_D + 1) \tag{2.24}$$

The charge is shared between the detector capacitance, C_{det} and C_i. With Q_s the signal charge we have:

$$\frac{Q_i}{Q_s} = \frac{Q_i}{Q_d + Q_i} = \frac{1}{1 + \frac{C_{det}}{C_i}} \tag{2.25}$$

From Eq. 2.25 we deduced that the entry capacitor must be much larger than the detector capacitor to avoid loosing charges: $C_i \gg C_{det}$.

In the high frequency domain, the amplifier has a limited bandwidth that corresponds to a limited frequency domain. In this region, the entry impedance, Z_i, becomes real (resistive):

$$Z_i = \frac{1}{\omega_0 \cdot C_f} \equiv R_i \text{ and } \tau_i = R_i \cdot C_{det} = \frac{C_{det}}{\omega_0 \cdot C_f} \tag{2.26}$$

where τ_i is the rising time of the signal (from 5% to 95%) and ω_0 the product of the gain and the cut-off frequency of the amplifier ($\omega_0 = G_{f_\mu} \omega_\mu$). From Eq. 2.26 we can see that, in order not to cut the fast rise of the signal, C_f must be smaller than C_{det}.

To summarize, an ideal CSA would have, at the same time, $C_i \gg C_{det}$ and $C_f \ll C_{det}$. This implies a moderate gain and similar values for C_{det} and C_f with $C_{det} > C_f$.

For a standard strip detector of a few decimeters strips length, $C_{det} \approx 40$ pF. To match this range of impedance, the AFTER has a tunable feedback capacitor from 100 fF to 1 pF [39], 0.5 pF for the SFE16 [37], and 150 pF for the APV25 [41].

2.4.2.3 Filtering and Shaping

The CSA is connected to several stages of filtering, often tailored for the application and the type of detector signals. There are two main aims that must be achieved by the shaping stage:

1. Limit the bandwidth in order to match the measurement time. A broader bandwidth would only increase the noise.

2. Avoid high-rate effects, such as piling-up signals, by shortening the signals as much as possible

To match the detector bandwidth, the shaper consists, at least, of one high pass and one low pass filter. The simplest way to design such a filter is a CR-RC filter as pictured in Fig. 2.20. The CR filter differentiates the signal and cuts low frequencies. The RC does the opposite, it is an integrator with high impedance that cut high frequencies, see Sec. 2.6.4.4 for noise optimization.

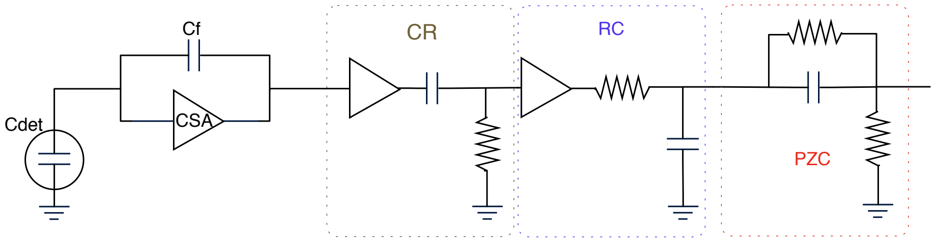

Figure 2.20: The pre-amplifier and a simple filtering chain. The shaping is done by the CR and the RC stage. The Pole Zero Cancelation (PZC) corrects for undershoot.

In order to obtain a more symmetrical shaping, a CR-nRC is usually used, as for the AFTER chip that embedded a 6th order CR-nRC filter [39]. The difference in signal shapes is shown in Fig. 4.2.
After this filter, the signal has an exponential tail that might lead to undershoot. A signal with a long negative tail leads to amplitude defects for the following signals. This undershoot is corrected by using a Pole Zero Cancellation (PZC) filter, where the terminology “pole” comes from the Laplace transformation terms. The PZC simplest architecture is shown in Fig. 2.20.

2.4.2.4 Analog Memory

After filtering, signals would be ready for digital recording. Nonetheless, in high-energy physics, the decision to record an event or not, the so-called *trigger*, is issued from other faster detectors (usually by plastic scintillators). Even if these detectors are very fast compared to our gaseous detectors, in addition comes electronic logic, used to combine the trigger signals, and the cables interconnecting the system. At the end, there are several microseconds between the physical event and the moment when the trigger arrives at the detector. The front-end electronics has to cover this delay, the trigger latency, by temporally storing the signals in a memory.
Both in the APV and the AFTER chips, the same type of memory has been chosen, the Switched Array Capacitor (SCA). The SCA consists of arrays of capacitors, constantly storing signals in between trigger signals, erasing the previous value stored in it (circular buffer). This buffer consists of 192 cells for the APV25 chip [38] and 512 cells for AFTER [39]. The basic cell of the SCA is described in Fig. 2.21. More complex architectures exist, where it is possible to write and read the circular buffer at the same time to avoid dead time between cycles, as for the APV25 or DREAM ASIC [42].

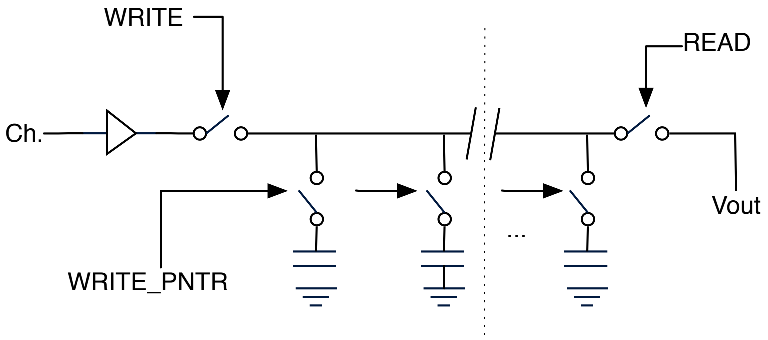

Figure 2.21: Principle of an analog memory: the Switched Capacitor Array (SCA). The signal “WRITE” connects a channel to the storing capacitor connected by the signal “WRITE_PNTR”. When the values need to be read, the “READ” signal connects the memory cell to Vout.

2.4.3 Trigger and Digitization

When a trigger signal is issued, the analog signals from the SCA are multiplexed and transported on a single differential line to an Analog-to-Digital Converter, the ADC. Physics requirements for this part are less critical than what is already available on the market, driven by the telecommunication technologies where high performance ADCs are crucial. 12 bits ADCs with a speed of 500 MS/s and consumption of less than 5 W are widely spread.

Fig. 2.22 shows the flash converter, one of the most common ADCs in particle physics thanks to its fast and simple one-stage architecture. Its synchronization with the multiplexer of the analog electronics might be a delicate point that limits cable length between the ADC and the analog FE.

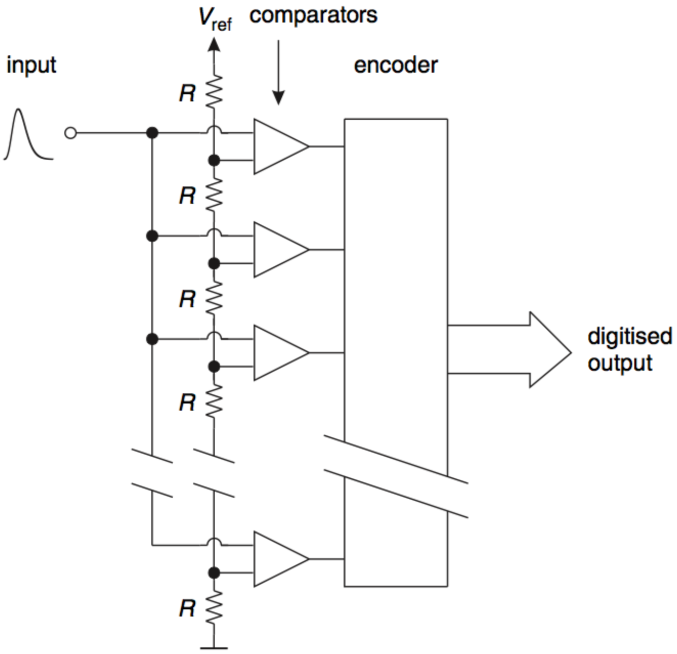

Figure 2.22: Principle of a flash ADC. “input” is compared to the reference voltage V_{ref} and its division by powers of two by the comparators. When “input”> V_{ref}, the overflow signal is at ‘1’. The ADC is synchronized with a clock signal that enables the encoder to convert its input into bits [35].

2.4.3.1 From ADCs to Data Storage

An ADC card is usually connected to more than one front-end ASIC. On the other side it is connected, via optical fiber in modern systems, to a data concentrator. In order to have a scalable acquisition system, it is needed to first go through a data concentrator that is connected to several ADC cards before being connected to the data acquisition (DAQ) computers. The DAQ computers are in charge of buffering and reconstructing data for a whole experiment setup, event by event. Then the data files are stored to be analyzed later. The volume of data from experiment can be huge and therefore communication and storage is a challenge by itself that is beyond the scope of this overview, at COMPASS annual data volumes are in the range of 1 to 2 PB.

The basic principles of a MPGD FEE have been exposed in this section. Important noise calculations and considerations will be found in Sec. 2.6.4. The next section is dedicated to digital reconstruction, where the goal will be to reconstruct the impinging particle characteristics.

2.5 From Raw Data to Track Parameters: Data Reconstruction

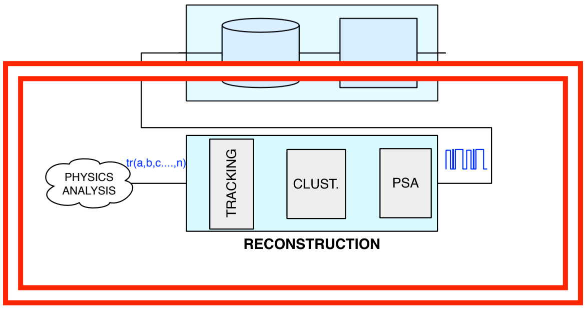

Figure 2.23: Sketch of the main steps of data reconstruction.

With tracking detectors, the final goal is to reconstruct the particles path and kinematic. This is done by combining the different information given by several detectors and searching for the expected trajectory of a particle, in the general case a helix (straight lines are a particular type of helices). In this section we will describe how, from the recorded pulses, we reconstruct tracks.

2.5.1 From Raw Data to Hits

Every FEE is transmitting raw data in a different format. It can consist of a continuous data stream, one or several samples taken after the trigger signal synchronized by a clock, time over threshold, the maximum amplitude or just a Boolean information (signal or not).
If needed, the first algorithm in which the data are processed is the Pulse Shape Analysis (PSA). Its goal is to identify signals in the data stream by looking at a characteristic shape. The PSA divides the raw signals and convert it into a “hit”. A hit position is given by the position of the electrode connected to the recorded channel. Here are the most common means to reconstruct these information:

Amplitude or charge : With a limited number of samples per event, usually taken over a certain threshold, the amplitude (and/or the sum of amplitudes) of a given pulse is proportional to the charge that has been deposited by the impinging particle. Another way to reconstruct the amplitude is to use the maximum of a pulse or the amplitude at given time after the trigger (as for the APV). In the case of a Time Over Threshold FEE, the amplitude is proportional to this time.

Position : The position of the impinging particle is determined by the position of the electrode connected to an electronic channel.

Time : In case of a TPC, the difference between the trigger time and the reconstructed time of the signal, multiplied by the drift velocity of electron in the particular condition of the setup (gas, pressure, temperature and space charge), gives the coordinate along the drift axis of the particle. The time of a pulse can be extracted from the position of the maximum amplitude or when the pulse crosses a certain threshold. Because of jitter (see Sec. 2.6.4.1) the error proportional to the noise might be large. To reduce errors on the time measurement, a constant fraction algorithm is used. It works in two steps as described in Fig. 2.24.

A list of hits, characterized by amplitude, time and position information, is extracted by this algorithm from real data for each event. The next section describes how these hits are used.

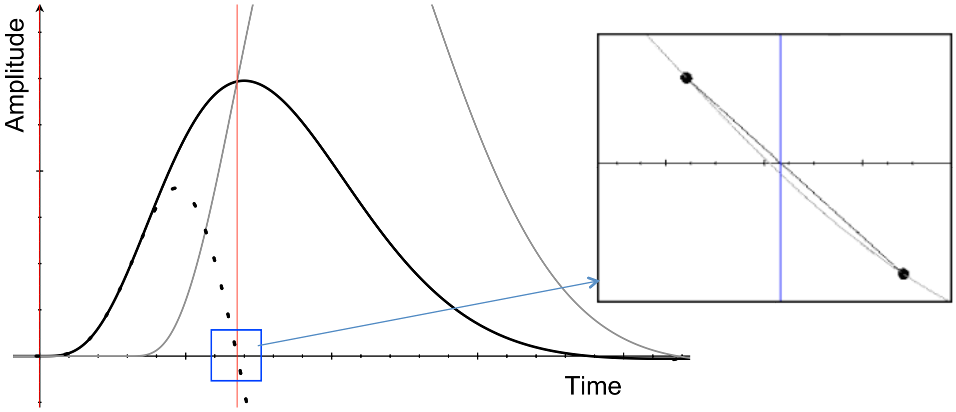

Figure 2.24: Precise time measurement given by a constant fraction algorithm. First two times the retarded signal (gray) is subtracted from the signal (black) giving the dotted line. When this function crosses the abscissa origin, it gives the hit time. Since only discrete numbers are used, the time value has to be extrapolated between to samples as shown in the right curve. The difference between the vertical blue line and the gray curve, in the right picture, shows the errors of the time reconstruction.

2.5.2 Position Finding Algorithm or Clustering

The charge cloud usually induces signal on several electrodes. To combine the hits that are likely to correspond to a unique primary ionization, an algorithm called clustering is used. By looping over the hits, the algorithm groups spatially close hits into clusters. This drastically reduces the quantity of data needed. Different clusters properties are calculated from hits:

Amplitude : The cluster amplitude is the sum of the hits amplitudes. To take into account capacitive coupling between electrodes, amplitudes that are considered as cross-talk can be artificially lowered in the cluster amplitude calculation.

Position and time: Reconstruction of the cluster position is a very sensitive part of the analysis. It will impact not only spatial resolution but also efficiency and track reconstruction. Depending on the experimental setup, here are the most common clustering algorithms:

- **Tracks with angle:** If a plane detector has a large angle with particles, they will leave longer tracks in the gas volume creating very large cluster in one dimension. In that case, one has to consider only the positions, u_h and u_t, of the head and the tail of a cluster. In most simple cases, the position of the particle is given by:

  $$u_{cl} = \frac{u_h + u_t}{2} \tag{2.27}$$

  Taking into account Landau fluctuations of the charge deposition, one can use the analog head-tail algorithm or its variation as described in [43]

- **Center of Gravity (COG)** Position and time are given by a weighted mean of the hits;

  $$\mathrm{t_{cl}} = \frac{\sum^i \mathrm{w}_i \cdot \mathrm{t_h}}{\sum^i \mathrm{w}_i} \text{ and } \mathrm{u_{cl}} = \frac{\sum^i \mathrm{w}_i \cdot \mathrm{u_h}}{\sum^i \mathrm{w}_i} \tag{2.28}$$

  where i is the index of the hit, $\mathrm{t_h}$ and $\mathrm{u_h}$ the time and position of the hit, $\mathrm{w_i}$, the weight of each hit given by its amplitude.

- **COG with non linear weight :** The same algorithm can be used with different weights. In some cases, w_i may be taken as function of the hit amplitudes or a more complex relation that better describes the charge repartition of hits inside a cluster. For example, with resistive Micromegas, the logarithm of the amplitude has produced good results [44]:

  $$w_i = w_0 + \log\left(\frac{Q_i}{Q_{cl}}\right) \text{ and } w_0 = -\log\left(\frac{Q_{min}}{Q_{max}}\right) \tag{2.29}$$

  Q_{max} and Q_{min} being the most extreme values that the charge amplitude of a hit can take, Q_i the hit charge and Q_{cl} the cluster charge.

  This method requires a good understanding of the spatial repartition of amplitudes inside a cluster.

- **η algorithm:** A more general way to correct a potential divergence between the linear and the actual case is to use the so-called η algorithm. By using the distribution of amplitudes in the 2 consecutive electrodes case:

  $$\eta = \frac{S_R}{S_R + S_L} \tag{2.30}$$

  where S_R is the amplitude of the signal on the right strip and S_L on the left. In an ideal case, the distribution of this amplitude should be flat because the distribution of particle positions is flat. Most of the time, due to capacitive coupling and field configuration in the induction gap, η is far from being flat. The second step of the algorithm is to use this distribution to deduce the position of the signal in between the two electrodes, from a particular ratio η_0:

  $$u_{cl} = P\frac{\int_0^{\eta_0} \frac{dN}{d\eta} d\eta}{\int_0^1 \frac{dN}{d\eta} d\eta} \tag{2.31}$$

  where $dN/d\eta$ gives the differential η distribution and P the detector pitch [43].

When two avalanches, from two different particles, overlap, they create a large cluster. Most of the time, the amplitude distribution within such a large cluster contains a local minimum. If the algorithm finds a local minimum, it divides the large cluster into two clusters corresponding to the different particles. The amplitude at the local minima is usually shared between the two clusters. The separation of overlapping clusters is a difficult talk when the rate per electronics channel is important. In addition capacitive coupling between neighboring channels modifies the way overlapping signals induce signals.

2.5.3 Pattern Recognition and Track Fitting

Once the raw data have been regrouped into a list of clusters for each detector, an algorithm, the *Pattern Recognition*, searches for a particular track pattern that corresponds to the known description of the path of a particle. A general description of particle trajectory is a helix that becomes a straight line in absence of magnetic field. The pattern recognition algorithm selects clusters that are likely to correspond to a track, and submits them as a track candidate. The last algorithm, *the track fitting*, adjusts the parameters of the track analytical description to best describe the track candidate. If the algorithm has converged to reasonable track parameters, they will be saved for later analysis, where the data will meet their physical description *i.e.* a particle type with its characteristics.

2.6 Intrinsic Limitation of MPGDs and their Electronics

Now that we have seen the detailed principles of MPGDs, we will consider their limitations to help us to understand this type of detectors. Our first interest is to study limitations that come from the physics of the detectors, how discharges can form and impact detectors performances, how the principle of a gaseous detector withhold the maximal rate achievable and in particular the effect of ions. Then the electronics limitations will be explored, first by looking how signal fluctuation propagates to measurement errors and then focusing on the origin of these fluctuations and the means to prevent them.

2.6.1 Gain/Rate Empirical Limitation Law

Gaseous detectors are limited in rate and gain by an empirical relation [45], as shown in Fig. 2.25, by several kinds of breakdowns and limitations.

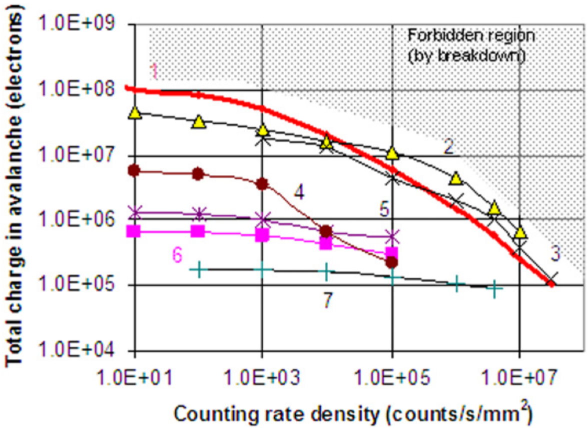

Figure 2.25: Maximum achievable gain, limited by breakdown, as a function of the X-ray flux for various detectors: (1, red line) Parallel Plate Avalanche Counter (PPAC) with 3 mm gap; (2, yellow triangles) Micromegas; (3, black X) PPAC with 0.6 mm gap; (4, brown dots) microstrip gas chamber with 1 mm strip pitch; (5, purple X) microstrip gas chamber with 0.2 mm strip pitch; (6, pink square) GEM; (7, teal +) microgap detectors with 0.2 mm strip pitch (from [46]).

Here we try to list the different known mechanisms that limit gaseous detectors in gain and rate. Limitations beyond the detection such as electronic occupancy or noise are not discussed here, only detector related problems before the front-end electronics are considered.

2.6.2 Discharge Mechanism

A discharge occurs when the charge density in the gas is so high that it locally creates a conductive plasma where the charges can freely move. Three processes are known to cause this high electron/ion density: the Townsend effect, the streamer mechanism and ageing or hot spots.

The Townsend effect : The plasma is created from multiple avalanches that occur at the same place in the detector. It typically happens when an ionizing particle creates a lot of primary electrons (*i.e.* delta electron, alpha particle) or when the beam rate is too high momentarily.

Kanalaufbau or streamer mechanism : A high gain avalanche develops into a discharge from a statistical fluctuation of the gain. According to [47], the streamer mechanism, illustrated in Fig. 2.26, can be summarized as follow: an avalanche creates a positive space charge that disturbs local electric field and gives rise to local avalanches. These avalanches increase the space charge and produce secondary electrons by photoionization. This process is repeated as the space charge develops toward the cathode as a visible glowing *ball-point*. This is the most intense part of the discharge where most of the current is recorded. It is followed by a weak secondary streamer and then a bright transient arc.

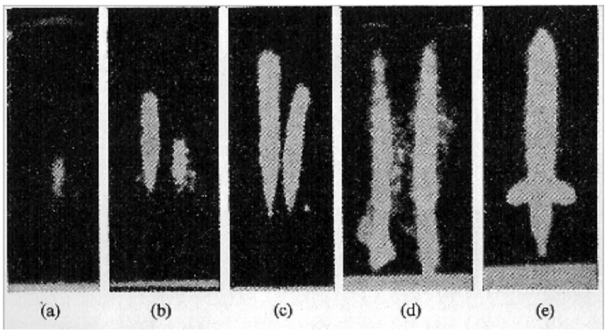

Figure 2.26: Development of a cathode directed streamer in a cloud chamber [47]. (a) From avalanche head near the anode starts the cathode streamer. (b) The cathode streamer almost at anode. (c) Streamer branches appear. (d) Cathode streamer reaches anode. (e) Channel established between electrodes.

Hot spots : With time, a detector might be affected by ageing effects and a thin layer of polymer is deposited on the cathode [45] from gas degradation, impurities or material outgassing. This insulating layer will charge and modify the electric field, possibly creating a hot spot where discharges frequently appear. One technique consists of increasing the gain to sublime the polymer layer or impurities (process called *cooking* for Micromegas at Saclay and *training* for GEM foils at TUM). Unlike the case of wire detectors, such ageing effects should not affect the detector efficiency with Micromegas, since the ion collection is done in the lower part of the micro-mesh and the drift field is not affected. Moreover no ageing deposits have been observed on detectors that have been used during several year at COMPASS.

2.6.3 High Rate Effects

In addition to the increase of the discharges frequency with the particle rate, the increased density of positive charges impacts performances. Since the mobility of ions is much lower than electron mobility: $\mu^- \approx 10^3 \times \mu^+$, $\mu^+ \approx 2\,\mathrm{cm^2 s^{-1} V^{-1}}$ in argon [19], the accumulation of ions will depend of the rate.

Accumulation of charges in amplification space: For a wire detector, the gain starts to decrease at 10^9 Hz/mm of wire [48]. With a gain of 10^4, 100 primary charges, and 2 mm space between wires, it gives a maximum rate of 1 kHz/mm^2. The small distance between amplification electrodes in MPGDs allows an ion evacuation in hundreds of nanoseconds. No decrease of gain has been measured below 1 MHz/mm^2 for GEM and Micromegas.

Ion backflow: The deformation of the drift field by the accumulation of charges in the drift space can lower efficiency, and decrease spatial and energy resolutions. These effects are major issues for long drift space detectors as in a TPC. There are two sources of ions: primary ions from particle

ionization and secondary ions from electron amplification. Several quantities are used to describe this phenomenon:
The ion feedback, ϵ, is defined as the ratio between the back drifting ions $\mathrm{N_{back}}$ and the total number of pairs before amplification $\mathrm{N_T}$:

$$\epsilon = \frac{\mathrm{N_{back}}}{\mathrm{N_T}} \tag{2.32}$$

ϵ can not be directly measured whereas we can access to the relative backflow IB:

$$\begin{aligned}
\mathrm{IB} &= \frac{\text{ion current on the drift cathode}}{e^- \text{ current on the readout anode}} && (2.33)\\
\text{With the gain } \mathrm{G_{eff}} &= \frac{\mathrm{N_{anode}}}{\mathrm{N_T}} && (2.34)\\
\mathrm{IB} &= \frac{\mathrm{N_T} + \epsilon \mathrm{N_T}}{\mathrm{N_T} \cdot \mathrm{G_{eff}}} = \frac{1+\epsilon}{\mathrm{G_{eff}}} && (2.35)
\end{aligned}$$

The suppression factor η is defined as the intrinsic efficiency of ion back-flow suppression:

$$\begin{aligned}
\eta &= \frac{\text{Nb of ions back drifting}}{\text{Nb of ions created in amplification}} && (2.36)\\
\eta &\simeq \frac{\epsilon \cdot \mathrm{N_T}}{\mathrm{N_T} \cdot \mathrm{G_{eff}}} = \frac{\epsilon}{\mathrm{G_{eff}}} \implies \epsilon = \eta \cdot \mathrm{G_{eff}} && (2.37)\\
& && (2.38)
\end{aligned}$$

It is important to precise that η, as defined here, is an approximation since $\mathrm{N_T} \cdot \mathrm{G_{eff}}$ is not exactly the number of ions created in amplification since electron/ion pairs can be created in amplification but not collected and therefore not included in $\mathrm{G_{eff}}$. It also depends on electron/ion extraction, see Chap. 9. Suppression factor of $\eta = 0.5\%$ can be achieved with triple GEM detector (even $\eta = 0.2\%$ with magnetic field) [49]. For Micromegas amplification, $\eta = 0.2\%$ [50].

“If anything can go wrong, it will.” 1st Murphy’s Law.

2.6.4 Electronics Noise and Reconstruction Errors

The Front-End Electronics is an important source of signal distortion. It modifies signals (at least for amplification) and is likely to introduce errors in the reconstructed information. In this section, we will only focus on the analog part on the system, *i.e.* before the ADC. Once digitized we consider that all errors can be virtually avoided on digital data by using correction algorithms.

The Signal to Noise Ratio, SNR, directly defines the detector performance in a particular operating conditions such as type of particle, gain, gas... Since the gain of a detector is often limited to a quite narrow operating range, the main source of SNR improvement is the noise optimization. The noise is studied as a power density over the frequency spectrum and expressed as a charge for which the $\mathrm{SNR} = 1$, the Equivalent Noise Charge (ENC).

In this section, the most common sources of reconstruction errors are developed as well as electronics noise calculation. A noise analysis of the front-end electronics will introduce the issue of amplification and filtering in the perspective of noise optimization.

2.6.4.1 Sources of Reconstruction Errors

Time and amplitude measurements can loss accuracy through interference with other signals or noise.

Pile-up Pile-up happens when two uncorrelated signals are overlapping because the signal length is longer than the time between signals. This can be avoided by decreasing the occupancy (percentage of the time while the electronics is processing signals). The occupancy can be lowered by increasing the segmentation of readout electrodes, by decreasing the incoming particle flux or by shortening the signal time length. Piling-up signals lead to the measurement of amplitude of all range greater or equal to the signal amplitude (considering a monochromatic source). If signals have an undershoot then amplitude of all range, including lower or negative amplitude, are measured, see Fig. 2.27.

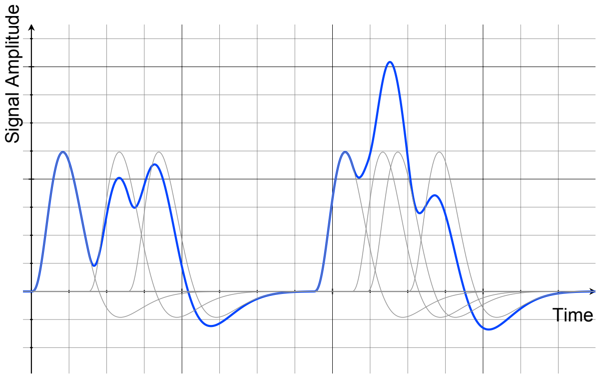

Figure 2.27: Effect of pile-up: signals in gray arrive faster than their shaping length, so they are added to give the blue curve. The blue curve shows a different shape, and different local maxima compared to the original monochromatic signals.

Ballistic deficit To measure the energy of the impinging particle, the FEE has to integrate and differentiate (shaping) the deposited charge. The same amount of energy can create, after the detector gaseous amplification, induction and integration, signals that have the same integrated value but various shapes in time. If the rising time of the signal is longer than the peaking time of the shaper, the output signal starts to decay before the input signal has reached its maximum amplitude. This leads to different amplitude measurements as shown in Fig. 2.28.

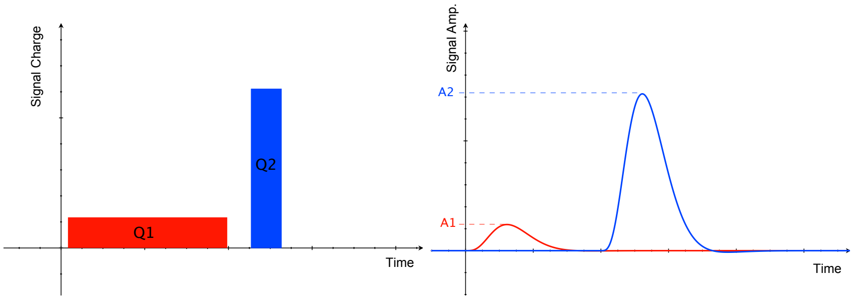

Figure 2.28: Effect of ballistic deficit, the same original charge, Q1 = Q2, leads to two different amplitudes A1 ≠ A2 after shaping because of two different rising times. Q1 typically represents a signal that had more diffused than Q2.

A longer peaking time can correct for the ballistic deficit.

Time jitter If the arrival time of a particle is measured by comparing the signal and a fixed threshold, then the time measurement is exposed to the instantaneous amplitude fluctuations of the signal for a fixed energy deposit. Fig. 2.29 shows the transposition of signal modulated by noise on time measurement. If σ_n is the RMS of noise and $(\mathrm{d}S/\mathrm{d}t)_T$ the derivative of the signal evaluated at the trigger time T, the time jitter (or timing variance) is:

$$\sigma_t = \frac{\sigma_n}{(\mathrm{d}S/\mathrm{d}t)_\mathrm{T}} \approx \tau_i \frac{\sigma_n}{\mathrm{S}_0} \tag{2.39}$$

With S_0 the amplitude of the signal and τ_i the rising time of the signal.

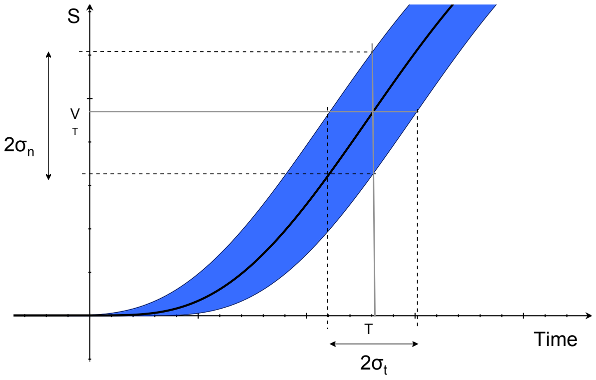

Figure 2.29: Time jitter: Fluctuations in signal amplitude translate into fluctuation in time measurements.

With real signals that have a finite bandwidth, the slope increases with the signal amplitude. As the minimum time jitter occurs for maximal slope, by increasing the signal amplitude and tuning the trigger level, one can decrease the time jitter.

Time walk As shown in Fig. 2.30, the relative time where the signal crosses the threshold depends on the amplitude of the signal. Timing measurements must be corrected using maximum amplitude or time-over-threshold (as in Compass [51]) to avoid time walk errors.

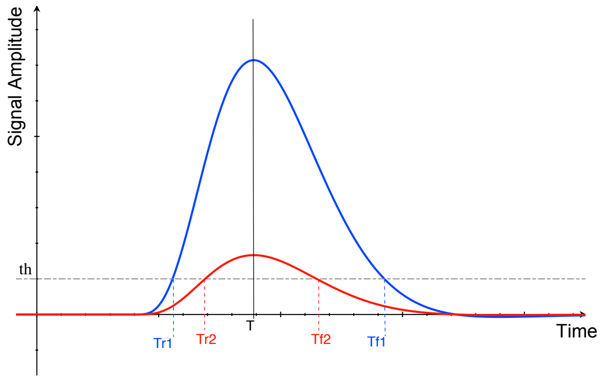

Figure 2.30: Effect of time walk: for two signals that have the same timing but not the same amplitude, rising and falling times (Tr and Tf), at a certain threshold th, show non linearity with respect to the time T.

Threshold effect To reduce occupancy and limit extensive quantity of data, it is necessary to ignore signals that are in the amplitude range of the noise. The boundary between noise and signal is usually set at an amplitude threshold of 3 to 5 σ_n. This leads to an inefficiency at low amplitude, degrading low gain detector performances.

Cross-talk Cross-talk is considered as a major source of errors. An important capacitive coupling appears in between narrow conductors in PCB, in particular strip detectors. Fast signals are likely to spread on the neighboring channels and decrease the position resolution. This coupling must remain low compared to the detector capacitance to avoid sharing an important fraction of the signal. The readout amplifier must have a low input impedance to prevent spreading signal to the neighboring electrodes and thus increase cross-talk. The input impedance of the CSA is discussed in Sec. 2.4.2.2.

These measurement errors are, except cross-talk, a consequence of signal fluctuations, the *noise*. A good noise analysis is necessary to understand the performances of an experimental setup. It could come from vibrations of electrodes or from another mechanical problem whereas the largest part of it is imputable to electronic and electromagnetic (EM) noise.

2.6.4.2 Noise Analysis of a Detector Front-End Electronics

From the electronics point of view, the noise, random fluctuations of voltage and current, are considered to be issued from 3 kinds of sources: *thermal noise*, *shot noise* and *trapping noise*.

Thermal or Johnson noise: Variation of velocity of charges due to thermal excitation in resistive material causes noise with a constant power per unit bandwidth (*white noise*). The spectral noise power density is:

$$\mathrm{d}P_n/\mathrm{d}f = 4k\mathrm{T} \tag{2.40}$$

with k the Boltzmann constant and T the temperature. Thanks to the Ohm law, $\mathrm{V}=\mathrm{R}\cdot\mathrm{I}$, the power P of a resistor R can be expressed using voltage or current :

$$\mathrm{P}=\mathrm{I}^2\cdot\mathrm{R}=\frac{\mathrm{V}^2}{\mathrm{R}} \tag{2.41}$$

Then the spectral voltage and current noise densities, e_n^2 and i_n^2 are:

$$\mathrm{e}_\mathrm{n}^2=\frac{d\mathrm{V}_\mathrm{n}^2}{d\mathrm{f}}=4k\mathrm{TR} \tag{2.42}$$

$$\mathrm{i}_\mathrm{n}^2=\frac{d\mathrm{I}_\mathrm{n}^2}{d\mathrm{f}}=\frac{4k\mathrm{T}}{\mathrm{R}} \tag{2.43}$$

Shot noise: In an insulator or a semi conductor, the probability of a carrier to cross the potential barrier is not zero. Since individual emissions are not correlated, the shot noise is a white noise ($\mathrm{d}P_n/\mathrm{d}f$ is constant) with a spectral density proportional to the average current I and the charge of carrier e:

$$\mathrm{i}_\mathrm{n}^2=2\mathrm{e}\cdot\mathrm{I} \tag{2.44}$$

Trapping noise: is a general mechanism that includes low frequency noise from Random Telegraph Noise to $1/f$ noise. These noises come from different trapping mechanisms that have different time constants. For instance imperfections in the crystal lattice in solid-state components (typically diodes), or impurities in gases, can trap charge carriers, and release them after a characteristic lifetime. This leads to a frequency dependent spectrum :

$$\frac{\mathrm{d}P_n}{\mathrm{d}f}=f^{-\alpha} \tag{2.45}$$

where α is typically in the range of 0.5 to 2.

These three effects enter in the noise calculation of a typical experimental setup as shown in the next section.

2.6.4.3 Noise at the Pre-Amplifier

To understand how the shaper affects the noise, the detector and its FEE are described as noise sources. For the system composed of a detector + CSA we have four sources of noise: the *detector*, the *parallel bias resistors*, the *series resistors*, and the *amplifier* as shown in Fig. 2.31

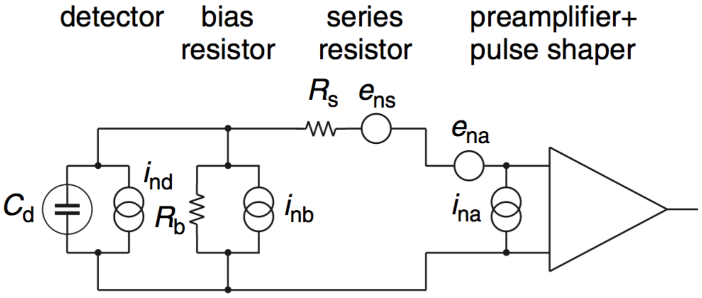

Figure 2.31: Schematic of a CSA with all the equivalent noise sources at the entry [35].

Detector noise : The shot noise coming from the detector (carrier trapping in gas), $\mathrm{i_{nd}}$, is represented by a parallel noise current generator and $\mathrm{i_{nd}^2 = 2eI_d}$ where $\mathrm{I_d}$ is the detector current.

Bias resistor : The bias resistor $\mathrm{R_b}$ and the current noise generator $\mathrm{i_{nb}}$ represent the thermal noise of the bias resistor (if any) and external noise between the bias and the ground. $\mathrm{i_{nb}^2} = \frac{4k\mathrm{T}}{\mathrm{R_b}}$

Series resistor : represents the thermal noise of all parasitic resistors between the detector and the amplifier from connections and protection circuits. $e_{ns}^2 = 4kTR_s$

Amplifier : e_{na} and i_{na} are the intrinsic noise of the CSA. Typical amplifier have noise densities in the order of $\mathrm{nV}/\sqrt{\mathrm{Hz}}$ and $\mathrm{pA}/\sqrt{\mathrm{Hz}}$ [48].

Since we use a charge amplifier, we are interested by the equivalent noise *charge*, which is, for the circuit shown in Fig. 2.31:

$$\mathrm{Q_n^2} = \frac{e^2}{8}[(2\mathrm{e}\cdot\mathrm{I_d} + \frac{4k\mathrm{T}}{\mathrm{R_b}} + \mathrm{i_{na}^2})\tau + (4k\mathrm{TR_s} + \mathrm{e_{na}^2})\frac{\mathrm{C_d^2}}{\tau} + 4\mathrm{A_f}\cdot\mathrm{C_d^2}] \tag{2.46}$$

where $e^2/8 \approx 0.924$ is the normalization of the noise to the signal gain and $\mathrm{A_f}$ the CSA noise coefficient in the order of the pV, from [35]. The first term combines sources that increase with the shaping time τ, the second term increases with the detector capacitance and decreases with τ, and the last term is the contribution of the amplifier $1/f$ noise. These different influences lead to a possible noise optimization by tuning the parameters (τ, C...).

2.6.4.4 Noise Optimization with the Shaper

A more general way to describe Eq. 2.46 in such a system that highly depends on the shaping is:

$$\mathrm{Q_n^2} = \mathrm{i_n^2 F_i}\tau + \mathrm{e_n^2 F_v}\frac{\mathrm{C_i^2}}{\tau} + \mathrm{F_{vf}A_fC_i^2} \tag{2.47}$$

with

$$\mathrm{F_i} = \frac{1}{2\tau}\int_{-\infty}^{\infty}[\mathrm{W}(t)]^2\mathrm{d}t \tag{2.48}$$

$$\mathrm{F_v} = \frac{\tau}{2}\int_{-\infty}^{\infty}\left[\frac{\mathrm{dW}(t)}{\mathrm{d}t}\right]^2\mathrm{d}t \tag{2.49}$$

$\mathrm{C_i}$ is the total parallel capacitor at the entry, $\mathrm{W}(t)$ the response of the system to a Dirac delta function, τ is the characteristic time of the shaper (for example the peaking time a CR-nRC) and $\mathrm{F_{vf}}$ depends on the pulse shape determined by the shaper as $\mathrm{F_i}$ and $\mathrm{F_v}$. $\mathrm{F_i}$, $\mathrm{F_v}$ and $\mathrm{F_{vf}}$ can be found in tables for the different circuits [36]. This way to calculate noise allows a clear vision of the effects of filtering.

Eq. 2.47 shows that the noise optimization can be done by tuning the ratio of input capacitance and the detector capacitance, and also by adapting the shaping time to the system. That is why front-end electronics is frequently built with specialized ASICs, commercial pre-amplifiers can not reach good noise performances with a multi-application approach.

In Fig. 2.32 we can see the effects of the shaping time τ. By selecting the τ value, one can choose to be more or less sensitive to voltage or current noise.

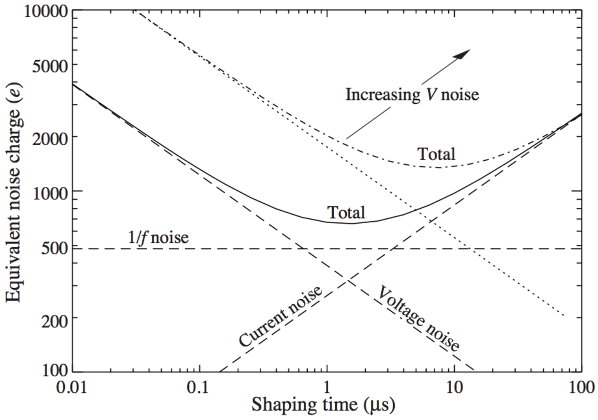

Figure 2.32: ENC in function of the shaping time τ. At small τ, voltage noise is dominating; at large τ it is the current noise. This creates an optimal ENC when the voltage noise equals the current noise. The $1/f$ noise is independent of the shaping time. An increase of the voltage noise increases the optimal τ [48].

2.6.4.5 Electromagnetic Compatibility Consideration

Until now we have only considered the noise as a consequence of front-end circuits, whereas the main source of electromagnetic noise is likely to come from the environment. Using low material budget, low noise detectors, in very noisy environment such as an experiment close to an accelerator, is a real challenge. Working with sensitive detectors means spending an important amount of time *hunting* EM noise and trying to protect the sensitive equipments. By following the rules of Electro-Magnetic Compatibility (EMC), one can improve his experimental setup by following a few simple rules:

Detector ground : Having a defined strategy of grounding is crucial for low-noise detectors. The whole detector must have only one ground, connected to the shielding and the front-end analog electronics. Soldering is preferable to make the connections. This is not due to ohmic consideration, but to the size of the contact. Connectors are usually much bigger and act as antennas.
The digital part of the electronics must be connected via differential lines to avoid propagation of noisy digital square signals. Ideally the detector should not be connected to power supply ground, low and high voltage, but this may cause security issues. An insulation transformer is recommended in order to insulate the setup from the rest of the experiment.

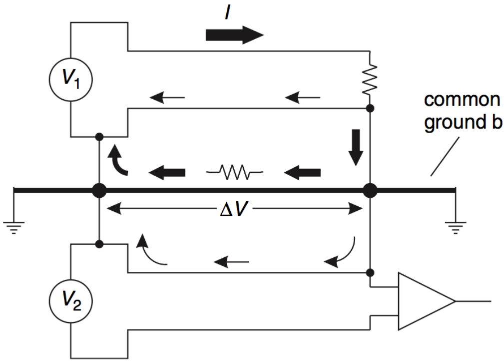

Figure 2.33: Two systems sharing the same grounding path. V_1 introduces a ΔV on the measurement of V_2 [35].

Ground loops also called shared current paths (the phenomenon is not limited to ground) are the must unpredictable phenomenon with low noise detectors. When two systems, or two parts of the same system, share a common current path, they interfere between each other. A voltage difference can be applied on a line by a system that will disturb another system, see Fig. 2.33. A single design mistake in this area can lead to important operational issues. They are two ways of approaching the problem:

1. **Lowering the impedance** of the shared paths is the usual counter measure. With low impedance lines, the voltage difference decrease. This is done by adding large copper wires. This is named the *copper braid syndrome* [35]. However this method is not possible when material budget is an issue, and it is also not reliable since changes in the current path scheme are unpredictable.
2. **Removing common ground :** By analyzing the electronic schematics, it usually appears that not all the FEE is critical. A design that takes into account the different parts of a setup can really achieve good performances by adding few components. First the low amplitude input signals of the CSA must be separated from the rest of the system, it should not be connected directly to the common ground. Another critical point is output stages that drive high currents. A special care should be taken to isolate the output amplification stage to the rest of the detector.

Cables (Sensitivity to electromagnetic noise) : Cables are very sensitive to EM noise. An external field can induce signals on a cable when its length is over a tenth of the field wavelength. Current induced on cables can be suppressed by using a ferrite that limits common noise. The other ways involve reducing cable length and improving shielding.

Cables (adaption and reflexion) : When a signal propagates through a cable, the ratio of voltage over current is defined by the cable impedance $\mathrm{Z} = \sqrt{\mathrm{L}/\mathrm{C}}$. Every connection will introduce a rupture in the impedance, forcing the signal to readjust his voltage/current ratio by creating an echo signal. To limit these reflexions, impedances of cables must match the one of connectors, cables and circuits. This can be done at both ends of the cable by a serial resistor on the sending side and/or by a parallel resistor at the receiver side [35].

2.7 Characterization of a MPGD, Definitions

The characterization of a gaseous detector consists on measuring its performances through 4 main parameters: *gain*, *efficiency*, *spatial* and *time resolutions*. Except for gain that can be measured with a source of ionizing particles, the characterization requires particle tracks to be compared with the reconstructed time and position of the particle by the detector. Particle tracks, from cosmic rays or from an accelerator, are reconstructed with an external tracking system or another part of the detector. The projected tracks at the detector position $\mathrm{u}_{\mathrm{track}}$, $\mathrm{v}_{\mathrm{track}}$ and time $\mathrm{t}_{\mathrm{track}}$ are compared to the measured ones $\mathrm{u}_{\mathrm{detector}}$, $\mathrm{v}_{\mathrm{detector}}$ and $\mathrm{t}_{\mathrm{detector}}$. In the case of a TPC, the time information is converted into the position along the drift axis using the drift velocity of the gas.

2.7.1 Gain

The gain of a gaseous detector is defined as the ratio between the number of charges in the amplification gap and the total number of electrons resulting created in the drift volume. For instance, in the case of a single GEM foil:

$$\mathrm{G} = \frac{\text{Number of e}^{-}\text{ in the GEM holes}}{\text{Number of e}^{-}\text{ collected into the GEM holes}} \tag{2.50}$$

This number is usually not measurable and the *effective gain* is used instead. The effective gain, $\mathrm{G_{eff}}$ is the number of charges in the induction gap divided by the number of electrons entering the gap:

$$\mathrm{G_{eff}} = \frac{\text{Number of charges in the induction gap}}{\mathrm{N_{TOT}}} \tag{2.51}$$

With $\mathrm{N_{TOT}}$ the sum of primary and secondary electrons.
For a given number of charges before amplification and a given noise, the gain will define the signal to noise ratio of our detector.

2.7.2 Transparency

The electron or ion transparency is the proportion of charges that pass through an amplification stage. Specifically it is defined as the ratio between the number of charges leaving and the number of charges approaching the amplification stage:

$$\tau^{\pm} = \frac{\text{Number of } \mathrm{e}^-,\, \mathrm{I}^+ \text{ leaving}}{\text{Number of } \mathrm{e}^-,\, \mathrm{I}^+ \text{ approaching}} \tag{2.52}$$

For instance the ion transparency ϵ^+ of a GEM foil is the number of ion leaving the holes divided by the number of ions approaching the foil.

2.7.3 Ion Backflow

As already defined in Sec. 2.6.3, the ion backflow is defined as the ratio of the number of ions at the cathode to the number of charges in the induction gap.

$$\mathrm{IB} = \frac{\mathrm{N^+_{cathode}}}{\mathrm{N_{induction}}} = \frac{\mathrm{N^+_{amp}} + \mathrm{N^+_{tot}}}{\mathrm{G_{eff}}} \tag{2.53}$$

With $\mathrm{N^+_{cathode}}$ the number of ions at the cathode, $\mathrm{N_{induction}}$ the number of charges in the induction gap and $\mathrm{N^+_{amp}}$ the number of ions extracted from the amplification stage.

2.7.4 Energy Resolution

From a monochromatic ionization source, we expect a defined amplitude of the detector response. In reality a finite width Gaussian function is observed around the energy E of the source, due to primary ionization, gain and many other fluctuations. The Full Width at Half Maximum, FWHM of the distribution, denoted as ΔE, is used to define the relative energy resolution $\mathrm{R_E}$ as [26] :

$$\mathrm{R_E} = \frac{\Delta \mathrm{E}}{\mathrm{E}} \tag{2.54}$$

In practice, the FWHM is deduced from the width of the Gaussian distribution, σ_{E}, fitting the energy peak and $\Delta_{\mathrm{E}} = 2\sqrt{2\ln(2)}\cdot\sigma_{\mathrm{E}}$.

2.7.5 Efficiency

According to [26] the efficiency ϵ is defined by

$$\epsilon = \frac{n_{\mathrm{det}}}{n_{\mathrm{source}}} \tag{2.55}$$

where n_{det} is the number of particles seen by the detector and n_{source} the number of particles emitted by the source. This value depends on the geometry of the source and the detector. In consequence we will only consider the intrinsic efficiency ϵ_{int} of the detector defined by

$$\epsilon = \epsilon_{\mathrm{int}} \cdot \epsilon_{\mathrm{geom}} \tag{2.56}$$

and

$$\epsilon_{\mathrm{int}} = \frac{\text{Number of particles detected}}{\text{Number of particles impinging on detector}} \tag{2.57}$$

Eq. 2.56 is only valid if the intrinsic efficiency does not depend on the position in the detector. This number also heavily depends on the type of radiation. Thin gaseous detectors have a much lower efficiency for neutral light radiation than for charged particles that interact a lot with matter. Later ϵ_{int} will only be discussed for charged particles. One should note that due their large size, MPGDs have a much better ϵ_{geom} than smaller detectors and can be coupled to large gas volumes to detect weakly interacting particles [52].

The counting of particles detected by the detector is done by finding (or not) a cluster within a defined distance around the projected track. Its radius is called road width. Using this way of counting, the detector has to be well aligned with the tracking system and the road width must be carefully chosen. It is obvious that the apparent efficiency ϵ_{app} will increase with the road width since noise clusters close to the track will be considered as signal as the road enlarges. To take this effect into account, the efficiency is corrected using the background pseudo-efficiency. It is defined as the probability *bg* to find at least one random cluster within the road width around the track. The corrected efficiency ϵ is given by:

$$\epsilon_{\mathrm{app}} = \epsilon + \mathrm{bg}(1-\epsilon) \iff \epsilon = \frac{\epsilon_{\mathrm{app}} - \mathrm{bg}}{1-\mathrm{bg}} \tag{2.58}$$

bg is estimated by considering the tracks of the previous event with the current clusters and calculate the efficiency for them. In that way effects of the different track and noise rate within a detector are taken into account. For instance it is more probable to find a track near the beam area but also *bg* is more probable there. A comparison between a Monte-Carlo simulation and real data for the road width is done in Sec. 8.4.6.

2.7.6 Spatial Resolution

The spatial resolution is one of the key parameters for tracking detectors. It will largely influence the precision of a spectrometer and therefore the physics that can be accessed. It can be extracted from the width of the residuals distribution. The residual is defined as the raw distance between the reconstructed position by the detectors and the track. For instance, in the u projection, the residual between $\mathrm{u_{track}}$ and $\mathrm{u_{detector}}$ is $\Delta\mathrm{u} = \mathrm{u_{detector}} - \mathrm{u_{track}}$. The raw resolution σ_{r} is then defined as the width of the Δu distribution, which is a convolution between the track spatial resolution ϵ_{tr} and the detector intrinsic spatial resolution σ_{d}. If these distributions are independent, then the resolution is

$$\sigma_{\mathrm{r}}^2 = \sigma_{\mathrm{d}}^2 + \epsilon_{\mathrm{tr}}^2 \iff \sigma_{\mathrm{d}} = \sqrt{\sigma_{\mathrm{r}}^2 - \epsilon_{\mathrm{tr}}^2} \tag{2.59}$$

2.7.7 Time Resolution

Time resolution is crucial to disentangle particles at high-rate to be able to distinguish between the triggered particle and another one which is not in time. As for the spatial resolution, the time resolution is defined by the width of the distribution of the time residual $\Delta\mathrm{t} = \mathrm{t_{detector}} - \mathrm{t_{track}}$. As for the spatial resolution, the time resolution σ_{T} is :

$$\sigma_{\mathrm{T}} = \sqrt{\sigma_{\mathrm{resT}}^2 - \epsilon_{\mathrm{trT}}^2} \tag{2.60}$$

with σ_{resT} the width of the time residuals and ϵ_{trT} the track resolution in time.

Chapter 3

A GEM-TPC for high rate experiments

3.1 The Time Projection Chamber

The Time Projection Chamber, *TPC*, is considered to be the most advanced ionization detector. This “electronic bubble chamber" provides an active volume that covers 4π without more material than gas, providing 3-dimensional particle trajectories and particle identification.

A TPC consists of a large cylinder, up to few meters in radius and length at high-energy colliders, with an electric and magnetic field along the axis. Like in any gaseous detector, ionizing particles interact with gas atoms and create electron-ion pairs. The electrons drift toward the anode where they are multiplied traditionally by MWPCs and read by cathode pads. The position of the ionization in the cathode plane is calculated from the center of gravity of the signals induced on pads. The position along the drift axis is obtained by the time difference between the ionization and the arrival of signals at the readout multiplied by the drift velocity. By reconstructing the particle path, its trajectory is reconstructed and gives its curvature from which the particle momentum is calculated. The reconstruction of the particle energy loss, dE/dx, allows the measurement of the particle velocity. The combination of the momentum and velocity leads to particle identification within the TPC alone, up to 1 GeV/c.

These great possibilities have to be put in perspective with the complexity of operating such a detector. First the long drift distance leads to large diffusion. To reduce the diffusion, a magnetic field, parallel to the electric field, confines the electrons to helical trajectories about the drift direction. To avoid E × B effects, an alignment of the magnetic and electric fields with a great precision is required [26]. The control of the electron drift imposes a good knowledge of the actual drift velocity inside the TPC. Therefore the temperature and the pressure must be measured. The gain homogeneity must also be monitored in particular for energy loss measurement. The control of these environmental parameters requires an advance system of calibrations that is the cornerstone of operating a TPC.

The other major difficulty comes from the production of ions at the cathode. Wire chambers are usually operated at a gain of several 10^4, producing as many ions per incoming electron. This leads to an important charge density in the drift volume that distorts the drift field, even canceling it completely. Additional wires are used to catch the ions before they enter in the drift volume, *the ion gate*, whereas this solution limits the maximal rate to ~ 1 kHz, making the use of a TPC problematic for modern high rate experiments.

3.2 A GEM TPC

A TPC is a sophisticated device that is delicate to operate. The design of a modern multipurpose chamber, operating in a high-rate dead-time free environment, constrained its amplification structure:

- High-rate capabilities
- Limited high back flow
- High SNR to reconstruct highly diffused cluster of electrons
- Large size
- Operating in magnetic field
- Good amplitude reconstruction for dE/dx
- No specific pad orientation (pad rows)
- Good spatial resolution

A triple GEM read-out with hexagonal pads meets to these requirement by the GEM features:

- Intrinsic ion back-flow suppression
- Fast electron signal that allows high-rate, good time resolution and complete integration for a good amplitude reconstruction
- Low capacitance providing good SNR
- Large size possible (1m^2 foils commonly produced)
- Performance improved by magnetic field by improving electron extraction
- Large cluster size that allows moderate segmentation with hexagonal pads and good spatial resolution

To understand these qualities, the microscopic behavior of the GEM structure is developed in the next section. These points are also developed in [53].

3.2.1 The Gas Electron Multiplier

As described in Sec. 2.1.2, a GEM is a 50 µm thin polyimide foil which is clad on both sides with a layer of copper 2 to 5 µm thick. Holes are etched into the foil in a hexagonal pattern at a pitch of 140 µm. These holes have a different shape depending on the manufacturing process, in the following development only foils with double conical holes are used as shown in Fig. 2.9.

In each of the $\sim 10^4$ holes/cm^2, a potential from 300 to 400 V is applied between sides of the foil creating an intense field of ~ 50 kV/cm inside the holes. This field is enough to allow electron avalanche which is the based on the gaseous amplification as described in Fig. 3.1.

The effective gain of a GEM results from the convolution of three characteristics:

- *The electron collection efficiency*: The proportion of electrons issued from the previous stage [1] that will enter of into a hole
- *The gain*: The number of pairs created per incoming electron
- *The electron extraction efficiency*: The number of electrons that is extracted into the volume below the GEM

These characteristics depend mostly on field ratios outside and inside the foil. They are usually not measurable directly and only the gain (number of extracted electron per incoming electron) and the ion back-flow (number of ions in the drift volume per incoming electron) are used to describe the operating regime of a GEM foil/stack.

As shown in Fig. 3.1, simulation allows to follow single electrons forming an avalanche inside a hole. Most of the electron cloud is created in the lower part of the hole where field lines are spreading toward the edge of the copper. This expands the transverse dimension of the electron cloud so a single electron can result into a 100 µm electron cloud. By drifting through the three GEM foils, the cloud will expand to a dimension of ~ 1 mm wide at the readout. This is an great advantage of the GEM structure, it leads to large cluster size so the detectors can be used with a moderate segmentation of the readout (as for the GEM-TPC) and 2D readout structure.

The ions created in the GEM hole follow the drift lines to end on the upper side of the foil. Some of the ions will escape into the drift volume, this is the ion backflow. By optimizing the field ratio, ion feedback as low as 4 to 6 ions per incoming electron have been reached [54]. The event considered on Fig. 3.1 has been calculated for the top GEM foil from where most the back drifting ions are produced.

Depending on the geometry of the holes, charges can reach the inner wall of the hole creating a space charge. With standard double conical holes, an excess of electrons in the tip of the inner ring compresses field lines, increasing the gain. This charging effect can reach 20% of the effective gain for triple GEM tracking detectors.

The amplification processes only take place inside holes and are decoupled from the induction of the signal on readout pads. If a discharge is ignited inside a hole, it is unlikely to propagate to the anode. To limit the charge transferred in such an event, the GEM foil is usually segmented. The GEM excellent stability allows the use of unprotected electronics with great noise performances.

The signal on the readout electrodes is induced when the electrons enter the gap between the most bottom GEM and the readout. The induced signal has a rectangular shape defined by a width that corresponds to the induction drift time (~ 50 ns, see Tab. 3.2). The pure electron signal allows fast shaping time and high rate capabilities that can even be increased by reducing the inducing time length.

3.3 The GEM-TPC Detectors

To prove the viability of a TPC read by GEMs, the E18 TUM group, which has acquired experience in the GEM technology with the COMPASS triple GEM detectors [55], has conceived several prototypes.

---

[1] In a GEM detector, the previous stage is either the drift volume or the transfer gap below another GEM foil

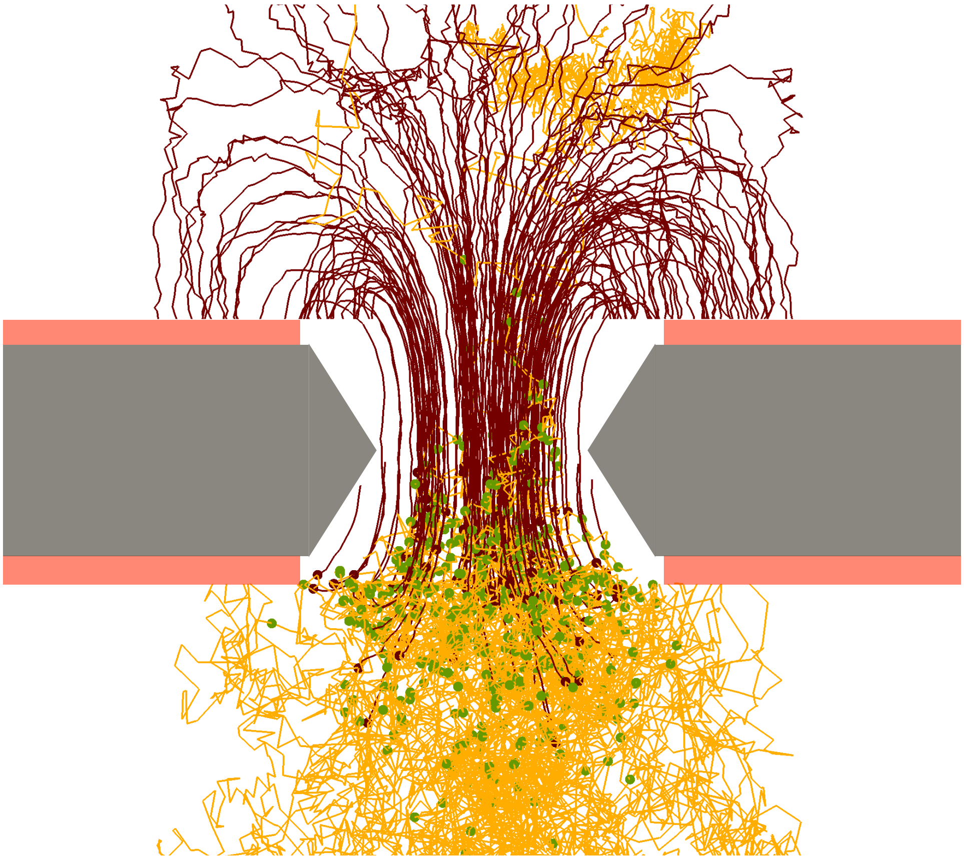

Figure 3.1: Simulation of an avalanche inside a GEM hole. Lighter lines represent the path of electrons, darker lines ions and dots ionization (different colors represent different ionizing processes). Two electrons arrive from the volume on the top of the picture and start an avalanche near the middle of double conical hole. The major part of the resulting electrons drift toward the next stage but some of them are captured by the lower side of the foil. The ions, whose paths show less Brownian motion (less diffusion), follow the lines toward the top volume or the upper side of the foil. Some of the charges end up in the hole walls showing the charging of the GEM foil.

A first modest 20 cm diameter × 7.7 cm drift length, the "Test Chamber"' in 2005, and then, in 2010, the "Large Prototype" with 30 cm diameter × 73 cm drift length.

3.3.1 The GEM-TPC Test Chamber

A small GEM-TPC has been built in 2005 by S. Neubert and Q. Weitzel. The test chamber is cylindrical with a diameter of 20 cm and a length of 7.7 cm. The $10 \times 10\,\text{cm}^2$ active area, see Fig. 3.2, is covered by a triple GEM electron amplification stage. On the top of the GEM foil, a 20 cm diameter copper plate, with a $10 \times 10\,\text{cm}^2$ hole, is mounted to shield the inactive region and to uniform the electric drift field. This field is homogenized inside the drift volume by cylindrical 3 mm copper strips printed on both sides of a 125 µm thick insulating polyimide foil, shifted by half a pitch and interconnected by 10 MΩ resistors.

This chamber has been characterized with cosmic rays using the PASA-ALTRO FEE that has shown rather high noise ($\sim 1900\,e^-$ RMS). Full description of the setup and result can be found in [56].

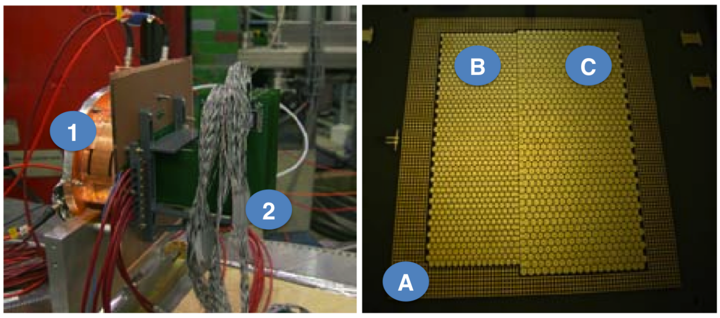

Figure 3.2: [Left] The GEM-TPC test chamber (1) and its electronics (2). [Right] Inside the test chamber, the $10 \times 10\ \text{cm}^2$ active area which is divided between (A) grid at ground potential to homogenize the induction field, (B) 1.25 mm hexagonal pads and (C) 1.5 mm pads.

In 2008, in view of the test beam period at the ELSA accelerator, see Chap. 6, the test chamber has been upgraded with two major improvements: the exchange of the FEE and the replacement of the thick electrodes that would have been incompatible with an electron beam. The new electronics and its calibration are presented in Chap. 4. The new pad plane is covered by 1500 hexagonal pads divided between two sizes, 1.5 mm and 1.25 mm, to study the evolution of resolution with pad size. The hexagonal shape homogenizes the charge distribution between pads and is compatible with any track topology. Both electrodes are made of a 2 mm PCB with 35 μm and 1 μm of gold. Each part is 1.33% of a radiation length.
The chamber is read by 24 chips, distributed between 6 FECs connected to 2 ADC cards. The description of the FEE is detailed in Chap. 4.

3.3.2 Electric Field Configuration

The 3 standard GEM foils (as described in Sec. 2.1.2) are stacked with a 2 mm space between each foils, and between the pad plane and the bottom GEM. The default voltage of the triple GEM amplification (that will later be referred as *100%*) was tuned to create an induction field of 3.75 kV/cm between GEM foils and a drift field of 250 V/cm. The HV in the GEM stack, from the top foils to the bottom one, are : $\Delta_{\text{VGEM1}} = 400\,\text{V}$, $\Delta_{\text{VGEM2}} = 365\,\text{V}$, and $\Delta_{\text{VGEM3}} = 320\,\text{V}$. These settings have been derived from the GEM detectors of the COMPASS experiment [55] and are known to be optimized for stability. Indeed, by using the minimal gain on the bottom GEM, the risk of a discharge that propagates to the readout is diminished but not the ion backflow. Settings optimized for ion feedback reduction would use the lowest gain on the top foil in order to reduce the number of ion created near the drift volume.

3.3.3 Gas

The chamber is mainly operated with Ar/CO_2 70/30 but it also in Ar/CO_2 90/10 and Ne/CO_2 90/10. In Ar/CO_2 70/30 with a 250 V/cm drift field, the maximal drift time is 14.4 μs. See Tab. 3.2 for more information.

3.4 The Large Prototype at FOPI

The large TPC has been designed to fit inside the spectrometer of the FOPI experiment, at GSI, Darmstadt. The longitudinal 0.6 T magnetic field and external tracking detectors are a great opportunity to operate and calibrate a GEM-TPC in real experimental conditions. Moreover, the GEM-TPC is used in interesting hadron physics measurements.

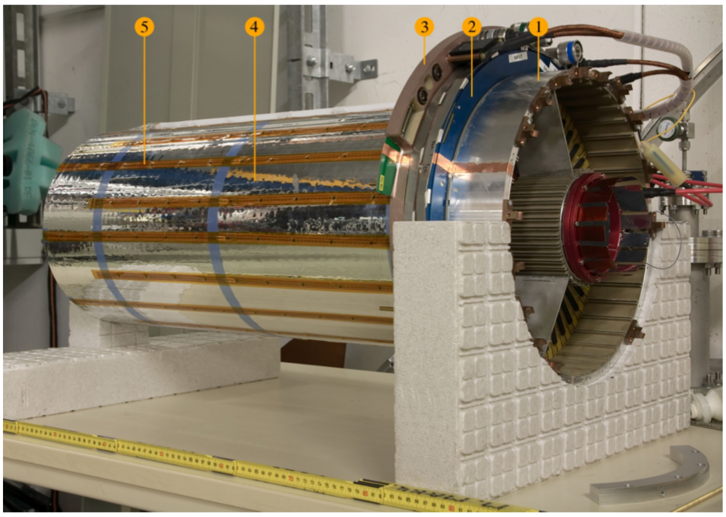

Figure 3.3: Photograph of the large GEM-TPC prototype. (1) cooling pot; (2) GEM-readout flange; (3) media flange; (4) outer field cage; (5) temperature sensors. From [57].

The *large prototype* has a drift length of 728 mm, the active area is included between an inner diameter ($\varnothing_i$) of 104 mm and an outer diameter ($\varnothing_o$) of 308 mm, see picture in Fig. 3.3. The amplification is made of 3 GEM foils that are segmented following an “iris shape” pattern. The active area is composed of 10254 hexagonal pads of 1.5 mm radius, connected to 42 small FECs and 11 ADC cards. The chamber operates in Ne/CO_2 90/10 with a drift field of 310 V/cm. See Tab. 3.2.

This detector has been calibrated using cosmic rays and radioactive krypton. In June 2011 it has been in data taking with a 1.7 GeV/c π^- beam impinging on different nuclear targets made of carbon, copper and lead.

3.4.1 Krypton Calibration

To calibrate the gain and its homogeneity across the pad plane, a gaseous radioactive krypton source is used. The ^{83m}Kr is obtained from a mother nucleus of ^{83}Rb. This source is produced at the Bonn cyclotron and has a half-life of 86.2 days. The ^{83m}Kr (half life: 1.83 h) decays dominantly via internal conversions and gives the spectrum describe by Tab. 3.1:

Energy [keV]	**Fraction** [%]	**R_P** in Ar/CO_2 [mm]	**R_P** in Ne/CO_2 [mm]
9.40	6.3	1.30	2.35
12.70	10.7	2.12	3.82
19.50	0.5	4.35	7.84
27.50	1.5	7.89	14.20
28.90	10.1	8.60	15.48
32.10	3.3	10.34	18.60
41.50	67.5	16.23	29.22

Table 3.1: Decomposition of the 83 mKr spectrum. R_P is practical range of slow electron at the energy and gas considered.

3.5 Characteristic Quantities and Numbers for the GEM-TPC Prototypes

	Test Chamber	**Large Prototype**
Dimensions	$\varnothing$=200 mm	$\varnothing_i = 104$ mm and $\varnothing_o = 308$ mm
Drift length	$L_{Drift} = 77$ mm	$L_{Drift} = 728$ mm
Pads	1500 of 1.25 and 1.5 mm radius	10254 of 1.5 mm radius
FEC	6	42
ADC cards	2	11
Gas	Ar/CO_2 70/30	Ne/CO_2 90/10
w_i	28.49 eV	35.70 eV
N_P	28 cm^{-1}	15 cm^{-1}
N_{TOT}	98 cm^{-1}	46 cm^{-1}
Gain	4000	from 800 to 2000
B	0 T	0.6 T
Drift field	250 V/cm	234 V/cm
Drift velocity	0.55 cm/µs	1.51 cm/µs
Max. drift time	14 µs	48 µs
SCA writing clock	f=20 MHz, T=50 ns	f=15.55 MHz, T=64.3 ns
Memory length	25.6 µs, 14.1 cm	32.9 µs, 49.6 cm
Transverse diffusion	$0.0157\sqrt{cm}$	$0.0213\sqrt{cm}$
Max. trans. diff.	436 µm	1.82 mm
Longitudinal diffusion	$0.0157\sqrt{cm}$	$0.0216\sqrt{cm}$
Max. long. diff.	436 µm, 79 ns	1.84 mm, 123 ns
Induction field	3.25 kV/cm	3.25 kV/cm
Induction drift velocity	7.5 cm/µs	8.0 cm/µs
Induction length	2 mm, 27 ns	4 mm, 50 ns

Table 3.2: Relevant numbers of the Test chamber at COMPASS and the Large Prototype for the conditions of the cosmic and krypton data taking that are used in Chap. 5. $\varnothing_i$ Inner, and $\varnothing_o$ outer, diameter respectively of the large prototype. w_i: Mean energy needed to create one pair electron/hole; N_P is the number of primary electrons per cm created by a MIP; N_{TOT} is the total number of electrons per cm created by a MIP. Velocity and diffusion constants calculated with GARFIELD at STP.

Chapter 4

The AFTER-based Front-End Electronics for the GEM-TPC

The major upgrade of the test chamber is the integration of the AFTER-T2K FEE, which has been developed for TPCs read by MPGD. Since the detector performances are, in fact, the one of the detector in association with the electronics, it is crucial to correctly commission, calibrate and characterize the electronic readout system.

The AFTER chips are digitalized and controlled by the ADC developed for the RICH MWPC at Compass (see Chap. 7), following the same front-end electronics scheme than for the APV, as described in Sec. 10.2.4. The calibration of the AFTER-T2K front-end electronics will be detailed in Sec. 4.4 to 4.7 after the presentation of the ASIC.

4.1 The AFTER Chip

The AFTER, for *"ASIC for the Readout of the Large T2K Time Projection Chambers"*, has been developed for the Micromegas TPC of the T2K experiment [58]. Derived from the architecture of the electronics developed for the STAR TPC, this ASIC has been developed to be a low noise, low consumption, long analog pipeline chip optimized for large detector capacitor (20-30 pF). Each of the 76 channels has a tunable preamplifier/shaper followed by a 511 deep analog memory; the architecture is shown in Fig. 4.1. A more detailed description of the chip architecture can be found in [39].

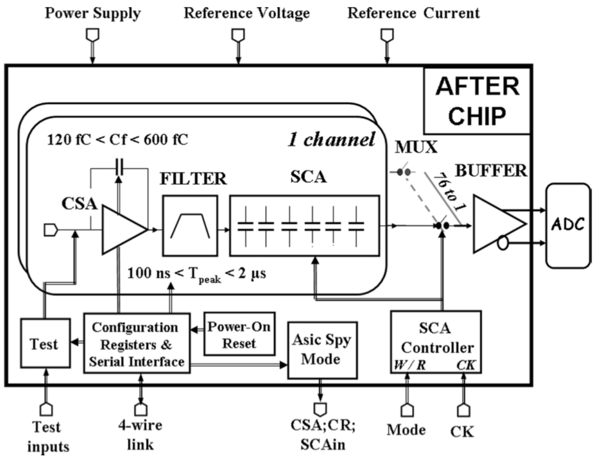

Figure 4.1: Internal architecture of the AFTER ASIC. From [39].

The first stage of this architecture is a Charge Sensitive Amplifier, as defined in Sec. 2.4.2.2, with a tunable charge range between 120 and 600 fC defined by the feedback capacitor of the pre-amplifier. The CSA is followed by a bandpass filter composed of a lowpass Sallen-Key associated with a highpass Pole Zero Cancellation (PZC, as defined in Sec. 2.4.2.3). The peaking time of the shaper, τ_P, can be chosen between 16 values from 100 ns to 2 µs.
The signals issued by the pre-amplifier/shaper are sampled and stored into the SCA (see description in Sec. 2.4.2.2). The sampling frequency can be set from for 1 to 50 MHz to match the maximal drift time. It is read by a 20 MHz clock, time slice by time slice, starting from the oldest sample. The full reading cycle takes 2 ms while writing is not possible. This is the principal rate limitation of this FEE. The analog samples are transmitted to the ADC via a differential line.

4.2 The Theoretical Pulse Shape of the AFTER FEE

The shaping of the AFTER is made by the 2 complex poles Sallen-Key and the PZC. This filter provides a semi-Gaussian shaping which slightly differs from the wide-spread 3rd order Gaussian filter (or CR-nRC). In comparison, the Sallen-Key based filter is more compact and it offers better timing performances, at the expense of a larger overshoot of 0.8% (0.025% in the Gaussian case). This overshoot is visible for the shortest peaking time on Fig. 4.2.

The analytical description of the shaper is not known and the theoretical pulse shape of the AFTER is approximated by fitting the response to a pulse with a 20 ns rising time [59]. A 6th order CR-RC fits correctly the overall signal shape but fails to describe the overshoot. That is why the best fit has a sinusoïdal term :

$$\mathrm{H(t)} = \mathrm{A_0} \cdot \frac{\mathrm{t}}{\tau}^{3} \cdot \sin(\frac{\mathrm{t}}{3\tau}) \cdot \exp(\frac{-\mathrm{t}}{\tau}) \tag{4.1}$$

With A_0 the amplitude scaling factor and τ a time constant (distinct from the shaper peaking time τ_P). The shaping varies with the peaking time so Eq. 4.1 is only valid for $\tau_\mathrm{P} = 100$ ns. Tab. 4.1 and Fig. 4.2 summarizes the different cases and corresponding constants.

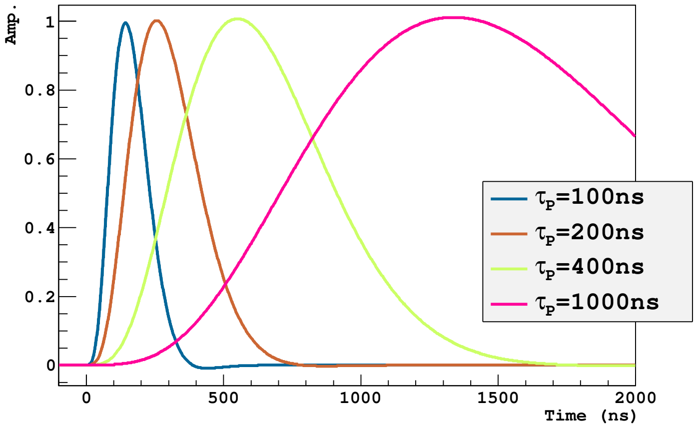

Figure 4.2: Best fit of the AFTER chip in response to a pulse of a rising time $\tau_\mathrm{i} = 20$ ns for the different peaking time settings.

The functions of Tab. 4.1 well describe the shaping for a constant pulse rising time τ_i. One should note that for the τ and τ_i parameters are not the rising time of the input signal. They correspond to the rising time of the pulse used to empirically determine an approximation of the shaper response.

τ_P	H(t)	A_0	τ
100 ns	$A_0 \cdot (t/\tau)^3 \cdot \sin(t/(3.00\tau)) \cdot \exp(-t/\tau)$	0.835065	$2.05 \times \tau_i$
200 ns	$A_0 \cdot (t/\tau)^3 \cdot \sin(t/(3.50\tau)) \cdot \exp(-t/\tau)$	0.916290	$3.55 \times \tau_i$
400 ns	$A_0 \cdot (t/\tau)^3 \cdot \sin(t/(3.70\tau)) \cdot \exp(-t/\tau)$	0.953960	$7.55 \times \tau_i$
1000 ns	$A_0 \cdot (t/\tau)^3 \cdot \sin(t/(3.85\tau)) \cdot \exp(-t/\tau)$	0.984186	$18.2 \times \tau_i$

Table 4.1: Descriptions of the AFTER shaping for the different peaking time. τ_i is the rising time of the input signal of the fitted data. Equations are normalized to 1. From [59].

For instance, in the case of long peaking time, the signal shape should not depend on the rising time of the input signal at the first order.

4.3 Front-End Cards

The front-end cards[1] house 4 ASICs directly connected to the pad-plane via a 300 pins SAMTEC BSH-EM-150 connector mounted sideways. 64 channels of the AFTER of the 72[2] available are connected to the PCB. As seen on Fig. 4.3, the overall volume of the small FEC is $103 \times 65 \times 4.8\,\text{mm}^3$, mainly constrained by the packaging of the chips (the ASIC itself is $7.8 \times 7.4\,\text{mm}^2$).

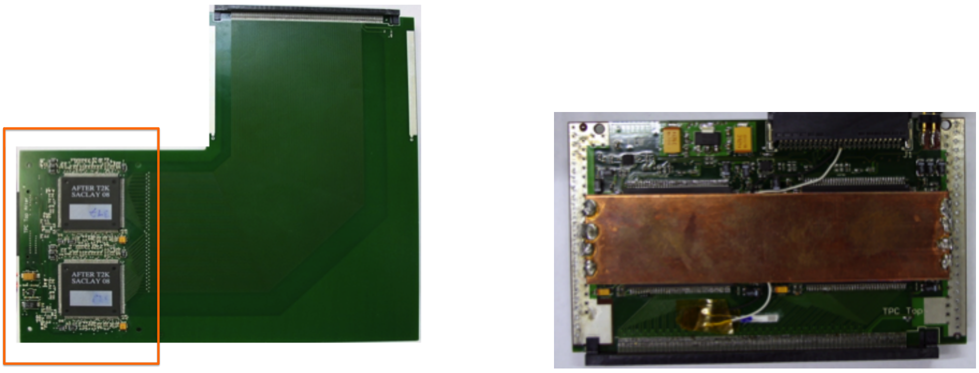

Figure 4.3: The two Front-end Cards developed for the GEM-TPC Test chamber. These FEC are called L-Card [Left] and Small card [Right]. The red frame on the L-Card corresponds to the small card size. On the small card, a copper plate covers the chips for cooling and EM shielding.

The L-Card has been designed to move the ASICs outside of the acceptance of the electron beam during the ELSA test beam campaign (see Chap. 6) whereas it has been later observed that it introduces noise and cross-talk issues (Sec. 4.5.3 and Sec. 4.7). The shorter strip version, the small card, has later been preferred to operate with the different GEM-TPC prototypes.

4.4 Gain Calibration of the AFTER

The commissioning, test and calibration of the AFTER-based FEE have been the first step in the path of the characterization of the GEM-TPC test chamber. Results of the calibration study are reported in the next sections.

---

[1] developed at TUM by H. Angerer and I. Koronov

[2] On the 76 channels of the AFTER, there are 4 FPN channels and 8 unconnected channels.

4.4.1 Pulse Injection

The first calibration is the gain measurement of the group AFTER plus ADC. To measure the gain, a known charge is injected on a pin of an AFTER chip via a standard SMD capacitor soldered on a readout pad. It is important to do this measurement in a situation as close as possible of the operating conditions, since the transfer function of the FEE, therefore the gain, depends on the input impedance and the configuration of the chip. Fig. 4.4 (left) shows a typical pulse injected on a 1 pF capacitor. The FEE is synchronized to the pulse generator to record several pulses that are superimposed to cancel jitter effects. Several different amplitudes are used to determine the linear gain function (right picture of Fig. 4.4) of the two different front-end cards. The gain of the L-Shape card is 0.071 fC/ADC ch. and 0.063 fC/ADC ch. for the small card.

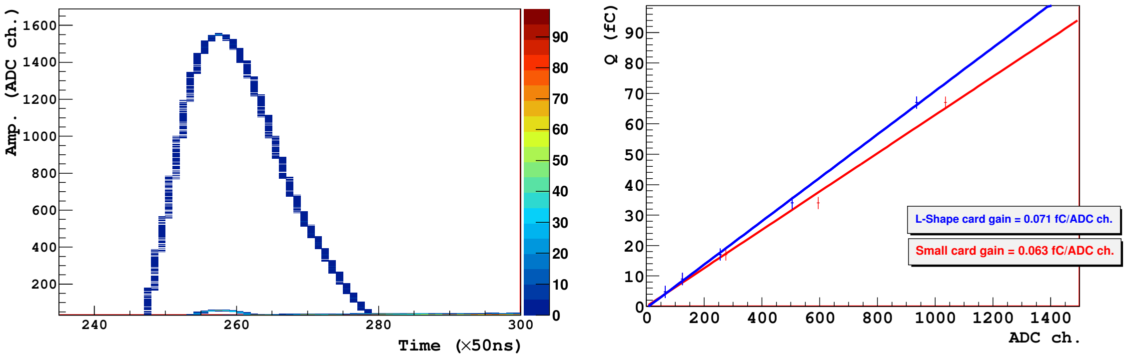

Figure 4.4: [Left] a typical pulse recorded by the AFTER-T2K FEE. The shaping time has been lowered to $\tau_P = 1000$ ns to have more measurement points with a 20 MHz clock. [Right] Data points and linear fit of the gain calibration for the two different front-end cards. This calibration is viable for the parameters used with the test-chamber ($\tau_P = 100$ ns,120 fC charge range).

The linearity, *i.e.* the variation of gain with signal amplitude, and with electronics channel or chip, corresponds to the specification (below 0.5%) and is in the order of the precision of this measurement.

4.5 Noise Characterization and Online Correction

The noise performances of the electronics of a TPC are a sensitive point since the signal to noise ratio is highly constrained. On one side, in order to minimize ion feedback, the gain of the detector must be kept as low as possible. On the other side, low amplitude signals are created by large diffusion over the drift length. So the capacity of the FEE to distinguish between signals and noise directly affects the detector performances, in particular for long drift distances.
Here, we define:

The noise: σ_{RMS} is defined as the RMS of the amplitude distribution of one electronics channel, without signals, after online corrections. More details are given in Sec. 2.6.4.2.

The pedestal: is the average amplitude of one channel without signal.

4.5.1 Zero Suppression

For each event, a chip generates 511×76 samples that are filtered and corrected online. Signals with amplitude below a defined threshold (usually between 3 to 5 σ_{RMS}) are considered as noise. These signals are suppressed from the recorded data by the *zero suppression*. This algorithm runs on the FPGA of the ADC cards, over data that have been previously corrected by the FPN correction described in the next section.

The first step of the Zero suppression is the computation, for each channel, of the average value, the *pedestal*, and the standard deviation, σ_{RMS}. The actual calculation is done offline on the first ten samples. The recording of these data uses a special mode, called *latch all*, to cope with the large data stream. The pedestals and thresholds (a multiple of σ_{RMS}), are then sent to the ADC card. The pedestal is subtracted from each sample and the resulting value is compared to the channel noise threshold.

This standard algorithm suppresses the offset between channels and reduces the overall data volume to a fraction of a percent of the original raw data size (see occupancy measurements in Sec. 4.5.4).

4.5.2 Fix Pattern Noise Correction

The study of latch-all data has shown a drop of the pedestal value along the memory. The first samples read out of the SCA have higher mean amplitude than the last ones. The overall drop has a distinct shape shown by the black curve of Fig. 4.5. This pattern is caused by a leakage current inside the SCA. Each cell of the memory is a capacitor on which charges are stored. But since the capacitor is not ideal, a small portion of the signal charge leaks into the chip substrate. This leakage current affects more the signals that have waited a longer time inside the memory array during the 2 ms readout phase, creating the drop in amplitude regardless of the physical position inside the memory.

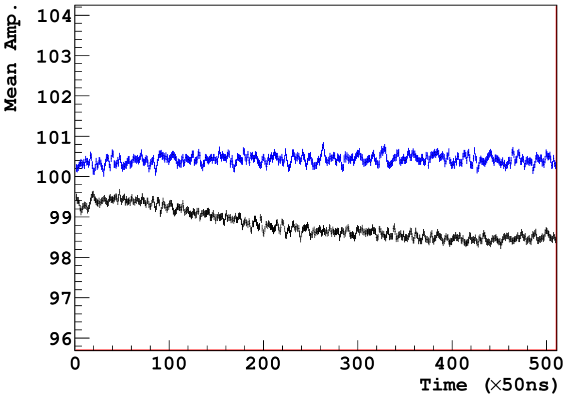

Figure 4.5: Mean amplitude of samples along the memory before (black) and after (blue) FPN correction. A different pedestal offset has been artificially applied on each curve to avoid overlap of the curves.

Since the pedestals are calculated at the beginning of the memory, the amplitude of signals that lie at the end of the memory would be underestimated. Moreover the end of the memory corresponds to large drift values, therefore to smaller signals due to diffusion, increasing the impact of this drop.

The chip designers have foreseen 4 “FPN” channels, for *Fixed Pattern Noise*, per chip, see Fig. 4.6. These channels are not connected to the packaging and their amplitudes are only affected by what happens in the memory. There are 2 SCA per chip, corresponding respectively to odd and even pin number, with 2 FPN channels each. For each SCA, the mean value of the 2 FPN channels is subtracted from the others on a sample basis. This method corrects the drop in amplitude, but also common mode noise, and for the dispersion of capacitor values inside the SCA. The common mode noise is a fluctuation that affects all the channels in the same way (noise on the chip power supply for instance) including the FPN channels. The capacitance dispersion is due to non-homogenized doping of silicon, for which the FPN channels have been designed to control. The resulting correction is shown with the blue curve of Fig. 4.5.

4.5.3 Noise Performance

Fig. 4.6 shows the typical noise spectrum of one chip for the 2 front-end cards. The noise amplitude is proportional to the capacitance connected to each channel. The longer strips on the PCB of the L-Card explain the overall difference between FECs. For each spectrum we observed a lower noise of the first and last 4 channels because those channels are not solder to the PCB circuit. The 4 FPN channels (at the channels numbered 12, 35, 50 and 63) have the lowest amplitude variations. On the small-card spectrum, one can observe the different of strip length connected to first and second half of the chip; it corresponds to a different side of the physical chip and an additional 2 cm of copper strip on the PCB.

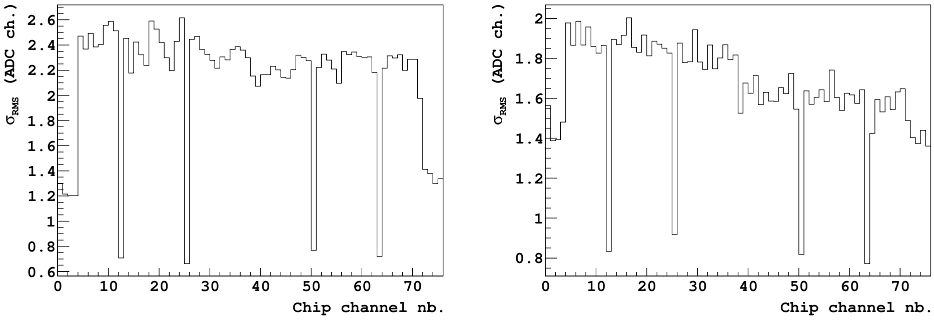

Figure 4.6: Noise spectrum of one ASIC of the L-shape [Left] and small [Right] FEC. For the L-card ASIC, the noise is 1.94 ± 0.11 ADC channels on connected channels (the error is the RMS of the noise distribution). The small card has a noise of 1.58 ± 0.05 ADC ch. The spectrum shows a division between the first and second half of the ASIC that are connected to a different side of the packaging, their noise levels are respectively 1.55 ± 0.10 and 1.63 ± 0.06 ADC ch. .

The average noise of the connected channels on the small FEC is 625 ± 63 e^- and 975 ± 89 e^- for the L-Card, both cards connected to the test chamber pad plane (the error is the RMS of the noise distribution). Using the linear extrapolation of the AFTER noise parameters [39] for the same settings ($\tau_P = 100$ ns and 120 fC charge range), the corresponding capacitance can be calculated: 12.6 pF for the small card and 26.1 pF for the L-Card. This corresponds to the expected value coming from the strip length in addition to the $\sim$ 10 pF of the chip packaging. According to the same extrapolation numbers, using a 200 ns peaking time would lower the noise of the small card to $\sim$ 550 e^-.
As a point of comparison, the small card noise performance is better than the 810 ± 100 e^- [39] quoted for the T2K FEC in the same conditions. This is explained by the absence of protection circuits needed by the Micromegas detectors. However, for the GEM-TPC FECs, electronics channels can

be destroyed by an accidental discharge that would overcome the internal protections of the AFTER packaging.

4.5.4 Occupancy

The occupancy is defined as the number of samples over the noise threshold divided by the maximal number of samples per event (for one chip: 510×64 connected channels $= 32640$ samples[3]). Tab. 4.2 shows the effect of different noise thresholds on the occupancy.
The occupancy is important to monitor the efficiency of noise suppression algorithm.

Noise threshold in $\sigma_{\mathbf{RMS}}$	**Occupancy on the Small FEC**	**Occupancy on the L-Shape FEC**
2	4.1 %	6.0 %
3	0.39 %	0.43 %
4	1.5×10^{-5}	2.4×10^{-5}

Table 4.2: Occupancy of the FEE for different noise thresholds.

The occupancy is higher than a pure Gaussian distribution[4] due to digitalization effects whereas it follows the expected order of magnitude. This shows that the online corrections are under control.

4.6 Power Consumption and Temperature Measurement

In a TPC it is crucial to maintain a good homogeneity of the drift velocity. That implies that the temperature must be homogeneous in the active volume, the heat introduced by the FEE must be minimal. A temperature of 42 °C has been measured on the functioning AFTER chip. An operating TPC would have to be equipped with a cooling system to keep the chips at room temperature.
The cooling power needed depends on the power consumption of the AFTER FEE. It has been measured to be ~ 2.5 W per FEC, this corresponds to 8.2 mW/channel. This is in the range of the 5.7 to 8.3 mW/ch. (depending on the bias voltage of the SCA) of the chip specification [60].

4.7 Cross-Talk Measurement

The autocorrelation of signals per channel is shown in Fig. 4.7. It indicates the propagation of signals of a channel (k) to the channel ($74 - k$). This correlation is explained by the proximity of those channels on the PCB design. The long strips of the L-Card introduced a crosstalk up to 10%. Offline correction methods, derived from the one used for the PixelGEM [61], effectively corrected this problem. However since the L-Card design has later been replaced, this correction is no longer necessary. The crosstalk on the small FEC has been measured to be lower than 1.5%.

4.8 Choice Between the Front-End Cards

Originally designed to put the ASICs outside of the beam acceptance, the longer strips of the L-shape front-end card have proved to be a major drawback. Specifically, the L-shape card has a noise more than 30% higher than the small card and more than a factor 6 in cross-talk. Since the small card have shown to be able to work with no problem in the acceptance of the electron beam at ELSA (see Chap. 6), the more conservative design of the L-shape card has been abandoned.

---

[3] The first of the 511 samples is not used due to a higher noise.

[4] The integral of a Gaussian outside 2σ is 4.55%. Since only half of the distribution is observed after pedestal subtraction, 2.3% is expected here.

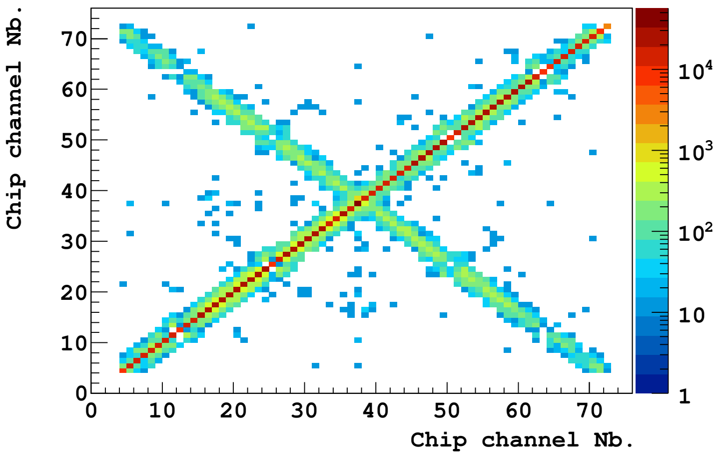

Figure 4.7: Autocorrelation of signals of the channels of one chip on one L-card. The "×" shows that signals of a channel (k) are correlated with the one of the channels ($74-k$).

Chapter 5

Pulse Shape Analysis of the GEM-TPC

The **Pulse Shape Analysis**, as defined in Sec. 2.5.1, is used to detect, separate, and analyze signals from the data stream of each electronics channel. In the naive representation of a fixed signal shape, the time and amplitude information can be extracted from the maximal sample of a signal, whereas it is not the most optimal solution when the signal shape varies.
In this chapter, after showing that the electronics signals often differ from the theoretical shape, the effects of these fluctuations on the extracted value of time and amplitude, are studied. Alternative algorithms are proposed.

5.1 Calibration of the AFTER Time Constant

A good description of the effective pulse shape is important for a realistic Monte-Carlo simulation, in particular to describe the effect of charge reconstruction of low amplitude signals, such as the one created by MIPs. This effective signal shape uses the analytical description of the AFTER shaper (see Sec. 4.2) with a time constant extracted from measurements in different conditions. Eq. 4.1 is used to fit $\sim 10^4$ signals and the time parameter τ is extracted. The distribution of this parameter is shown in Fig. 5.1 for krypton data, cosmic data taken with the large prototype, and high-energy muon in the test chamber.

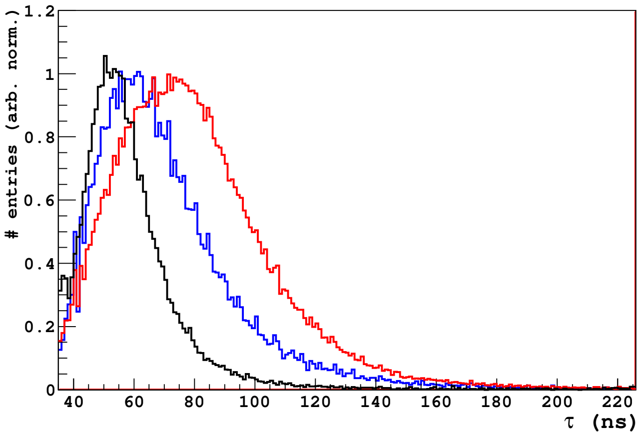

Figure 5.1: Distribution of the time parameter of the theoretical function of Eq. 4.1 fitted to 3 different set of data: black for high-energy muons at COMPASS with the test chamber, blue and red for respectively cosmic and krypton at FOPI for the large prototype. The most probable value for krypton is 73.4 ns, 61.9 ns for cosmic and 53.4 ns for the test chamber with high energy muons.

The most probable value of these distributions is related to the relative length of the rising edge of input signals. Indeed, the diffusion is less important within the test chamber than is the larger prototype, see Tab. 3.2, and cosmic rays leave a more localized and homogenous energy deposit than krypton decay. The width of the distribution shows the variety in signal shapes which is larger for krypton than cosmic rays, and larger for the long drift of the large prototype than for the test chamber.

In addition to providing a more realistic description of the signal shape in Monte-Carlo simulations, this study has shown that the recorded signals have a rather large distribution for the time constant. This distribution and its MPV highly depend on the type of data concerned, the simulation should incorporate this behavior.

This situation is not ideal and algorithms have to be as little sensitive to signal shape as possible.

5.2 Amplitude Calculation and Effect on the Energy Resolution

The important fluctuations of the signal shape imply that the relation between maximum amplitude and charge is not linear. That would explain the bad energy resolution obtained by the observation of the maximal amplitude distribution shown in Fig. 5.2 where $\sigma_E/E > 50\%$ (E is the peak position and σE the width of the peak distribution). Krypton calibration data of the large prototype are used here so the rich spectrum of Tab. 3.1 can be used as a reference.

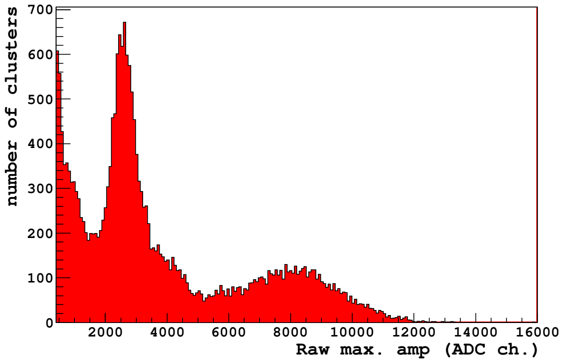

Figure 5.2: Maximum amplitude distribution for krypton calibration for the large prototype.

To be less sensitive to signal shape, the sum of all samples bellowing to one signal, the *integrated amplitude*, is used instead of the maximal sample amplitude. In addition to that change, two modifications of the reconstruction algorithms are necessary: *saturation cut* and *cluster merging*.

5.2.1 Saturation Cut

The wide range of the possible energy deposit with krypton, from to 9.4 to 41.6 keV (see Tab. 3.1), is in the order of the dynamic range of the FEE. Even with a moderate gain of ∼ 2000, saturation is frequent and creates fake peaks as shown in Fig. 5.3. The saturation peak is clearly visible on the sample amplitude distribution (left histogram of Fig. 5.3). Samples over a threshold of 1700 ADC ch. are considered saturated and cannot contribute to energy measurement. These samples have to be suppressed in the amplitude distribution whereas this suppression has to be applied later, at the cluster level. Indeed applying a simple threshold at the sample level would introduce an artificial loss of charges in the final cluster. Samples over the threshold are tagged and clusters that contain such

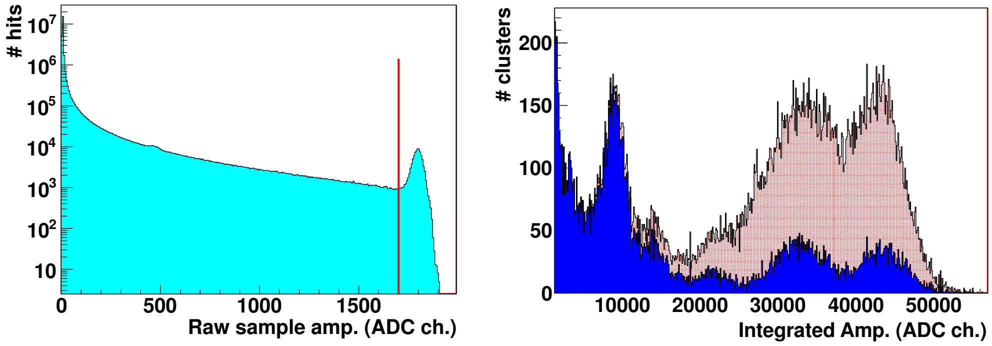

Figure 5.3: [Left] Sample amplitude spectrum with the saturation bump above the threshold (red vertical line). [Right] Impact of the saturation cut on the integrated amplitude spectrum at a gain of 2000. The red distribution shows the spectrum before the cut and the blue is after. The resolution of the two highest peaks is improved and a peak at 22000 emerges.

samples are suppressed from the reconstructed amplitude spectrum as on Fig. 5.3. This correction affects mainly the clusters of the 41.5 keV peak that have not diffused enough to avoid saturation. This effect is important ($\sim$ 20% of clusters at a gain of 2000), so it highly modifies the relative peak amplitude of the spectrum. Nevertheless the position of the peaks, which is relevant for gain calibration, is not impacted at the first order[1]. To avoid cutting a large part of the statistics available, data taken at lower gain are used where the saturation effect is less important.

5.2.2 Cluster Merging

The clustering algorithm used with the GEM-TPC has been optimized for position reconstruction and pattern recognition of charged particle tracks. It divides clusters following local minima in time and space. Since the practical range of slow electrons is increasing with the energy, up to 29.22 mm for the 41.5 keV peak in Ne/CO_2 (see Tab. 3.1) these large clusters contain several local minima and are divided. This artificial division degrades the energy resolution. An algorithm to merge the divided clusters has been implemented and its effect can be seen on Fig. 5.4.

This algorithm merges all clusters within a sphere of 3 cm, starting from the largest cluster. Since the even rate with krypton is low, only a few events per drift frame, the probability of merging two different physical clusters is low and has not been observed in the available data set.

5.2.3 Impact of Amplitude Calculation on Energy Resolution

The use of integrated amplitude, saturation cut and cluster merging allowed a better energy spectrum reconstruction as shown in Fig. 5.5. For low gain data, the spectrum agrees with the theoretical spectrum for the peak position and in terms of relative amplitude. The energy resolution of the 41.6 keV peak is $\sigma_{\mathrm{E}}/\mathrm{E} = 7.3\%$. Using the results of the relative gain calibration to correct spatial inhomogeneity, the large prototype achieves a resolution of $\sigma_{\mathrm{E}}/\mathrm{E} = 5.1\%$ at 41.5 keV [62].

5.2.4 Impact of Amplitude Calculation on Position Reconstruction

The spatial position of a cluster is the center of gravity (COG, see Sec. 2.5.2) of the signals that constitute the cluster weighted by the signal amplitude. This depends on relative amplitudes, and is

---

[1] After saturation cut, the high energy peaks are mainly composed of signals that have diffused a lot in the chamber, and since these signals are more sensitive to the electronics noise threshold, the position of the peak are slightly shifted toward low amplitudes

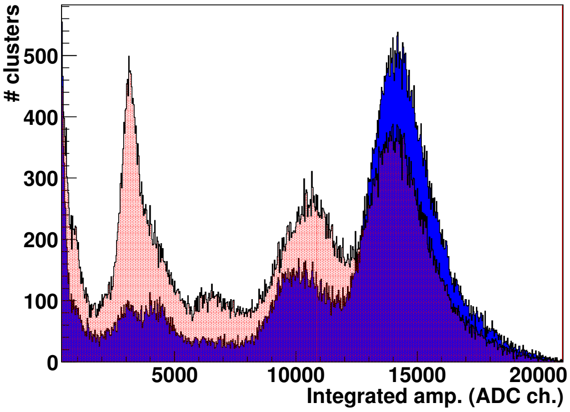

Figure 5.4: Effect of the cluster merging, the red curve shows the spectrum before the merging and the corrected is in blue. One can see, for instance, that the peak at 8000, corresponding to the amplitude of the highest peak divided by 2, has disappeared. Krypton data with the large prototype at a gain of ∼ 800.

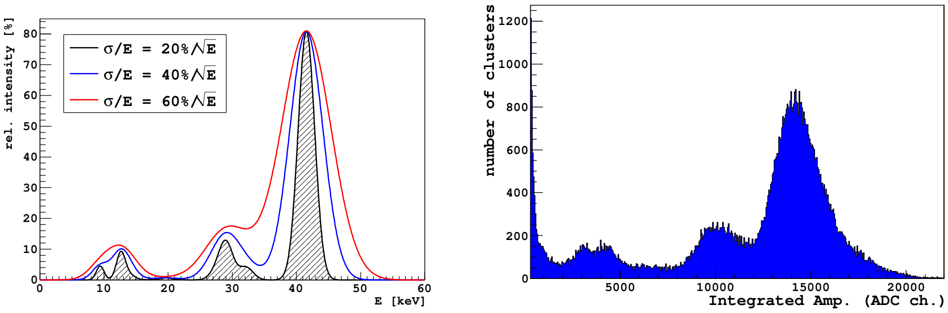

Figure 5.5: [Left] Monte-Carlo simulation of the krypton spectrum for different energy resolution (Simulation from R. Schmitz [62]). [Right] Energy spectrum of krypton calibration with the large TPC. The 41.5 keV peak has a energy resolution of σE/E = 7.3%.

therefore sensitive to fluctuations of the maximal amplitude. By using the integrated amplitudes in the COG calculation, the residuals distribution is improved, see Fig. 5.6. These residuals concern the test chamber at COMPASS with high-energy muons; a complete description of the analysis can be found in Chap. 6.

The width of the residual distribution is lowered from 240 to 220 µm, and the secondary aisles, corresponding to neighboring pads, have been significantly attenuated. Moreover the better amplitude definition also allows a clear distinction between noise and signal in these data, lowering the overall background.

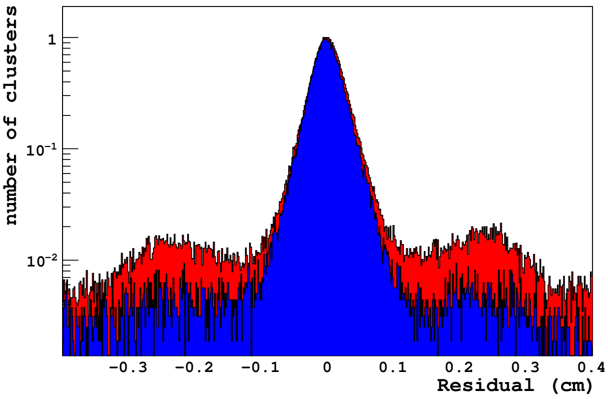

Figure 5.6: Effect of the integrated amplitude on residuals distribution of the test chamber (V projection, perpendicular to the beam, parallel to the pad plane). The red distribution shows the residuals using maximal amplitude for the cluster COG computation, blue uses integrated amplitude.

5.3 Time Reconstruction

As for the amplitude calculation, the standard reconstruction algorithm uses the information of only the maximal sample within a signal. In this section, alternative ways of computing the time of a signal are studied. To make use of the additional information provided by the whole signal shape available in the data stream, 4 time reconstruction algorithms have been studied (the number in parenthesis refers to Fig. 5.7):

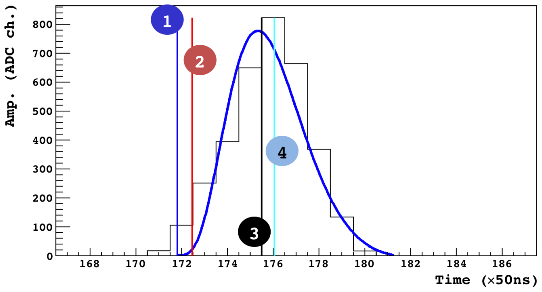

Figure 5.7: Example of the time reconstruction with krypton data (vertical bars). The signal is fitted with the theoretical AFTER shape (blue line). The vertical lines shows the reconstructed times for the different methods: (1) $\mathrm{T_{Fit}}$, (2) $\mathrm{T_{Diff}}$, (3) $\mathrm{T_{Max}}$ and (4) $\mathrm{T_{CF}}$.

(1) $\mathbf{T_{Fit}}$: The time information is extracted from the fit parameters of the signal by the function of Eq. 4.1. This method consumes important CPU resources for minimization and would not be a practical solution ($\sim$ 30 min for 5000 events on a standard desktop computer). However the study of the fit reveals the signal fluctuations compared to the theoretical shaping. The reconstructed time corresponds to the beginning of the signal (the time offset of the fit function).

(2) $\mathbf{T_{Diff}}$: The maximal differential method uses the maximal difference, between two consecutive signals of the rising edge, to extrapolate linearly the time to the abscissa axis.

(3) $\mathbf{T_{Max}}$: The time of the maximal sample is used. This is the current algorithm, it will be used as a reference.

(4) $\mathbf{T_{CF}}$: The constant fraction algorithm considers the time for which $s(k) - 2s(k-2)$ crosses the abscissa axis, with $s(k)$ the processed digital signal and k a positive integer. A complete description can be found in Sec. 2.5.1. The delay of 2 time bins is chosen to set the reconstructed time at the maximum amplitude of the signal.

Except for $\mathrm{T_{Fit}}$, these algorithms do not require more than one iteration over the data stream and could be implemented in an FPGA for online processing.

Fig. 5.8 shows the superposition of normalized signals for the different timing. For each signal $s(k)$, $s(k-T)/\max(s(k))$ is plotted, with T the time reconstructed by the different methods and $\max(s(k))$ the maximal amplitude of the signal. These figures have been computed for krypton data with the large prototype where the fluctuations are the most important in order to be in the least favorable case. Only signals with more than 4 samples on the rising edge (including the maximum sample) are considered here.

The more the signal is well defined (more "red"), the best is the time reconstruction. That means

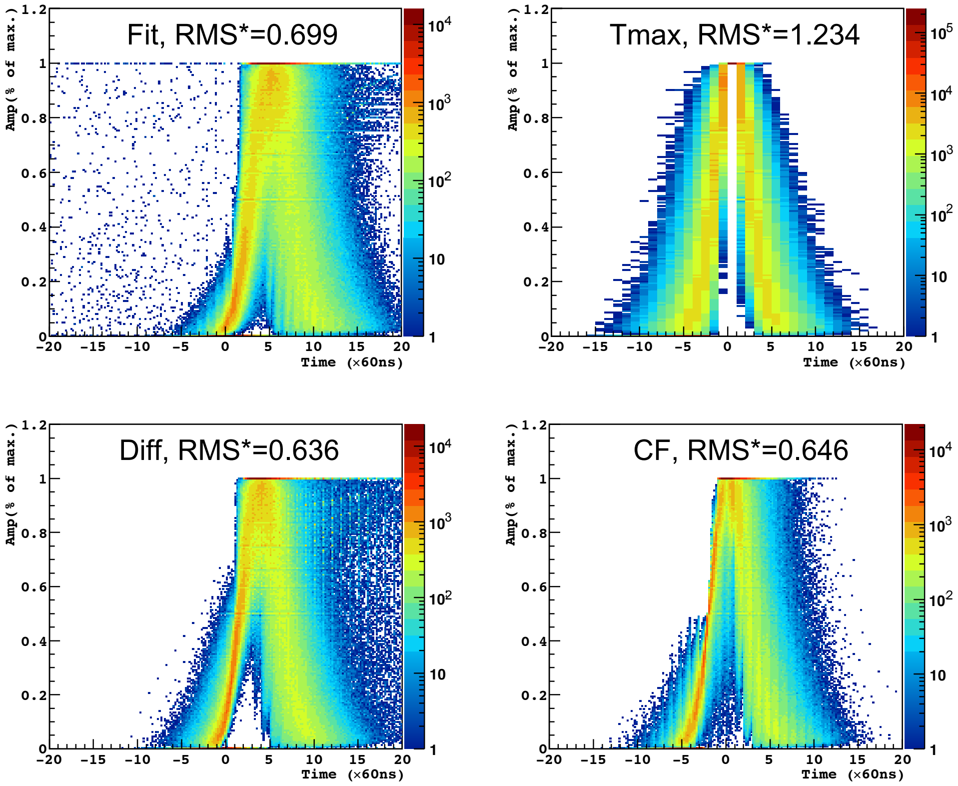

Figure 5.8: Superposition of normalized signals from krypton data, shifted at the different reconstruction signal time, see text. The "RMS*" is computed for the rising edge (left leg of the signal) between 0.18 and 0.22.

that the time is reconstructed at the same relative position for most of the signals. The "RMS*" is calculated for the rising edge at 20% of the maximum of the signal, it shows how well the rising edge of the signal is defined. From that number, one can qualitatively appreciate how precise is T_{Diff} and T_{CF} compared to T_{Max} and even T_{Fit}.

The impact on time resolution (or the spatial resolution along the drift coordinate) using T_{Diff} instead of T_{Max} have shown to be negligible on the test chamber. This is due the fact the improvement of the time definition is smeared by of other effects, in particular diffusion and trigger jitter. Indeed the phase between the FEE clock and the trigger is not known introducing a jitter of one clock cycle (50 ns in the test chamber case). Nevertheless, the benefit of a better time definition could be seen with an optimized diffusion and the recording of the trigger phase. Moreover, online data processing algorithms, such as tail cancelation, requires the best time definition.

The right part of these signals is also important. It shows how well the exponential decay is described. This is crucial to consider tail cancellation. An early attempt of an offline tail cancelation, based on T_{CF}, has not been successful due to the large fluctuations of signal tail that introduce resonances in the digital filter: a tail suppression applied on a longer tail than expected creates a fake signal.

On Fig. 5.8, only signals with a defined rising edge are considered. Noise, low amplitude and truncated signals, represent a large proportion of the data, up to 60% in cosmic. Special cases in the algorithm of T_{Diff} and T_{CF} have to be considered when the rising edge is too short to compute T_{Diff} or

T_{CF}. The difference between special cases must be calibrated.

5.4 Conclusion on the Pulse Shape Analysis

The width of Fig. 5.1, the T_{Fit} plot of Fig. 5.8 and the maximal amplitude distribution of Fig. 5.2, reveal that the GEM-TPC signals recorded by the AFTER FEE are fluctuating compared to the theoretical shape. Therefore the reconstruction algorithms have to be less sensitive to the pulse shape.

The amplitude, defined as the integration of all samples belonging to one signal, has proved to be a significant improvement compared to the use of the maximal sample only. It allows the measurement of the 41.5 keV peak of the raw krypton data with an energy resolution of $\sigma_E/E = 7.3\%$. The spatial resolution is also positively impacted.

The time reconstruction can be improved by using different methods that use the rising edge information. The constant fraction and the maximal differential algorithms have shown promising results whereas it requires several measurement points on the rising edge. The tail description appears to be more precise with T_{CF}.

The shaping stability would improve with a longer peaking time. It would increase the signal to noise ratio, ease time and amplitude reconstruction and thus improve the performances of the detector whereas signal pile-up would increase. In this matter with a TPC, two options are available, either a fast shaping time to avoid pile-up that introduces shape fluctuations observed here, or a slower shaper with a more stable shaping. This has to be optimized for the track topology and the diffusion in gas of a given experiment. For instance the importance of double tracks resolution would require a faster peaking time whereas single parallel tracks to the readout would be better defined with a slower peaking time. This optimization is even more challenging in the case of a general purpose GEM-TPC.

Chapter 6

The GEM-TPC Test Chamber Data Taking

The test chamber, newly equipped with the AFTER front-end electronics and the hexagonal anode pads, has been installed together with an external tracking system at the ELSA facility at Bonn, Germany, for commissioning. In a second campaign, the test chamber has been quantitatively characterized using the high-energy muon beam of the COMPASS experiment at CERN. Spatial residuals have been studied for both the test chamber and the tracking detectors.

After presenting the test bench and the tracking detectors, the results of the commissioning at ELSA will be briefly developed before the characterization at COMPASS is described.

6.1 Test Bench and Tracking Detectors

The test bench, as shown in FIg. 6.1, is a small experiment in itself with 7 planes of detection, 4060 active electronics channels, and its own DAQ based on DATE [63]. The tracking detectors consist of two GEM detectors (see Sec. 6.1.2), and two silicon detectors (see Sec. 6.1.1) triggered by 4 plastic scintillators.

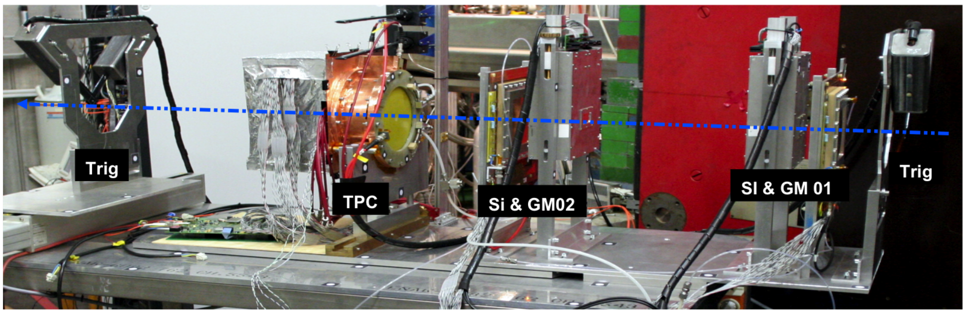

Figure 6.1: Test bench at the ELSA facility, the dashed blue line represents the electron beam. Along the beam direction, from right to left : (Trig) First trigger station; (SI & GM 01 and 02) First and second silicon stations and GEM detectors 01 and 02; (TPC) GEM-TPC test chamber with its FEE protected with EM shielding; (Trig) last trigger station.

The test bench support structure is a dedicated aluminum table[1] designed to offer mobile supports for the tracking detectors and trigger, in addition to a moveable, both in rotation and translation, mechanical holding for the GEM-TPC. A detailed description of the structure can be found in [64].

---

[1] developed at HISKP Bonn

The trigger signal is issued by the coincidence of 4 plastic scintillators of 20×150 mm^2, 2 at each side of the test bench forming an angle of 90°. They have a 0.7 ns time resolution, the trigger acceptance is 20×20 mm^2 with a material budget of less than 1% of X_0.
The test chamber is placed perpendicularly to the Z-axis, so the beam and the drift direction are overlapping, which is the least favorable case for data reconstruction in the TPC.

6.1.1 Silicon Detectors

Silicon detectors are ideal for high precision tracking. A silicon detector consists of an array of diodes, reverse-biased with a potential difference of 35 V. When an ionizing particle deposits a charge in the depletion zone, a current is collected on the corresponding strip. The 4 planes of silicon detectors, built at HISKP Bonn, are divided into 2 stations : SI01 and SI02, see Fig. 6.1 and 6.3. In each station, the two perpendicular strip planes are spaced by 3 mm. Each plane has a 1.92 cm long active area composed of 384 strips, at a pitch of 50 µm, read by the APV chip. (see Chap. 10). It is made of a 300 µm thick silicon wafer of 0.68% of a radiation length.

6.1.2 GEM Detectors

The test bench GEM detectors have been built during a student project in 2008 at TUM. The 10.24×10.24 cm^2 2D strip readout uses a triple GEM gaseous amplification at a gain of 8000. Each projection is composed of 256 strips at a pitch of 400 µm. To equally share the charge of an avalanche, the top wires have a width 80 µm and the bottom one 340 µm. The overall detector is 0.67% of a radiation length. More details can be found in [65].

6.1.3 Test Bench and Detectors Coordinates

We defined two coordinate systems, XYZ for the test bench ("lab" coordinates) and UVW for the detectors. The origin of the test bench coordinate system, XYZ, is placed the first trigger station. The Z axis is defined by the trigger acceptance, following the same direction than the beam. The X and Y axis are perpendicular to the Z axis and respectively along the horizontal and vertical direction of the test bench. The Euler angles θ, ϕ and ψ are defined by the XYZ coordinates. In the detectors, the UV coordinates are defined by the read-out plane and W along the drift axis from the anode toward the cathode (see the projection of the beam in the TPC detector coordinates in Fig. 6.4).

6.2 Commissioning of the Test Bench at ELSA

6.2.1 Conditions

The ELSA facility produces a beam of 0.5 to 3.5 GeV/c electrons, 2.4 GeV/c during the test beam time. The test bench was running parasitically in parallel of the Crystal Barrel experiment [64]. Placed behind a photon-tagging magnet, the electron beam in trigger acceptance has an energy of 400 MeV/c with a mean coincidence rate of 300 Hz.

6.2.1.1 Alignment of the Tracking Telescope

The pre-alignment of the test bench detectors and test chamber, with respect to each other, have been made using a 3D model created by photogrammetry. Pictures at different angles of the several visual markers, stuck to the detectors, were processed by computer software to obtain a geometry file of a precision of few mm. A standard χ^2 minimization software using tracks achieved the final alignment. Tracks reconstructed in the telescope gave a ~ 2 µm biased residuals for the silicon detectors and ~ 200 µm for the GEM [65].

6.2.1.2 TPC Tracks and Multiple Scattering

In addition to the commissioning phase, a first look at the test chamber performances was possible. A GEANT based Monte-Carlo simulation has shown that the expected resolution of the test chamber in this geometry would be $\sim 140\,\mu\text{m}$. This simulation uses the same reconstruction algorithms than for real data, whereas it does not take into account material effects because the description of the detector materials was not included in the simulation. The first data have shown a residuals width over 1 mm, which is due to the electron beam scattering.

At 400 MeV, electrons are easily deflected by matter, decreasing the resolution of the test bench tracks. This deflection is mainly due to Coulomb scattering, which is well represented by the theory of Molière [48]. The distribution can be estimated by a Gaussian of a width described by:

$$\theta_0 = \frac{13.6\,\text{MeV}}{\beta c p} z \sqrt{X/X_0}\,[1+0.038\cdot\ln(X/X_0)] \qquad (6.1)$$

Here p, βc and z are the momentum, velocity, and charge number of the incident particle of the beam, and X/X_0 the radiation length of the material.
Using the material definition from [65], we can calculate the deflection angle at each detector plan using Eq. 6.2.1.2. Here we considered that the track is fixed at the second silicon (due to their higher spatial resolution, silicon detectors almost fix the track position) and we will only consider material encountered after this detector. Results are given in Tab. 6.1. The resulting displacement in Y gives is 1.1 mm which is closed to the 1.175 mm shown in Fig. 6.2.

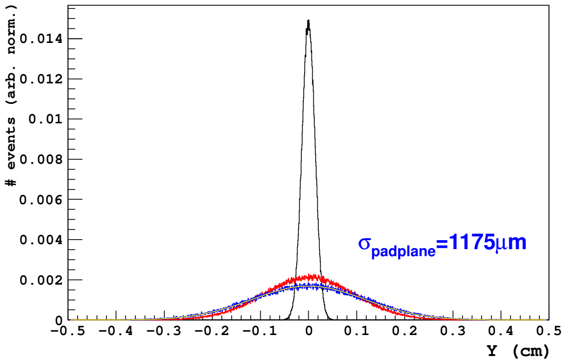

Figure 6.2: Monte-Carlo simulation of the effect of multiple scattering on a point-like 400 MeV electron beam. The origin of the beam is placed at SI2, the diffuse beam at the GEM2 detector is represented by the black curve, the red curve at the TPC drift and the blue one is the projected at the pad plane. The width of the fitted distribution is 1.175 mm.

Material	**X/X$_0$**	**θ_0**	**leverage arm**	**Displacement in Y**
Silicon Box	0.32%	0.086°	9 cm	135 μm
GEM 2	0.61%	0.12°	33 cm	707 μm
TPC Drift	1.33%	0.19°	8 cm	263 μm

Table 6.1: Effect of multiple scattering from the SI2 to the test chamber.

The test bench has been successfully commissioned at ELSA, clear correlations in tracking detector and first residuals in the test chamber have been observed. In order not to be dominated by multiple scattering, a higher momentum is needed since the multiple scattering scales with the inverse of particle momentum (see Eq. 6.2.1.2). That is why the test bench has been transported to CERN, behind the COMPASS experiment, where the 160 GeV/c muons have a negligible 3 µm scattering (according to the same MC simulation than Fig. 6.2).

6.3 Characterization with High-Energy Muons

In 2010, the test bench has been installed nearby the COMPASS experiment located on the M2 line of the SPS. The commissioned test chamber operated smoothly. However, a bad computer crash damaged most of the data and configurations files. As a result, this study is based on one a unique data set of ~ 15500 events where all the detectors and the test chamber are working well.

6.3.1 Setup at COMPASS

The acceptance of the test bench is in the halo of the 160 GeV/c muon beam focused on a NH_3 target ~ 60 m upstream. More details about COMPASS beam can be found in Chap. 7. In the $20 \times 20\,\mathrm{mm}^2$ trigger acceptance, the measured rate is 20 Hz during spill. The chamber was operating in Ar/CO_2 70/30 at a gain of ~ 4000 (100% of GEM HV) (see Tab. 3.2). Unlike the previous situation, the pad plane of the chamber is almost parallel to the beam, which is optimal for internal tracking.

As shown in Fig. 6.3, the test bench has been reorganized to bring the silicon detectors closer to the test chamber, increasing the track precision within the TPC. The GEM detectors are at each end of the test bench to provide beam monitoring and particle disentanglement for tracking. Tab. 6.2 gives the relative position of the test bench detectors along the beam axis.

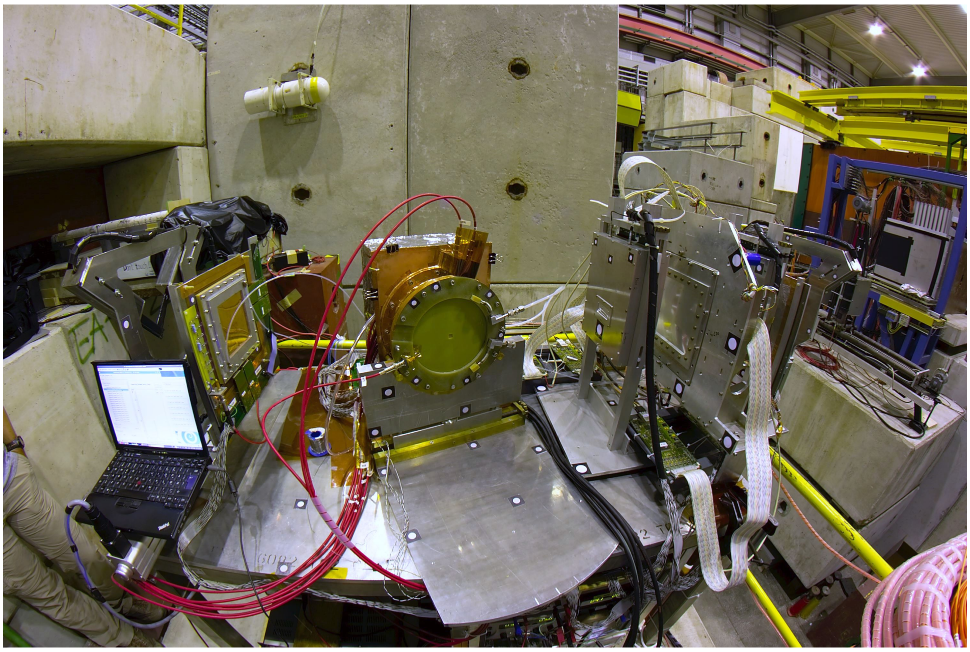

Figure 6.3: Test bench behind the COMPASS spectrometer (on the right of the picture).

To obtain a good track extrapolation inside the chamber, it is necessary to align the tracking telescope detectors between each other. Then by using the telescope tracks, it will be possible to align the test chamber and have a coherent ensemble, see Sec. 6.3.1.2.

6.3.1.1 Alignment of Test Bench Detectors

After a first manual alignment using the center of residual distributions, a standard χ^2 minimization, based on Minuit [66], has been used to correct the position of the test bench detectors.

Detector	Position in cm
Plastic Sc.	0
GEM 01	11
SI 01	20
SI 02	61.9
TPC (center)	110.3
GEM 02	154.7

Table 6.2: Relative detector position along the beam axis.

First step: The silicon detectors positions are fixed, and used to create a set of tracks. When there is one and only cluster per silicon plane, a track is built from the extrapolation between the 2 space points derived from the 4 silicon strip clusters.

Second step: The offset position of the first strip, θ and ϕ angles of the GEM detectors are used as free parameters in the minimization function. The quantity to minimize is the RMS of the residuals between telescope tracks and detectors clusters. The alignment is successful if the minimization algorithm converged.

With this particular set of data, it has been necessary to remove from the data ten strips at the edge of each silicon detector to avoid converging on EM noise. The beam profile inside the tracking detectors can be observed on Fig. 6.4, the width of the corresponding biased residuals are summarized in Tab. 6.3. The residuals are biased because the detectors clusters have been used for the definition of the tracks. The difference between the X and Y projections, for the GEM detectors, indicate that the alignment is not optimal. Indeed misalignment corrections, in particular angular, are limited by the size of the trigger acceptance and the statistics available.

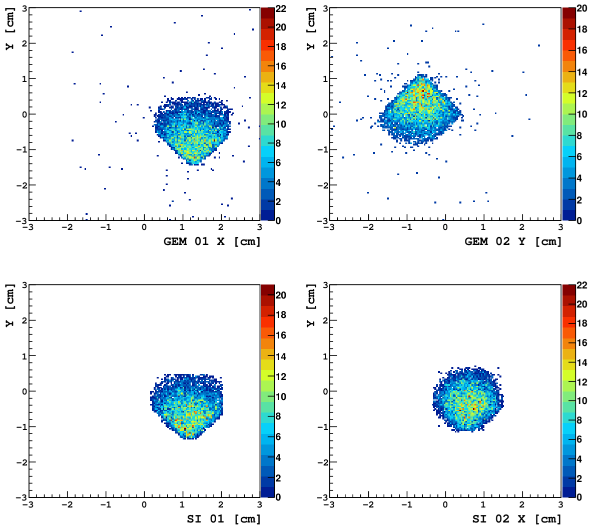

Figure 6.4: Hit position of the tracking detector clusters for 10000 events with a reconstructed track (∼ 72% of all events). The angle of the halo beam with respect with the trigger acceptance appears.

	GEM 01	GEM 02	SI 01	SI 02
X Projection	101 µm	140 µm	7 µm	7.6 µm
Y Projection	75 µm	69 µm	8 µm	8 µm

Table 6.3: Width of biased residual distributions for the tracking detectors compared to telescope tracks. The fit errors are below 1 µm.

6.3.1.2 Alignment of the Test Chamber

The alignment is the minimization of the residual distributions between telescope tracks and the TPC clusters. To obtain these residuals, the difference between the TPC clusters (space points) and the tracks is calculated in virtual detector planes. These planes are perpendicular to the tracks. The resulting vector is then translated in lab coordinates for minimization.

The alignment of a TPC is more complicated than that of plane detectors. Indeed since the TPC clusters are not constrained to a physical detector plane, the alignment has more degrees of freedom. Moreover, the reconstruction along the drift coordinate requires a good knowledge of the drift velocity v. A good way of measuring it would by using the distribution of signals along the full drift length whereas this is not possible with the test bench geometry (the beam is only present in a fraction of the test chamber drift length) and the v parameter has also to be aligned.

The Z position of the center of the chamber is fixed, X, Y, θ, ϕ, ψ and v are free parameters. The alignment of the TPC is a sequence of minimizations of the residual distribution RMS of TPC clusters compared to telescope tracks. The sequence consists of the alternation between position and angle optimization. The first step align X, Y and v, then these parameters are fixed, and θ is released. The same strategy is used for ϕ and ψ and at the end, all parameters are released to see if the algorithm converges. The effect of the alignment sequence is shown in Fig. 6.5. The full procedure is then repeated until the parameters remain unchanged within a percent of their value.

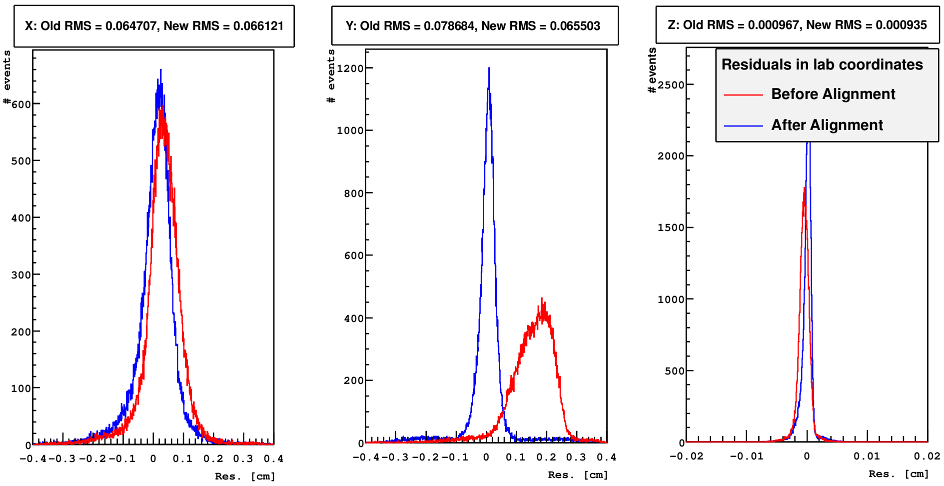

Figure 6.5: XYZ projection of the test chamber residuals before (in red) and after (in blue) the first alignment procedure. The Z position of the TPC is fixed whereas the alignment of the other parameters slightly change the distribution.

This alignment procedure successfully converged with a correction in XY in the order of ∼ 1 cm, a few degrees in angles and a 1.2% correction of the drift velocity. After alignment, the beam projected inside the chamber can be seen on Fig. 6.6.

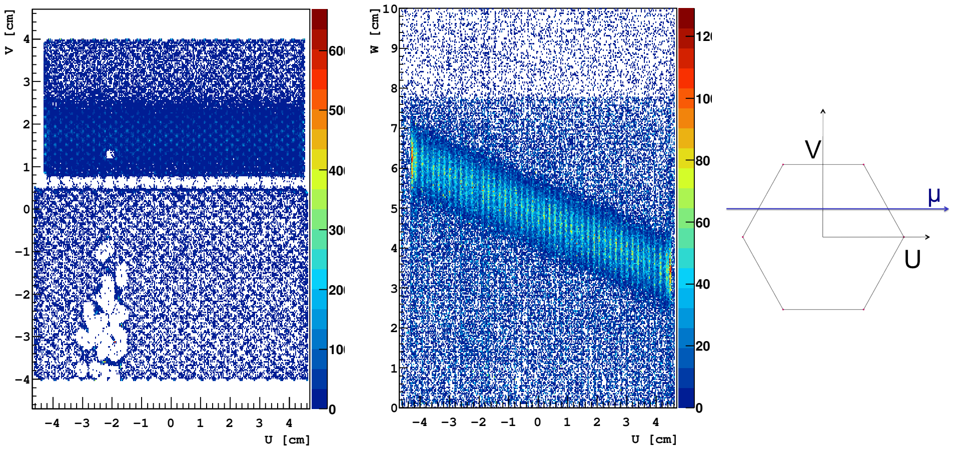

Figure 6.6: 2D hit map inside the test chamber projected in the detector coordinates. The UV projection (left) shows the readout plane of the test chamber. The beam is coming from negative U (silicon detectors are at U ≅ -49 cm). The pad plane is divided into two areas, one above V=0.7 cm with 1.25 mm pads, where is the beam, and below, filled with 1.5 mm pads. One unconnected small pad can be seen on the UV projection (at $[-2, 1.4]$). The missing pads in the lower part of the pad plane are due to a large noise threshold. On the UW projection (middle), one can see the angle of the beam compared to the readout plane. The lighter area, above W=7.7 cm, corresponds to data outside the drift frame, since the AFTER memory is longer than the maximal drift time (see Tab. 3.2). The right schematic shows the orientation of the hexagonal pads with respect to the beam direction.

6.3.1.3 Pad Response

Fig. 6.7 shows the pad response for different cluster sizes. It is defined here as the 2D distribution of the reconstructed cluster position, with respect to the center of the pad that contributes the most to the cluster. For cluster size 1, see the first figure starting from the left on Fig. 6.7, the cluster and the pad position are the same. For size 2, the cluster position is moving toward one of six direct neighbors. One the last figure, all the cluster sizes are represented and the hexagonal shape starts to appear but is still dominated by the areas that connect them to neighboring pads. These pictures are made for the 1.25 mm pads of the test chamber in the UV plane.

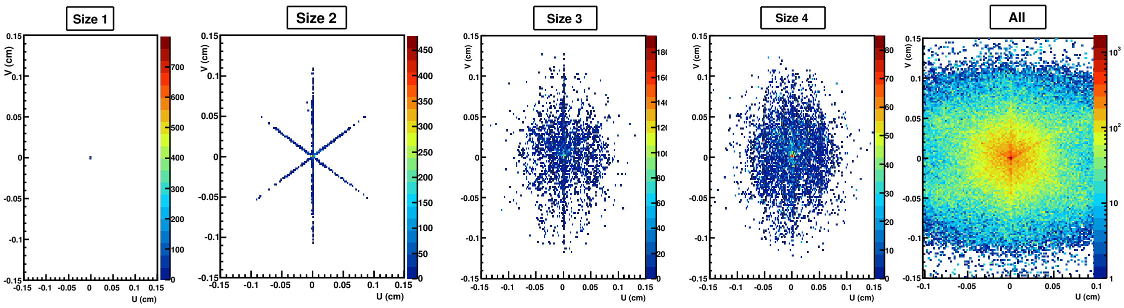

Figure 6.7: Pad response of the test chamber, see text for explanation.

6.3.1.4 Test Chamber Characterization with Internal Tracking

By using the test chamber data only, it is possible to obtain a first characterization. The standard pattern recognition of the TPC, based on the Hough Transform, finds pattern that correspond to a helix shape. Since the straight lines are a special type of helix, this algorithm can be used in the test bench situation where $B = 0$ T. It selects clusters that lie in line in the chamber (in 3D) so they can be fit by the Runge-Kutta method. The resulting biased residuals are shown in Fig. 6.8. These residuals are biased by the fact that the TPC clusters have been used for the definition and fit of the tracks.

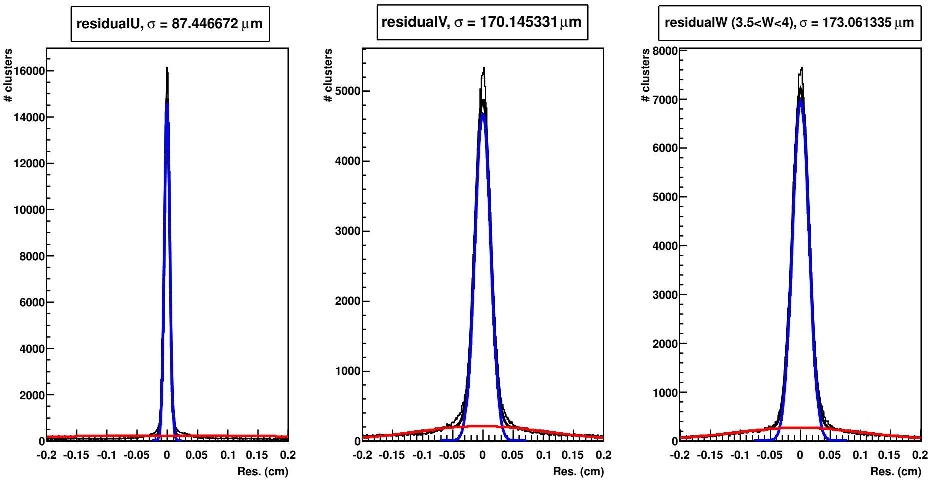

Figure 6.8: Biased residuals between the test chamber clusters and internally reconstructed track, projected in detector coordinates. Only the 1.25 mm pads are used here. Residuals are fitted with a sum of 2 Gaussians (black line) composed of a large Gaussian (red) and a narrow one (blue). σ is the weighted mean of the red and blue Gaussians for each projection. Fit errors are below 1 μm.

The U residual distribution is narrower because it is along the beam direction. In the perpendicular VW plane, the 170 μm residuals show the great performances of the chamber. The good agreement between the V and W projections, expected by the equality between transverse and longitudinal diffusion, shows that reconstruction of the ionization position, in time and in space are under control.

The good spatial resolution allows to see electric field distortions, see Fig. 6.9. The evolution of the U residual along U shows distortions in the chamber. Along the drift coordinate, the situation is more stable and the transverse diffusion (from 272 μm at W = 3 cm to 415 μm at 7 cm) has little impact the spatial resolution in W. The fluctuations seen at W ≈ 4.6 cm correspond to the ones at U ≈ -0.2 cm because of the beam geometry inside the chamber. Nevertheless the rather small variations along W means that the gain is sufficiently high to allow a good amplitude reconstruction, even for widely distributed signals.

The internal tracking also allows to access areas of the chamber outside the trigger acceptance. Since these tracks are in accidental coincidence with the trigger, they are not completely in the time window and only partly visible in the drift frame, offering less precision in track definition. Nevertheless, by comparing the narrower Gaussian fitted to the peak of the residual distribution (blue on Fig. 6.8), the impact of the background is diminished. A degradation of the spatial resolution with the pad size is observed, see Tab. 6.4. Nevertheless a precise measurement of this effect would need to trigger beam over the larger pads area.

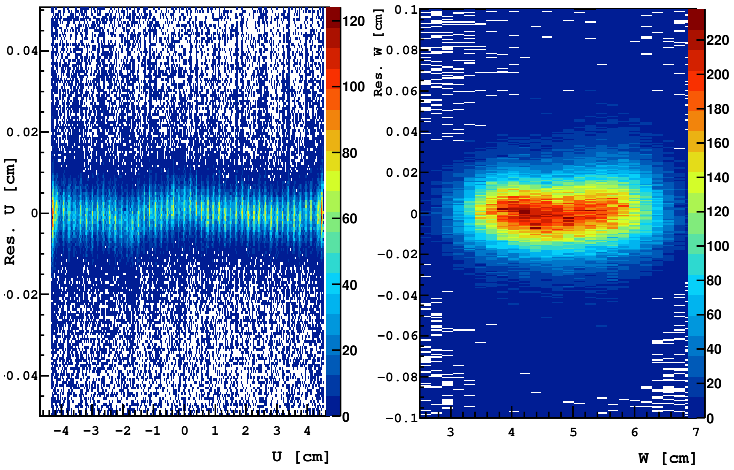

Figure 6.9: Evolution of residuals along the measured coordinate for U and W. The fluctuations at W ≈ 4.6 cm and U ≈ -0.2 cm indicates a local field distortion in the middle of the TPC. U and W are correlated via the beam geometry.

	Residuals V	**Residuals W**
1.5 mm pads	212 µm	195 µm
1.25 mm pads	170 µm	154 µm

Table 6.4: Width of the Gaussian fitting the narrow peak of the residual distribution of small and big pads of the test chamber using internal tracking. Fit errors are below 1 µm and the track error ∼ 18 µm and ∼ 31 µm for the small and big pads respectively.

6.3.1.5 Test Chamber Characterization with External Tracking

To define tracks within the tracking telescope, events where one, and only one cluster is present in each of the 4 planes of the silicon detectors are selected. A linear extrapolation from these clusters is used to select GEM clusters within a road of $3 \times \sigma_{\text{GEM}}$. Here σ_{GEM} is assumed to be the 400 µm pitch divided by $\sqrt{12}$. The selected GEM and silicon clusters, and the extrapolation, are then used to initialize a track within the GENFIT package [67] using Runge-Kutta track representation. The GENFIT package allows the use of clusters of strip detectors, so the exact geometry is correctly handled during the track fitting. A set of ∼ 11200 fitted tracks is created. Then track parameters are extrapolated in front of the TPC and their extrapolation inside the chamber is used for alignment (see Sec. 6.3.1.2) and test chamber characterization.

Fig. 6.10 shows the residual distribution for the TPC clusters compared to the tracking telescope tracks. Since there is a large dependence of the W residual with the W coordinate, the distribution is selected for a slice between 3.5 and 4 cm in the drift direction. As for the internal tracking, the residual distribution in U, along the track direction is the thinner and residual in V and W are in a relative good agreement (within 10%). These residuals use the improvement in the amplitude reconstruction described in Chap. 5. The projected track resolution at the middle of the chamber is 33 µm assuming a resolution of 10 µm for silicon detectors. In that case, the resolution of the chamber is equivalent to the residual width.

Both residuals for U and for the drift coordinate show a degradation that increase with the coordinate, see Fig. 6.11. This is due to the non-optimal alignment of the test chamber compared to tracking telescope.

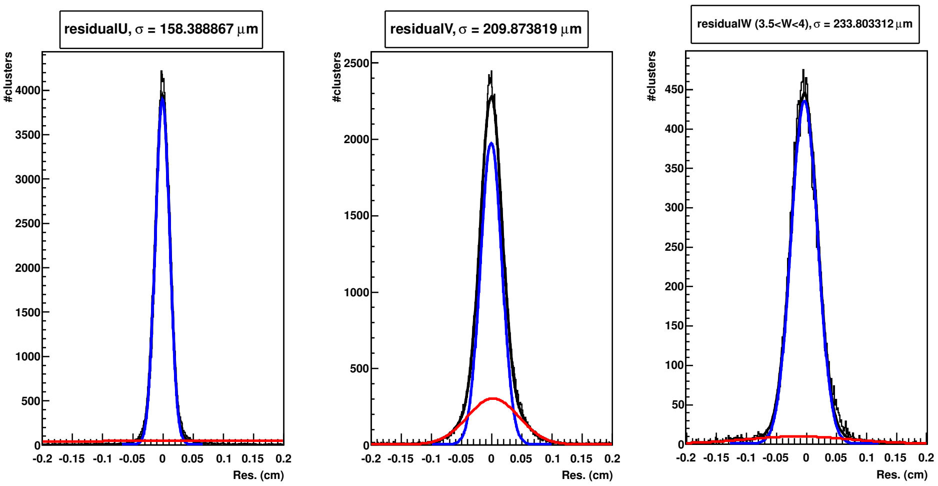

Figure 6.10: Residuals between test chamber cluster and tracks reconstructed by the telescope projected in the TPC coordinates. Residuals are fitted with a double Gaussian (black line) composed of a large Gaussian (red) and a narrow one (red). σ is the weighted mean of the red and blue Gaussians for each projections. Fit errors are below 1 μm.

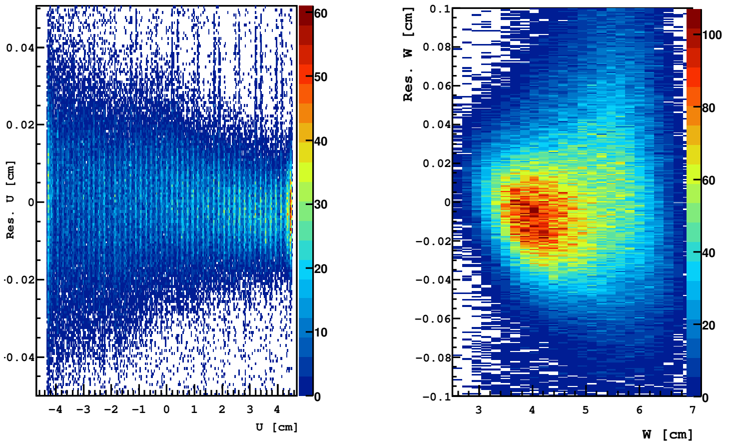

Figure 6.11: Evolution of residuals along the measured coordinate for U and W. The broadening of the residual at negative U and positive W, not observed in Fig. 6.9, indicates that the alignment of the test chamber with respect to the tracking telescope is not optimal.

6.4 Conclusion on the Test Chamber Characterization

The AFTER front-end electronics has been successfully integrated to the newly upgraded GEM-TPC test chamber. The noise performances have been optimized with the FPN online correction algorithm and by making the use of smaller front-end cards. A noise of 625 ± 63 e$^-$ has been obtained for connected cards configured with a peaking time of 100 ns. This short peaking time introduces fluctuations when processing the largely diffused signals of the large prototype. By modifying the amplitude calculation, performances in term of energy resolution and spatial resolution have been improved. In particular the resolution of the 41.5 keV krypton peak has been improved from 50% to 5.1%. Algorithms to increase the accuracy of the time reconstruction have been proposed whereas a conclusive study requires data with including the phase between the trigger and the AFTER writing clock. A longer shaping time would also improve the time reconstruction and the noise performances.

The GEM-TPC test chamber has been installed on a test bench together with a tracking telescope. This setup has been successfully commissioned with a 500 MeV electron beam at the ELSA facility. Beam profiles have been observed in the GEM and silicon detectors. However multiple Compton scattering dominates residual measurements in the TPC as expected from simulations. Therefore the test bench setup has been relocated to CERN, behind the COMPASS experiment, to make use of high-energy muons for precise measurements without almost any scattering.

Biased residuals using internal tracking of 170 μm have been achieved with no degradation due to diffusion, demonstrating the good signal to noise ratio of the chamber. A ~ 210 μm un-bias residuals have been obtained with the external tracking detectors of the test bench. The evolution of the residuals with respect to the measured coordinate indicates a non-optimal alignment. This could be improved by an external measurement of the drift velocity that would reduce the number of free parameters in the alignment procedure. Residuals about the drift and parallel the pad-plane are equivalent, showing the correct reconstruction by the framework. These performances open the possibilities of systematic studies to explore other characteristics of the GEM-TPC.

The GEM-TPC hexagonal pads readout in association with the powerful reconstruction algorithms have shown to be adaptable to several situations. The test chamber has successfully been operated with the perpendicular electron beam at ELSA, cosmic rays, and a parallel muon beam at COMPASS during this thesis. In parallel, a larger prototype has been used with heavy ions collision at FOPI and krypton calibration. The ability to operate in such different conditions opens to the GEM-TPC a wide range of applications thanks to the GEM amplification and the low noise level reached.

Chapter 7

Micromegas Detectors for the COMPASS Experiment at CERN

Proposed in 1996, [68], the COMPASS experiment, for *COmmon Muon and Proton Apparatus for Structure and Spectroscopy*, is a fixed target experiment at CERN that studies the nucleon spin structure and hadron spectroscopy. The main goal of the nucleon spin structure program is the determination of the quark and gluon polarizations inside the nucleon. To carry out these measurements, the experiment makes use of a muon beam. For the second part of its physics program, which encompasses the production of exotic hadrons and the measurement of the polarizabilities of pions and kaons, it makes use of various hadron beams.

COMPASS is a two-stage magnet spectrometer located at the M2 beam line of the Super Proton Synchrotron (SPS) at CERN. The rate conditions and performances required in the first stage could not have been achieved with standard detectors of the late 90's. That is why COMPASS was the first experiment to develop large area tracking detectors based on MPGDs as described in Sec. 7.3.2.

In 2011, the SPSC accepted the future COMPASS-II experiment that is based on the COMPASS setup with important improvements. Among them the Micromegas detectors will be replaced by the Pixel Micromegas.

After a general description of the COMPASS experimental setup (see Sec. 7.1), an overview of the different tracking detector technologies (see Sec. 7.1.3) will be presented. Micro-Pattern Gas Detectors, and in particular Micromegas will be developed, as well as the new Pixel Micromegas object of the present thesis work.

7.1 The COMPASS Experiment

From a simplified point of view the COMPASS experiment makes use of a polarized muon (or hadron) beam impinging on a polarized nucleon target (unpolarized targets with hadron beam) creating numerous products that are reconstructed and identified by the spectrometer. Here we will focus on the spectrometer, in particular on the tracking detectors where the MPGDs occupy a central position. COMPASS has played a pioneer role in the development of GEM and Micromegas detectors. A more complete description of the experimental setup can be found in [68] [69] and [57]. The spectrometer described here corresponds to the setup used in 2010 and 2011, Fig. 7.1 shows the schematic top view of this setup.

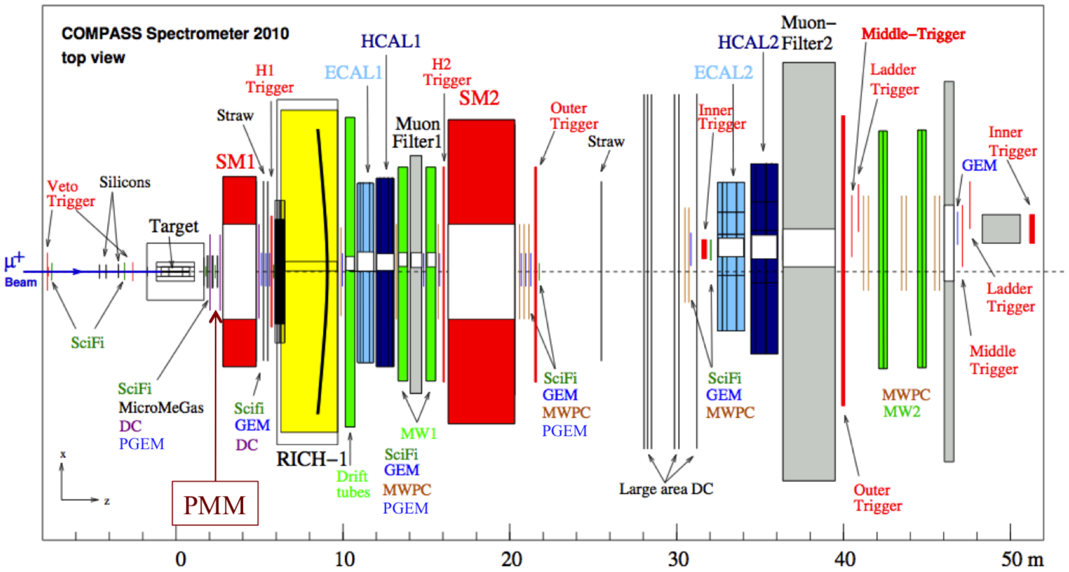

Figure 7.1: Top view of the Compass spectrometer setup in 2010 with the PMM prototype position at $\sim 2\ m$ from the target, in between Micromegas detectors. Picture taken from [70].

7.1.1 Hadron and Muon Beam

The naturally polarized muon beam of Compass is obtained from the intense proton beam of the SPS impinging on a 500 mm beryllium target (T6). From the emerging interaction products, the beam optic selects 172 GeV/c hadrons, mainly π^+. The positive pions decay in a 600 m long tunnel into μ^+ from which magnets select only those with a momentum of 160 ± 5 GeV/c. Since the muons emitted by the weak decay of $\pi^+ \rightarrow \mu^+ \nu_\mu$ along the flight direction carry more momentum than the ones emitted against the flight direction, the 160 GeV/c beam is polarized at 80%. The complex beam optics introduces a muon halo of a few tens of cm around the beam that increases background in the spectrometer.

The accelerator cycle is ~ 45 s with a beam period, the *spill*, that lasts 9.8 s.

The hadron beam also originates from the 400 GeV/c proton beam that impinges on the beryllium targets from 0 to 500 mm width. Hadrons of an energy of ~ 190 GeV/c are selected to give an intensity of up to 10^7 h/spill. The positive hadron beam is composed of p, π^+ and K^+ with a proportion of 78.3/20.5/1.2 and the negative beam consists of $\bar{p}$, π^- and K^- with of proportion of 0.7/96.9/2.4 [71].

7.1.2 Overview of the Compass Spectrometer

To reconstruct the charged particle tracks, the spectrometer consists in two stages covering two different angular domains defined by the two Spectrometer Magnets, SM1 and SM2, see Fig. 7.1. The dipoles bend the particle trajectories, depending on their momentum, via the Lorentz force. The *Large Angle Spectrometer* (LAS) built around SM1, with its large opening angle of 180 mrad and integrated field of 1 Tm, is dedicated to the reconstruction of small momentum particles (0.5 GeV/c $< p < 5$ GeV/c), in particular low energy hadrons. On the downstream part, the *Small Angle Spectrometer* (SAS) is located around SM2. It has a smaller opening angle of 30 mrad but an important 4 Tm field which, combined with the ~ 10 m lever arm, makes possible the reconstruction of particles with higher momentum.

The reconstruction of the track curvature gives the particle momentum and the energy is measured by one hadronic and one electromagnetic calorimeter per spectrometer stage. In addition a *Ring Imaging CHerenkov* (RICH) detector determines the particle velocities and performs the hadron identification in the momentum range from 2.5 to 43.6 GeV/c. It is used in particular to discriminate between pions and kaons [69].

Nearly 200 tracking detector planes contribute to the measurement of the particle position before and after magnets. They are categorized according to different angular domains corresponding to different particle flux and detector performances:

VSAT: The Very Small Area Tracking is in a $5 \times 5\,\text{cm}^2$ zone around the beam. It includes particles scattered at small angles and the beam itself. The rate reaches $50\,\text{MHz/cm}^2$ and the detectors have to be particularly fast, precise and efficient in the VSAT area. Silicon detectors, scintillating fibers (SciFi), and the pixel part of the PixelGEM are used.

SAT: The Small Area Tracking forms a corona from 2.5 cm to few tens of cm where the rate reaches up to $3 \times 10^5\,\text{Hz/cm}^2$. The detectors have to feature high efficiency and a precision of $100\,\mu\text{m}$ for the tracking of low energy hadrons. These detectors, mainly located between the target and SM1, also have to be light to avoid degrading the resolution of the rest of the spectrometer by multiple scattering and photo-conversion. Two MPGDs, Micromegas and GEM detectors, have been chosen here.

LAT: The Large Area Tracking covers the rest of the acceptance up to a few meters. Since the rate is only of a few kHz/cm^2 and the constrains on precision more relaxed, wire detectors are used, like Drift Chambers, MWPCs and Straw Tubes.

The main characteristics of those detectors are summarized in the next section.

7.1.3 The Tracking Detectors of COMPASS

The spectrometer comprises different tracking detectors covering different angular domains corresponding to different requirements and therefore technologies. From the fast, precise, but small silicon detectors, to the large MWPCs, the COMPASS tracking detectors use a relevant sample of nowadays tracking detector technologies. The place of MPGDs among these detectors will be given. Emphasis is put on rate capabilities, size, spatial resolution $\sigma_\mathbf{s}$, time resolution $\sigma_\mathbf{t}$ and efficiency ϵ.

Silicon detectors (VSAT) The COMPASS silicon micro-strips detectors are divided into 3 stations located upstream to the target and used as a beam telescope. One station contains 2 double sided micro-strips detectors with a 5° stereo angle. Each detector has a $5 \times 7\,\text{cm}^2$ active area divided into 1280 strips on the n-side and 1024 on the p-side at a pitch of $50\,\mu\text{m}$. The $300\,\mu\text{m}$ wafer is glued on a L-shape PCB that carries the 18 APV25-S1 (see Sec. 10.2.4) readout chips. The detectors see directly the beam and are subject to radiation damages. To limit this effect, the detectors are cooled to 200 K with liquid nitrogen [71].
The spatial resolution of silicon is limited by the cluster size of 1.5 for the n-side (1.6 for the p-side) that leads to a resolution of $8\,\mu\text{m}$ ($11\,\mu\text{m}$ for the p-side). Solid state detectors have a fast signal that leads to a time resolution of 2.5 ns.

Scintillating Fibers (VSAT) The SciFi detectors consist of plastic scintillating fibers of 0.5 to 1 mm diameter at a pitch of 410 to 700 µm arranged in columns. The fibers of each column are connected to a single photomultiplier channel; the diameter of the fiber and the column size (8,12 or 14) depend on the required time resolution. 8000 fibers are read by 2500 PMT channels, they are distributed in 8 detectors, 2+2 around the target and 2+2 around SM2. Each detector consists of 2 or 3 projections: X, Y and at 45° from the vertical (U). These detectors have an excellent time resolution of 400 ps and a spatial resolution of 130 µm.

Pixel-GEM detectors (VSAT, SAT) First used in 2008 the Pixel-GEM [72] is a 10×10 cm^2 triple GEM detector (as the GEM-TPC, see Sec. 3.2) with a pixelized zone in the beam area. The GEM foils follow the geometry shown in Fig. 2.9 with a reduced copper thickness of 2 µm to minimize the material budget, a pictures of the foils is shown in Fig. 7.2. The detectors operate in Ar/CO$_2$ 70/30 at a gain of 8000 using the asymmetric voltage configuration of the GEM detector optimized for stability. The GEM foils are spaced out by 2 mm, like the induction gap; the drift gap is 3 mm.
GEM detectors have proven to stand the beam rate however the occupancy was too high for the central strips. Thanks to the readout board being based on a 100 µm polyimide foil with 3 conductive layers, pixels can be read outside the active area with an increase of only 0.2% of a radiation length. The readout electrodes are etched on a PCB consisting of two layers of 512 strips each (similar to the GEM detectors). The first layer of strips forms an angle of 90° with the strips of the other layer, providing a 2D readout. In addition the 32×32 mm^2 central area consist of 1 mm^2 squared pixels.
With a hadron rate of 3.5×10^3 h/mm^2/s, the Pixel GEMs reach 99% background corrected efficiency, 8.5 ns time resolution and 90 µm spatial resolution. With the rate of 2.4×10^4 h/mm^2/s the efficiency is 97%, $\sigma_\mathbf{s} = 10$ ns and $\sigma_\mathbf{t} = 130$ µm.

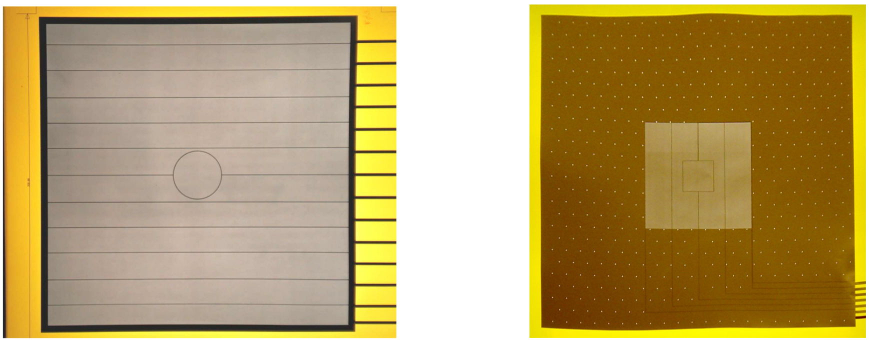

Figure 7.2: 31×31 cm^2 GEM foils for the COMPASS GEM [Left] and Pixel GEM [Right]. On the latter, only the inner 10×10 cm^2 are covered with GEM holes.

GEM detectors (SAT) 11 stations of GEM detectors (2 detectors rotated by 45° between each other) are located along the spectrometer. They are read out by a 31×31 cm^2 strips with 2×768 channels with a pitch of 400 µm. The strips are divided into two layers, each layer reading a projection at 90° to the other. The strips are connected to the APV25-S1 based FEE. There is a 5 cm diameter inactive area in the center (circular zone on Fig. 7.2) that can be activated for low intensity beam used for alignment of the spectrometer. Close to the center the rate can reach 25 kHz/mm^2. It has an efficiency of 97.2% (including 2% of dead area due to spacers between GEM foil. The 3.1 to 3.6 mean cluster size gives resolutions of $\sigma_\mathbf{s} = 70$ µm and $\sigma_\mathbf{t} = 12$ ns.

Micromegas detectors (SAT) The 40×40 cm^2 detectors have resolutions of $\sigma_s = 90$ µm, $\sigma_t = 12.5$ ns and efficiency of $\epsilon = 97\%$ at a rate up to 3×10^5 Hz/cm^2. A detailed description of the detectors is given in the next section (Sec. 7.2).

Drift Chambers (LAT) The DC stations cover the large angle area upstream and downstream of SM1 to complete the acceptance. Two detectors with an active area of $180 \times 127\,\mathrm{cm}^2$ are located upstream of SM1 in addition to another detector, downstream of SM1, of $248\times208\,\mathrm{cm}^2$. Each detector is composed of 8 layers of wires with 4 different plane orientations: X, Y, $X+20°$ and $X-20°$. Every second layer of each orientation is staggered by half a drift cell to solve left/right ambiguities. A drift cell is composed of one 20 µm diameter readout wire between two 100 µm potential wires enclosed between two layers of 25 µm Mylar thick foil cathodes. Each drift cell is $8 \times 8\,\mathrm{cm}^2$ which is small enough to stand the particle rate of a few $\mathrm{kHz/cm}^2$. The cathode inside the 28.6 cm diameter around the beam has a separate high voltage and is only activated during alignment runs with low intensity beam. The analog signal of the 176 active wires of each plane (256 for DC4) are read by the ASD8 pre-amplifier/amplifier/discriminator. A single DC wire plane has a 270 µm spatial resolution.

Straw Tube Detectors (LAT) The Straw detectors cover a large angle from 15 to 200 mrad with 2440 tubes distributed in 15 detectors of $9\,\mathrm{m}^2$ with a square hole of $20 \times 20\,\mathrm{cm}^2$ for the beam. A straw tube functions as a single wire drift chamber. A detector consists of 2 layers of tubes of 6 or 10 mm diameter depending on the rate, in order to keep the occupancy below 2%. As for the DC, the wires are connected to the ASD8 front-end electronics. In average, a detector has a 99% efficiency and a spatial resolution of 190 µm per view.

MultiWire Proportional Chambers (LAT) 34 layers of MWPCs of $178 \times 120\,\mathrm{cm}^2$ cover the large angles of the spectrometer. Four wire views X, Y, $\pm10.14°$ are equipped with 20 µm wires with a pitch of 2 mm, and are read by the MAD4 pre-amplifier/discriminator. The MWPCs have a spatial residual distribution with an RMS of 1.6 mm.

More information on these detectors can be found in [68] and [71].

7.2 The COMPASS Micromegas Detector

In 1997, the physics program of COMPASS required, in the region between the target and SM1, a tracking detector with the following specifications :

- Active area from 2.5 to 20 cm from the beam axis
- Spatial resolution of 100 µm
- 10 ns time resolution
- Efficiency close to 100%
- Rate capabilities of $300\,\mathrm{kHz/cm}^2$, corresponding to 20 MHz integrated on the full detector
- Low material budget

A detector reaching these performances did not exist. A drift chamber, in the same condition, would have a rate of ~ 1.8 MHz/wire which is beyond the capabilities of such detectors. A MWPC with a pitch of 1 mm could have stood the rate but with a heavy frame in the LAT acceptance and a spatial resolution not better than 250 µm. That is why the new MPGD technologies have been considered as good candidates even though they had not yet proved to work in such conditions and to be produced in that size.

Since the beginning of data taking in 2001, COMPASS has shown the feasibility, and great performances, of GEM and Micromegas detectors. The original design is described in Sec. 7.2.2 before the modification that happened in preparation for the hadron beam (Sec. 7.2.3). Some of the limitations of these detectors will be explained, and the new detectors in development, the Pixel Micromegas, will be presented in Sec. 7.3.

7.2.1 Gaseous Amplification with Micromegas

As introduced in Sec. 2.1.2, a Micromegas is a gaseous detector, which uses a parallel plate structure with micro-strips for readout. The central element is the micro-mesh that divides the volume of the detector in two parts: the **conversion gap** and the **induction gap**:

- The **conversion gap** is the volume where the charged pairs are created from ionization (see Sec. 2.3). The resulting electrons drift toward the micro-mesh in a 1 kV/cm *drift field* (E_{drift} in Fig. 7.3). In tracking plane detectors, this conversion gap is typically a few mm thick.

- The **induction gap**, beneath the micro-mesh, is only $\sim 100\,\mu m$ thick. The intense electric field of 10 to 50 kV/cm, the *amplification field* (E_{amp} on Fig. 7.3) produces an electron amplification via an avalanche processus Sec. 2.3.3.

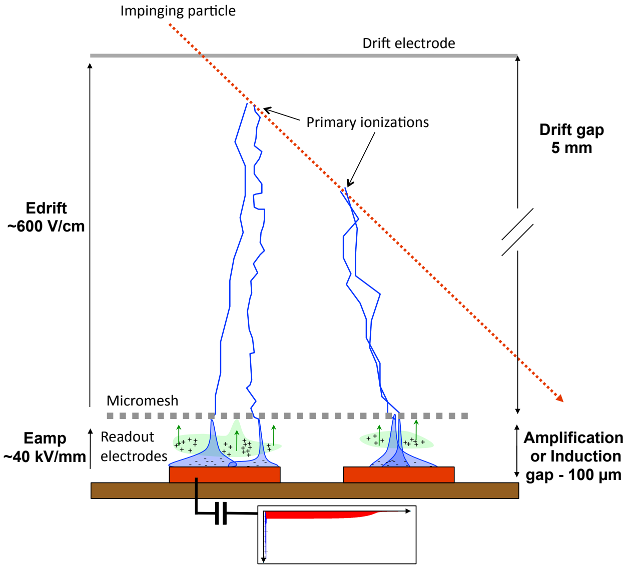

Figure 7.3: Principle of the Micromegas detector.

At the frontier of the two volumes, the electrons follow the intense gradient of the electric field between the holes of the micro-mesh. The ratio of the drift to the amplification field (which is the main parameter to be tuned for operating Micromegas) is such that the electron transparency is usually almost 100%. Symmetrically, most of the ions created in the induction gap do not enter the drift volume, and end up in the lower part of the micro-mesh as shown in simulation in Fig. 7.4.

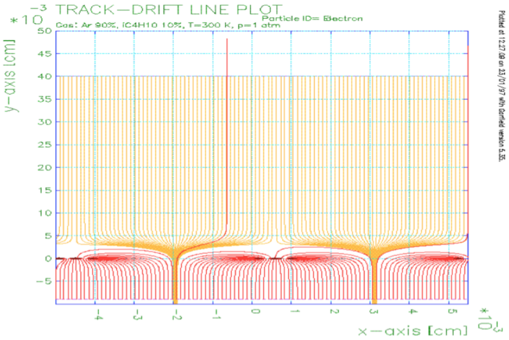

Figure 7.4: Field simulation of a Micromegas. The large majority of field lines goes from the readout to the micro-mesh without connecting the amplification gap to the drift gap. From [73].

7.2.1.1 Signal Formation

As an electron enters the induction gap, it starts inducing a signal on the cathode strips and also develops into an avalanche. Most of the avalanche process happens very closely to the strips and the ions have to drift back through the whole induction gap as shown in Fig. 7.3. The motion of the electrons moving toward the cathode and the ions in the opposite direction sum up into a negative signal. This signal begins with a very sharp electron peak (in blue on the graph at the bottom of Fig. 7.3) that lasts less than 1 ns and a longer ion tail (in red) of ∼ 100 ns. This signal is short enough to be fully integrated by a fast CSA (see Sec. 2.4.2.2) where ∼ 90% of the charge has been induced by ions. Here is one of the main advantages of Micromegas, the use of both ions and electrons allows operating at a moderate gain, and the signal is fast enough to support very high rate (flux of 10^9 particles/mm^2/s have been measured without any drop of gain).

The spatial occupation of the avalanche is defined by the diffusion of electrons inside the induction gap. Since the transverse diffusion is rather low at high field, after a drift of 100 µm, the electron cloud has a width of ∼ 100 µm (depending on the gas and magnetic field). This effect is dominated by the spread of charges at the micro-mesh caused by diffusion in the drift volume. The cluster size can be tuned by controlling the diffusion in the drift area to match the pitch of the readout electrodes. The small avalanche size would become an advantage to reach high flux and high precision if a pitch of the order 100 µm becomes feasible in large and light PCBs.

7.2.1.2 Gain

The number of charged pairs, per incoming electron, created inside the amplification gap follows a Furry distribution (also called geometric distribution) at low gain and a Polya at high gain [74]. This distribution converges toward the Gaussian limit with the number of electrons coming from the drift region (central limit theorem). The width of this distribution enters in the energy resolution convoluted with the variation of the number of primary electrons and the fluctuation of the amplification gap thickness. Another factor that affects significantly $\Delta E/E$ is the size of the micro-mesh holes [75]. Larger holes introduce field distortions that degrade $\Delta E/E$.

The gain depends on the condition inside the amplification gap. By introducing V_{MESH} the mesh voltage and g the gap length in the Rose and Korff equation (Eq. 2.13), one can see that the gain, for a given gas pressure and V_{MESH}, presents a maximum $g(G_{max})$ for a certain gap length [75]:

$$G = \exp(gAP \cdot e^{-gBP/V_{MESH}}) \tag{7.1}$$

$$\Longrightarrow g(\mathrm{G_{max}}) = \frac{\mathrm{V_{MESH}}}{\mathrm{B \cdot P}} \tag{7.2}$$

with A and B constants specific of the gas mixture and P the pressure. Eq. 7.1 shows that the gain increases with the field (when the gap thickness decreases at a constant potential) and that it reaches a limit when the avalanche is limited by the number of atoms on its path. The existence of this maximum allows to operate a detector in stable way since in this region the gain does not depend exponentially on the gap thickness. The inevitable small variations of the amplification gap thickness does not degrade significantly the gain uniformity, that is mainly reason why small gap detectors can be operated stably.

Fig. 7.5 shows that the gain is maximal for a gap thickness of ∼ 100 µm for a parallel plate detector in $\mathrm{Ar/iC_4H_{10}}$ 95/05. However this model does not predict absolute gain values accurately, which need to take into account more complex gas effects.

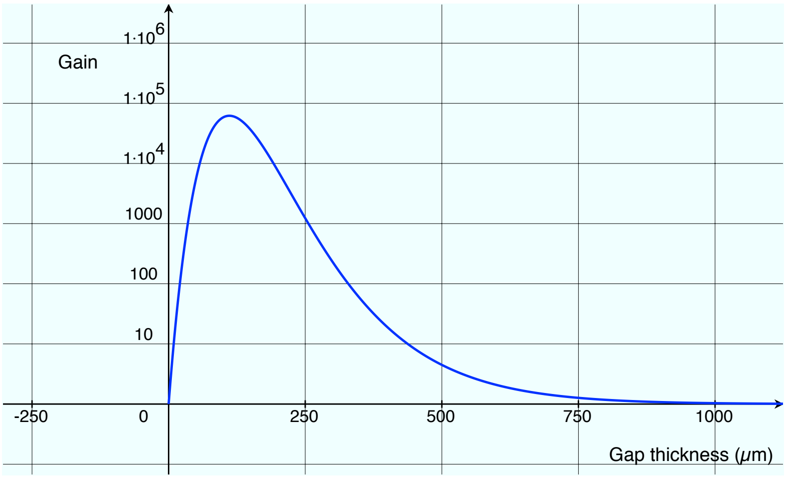

Figure 7.5: Evolution of the gain (in log) of a parallel plate detector with respect to the amplification gap thickness. Eq. 7.1 in $\mathrm{Ar/iC_4H_{10}}$ 95/5 with $\mathrm{A} = 3 \times 10^3\ \mathrm{m^{-1}\ kPa^{-1}}$, $\mathrm{B} = 6 \times 10^3\ \mathrm{m^{-1}\ kPa^{-1}}$ (from [76]), $\mathrm{P} = 90$ kPa and $\mathrm{V_{MESH}} = 60$ V.

7.2.1.3 Discharge

The electron density in the amplification can reach the Raether limit[1] (see Sec. 2.6.2) and creates a discharge between the micro-mesh and a readout strip. The resulting drop of potential of the micro-mesh results on a dead-time defined by the protection circuit on the strips and the HV filters on the micro-mesh. If the gas is not inert (presence of O_2) it might damage the detector. Fig. 7.6 shows an extreme case of damage of the micro-mesh by a malfunctioning HV supply in air.

7.2.2 Characteristics of the COMPASS Micromegas Detectors

The 12 detectors used in COMPASS are single sided strip detectors with an active area of 40 × 40 $\mathrm{cm^2}$ and with a 5 cm diameter inactive central disk. This detector mounted on the spectrometer with its electronics is shown in Fig. 7.7.
The gaseous volume of the detector is divided into two regions by the micro-mesh, a 3.2 mm drift or conversion gap on the cathode side and a 100 µm induction gap on the anode side. The latter is

---

[1] The Raether limit is originally a limit on the avalanche size but is used as a limit on the electron density.

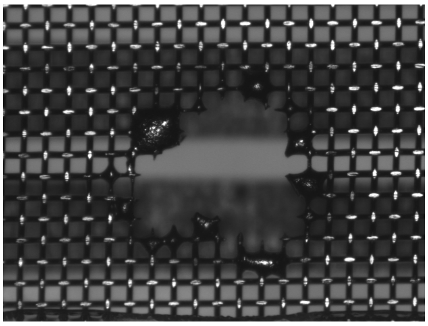

Figure 7.6: Microscope view of a damaged bulk micro-mesh after an important discharge.

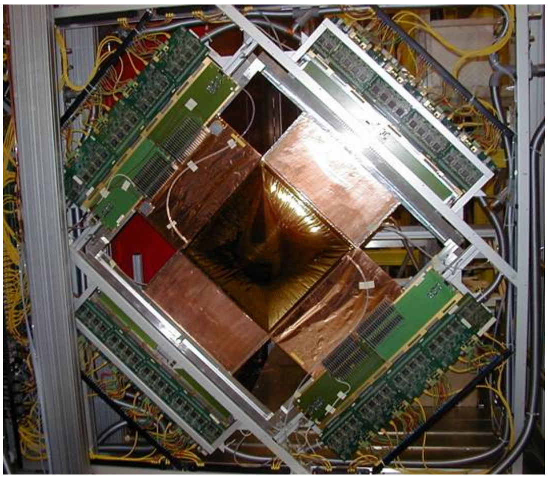

Figure 7.7: The first UV doublet of Micromegas in the COMPASS spectrometer.

segmented into 1024 strips with a pitch of 360 µm for the 512 most central strips and 420 µm for the 2×256 external one. The strips are made of 15 µm thick copper 200 µm width, etched on a 100 µm epoxy PCB. It is mounted on a 5 mm honeycomb glued on a 100 µm PCB with a 15 µm copper layer for mechanical stability and EM shielding. Spacer plots with a diameter of 150 µm made of photosensitive material are distributed over the readout to insure a good mechanical holding of the micro-mesh at 100 µm. They represent 6% of the active area. The micro-mesh and the drift electrodes are made of 4 µm thick nickel at a pitch of 500 lpi[2] for the micro-mesh and 200 lpi for the drift electrode. The overall detector, with a strip extension of 35 cm for exporting FEE cards outside the acceptance of the spectrometer, only weight 500 g and represent 0.3% of a radiation length.

A coppered kapton window closes the 16 L of neon based gas volume. When ionized, a pure noble gas mainly produces UV light that induces discharges through the divergence of the secondary avalanches. A polyatomic gas is added, here C_2H_6, to quench these discharges by absorption and photo-ionization. The latter is also very useful in the avalanche process where the 10 times larger photo-ionization cross-section drastically increases the detector gain. CF_4 is added to improve the number of primary electrons and to increase the electron drift velocity (and therefore improve the time resolution). After an extended test campaign [77], $Ne/C_2H_6/CF_4$, at the proportion 80/10/10 has been proven to be a good compromise.

A feature of a single Micromegas amplification stage is the occasional discharge that forms in the am-

---

[2] lpi: lines per inch

plification gap. Thanks to the channel-wise protection circuit (see Sec. 2.4.2.1), a discharge causes a relatively short dead time of 3 ms. The discharge rate in COMPASS has been measured to be 2×10^{-3} discharge/s/detector with the muon beam and 0.1 discharge/s/detector with the hadron beam.

These detectors have shown a 97% efficiency, 9.3 ns, and 90 µm resolutions (with a mean cluster size of 2.6).

7.2.3 Upgrade for Hadron Beam

In 2006, the COMPASS Micromegas detectors have been adapted to the two new environmental changes: the installation a superconductive magnet for the target and the use of an intense hadron beam. The fringe field of the magnet reached 1T in the active area of the chamber, stressing the slightly ferromagnetic nickel electrodes. As shown in Fig. 7.8, the nickel micro-mesh has been replaced with a 5 µm copper mesh obtained by keeping one side of a standard GEM foil.

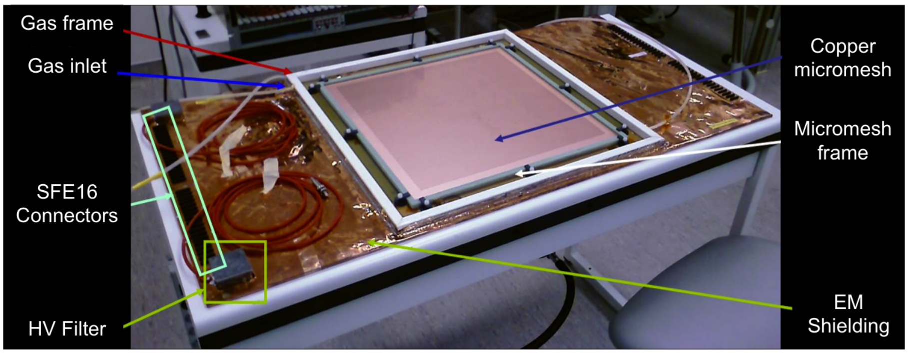

Figure 7.8: Upgrade of a COMPASS Micromegas with a copper micro-mesh at Saclay.

Hadrons are highly interacting particles that favor the formation of discharges. To avoid high spark rate, the gain has been lowered by diminishing the mesh voltage from 400 to 390 V. To keep the efficiency close to 100% the conversion gap has been increased to 5 mm. For the same purpose, the proportion of CF_4 has been lowered to 5%. By reducing the electron drift velocity, the time resolution has been degraded to 12.6 ns.
The first station that is the closest to the target magnet has a resolution from 110 to 130 µm due to the Lorentz force. The other detector remains at $\sigma_s = 90$ µm. The efficiency of 97% is not affected by the higher discharge rate of 0.3/spill.

7.2.4 Limitations of Micromegas Detectors

One issue that may not be fixed by the introduction of the copper mesh, is the possible deformation of the mesh with respect to the readout plane. Since the gain depends exponentially with the electric field, a small variation of the amplification gap length creates inefficient areas as shown in Fig. 7.9. These defects appeared slowly along the years and eventually become an issue. The next generation of detectors will have to be more stable and the bulk technology will respond to this challenge.

To investigate the performances of these detectors at nominal beam intensity ($4 \times 10^7 \mu$/spill and 1.5×10^7h/spill), two detectors have been shifted away from their normal position so the beam impinged on the active area, see Fig. 7.10. On the left picture, it appears a neat loss of efficiency in the strips that sees the muon beam ($4 \times 10^7 \mu$/spill). This loss of efficiency barely appears with hadron beam (1.5×10^7h/spill) (right picture). This indicates that the SFE16 based FEE can not stand this

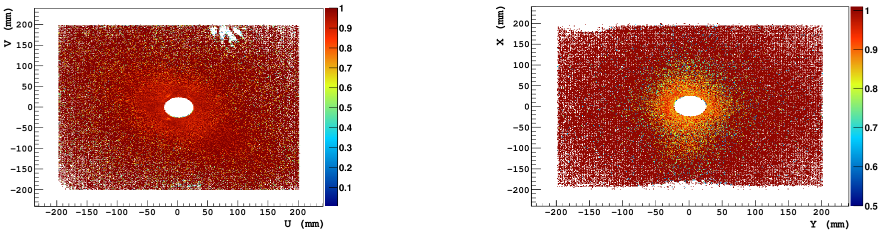

Figure 7.9: Efficiency map of U and Y planes of station 3 showing defects due to detachment of the micro-mesh.

beam rate because of the high occupancy, an increase of the electrode segmentation is needed. A rate of 0.1 discharges/s with the hadron beam has been observed showing that the discharge rate does not affect the efficiency.

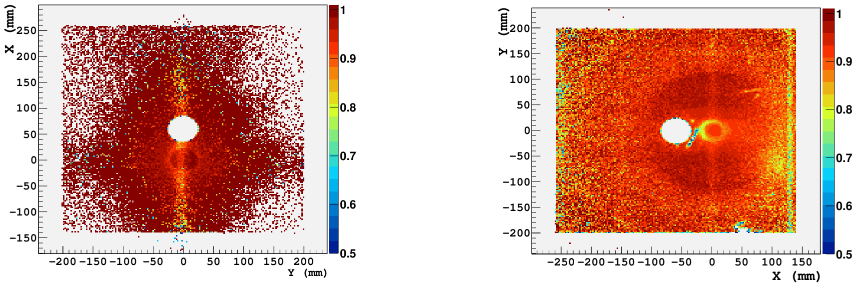

Figure 7.10: Efficiency map of [Left] MM02Y shifted in the 2008 muon beam and [Right] MM02X in the 2008 hadron beam. The white 5 cm diameter disk is the detector inactive area, the second (yellow) is the shadow of the others Micromegas that creates a loss in the number of reconstructed track. The disk of $\varnothing \approx 25$ cm that appears on MM02X is the shadow of the inactive area of the drift chamber. The vertical band at $x = 0$ shows the higher occupancy on the channels that are in the beam area, the effect is more pronounce with muons, which has a higher intensity.

These observations constitute a starting point for the specifications of the next generation of Micromegas that is designed for the upgrade of the Compass experiment.

7.3 The Pixel Micromegas Detectors for the Compass-II Experiment

Approved in 2011, Compass-II is succeeding to the Compass experiment. The main topics of the rich physics program of Compass-II include the study of Generalized Parton Distribution (GPD) from Deep Virtual Compton Scattering (DVCS), the test of chiral perturbation theory via Primakoff reactions, the Drell-Yann process in polarized mode and further measurements in light mesons and hadron spectroscopy [70].

The next generation of Micromegas will have to stand a 5 times higher hadron flux. An extrapolation from preliminary tests, described in Sec. 7.2.4, gives a rate of several discharges per spill that eventually create instabilities and ageing issues. This requires a more reliable holding structure of the micro-mesh. To get a better resolution in the beam region, the center of the detector will have to be active.

For example, this will be an asset in the Primakoff program for several reasons. The Primakoff reaction uses ultra-soft processes where both the scattered hadron and the photon remain in the beam region. By improving the spatial resolution in this region, the hadron will be better reconstructed and the energy reconstruction of the photon will benefit from the diminishing of material budget in this region if Scintillating Fibers are replaced by gaseous detectors.

To summarize, the next generation of Micromegas will have an active center, will stand an intense hadron beam and be more mechanically stable. This defines the specifications of the Pixel Micromegas developed in this thesis work.

7.3.1 Pixel Micromegas Requirements

- Active area of 40×40 cm^2 including beam area
- Fast electronics to cope with the 50 MHz/cm^2 in beam area and integrated enough to read more than twice the number of channels of the previous detectors
- Discharge rate reduction by a factor of 10 to 100
- Spatial resolution of 100 µm
- 10 ns time resolution
- Efficiency close to 100%
- Material budget similar to COMPASS Micromegas chambers
- Good mechanical holding of the micro-mesh

The next chapter will study which solutions can be chosen to fulfill these technical challenges. They will be applied to the Pixel Micromegas project.

7.3.2 COMPASS and MPGDs

As mentioned before, COMPASS was the first high-energy experiment to use MPGDs in a large scale. Since then, MPGDs have demonstrated their great capabilities and have obtained, via a constant development, an increasing place in high-energy experiments.

A growing interest toward these technologies is shared with other experiments, in particular with projects for the upgrade of LHC experiments but also in neutrino and rare event physics. As a result, better dedicated electronics is being developed and progresses are made in photolithography for large PCB on light material (better segmentation, larger size, bulk Micromegas, thin PCB...). This will help MPGDs to pretend to higher rate and better performances allowing them to enter the beam region with several other advantages. They do not need to be cooled, they are cheaper than silicon detectors, lighter than Scintillating Fibers and have a better spatial resolution than fibers. Although neither GEM nor Micromegas can yet reach the time resolution of Scintillating Fibers or the spatial resolution of Silicon detectors, MPGDs are becoming a serious concurrent to these technologies.

On the other side, large area detectors, over 1 m long, are becoming common within the RD51 collaboration. Combined with an industrialization of the processes, MPGDs could also be considered as a relatively cheap and realistic solution for detectors with an active area of a few square meters.

Meanwhile COMPASS continues to be at the edge of these technologies as the Chap. 10 about the Pixel Micromegas project will prove after the presentation of the R&D on discharge rate reduction technologies in the next chapter.

Chapter 8

Micromegas R&D for Spark Reduction

8.1 Motivation

The 1.5×10^7 hadrons/spill beam of COMPASS causes from 0.04 to 0.1 discharge per second in a standard Micromegas detector. The factor 5 in rate foreseen for the future physics program in addition to the activation of the beam area of the Pixel Micromegas would lead to several discharges per spill. Even if the dead time of 3.5 ms does not imply a significant loss in efficiency, the transfer of a $\sim 0.3\,\mu$C charge will create instability and ageing issues. That is why a spark reduction factor, in frequency or/and in amplitude, of 10 to 100 is aimed at for the next generation of Micromegas.

This goal triggered an active R&D at Saclay with two beam test periods in August 2010 on the Proton Synchrotron (PS) T11 hadron beam line, and in October 2010 on the SPS H4 hadron and muon line. For these tests, a dozen of strip Micromegas prototypes has been built to investigate the different discharge rate reduction technologies. The PS beam period was focused on the discharge probability measurements with 0.2 to 3 GeV/c hadrons. The SPS tests used 190 GeV muons to measure the performances of the prototypes in terms of efficiency and spatial resolution. After the description of the solutions against discharges, the gain calibration of the prototypes will be described as well as the test beam conditions and their results.

8.2 Technologies

8.2.1 Pre-Amplification with a GEM Foil

A standard GEM foil, as described in Sec. 2.1.2, is placed over the micro-mesh, inside the detector, see Fig. 8.1. The space in between the GEM foil bottom and the micro-mesh is called transfer gap and the electric field is written E_{TR}. Two effects lower the discharge rate:

- Spread of the charge cloud at the bottom of GEM holes and in the transfer gap
- Transfer of a fraction of the gain to the GEM stage

The first effect help to lower the electron density in the amplification gap and escape from the Raether limit (see Sec. 2.3.3). For the same number of electrons inducing signal (same gain), the density of electrons in the amplification gap is lower thanks to the diffusion by the GEM and the transfer gap. A typical situation that ignites a discharge is due to an interaction where a lots of energy is deposited (a nuclear interaction for example). To create a discharge such an event has to happen in the drift gap in order to see the complete amplification, and, in that case it needs the GEM pre-amplification that also diffuses the electron cloud.

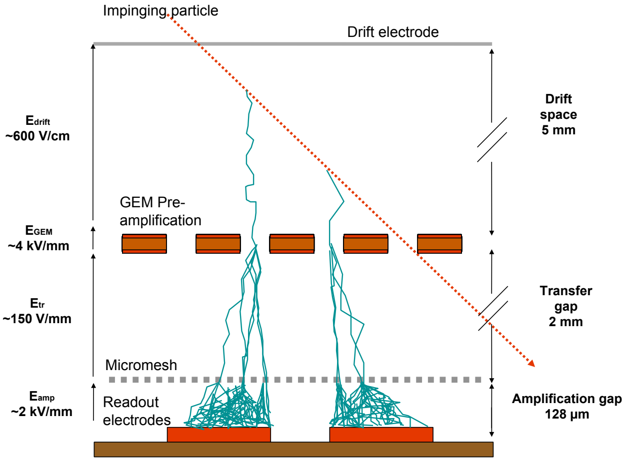

Figure 8.1: The GEM-Micromegas detector principle. A pre-amplification stage with a GEM foil is placed over a standard Micromegas. The electron cloud, created by the amplification at the output of the GEM holes, diffuses through the transfer gap before reaching the micro-mesh [78].

The second effect is coming from the fact that the discharge probability might vary with the electric field, not only with the avalanche size as in the Raether model. This hypothesis of a voltage dependence of the Raether limit is not yet fully understood [79] but it enters in the spark reduction mechanism of the GEM-Micromegas concept that have a lower electric field than a pure Micromegas.

8.2.2 Resistive Technologies

Resistive technologies use the charging property of a resistive material. When a discharge is igniting, the resistive surface reaches locally the potential of the mesh, quenching the spark. Fig. 2.7 represents this idea.

Here, we have tested three resistive technologies. The first one ((A) on Fig. 8.2) consists of a layer, which is made of a resistive paste or a carbon loaded Kapton , of ~ 10 MΩ/□ deposited on an insulator layer that covers the strip readout. The signal is formed by capacitor effect through the insulator layer. For the second technology ((B) on Fig. 8.2), the layer is segmented in strips using a resistive paste and coverlay walls in between. A recent technology proposed by Rui de Oliveira *et al.* from CERN consists of resistive pads that are connected to the underlying copper strips through buried resistors of a few MΩ in horizontal position ((C) on Fig. 8.2). This pattern is also adapted to a pixelized readout electrode.

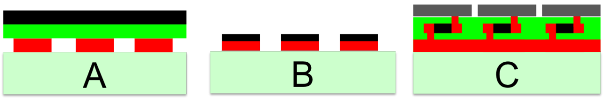

Figure 8.2: Schematics of the 3 resistive technologies tested (not to scale).(A): A carbon loaded Kapton layer (black) is disposed on an insulator layer (green) that covers the copper strips (red). (B): a resistive paste (black) is put on the copper strips (red). (C) a resistive pad (gray) is connected to the copper strip (red) via a buried resistor (black). See Fig. 2.7 for a microscope picture of a type (C).

Two detectors of each resistive type were built for these tests.

8.3 Setup and Prototypes

Twelve detectors have been built and installed on a standardized structure for a comparison of the technologies. All the detectors consist of a 0.8 mm thick Printed Circuit Board (PCB) with an active area made of 140 copper strips of $100 \times 0.27\ \mathrm{mm}^2$ at a pitch of 400 µm. On this PCB, a woven stainless steel micro-mesh of 18 µm thick wires, spaced by 45 µm (45/18 in condensed notation), was integrated at 128 µm of the readout electrode using the bulk process. Some of the detectors have been manufactured at the bulk lab of CEA Saclay and others at the CERN detector lab for quality comparison purpose. 5 mm above the micro-mesh, a 25 µm aluminized Mylar was used as a drift electrode. All the parts are shown in Fig. 8.3. To increase the spark probability, a heavier gas mixture, compared to Compass neon one, was used: Ar/iC_4H_{10} 95/05. For particles at the minimum of ionization, the total number of ionizations is 49 e^- for this argon based mixture and 27 e^- for $Ne/C_2H_6/CF_4$ at 80/10/10.

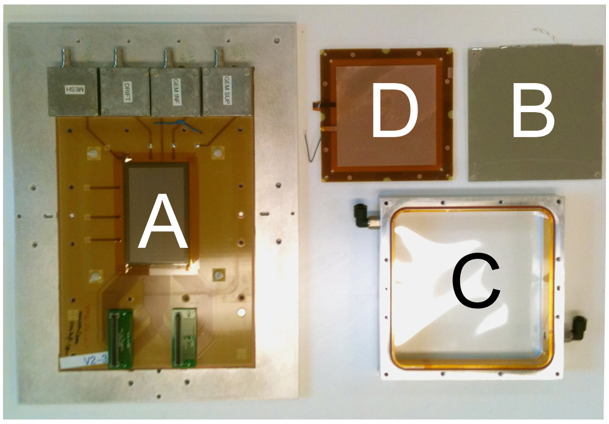

Figure 8.3: The different part of a standard prototype with a GEM foil. A: PCB mounted on an aluminum frame. B: the 25 µm aluminized Mylar drift electrode. C: gas vessel aluminum frame and Mylar window. D: $10 \times 10\ \mathrm{cm}^2$ gem foil

The test bench consists of an aluminum structure with a central rail on which 12 detectors can be screwed with a millimeter precision. Gas distribution is made in series and the front-end electronic cards (FEC) are mounted on the side of the bench; see Fig. 8.11 and Fig. 8.12. Three $15 \times 15\ \mathrm{cm}^2$ plastic scintillators are used in coincidence to generate trigger signals. The plastic scintillators and their photo-multipliers have been mounted and characterized with cosmic rays at Saclay where they have shown a 99% efficiency. Six FECs developed for the T2K experiment, using the AFTER chip (see Chap. 4), read the 1728 electronics channels of the test bench. For each channel, 60 samples are read-out per trigger and the trigger rate is 150 Hz.

To count the number of sparks inside each detector, a capacitor is connected to the micro-mesh. The discharge signals propagate through the capacitor and are connected to a voltage discriminator in a standard VME crate. The threshold is set over the noise of the long cables at a few Volts. Discriminators are then connected to a counter that is read by a dedicated acquisition system. Plastic scintillator coincidences are also recorded to normalize the number of sparks to the particle flux.

For each test beam period, we used 4 standard bulk detectors as references in both X and Y projections to reconstruct tracks. The detailed list of the detectors is shown in Tab. 8.1.
Two GEM-Micromegas detectors, TF10V2-03 and TF10V2-04, have a gap separating the micro-mesh and the GEM foil of respectively 2 and 1 mm.

Different micro-meshes compatible with the bulk process have been studied. The TF10V2-07 embeds a micro-mesh with a larger pitch of 56 µm and a wire diameter of 16 µm (compared to the standard 45/18), which improves the material budget. The micro-mesh TF10V2-08 is thicker with 50 µm wire diameter and a pitch of 265 µm. This micro-mesh is noticeably cheaper but it imposes to have a 192 µm amplification gap.

TF10V2-SEG1 is a standard bulk detector where the micro-mesh has been divided into 3 parts with an independent high-voltage connection. One detector, the TF10V2-05, was mounted on a rotating support along the vertical axis to test the influence of the particle incident angle on the discharge rate.

The group of resistive detectors is constituted of 5 detectors. Resistive paste on strips (type B of Fig. 8.2) is composed of TF10PI-RP2 and TF10PI-RP1, buried resistor (type C) of TF10V2-BR1 and TF10V2-BR2, and TF10V1-03 for the type A.

Detector	type	position at PS	position at SPS
TF10V2-01	standard bulk CEA	1 (ref X)	11 (ref Y)
TF10V2-02	standard bulk CEA	2 (ref Y)	12 (ref X)
TF10V2-03	MM+GEM 2mm	3	3
TF10V2-04	MM+GEM 1mm	4	4
TF10V2-05	std. bulk on rotating support	5	-
TF10V2-07	bulk mesh 56/16	6	-
TF10V2-08	bulk mesh 265/50	7	-
TF10V1-03	Kapton resistive	8	7
TF10V2-09	bulk drift mesh	9	-
TF10V1-04	standard bulk CERN	10	-
TF10V2-06	standard bulk CEA	11(ref X)	2 (ref Y)
TF10V1-20	standard bulk CERN	12 (ref Y)	1 (ref X)
TF10PI-RP2	resistive strips	5’	5
TF10PI-RP1	resistive strips	6’	6
TF10V2-SEG1	segmented mesh	-	8
TF10V2-BR1	buried resistor	-	9
TF10V2-BR2	buried resistor	-	10

Table 8.1: List of the prototypes characterized in 2010. The ’ indicates that the detector has been replaced during the test beam period.

8.4 Characterization of the Prototypes

The TF10 prototype gains have been measured, with an iron radioactive source, before being brought to CERN for characterization beam periods. After detailing the gain measurement, we will see the full characterization of the detectors in beam at CERN.

The results with high energy muon beam will be first presented and then discharge rate measurements with low energy hadrons will be shown. These studies will lead to the conclusion on the viability of each discharge rate reduction technologies.

8.4.1 Gain and Energy Resolution

The first characterization of the prototypes is the gain measurement. It allows the comparison of performances between detectors at the same gain. As seen in Sec. 2.7.1, in order to measure the gain, we have to know the number of primary electrons created in the conversion volume and the number of electrons that reach the readout electrodes. ^{55}Fe emits 5.9 keV photons that create primary charges in the gas by photoelectric effect. When a photon interacts with an electron of a gas atom, it is absorbed by an electron with a link energy ϵ_l that is equal or lower than the energy ϵ_γ of the incoming photon. The electron is ejected with an energy $\epsilon_e = \epsilon_\gamma - \epsilon_l$. To reorganize its energy band either:

- One electron from a higher energy band j will transit to the lower energy band i and emit a photon of an energy of $\epsilon = \epsilon_j - \epsilon_i$; the transition is radiative
- More than one electron is implicated in the reorganization and an Auger electron is emitted [26]

In argon, 85% of the time, an Auger electron is emitted and produces pairs; all the photon energy is converted in the detector gas volume. On the spectrum, a main peak appears for a corresponding energy deposit of 5.9 keV. For the other 15% of events, a photon of 2.9 keV is emitted from a K-L transition. This energy is lower than the binding energy of argon and the photon is likely to escape the gas volume. The missing energy creates a secondary peak at 3 keV.

In a given gas mixture, we can estimate the number of pairs created by the impinging 5.9 keV photon using the mean energy $< W_{mix} >$ needed to created a pair for a gas with:

$$< W_{mix} >= \sum_{i=1}^{n} W_i \tag{8.1}$$

where i is the gaseous species. For Ar+5%iC$_4$H$_{10}$, we have $< W_{mix} >= 25.9$ eV that gives $n_p = 228\ e^-$ for the 5.9 keV photon of ^{55}Fe. See Sec. 2.3 for a complete description of ionization processes.

8.4.1.1 Measurement

To measure the number of charges after the gaseous amplification, the readout strips or the micro-mesh are connected[1] to a Charge Sensitive Amplifier (CSA) read out by a Multi Channel Analyzer (MCA), see Fig. 8.4. In the distribution of the collected charge appears the two peaks of ^{55}Fe source in argon, see Fig. 8.5. Using the position of the main peak and the calibration of the measurement chain, the average number of created electrons in the amplification gap is reconstructed.

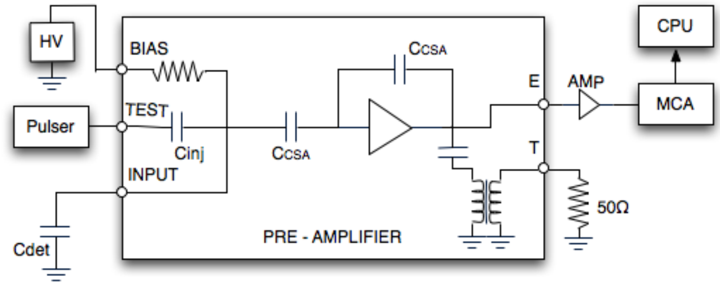

Figure 8.4: Simplified schematics of the Ortec pre-amplifier 142A used for calibration and gain measurement.

The FWHM of this peak gives ΔE and its mean value the energy E, as seen on Fig. 8.5, from which we deduce the energy resolution $R_E = \frac{\Delta E}{E}$.

---

[1] In a Micromegas, it is equivalent to measure the signal on the micro-mesh or on the readout strips since the signal is induced on both electrodes (with a difference of polarity)

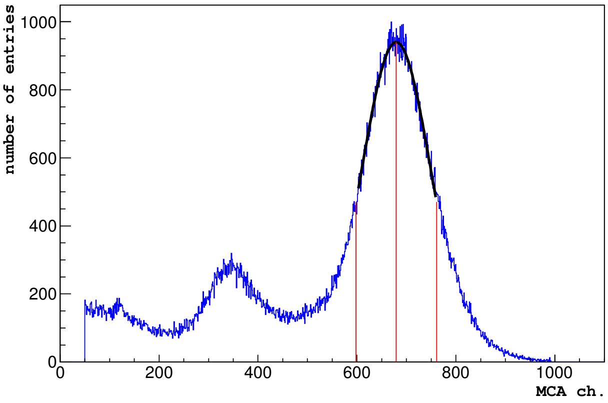

Figure 8.5: Spectrum of ^{55}Fe in Ar+5%iC_4H_{10} for the TF10V2-06 prototype. The 3 keV and 5.9 keV peaks can be seen. The second peak is fitted with a Gaussian (in black), reconstructed maximum (E) and FWHM (ΔE) from the fit parameter are shown with the red vertical lines.

8.4.1.2 Calibration

To guarantee a stable and reliable measurement, we calibrate the entire amplification chain from the CSA to the MCA. It is important to keep the same setup and settings to avoid recalibration at each measurement point. The calibration is done by injecting a pulse with a short rising time (< 100 ns) on the calibration capacitor of the ORTEC pre-amplifier while the setup is ready for measurement with the detector connected to the INPUT entry, and the HV switched on as seen on Fig. 8.4.

Several pulse amplitudes are used to calculate the relation between the charge injected on C_{inj} and MCA units. The value and the errors are used in the analysis to reconstruct the accurate number of pairs moving in the amplification gap: $n_{e^-_{\text{measured}}} = \mathrm{E} \cdot \mathrm{p}_0 + \mathrm{p}_1$ with E the position of the peak in MCA channels and $\mathrm{p}_0, \mathrm{p}_1$ the parameters of the first order polynomial fitting the calibration data. With the TF10 prototypes, typical calibration values are: $\mathrm{p}_0 \approx 2 \times 10^4 \mathrm{e}^-$ and $\mathrm{p}_1 \approx 6 \times 10^3 \mathrm{e}^-/\mathrm{MCA}$ channel.

A sensitive point of this calibration is the dependence of the transfer function of the CSA with the input impedance, here the detector capacitor C_{det} that is in the order of several tenths of pF, which is closed to the 2 pF of C_{inj}. A small variation of this capacitor changes the transfer function of the CSA. For instance a difference of more than 20% is observed between a measurement done on the readout strips and the micro-mesh of a same detector since they do not have the same capacitance due to different parasitic coupling. The presence of CSA on one electrode also modifies the absolute measurement on the other but this is corrected with calibration.

8.4.1.3 Gain and Energy Resolution of Micromegas Bulk Prototypes

The gain of the standard bulk Micromegas, according to the micro-mesh voltage, is well known [80]. As seen on Fig. 8.6, it is well described by an exponential fit. The gain is typically of several thousands at 400 V. All results for the standard detectors are shown in Fig. 8.10. These standard prototypes have a comparable gain/energy resolution except for the one with the thick mesh (265 µm pitch, $\varnothing = 50$ µm) that shows lower gain and higher energy resolution due to the thicker amplification gap.

The error on the gain value is the propagated error of the calibration, in addition to the errors on the parameters of the Gaussian fit. In abscisa, the error represents the precision of the HV supply

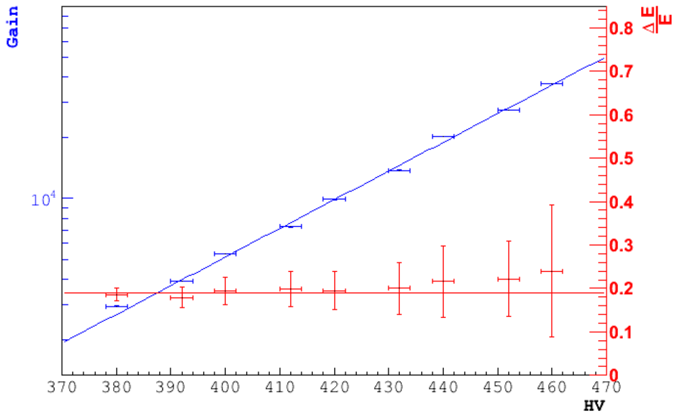

Figure 8.6: Gain (in blue) and $\Delta E/E$ (red) versus mesh voltage for TF10V2-06. The gain is fitted with an exponential function and the energy resolution with a constant.

plus the experimenter turning the knob. The energy resolution does not depend on the gain at the first order and is around 20%. The significant error on the ratio $\frac{\Delta E}{E}$ is coming from the addition of the relative errors of the Gaussian fit (as shown in Fig. 8.5). If ϵ_E is the error on E, the mean of the Gaussian fit gm, and $\epsilon_{\Delta E}$ the error on ΔE we have:

$$\epsilon^2_{\frac{\Delta E}{E}} = \left(\frac{\Delta E}{E}\right)^2 \left(\frac{\epsilon^2_{\Delta E}}{\Delta E^2} + \frac{\epsilon^2_E}{E^2} - 2\times COV_{\epsilon_{\Delta E}\epsilon_E}\right) \tag{8.2}$$

with $\epsilon_E = \epsilon_{gm}$ and $\epsilon_{\Delta E} = 2\sqrt{2\ln(2)}\cdot\epsilon_c$, ϵ_c is the error on the σ of the Gaussian and $COV_{\epsilon_{\Delta E}\epsilon_E}$ the covariance between the errors. An increase of the error on the resolution is observed at high gain due to the increase of the amplitude distribution width for the same statistics.

8.4.1.4 Gain of Prototypes Featuring a Resistive Structure

Resistive technologies introduce a complex repartition of charges between the capacitive coupling with strips and the resistive connection to the mass and to the strips. Due to this sharing of the charges, the gain is lower than for conventional Micromegas detectors, as can be seen in Fig. 8.7 where the exponential curve is shifted by 200 V. Similar results have been observed in other groups [81] [44]. Only the TF10V2-BR2, one of the buried resistor ((C) on Fig. 8.2), has shown comparable gain with the standard detectors. One should note that this measurement requires more time to stabilize (more than a week) than for standard detectors. This is probably due to outgassing of the resistive complex layers.

The energy resolutions of these detectors are bad and hardly measurable (over 60%). This is due to the large dispersion of the resistivity and thickness of the material used in each different technology. More than half of the detectors had such a bad resolution that the maximum of the energy peak could not be distinguished from the background. In that case only the exponential decay of the background moves with the HV. Hence previous error calculation cannot be used. Multiple measurements, in different conditions, indicate that the relative error remains below 10%.
One should note that we could not investigate charging effect with a low intensity ^{55}Fe source. High intensity X-ray tests have been planned but not finished before the end of this work. Nevertheless, a complete drop of the gain is observed in matter of minutes when resistive layer is disconnected from

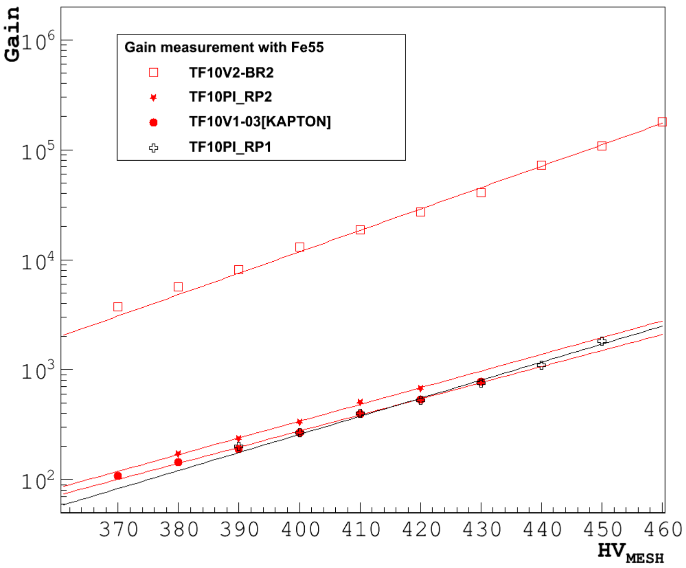

Figure 8.7: Gain of the resistive prototypes and exponential fit, errors are not shown for lisibility.

the ground (for type (A) and (B)). This drop indicates that the resistive layers are charging up and are canceling the amplification electric field below the avalanche mode.

Charging effects have been observed on type (A) and (B) and are expected on the buried resistor technology. Thanks to the low electron mobility (below 10 $\mathrm{cm^2V^{-1}s^{-1}}$ for polymer) in the buried resistors, the charges do not have the time to evacuate to the ground before the next impinging particle. This decreases the $\Delta E/E$ and efficiency of the detector over a certain rate.

8.4.1.5 Gain of Prototypes Featuring a GEM Foil

Gain: Very high gains up to 10^6 can easily be reached with the two GEM-Micromegas detectors. A single GEM foil at a standard high-voltage of 300 V has typically a gain of 20 that is multiplied by the 10^4 of the Micromegas. The gain dependence on the GEM high voltage is plotted on Fig. 8.8. As with the mesh, the gain increases exponentially with ΔV_{GEM} whereas it has been observed, for high transfer field, unexpected high gain.

Gain dependence with the transfer field: is an important characteristic of the GEM-Micromegas concept. An important influence of the transfer field on the gain would impose constrains of the error on the distance between the GEM foil and the micro-mesh. For instance it is important that a tilt of the GEM foil does not produce a significant gradient of gain. The gain at a transfer field of 300 V/mm is slightly higher than at 100 V/mm due to a better electron transparency of the Micromegas. The effect of the transfer field has been measured and shown in Fig. 8.9. The gain is quite stable between 100 and 700 V/mm. This independence is not trivial and comes from the compensation of two effects: the extraction of the charges from the GEM holes and the electron transparency of the micro-mesh. At low field, the bad charge extraction from the GEM overcomes the very good Micromegas electron transparency. From [49] and [82] these effects have been estimated and the detailed simulations presented in Chap. 9 describe well the data.

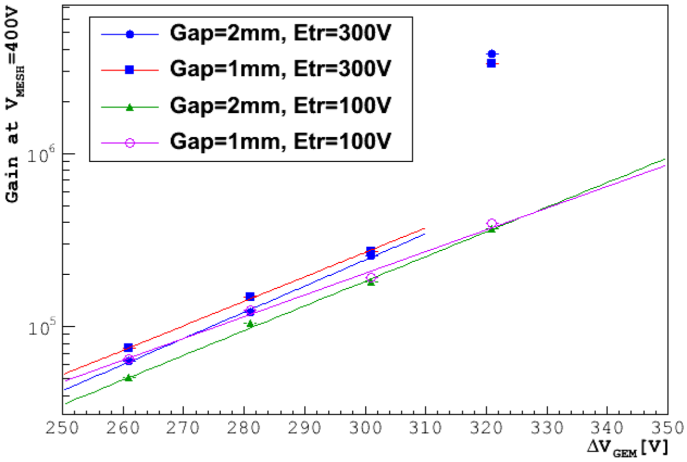

Figure 8.8: Gain of the GEM-Micromegas prototypes for different ΔV_{GEM}. The values are an extrapolation of the fit of the gain function at $V_{\text{MESH}} = 400$ V. Errors include errors on data points of $G(V_{\text{MESH}})$, fit errors and HV settings uncertainties.

Energy resolution: Ideally, the GEM-Micromegas detector energy resolution is the quadratic sum[2] of the GEM foil and Micromegas energy resolution :

$$\Delta E/E = R_E = \sqrt{R_{GEM}^2 + R_{MM}^2} \tag{8.3}$$

We measured the resolution of the detector with and without the GEM foil, and we obtained $R_E = 35\%$ and $R_{MM} = 22\%$. That gives $R_{GEM} = 27\%$ which is high for a standard GEM foil showing that either the quadratic sum might be an over-simplification or that the GEM foil quality was not optimal. As for the gain, R_E is stable with E_{TR} within the region of interest between 100 V/mm and 700 V/mm. An optimal value of 31% is obtained for $E_{\text{TR}} = 100$ V/mm, see Fig. 8.9.

8.4.1.6 Summary of Gain Measurements

Fig. 8.10 summarizes the gain measurement made with ^{55}Fe on the TF10 Micromegas prototypes.

The standard bulk detectors: either built at CERN or at Saclay, have shown comparable gain and energy resolution. The bulk manufacturing process is expected to introduce an uncertainty of 5 µm of the amplification gap [83]. Integrated over the active surface of the detector, this effect would lead to an energy resolution of 30%. The bulk technology is not well fitted to build detectors with a good energy resolution, even if our prototypes had a better energy resolution than expected. The TF10V2-08 detector embedding a thick micro-mesh have shown bad gain performance proving that its cheap micro-mesh is not viable.

The GEM-Micromegas detectors: reach higher gain than standard detectors, but worse energy resolution. This is due to the addition of the resolution of the two amplification stages. The electric field between the GEM foil and the micro-mesh, E_{TR} has shown a range between 100 and 700 V/mm where it does not affect the gain.

---

[2] The width of the convolution of two Gaussian distributions is the quadratic sum of the gaussians' widths.

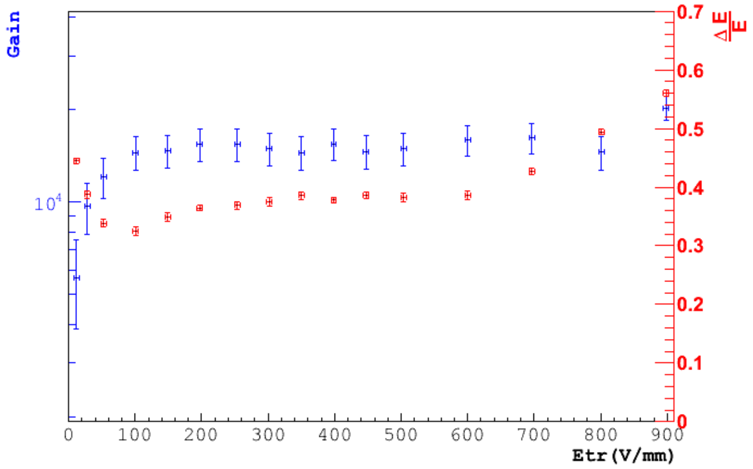

Figure 8.9: Gain and $\frac{\Delta E}{E}$ for TF10V2-04 (standard bulk + GEM with a gap of 1 mm) for different transfer fields. Large errors on gain are due to the uncertainty on the GEM voltage that is multiplied by the gain of the mesh. The drift field is set at 800 V/cm, $V_{\mathrm{MESH}} = 280$ V and $V_{\mathrm{GEM}} = 300$ V.

The resistive technologies: have low gain and bad energy resolution except for the buried resistor. The production of the resistive detectors was not mature: half of the detectors did not work properly. Charging effects have not been observed with the ^{55}Fe source. The TF10V2-BR2 has shown promising gain, slightly higher than standard detector.

8.4.2 Experimental Conditions at the T11 line of the Proton-Synchrotron

The test bench was installed on the T11 line of the Proton Synchrotron, the first circular accelerator of the CERN facilities, see Fig. 8.11. Depending on the momentum, the PS delivers an intensity around 1.4×10^5 hadrons per spill. The spill last 0.4 s every 50 s so the instantaneous rate, in spill, is 3.53×10^5 $\mathrm{h \cdot s^{-1}}$. Both polarities of current in the beam line magnet could be used, focusing a π^- or a π^+ beam. Since it modifies the shape of the beam, data have been corrected from this effect, as explained in [84]. The positive beam was contaminated with protons, deuterons and tritons.

The momentum of hadrons, from 0.2 to 3 GeV/c, has been chosen because it corresponds to the experimental conditions of the CLAS12 experiment. One goal was to investigate the dependence of discharge rate with momentum.

Over the 2 weeks of data taking during summer 2010, more than 27000 spills were delivered, corresponding to 3.8 billion particles.

8.4.3 Discharge Rate Measurement in a Hadron Beam

Using the π beam from 0.2 to 3 GeV/c, the energy dependence of the spark probability has been studied. The beam intensity of 1.4×10^5 hadrons per spill allows a measurement of discharge probabilities down to 10^{-8}.

The first result is the confirmation of the independence of the discharge probability with hadron momentum. High discharge probabilities appear when some particles contaminating the beam (protons, deuterons and tritons), are stopped in the test bench material and deposed their entire energy

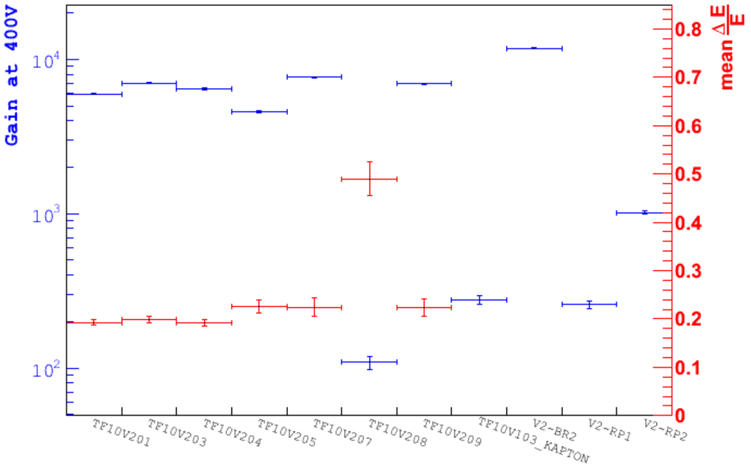

Figure 8.10: Summary of gain and energy resolution measurements at V_{MESH} =400V for the TF10 Micromegas prototypes. V2-BR2, V2-RP1 and V2-RP2 are the values for TF10V2-BR2, TF10PI-RP1 and TF10PI-RP2.

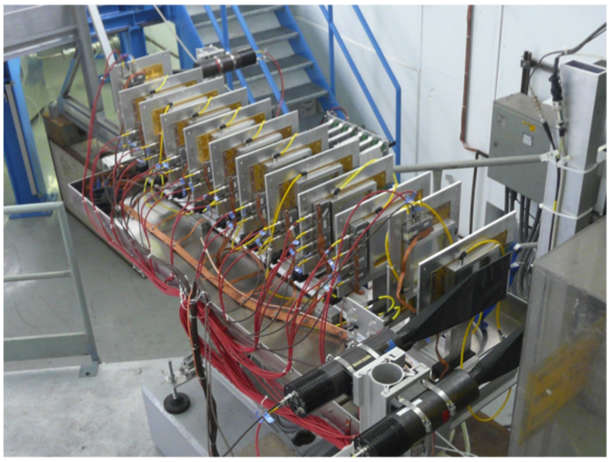

Figure 8.11: The 12 detectors on the test bench on the T11 PS line at CERN.

inside the gas volume of detectors. Simulations have shown that p^+ of 200 MeV/c depose 10 times more energy than at a few GeV/c. Nevertheless the energy deposit in the order of 10 keV is not enough to reach the Raether limit and the discharge probability remains unchanged at the first order. The exception to this rule is when the particles stop inside the detectors and depose all their energy producing important increase in the discharge probability.

At a gain of 10^4, where the detectors are fully efficient, a discharge probability of 2×10^{-5} for standard bulk detectors is measured. This value agreed with a previous measurement obtained at 15 GeV/c with the same gas mixture [77].

The two detectors with a GEM amplification stage show a discharge rate reduction factor from 10 to 100. When $V_{GEM} > 280$ V, the detector with 2 mm transfer gap has a discharge rate probability 10 times lower than the 1 mm depending on how the gain is shared between the Micromegas and the GEM foil. This effect comes from the diffusion of the electron cloud in the thicker transfer gap. This difference coming from the larger diffusion becomes visible when the gain on the micro-mesh is low enough to avoid discharges coming from interaction that would have happened in the transfer gap.

The spark measurement setup was not able to detect low amplitude discharges generated by resistive detectors. Indeed standard Micromegas have discharges of several hundreds of volts[3] where resistive layers limit their amplitude to a tenth of a volt. The difference between discharge and noise was not large enough to distinguish between them. Nevertheless with this low amplitude, discharges are believed to have no consequence in terms of performance or ageing; no sign of undesired effect has been observed or reported by the Micromegas community.

The detector with a segmented micro-mesh has discharges with a lower amplitude. Indeed, the lower capacity decreases transferred charge and dead-time. In addition the drop of potential of the micro-mesh is limited to one third of the active area. This solution could be used to divide large detectors, but it increases the complexity of the high-voltage distribution and, with the current technology, it introduces a dead space between sectors of 1 mm.

The detailed information on these results has been published in [84]. Evolution of the performances with the momentum and charge of the hadrons is described in Sec. 8.4.8.

8.4.4 Experimental Conditions at the H4 Beam Line of the Super-Proton-Synchrotron

The test bench has been installed on the H4 beam line of the Super Proton Synchrotron, in October 2010, during the test beam period of the RD51 collaboration, see Fig. 8.12. The SPS delivers 5 to 6×10^{12} protons on the T2 target per spill, from which 8.5×10^{5} muons of 170 GeV/c were counted by the coincidence of three scintillators.

Figure 8.12: The 12 detectors on the test bench at the H4 beam line of the SPS in front of the GOLIATH magnet.

The experimental conditions were not optimal. Several other groups were using the beam upstream and downstream of our test bench. Other setup material in the beam created a high background. The frequent accesses to the beam area and the 1.4 T magnet, Goliath, were disturbing the alignment of the detectors. It was found later that the muon beam was contaminated with 80% of hadrons and an

---

[3] The amplitude of the discharges in standard Micromegas detectors depends mostly on the size of the micro-mesh and the values of the components of the HV filter.

important cut on track quality was required.

A hundred of runs has been taken with muon beam *i.e.* $5{\times}10^9$ particles in total. 25 runs of pure hadron beam with 10^8 hadrons per spill have been used at the end of the period to quantify the impact the hadron contamination. No significant differences have been observed.

8.4.5 Reconstruction and Alignment

In order to have a complete characterization of the prototypes, we need to reconstruct clusters and tracks from the data. The data acquisition system (DAQ) records fifty 25 ns samples per trigger for each strip, and suppresses zero signal data. The reconstruction was done with a dedicated software that converts raw data into, successively, *hits*, *clusters* and *tracks* following the logic of Sec. 2.5.

Pulse Shape Analysis : Hits are computed for each strip for one event. If an amplitude goes over the noise amplitude threshold, a hit is created from the 5 samples around the maximal amplitude of the 50 samples recorded by the DAQ. The amplitude of one hit is the sum of the selected samples amplitudes and its time is the maximal sample time.

Clustering : A cluster groups together contiguous hits. The charge amplitude of one cluster is the sum of the hit amplitudes. The time and position are the weighted mean of the hit time/position. Several other weighted algorithms have been tried for resistive detectors as detailed in Sec. 8.4.7.3.

Track reconstruction with fix references: Tracks are reconstructed using 4 dedicated detectors (2 along the X coordinate, 2 along Y) situated at both ends of the test bench. After selecting only the events with one and only one cluster per tracking detector (≈ 80% of the events), the track is created assuming a straight line.

Track reconstruction with fitted tracks: In a second method used for crosscheck, tracks are reconstructed by fitting a straight line to the clusters of all detectors expected the one being studied. In that case the track error is not well known because it depends on other detectors spatial resolutions that are being measured. The alignment of the detectors becomes much more complicated with no fix reference detector and a different set of tracks is needed for each detector.

Only the results using the fixed tracking detector method are presented here. No significant difference between both methods has been observed for stable conditions. When the alignment is disturbed, it is difficult to correct it with a tracking algorithm that has a lot of degrees of freedom and the performances of detectors depend on the quality of their alignment.

Alignment : The unstable experimental conditions imply to cut on data quality and reduce the available statistics. The limited statistics, the frequent displacement of the test bench, the low number of detection planes and the 2 m baseline, stressed the issue of alignment. For each period of data tacking, a first alignment is performed using the χ^2 minimization software MIGRAD [66] on the longest run. Then a correction is applied on each run using the center of the residual distribution. This correction in two steps implies to reconstruct data twice but isolated runs lack statistics to allow the alignment procedure to converge.

8.4.6 Efficiency in Muons Beam

The first performance analyzed here is the efficiency. The interdependence of the raw efficiency, and background probability, with the road width (as defined in Sec. 2.7), is studied to choose an optimal value.

On Fig. 8.13 we observe a fast increase of the efficiency with the road width below the resolution of the detector σ_{det}. With a wider road, background and raw efficiency increase. Corrected efficiency stays stable until of the road width becomes comparable to the detector size. Monte-Carlo simulation of a 98% efficiency detector shows a similar behavior. However, the Monte-Carlo background was overestimated in Fig. 8.13 to show the stability of the method. Simulation and data indicate that the efficiency plateau is reached at about $4 \times \sigma_{\text{det}}$. The road has to be kept narrow to avoid edge effects and un-physical performances.

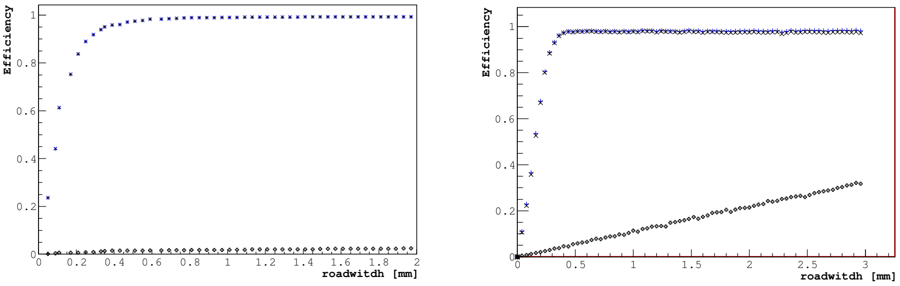

Figure 8.13: [Left] Evolution of the raw efficiency (black crosses), corrected efficiency (blue ×) and background probability (black +, almost superposed to the blue ×) on TF10V2-03. [Right] Monte-Carlo simulation of a 98% efficiency detector with one background cluster for each event.

8.4.6.1 Efficiency of Standard Bulk Micromegas with a Segmented Micro-Mesh

The TF10V2-SEG1 detector shows an efficiency of 91% on the plateau with a few percents degradation at high gain, see Fig. 8.14. The dead space between sectors introduces an inefficiency. For a 2 mm dead area along the detector, a 96.5% efficiency is expected. Since the beam is not equally distributed over the active area, the weight of the dead areas lowers the mean efficiency.

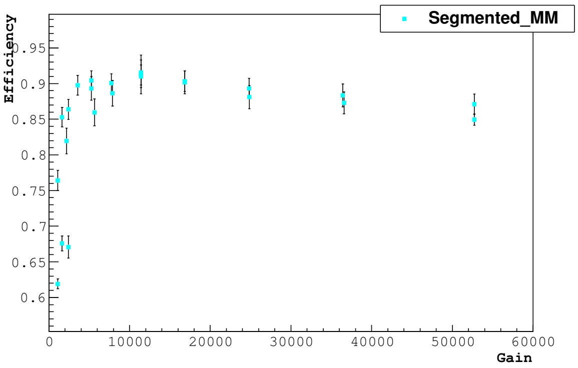

Figure 8.14: Background corrected efficiency of the segmented Micromegas detector.

The drop at high gain, which is also observed on GEM-Micromegas and resistive detectors is not fully understood, it might come from the increase of the background. This is collaborated by the observation of a decrease of the mean cluster size at high gain. The average cluster size shows that there are more signals with a cluster size of one or two (background). They are equally distributed over the detectors channels and broaden the residual distribution.

8.4.6.2 Efficiency of the GEM-Micromegas Detectors

As shown in Fig. 8.15, the GEM foil does not introduce any inefficiency, even with 50% electron transparency (as shown in Fig. 9.4), thanks to the large number of primary charges. Therefore the efficiency of these prototypes is greater than 99% with a slight decrease at gains over 25000, as for the other prototypes.

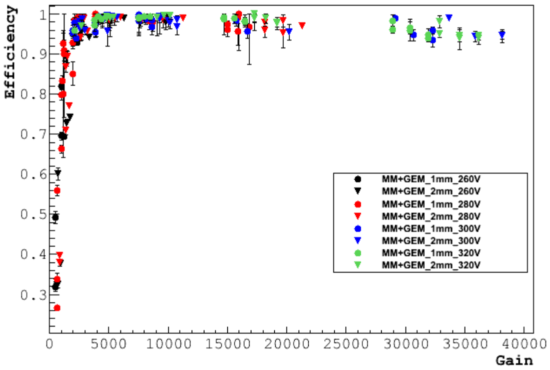

Figure 8.15: Background corrected efficiency of the two GEM-Micromegas detectors. The colors of the symbols represent different gains of the GEM foil corresponding to a ΔV_{GEM} from 260 to 320 V.

8.4.6.3 Efficiency of Resistive Detectors

The prototypes featuring a resistive layer have shown very low efficiency, below 30%, except for TF10V2-BR2 that reaches full efficiency with a small loss at high gain, see Fig. 8.16.

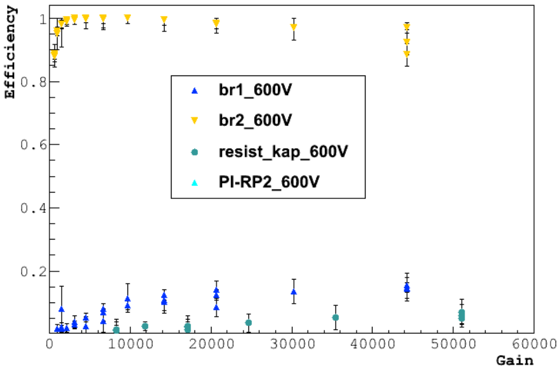

Figure 8.16: Background corrected efficiency of the Micromegas detectors featuring a resistive structure at 600 V drift voltage (standard settings).

The poor performance of the resistive detectors probably come from the production. For instance TF10V2-BR1 has been opened, its micro-mesh removed, and a chemical substance was found on the active area. It might have come from PCB chemical processes or from the gas system. The few percent loss of the efficiency of TF10V2-BR2 appear at a higher gain than for the GEM-Micromegas detectors. It might indicate a charging of the resistive layer.

8.4.7 Spatial Resolution in Muon Beam

For tracking detectors, the spatial resolution is the most important characteristic with efficiency. The resolution, as defined in Sec. 2.7, is the width of the residual distribution corrected from the track error. Here to control the track error, the tracking is done by fixed detectors (see sec. 8.4.5) and the error is the extrapolation of the estimated reference detector resolution, see Fig. 8.17. If we consider two tracking detectors d_1 and d_2, at the position along the beam z_1 and z_2, measuring x_1, x_2 with the error ϵ_1 and ϵ_2 we have:

$$\begin{array}{ll} d_1 : (x_1 \pm \epsilon_{x1}, z_1 \pm \epsilon_{z1}), & d_2 : (x_2 \pm \epsilon_{x2}, z_2 \pm \epsilon_{z2}) \\ \Delta x = |x_1 - x_2|, & \Delta z = |z_1 - z_2| \end{array}$$

Here we use a simple straight line extrapolation:

$$x = a \cdot z + b \implies a = \frac{\Delta x}{\Delta z} \text{ and } b = x_1 - a \cdot z_1 \tag{8.4}$$

In order to get the error on x as a function of z: $E_x(z)$ Eq. 8.4 is differentiated: $\mathrm{d}x = \mathrm{d}a \cdot z + \mathrm{d}z \cdot a + \mathrm{d}b$ Assuming that all the standard references have the same resolution $\epsilon_{x1} = \epsilon_{x2} = \epsilon_x$ and $\epsilon_{z1} = \epsilon_{z2} = \epsilon_z$ and then :

$$\begin{array}{ll} \mathrm{d}a & = 2[\frac{\epsilon_x}{\Delta z} - \frac{\epsilon_z \Delta x}{\Delta z}] \\ \mathrm{d}b & = \epsilon_x - \mathrm{d}a \cdot z_1 - \epsilon_z \cdot a \\ \mathrm{d}x & = \epsilon_x[\frac{2z}{\Delta z} + 1] - 2\epsilon_z(\frac{z\Delta x}{\Delta z^2}) \end{array}$$

$$\implies E_x(z) = \sqrt{(\epsilon_x[\frac{2z}{\Delta z} + 1])^2 + (2\epsilon_z(\frac{z\Delta x}{\Delta z^2}))^2} \tag{8.5}$$

This equation is traced with the residuals of the SPS test bench detectors assuming a 80 µm[4] resolution for the reference detectors on Fig. 8.17. The residual shape along the beam axis is well reproduced.

$E_x(z)$ is then quadratically subtracted from the residual to access the intrinsic resolution of the detector, as explained in Sec. 2.7.6.

8.4.7.1 Segmented Mesh Micromegas Spatial Resolution

The segmented mesh detector reaches a resolution of $\sim$ 90 µm as shown in Fig. 8.18. This spatial resolution and the 1.9 mean cluster size correspond to the expected performances of a standard bulk detector in these conditions. The spatial resolution is 10 µm larger than the supposed 80 µm for a standard detector due to the edge effects nearby the mesh segmentation.

---

[4] The 80 µm resolution has been measured on similar detectors in a previous study [85]

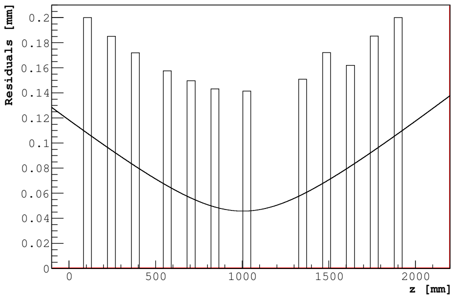

Figure 8.17: Width of the residual distribution along the Z axis for each detector (vertical bars). The plain line represents the analytical formula of Eq. 8.5. The spatial resolution for the reference detector is 80 µm.

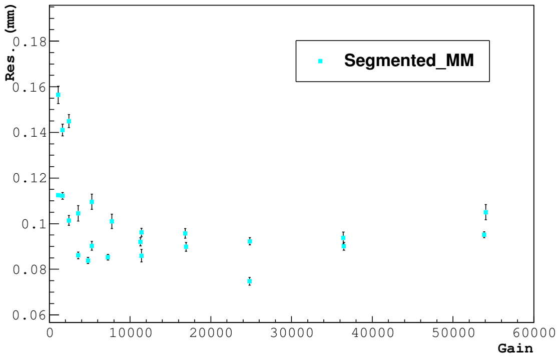

Figure 8.18: Resolution of the segmented Micromegas detector with respect to the detector gain.

8.4.7.2 GEM-Micromegas detectors Spatial Resolution

The GEM-Micromegas detectors have a resolution from 60 to 80 µm as shown in Fig. 8.19. The relatively wide distribution of the resolution values are due to the alignment instability. For further discussions we assume a resolution of 80 µm knowing that it is underestimated to be on the same side.

This resolution is obtained for a cluster size of 3.8 strips that facilitates the center of gravity reconstruction. The lower resolution at low gain is explained by the bad signal to noise ratio. In average, the detector with a 2 mm transfer gap shows a better resolution thanks to a greater diffusion within the transfer gap.

8.4.7.3 Resistive Detectors Spatial Resolution

With a maximal cluster size of 3 strips, we expect a resolution for the buried resistor prototypes between the Micromegas and the GEM-Micromegas. The BR2 prototype shows a resolution of 100 µm. Both detectors have a larger residual distribution at high gain, see Fig. 8.20. That could indicate a charging of the resistive layer. If a charged space was formed, it would deviate the electron shower in the Micromegas amplification gap and therefore worsen the resolution of the detector.

To improve this relatively bad resolution, several different algorithms, for the cluster time/position

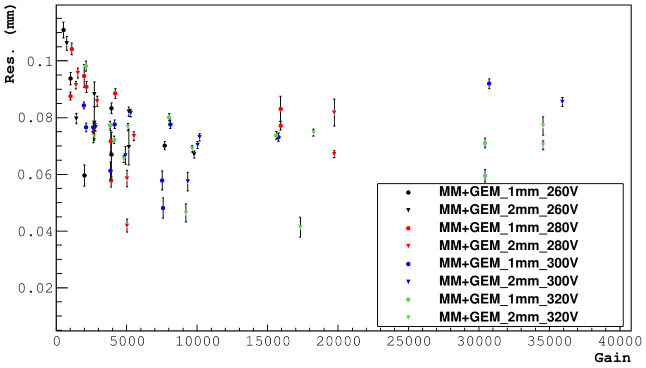

Figure 8.19: [Left] Resolution of the GEM-Micromegas detectors with respect to the detector gain. The colors of the symbols represent different gains on the GEM foil corresponding to a ΔV_{GEM} from 260 to 320 V.

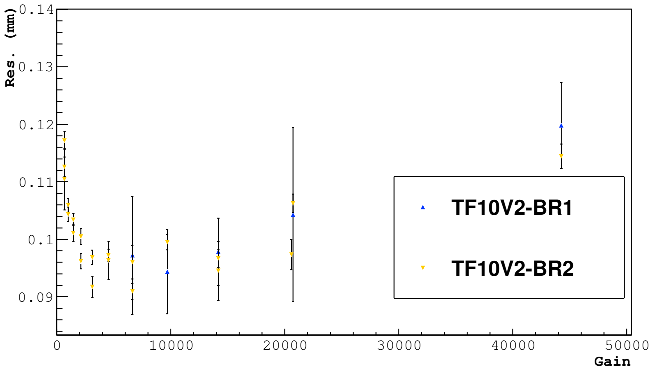

Figure 8.20: Evolution of the resolution of the TF10-BR1 and TF10-BR2 detectors with gain.

calculation, have been tried to calculate the cluster and time position. The center of the cluster x_{cl} is:

$$x_{\text{cl}} = \frac{\sum_i w_i x_i}{\sum_i w_i}$$

We modify w_i to match the charge distribution within the buried resistor and compare the residual distribution to the weighted mean algorithm where $Q_i = w_i$. Results are summarized in Tab. 8.2. Tab. 8.2 shows that no improvement has been obtained except for the η algorithm (see Sec. 2.5.2) and only for cluster size of 2, for which the algorithm is optimized (as in silicon detectors [43]). The weighted mean algorithm remains the best option.

8.4.7.4 Discharge Rate Measurement with the SPS Beam

By comparing the number of coincidences of the three scintillators and the number of recorded discharges per detector, we measured the spark probability. This number may be overestimated because background particles that have highly scattered on the material of the different test detectors have not been necessarily counted by the trigger. Discharge of resistive detectors had too low amplitudes to be detected by our setup, and were not counted.

w_i	$\sigma_{\text{RES}}(\mu m)$
Q_i	115
$6+\log(\frac{Q_i}{\sum_j Q_j})$	135
$\exp(\frac{Q_i}{\sum_j Q_j}+1)-e$	119
$\left(\frac{Q_i}{\sum_j Q_j}\right)^2$	118
$\sin(\frac{Q_i}{\sum_j Q_j})$	179
$\cos(\frac{Q_i}{\sum_j Q_j})$	152
Q_i for cl. size 2	142
η for cl. size 2	130
η	154

Table 8.2: Width of the residual distribution σ_{RES} of TF10-BR2 for different weighting methods. Q_i is the classic weighted mean methods. The three last lines shows the different of the weighted mean and the η algorithm. First for a cluster size of 2, and then the η algorithm with all clusters.

The Micromegas with the segmented mesh prototype (TF10V2-SEG1) shows a discharge probability of $\sim 0.02 \times 10^{-3}$ for a gain of 10^4 as seen in Fig. 8.21. This is the expected value for a standard TF10 detector. At the same gain, the detectors embedding a GEM pre-amplification stage have a discharge probability of $\sim 0.01 \times 10^{-4}$. A lower spark probability is observed when the gain of the GEM is higher.

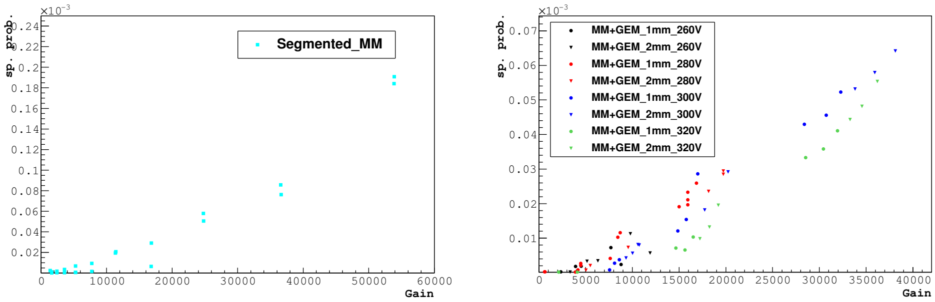

Figure 8.21: Discharge probability of the segmented Micromegas [Left] and GEM-Micromegas [Right] detectors with respect to the detector gain. These measurements are done with the SPS beam of the 2010 RD51 beam period, *i.e.* hadrons (80%) and muons (20%) at 170 GeV/c.

8.4.8 Performances in Low Energy Hadron Beam

Using the data of the T11 test beam and the same offline analysis as for the SPS data, the impact of discharges on detector performances has been studied. The detectors present on the PS test bench (see Tab. 8.1) have been characterized with low energy hadrons beam. The large scattering of these particles increases the track error and impedes the convergence of the alignment (the algorithm virtually moves the detector planes so their active area is entirely inside the beam area and the average χ^2 is minimized).

Before presenting the results, the intrinsic limitation in the precision of track reconstruction with 0.2 to 3 GeV/c hadrons is demonstrated with a GEANT simulation.

8.4.8.1 Simulation of the Effect of Multiple Scattering of the Beam Setup at the Proton Synchrotron

Using a GEANT4 simulation of the T11 test bench made by S. Procureur (full description can be found in [85]) the diffusion of the hadrons by multiple scattering has been studied. In Fig. 8.22 one can appreciate the precision of the model with the energy deposited inside a GEM-Micromegas detector. The two metallic sides of the GEM foil can be distinguished thanks to the high interaction probability of copper with low energy hadrons. The projection of the width of a point like beam to the middle of the test bench shows the scattering of hadrons in the energy range of 0.2 to 3 GeV/c. It indicates that the errors of the tracks, which enters (as defined in Sec. 2.7.6), and here dominates, the spatial residuals as shown in Fig. 8.22 [Right].

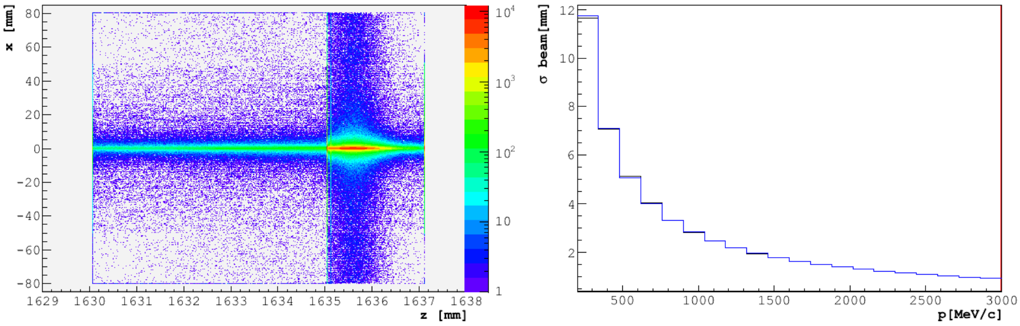

Figure 8.22: [Left] Simulation of the deposited energy inside the GEM-Micromegas detector for pions from 0.2 to 3 GeV/c. The interaction between the beam and the two copper sides is clearly visible at z=1635 mm. [Right] Projected beam width in the middle of the test bench according to the energy of the particles. π^+ are represented with the blue line, π^- with the black line.

8.4.8.2 Resolution in Hadron Beam

As expected, the low energy hadron tracks are too much distorted by multiple scattering to be reconstructed with a good resolution. A measurement of the intrinsic resolution of the prototypes is difficult, as shown in Fig. 8.23. The track error dominates the measurements and follows the same trend as the beam size in simulation (Fig. 8.22).

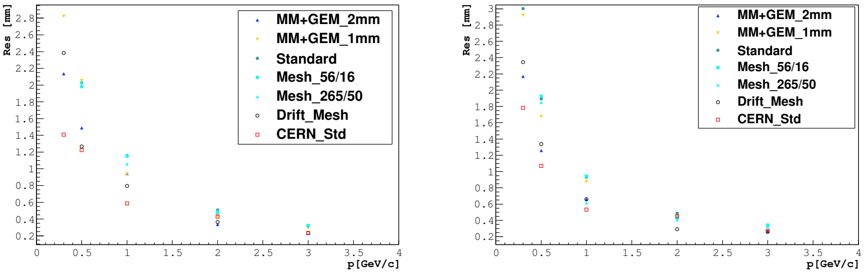

Figure 8.23: Residual width measured for the various detectors as a function of the momentum of incident π^+ [Left] or π^- [Right].

8.4.8.3 Efficiency in Hadron Beam

As for the resolution, the efficiency measurement is difficult due to multiple scattering. To follow the degradation of the resolution, an increase in the road-width is needed. However the road-width becomes not negligible compare to the size of the TF10 detectors and the maximal efficiency reached is lower with low momentum hadrons, see Fig. 8.24.

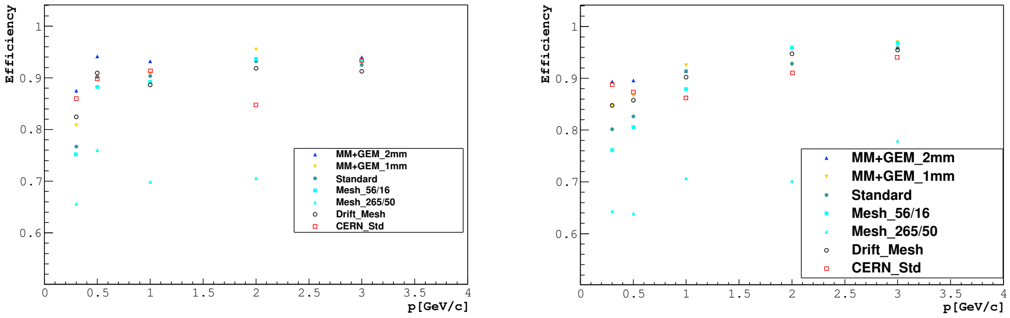

Figure 8.24: Efficiency versus beam energy for π^- [Left] and π^+ [Right].

Fig. 8.25 shows the efficiency plateaus for the GEM-Micromegas detectors. A decrease of the efficiency is observed at high gain showing the impact of the discharges on these detectors. This effect is visible since these detectors are not optimized for fast high-voltage recovery. This decrease is not observed with resistive detectors, the low amplitude discharges have apparently no impact on the detector performances.

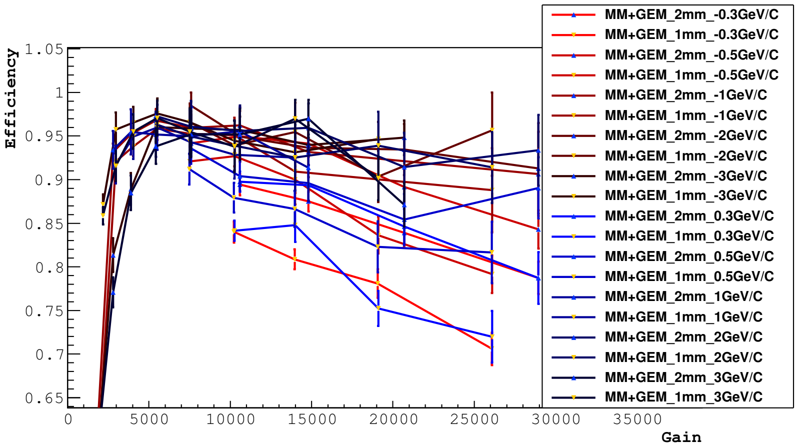

Figure 8.25: Efficiency versus gain for various momentum for GEM-Micromegas with a 0.2 to 3 GeV/c hadron beam. Blue lines represent positive hadrons and red is for negative.

8.5 Conclusion

Tab. 8.3 summarizes the performances measured during the two test beam periods at CERN, with 0.2 to 3 GeV/c hadrons at the PS and with muons of 170 GeV/c at the SPS. Time resolutions and the possible propagation of signals have not been studied since the trigger phase was not recorded. This R&D on discharge reduction concludes on the viability of two solutions for the large Pixel Micromegas: **the GEM-Micromegas** and **the buried resistor** detectors.

Detector	gain at 400V	Spark prob.	Efficiency	σ_{det} (μm)	cl. size nb. of strips
MM+GEM 1mm	10^4 to 10^6	0.1 to 1×10^{-6}	$>99\%$	80	3.3
MM+GEM 2mm	10^4 to 10^6	0.1 to 1×10^{-6}	$>99\%$	80	3.7
Buried Resist. 2	10^4	-	$>98\%$	100	3
Buried Resist. 1	800	-	15%	100	2.1
Segmented Mesh	4000	2×10^{-5}	91%	90	1.9

Table 8.3: Summary of the performances measured on the TF10 prototypes.

One of the buried resistor detectors did not work properly, which suggests that this new technology is not fully reliable. However the BR2 prototype has shown no significant discharge and proved to be fully efficient. Despite an intense effort on position reconstruction, its spatial resolution remains above 100 µm, which is better than the expected resolution without clustering of $\text{pitch}/\sqrt{12} = 115.5\,\mu\text{m}$ but worse than the other non-resistive prototypes. Charging effect in resistive material has not been observed and are believed to happen at much higher rate. A $40\times40\,\text{cm}^2$ prototype, the PMM_BR_2011 has been built and tested at COMPASS, results are presented in Chap. 10.

We have seen that the GEM-Micromegas detectors reach the COMPASS-II specifications in terms of discharge rate reduction, spatial resolution and efficiency. The spatial resolution has been measured to be between 60 to 80 µm depending on the field configuration. This measurement could have been improved within a more stable environment. Advantages of the greater diffusion in the 2 mm transfer gap compared to the 1 mm have been highlighted. To reach a better understanding of the two stages gaseous amplification, a simulation at the microscopic level has been performed and is presented in the next Chapter. Full size prototypes have been tested in the COMPASS environment, see Chap. 10.

Chapter 9

Simulation of the GEM-Micromegas Detector

To investigate the gaseous processes within the GEM-Micromegas prototype, a computer model of this detector has been built with the GARFIELD++ and MAGBOLTZ softwares. GARFIELD is used to propagate charges in the electric field and the package MAGBOLTZ for gaseous processes simulation. An event display of such a simulation is shown in Fig. 9.1. This type of simulation allows to describe gaseous processes in the detector with a good precision thanks to the numerous excitation modes of gases and gas mixtures taken into account in MAGBOLTZ. Such simulations were able to reproduce MPGD gain in gas mixture with a precision of a few percents.

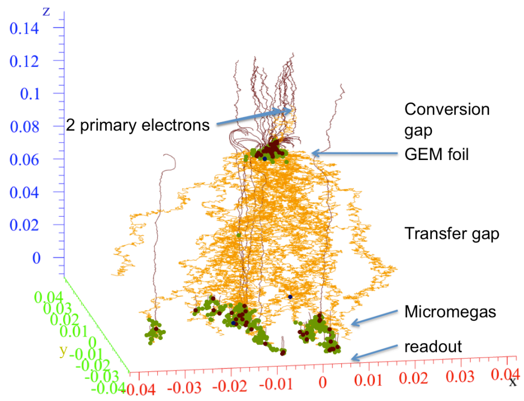

Figure 9.1: Simulation of 2 electrons created above the GEM foil. Orange lines show the tracks of electrons, heading toward the readout and colliding with gas molecules. Black lines represent the ions path leading toward the drift, some of them are captured by the top of the GEM. Dots represent ionizing processes with a different color for each different excitation mode of the gas mixture.

We are interested in particular in the dependence of the gain with the transfer field E_{TR}. A large dependence of the gain with E_{TR} would be a constrain on the mechanical precision needed to hold the GEM foil at a constant distance of the micro-mesh. A tenth of millimeter precision in a $40 \times 40\,\mathrm{cm}^2$ light detector would be challenging. Experimental gain measurements have shown an operating mode where the gain is independent of E_{TR}, see Chap. 8. This effect will be confirmed in Sec. 9.2.2.

Other gaseous effects are investigated, like the mechanism of ion backflow suppression, ion and electron transparencies and diffusion in Sec. 9.2.3 and 9.2.4.

9.1 Principle of the Simulation

To perform a realistic simulation of avalanche processes at the detector scale, the numerous excitation modes that enter in the complex ionization processes have to be simulated. This is done by the MAGBOLTZ package [86] of GARFIELD [33]. The latter needs a digital model of our detector: an electromagnetic field map computed with the ANSYS simulation software.
The effect of UV photons is not yet implemented in MAGBOLTZ so the development of secondary avalanches at the origin of discharges, are not simulated here.

9.1.1 Optimization of Computational Time

The computational time limits the gain of the simulated detector. Indeed the simulation of 250 electrons on a single GEM stage ($\Delta V_{GEM} = 360\,V$ in Ne/CO_2 90/10) takes 20 hours of CPU time on the CERN computer farm. With the second amplification stage, the simulation of the GEM-Micromegas at the same gain is not practically possible, the number of particles to simulate has to be reduced. The dimensions of the GEM and Micromegas have been almost kept since non-linear effects are known to affect MPGDs at small-scale [75]. The electromagnetic field has also been conserved to keep the drift velocity and the diffusion of the charges. That is why it has been preferred to change the gas mixture to limit the gain. Simulations were performed in Ar/CO_2 90/10 instead of the high gain gas Ar/iC_4H_{10} 95/05. A reduction factor greater than 200 in CPU time is obtained that way. Ar/CO_2 90/10 has been chosen to replace Ar/iC_4H_{10} 95/05 because both are well-known mixture and results can be compared to the literature. In addition the 1 mm transfer gap has been studied to limit the simulated volume. Nevertheless the simulation allows to separate effects happening in the different volumes of the detector so the results can be easily extrapolated to the 2 mm gap. A last optimization is the limitation of the number of primary electrons to 200.

9.1.2 Electric Field from ANSYS

The base of the simulation is an electric field map where the geometry of the detector is defined with the potential applied and the symmetry conditions. This was done with the engineering simulation software ANSYS [87]. An elementary pattern that includes the double conical GEM and the micromesh is shown in Fig. 9.2. The model also contains boundary conditions so the map can be used with reflective symmetries. The
electric and magnetic permeability, specific to the different materials, are given there.

The standard double conical GEM geometry is described here with holes of 37 µm diameter with a pitch of 140 µm. In order to match the GEM pattern, the pitch of the micro-mesh has been slightly change to 61 µm × 70 µm with wires of 18 µm diameter, less than 10% change from the TF10 prototypes geometry. This matching is necessary to use reflective symmetries on the elementary pattern.

The 3D model is then divided in thousand of finite elements (this operation is called meshing) so that the Maxwell field equation can be solved in each element. The resulting field map is used in the GARFIELD framework. Since all the voltages have to be defined to solve the field, it is necessary to create one different map for each different voltage configuration.

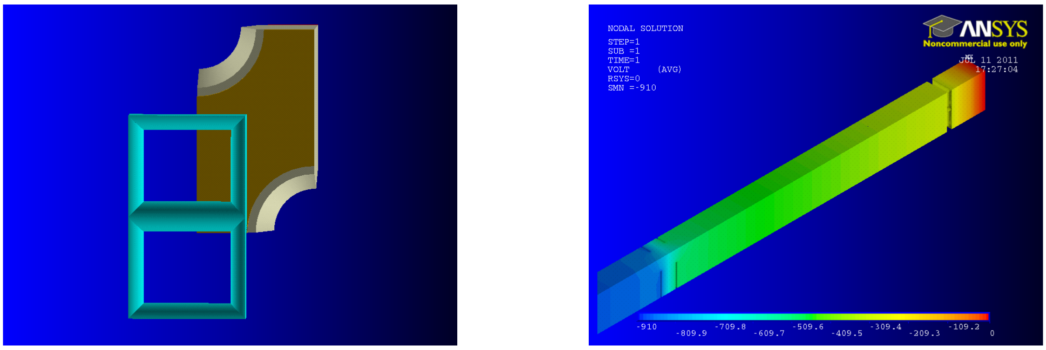

Figure 9.2: [Left] 3D model of the elementary pattern used to compute the field map. At the forefront of the picture stand 2 stitches of the micro-mesh. Two times one quarter of a GEM hole lay at the background. By symmetrically repeating this pattern, a complete detector can be built. [Right] Result of the field solver, the scale is in Volt. The readout plane is on the right of the picture at 0 V (in red). Empty volumes are the metallic parts (copper layers of the GEM and the micro-mesh) where there is no field.

9.1.3 The MAGBOLTZ Package

The FORTRAN MAGBOLTZ package solves the Boltzmann transport equation for charges in gas mixtures under the influence of an electromagnetic field. The first version of MAGBOLTZ is now used for pure noble gas thanks to its algorithm based on an analytical solution in the elastic limit. MAGBOLTZ 2 uses the Monte Carlo integration technique to solve the Boltzmann transport equation for any gaseous mixture and any electromagnetic field geometry [88]. The inputs needed by this framework are the EM field maps (that includes the angle between the fields), the temperature, pressure and the gas composition. The program usually reaches an accuracy better than 1% for the drift velocity and 2 % on the diffusion coefficients.

9.2 Simulation of the GEM-Micromegas Detector

The relative independence of the gain with the transfer field observed with ^{55}Fe gain measurements (see Fig. 8.9) is not trivial. Two non-linear processes, the GEM electron extraction and the electron transparency of the micro-mesh, depend on the transfer field. E_{TR} is, at the same time, the GEM extraction field and the Micromegas drift field. In this section their relative influence on the gain will be described before the ion backflow and diffusion.

The high voltage configuration used here is the same than for Fig. 8.9 *i.e.* $\Delta V_{GEM} = 300\,V$, $V_{MESH} = 280\,V$ and $E_{DRIFT} = 800$ V/cm, as shown in Fig. 9.3. V_{TR} varies from 20 to 900 V/mm.

9.2.1 Gain of the GEM-Micromegas Detector

Preliminary studies have successfully reproduced the gain of a standard Micromegas and a single GEM detectors in Ar/CO_2 90/10 for several voltage configurations. Within the same field configuration the gain of the TF10 GEM-Micromegas detector is about 2×10^4 in Ar/iC_4H_{10} 95/05, see Fig. 8.9. This represents a factor of 500 higher than with Ar/CO_2 90/10.

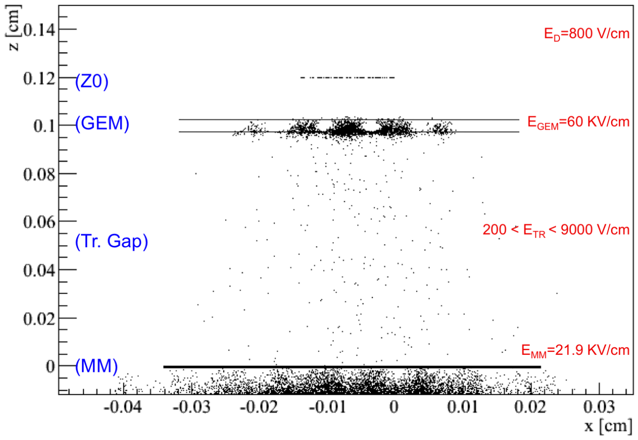

Figure 9.3: Side view of the GEM-Micromegas detector volume, the z coordinate is along the drift direction and the x coordinate along the strip direction. Black dots represent electron creations. The plane formed at (Z0) is the starting point of primary electrons. Electrons are then created in the GEM holes at $z = 0.1$ cm and in the amplification gap below $z = 0$ cm. The GEM holes pattern appears in the amplification gap below the micro-mesh. There are ionization in the transfer gap because the transfer field of $E_{TR} = 900$ V/mm is at the beginning of the proportional mode. Plain black lines indicate the positions of the micro-mesh and the GEM foil.

9.2.2 Gain and Electron Transparency of the GEM-Micromegas Detector

By using the repartition of the creation/annihilation of charges, we can reconstruct the gain of each active area of the detector. The gain of each stage is calculated by the ratio between the number of electrons coming from the area above and the number of electrons transmitted to the next stage. Since the voltage configuration of the GEM and Micromegas is fixed, the overall gain of the detector according to the transfer field (E_{TR}) mainly depends on the ability of each stage to get and transmit electrons. The electron transparency is defined as the ratio between the number of electrons after the amplification stage and the number of incoming electrons corrected from the amplification in the area. The three areas are defined as:

- Micromegas : from the top of the micro-mesh wires to the readout plane
- GEM : from the top of the upper metal part of the foil to 5 µm under the foil to include the area where the amplification still happens
- Transfer gap : Between the top of the micro-mesh and the GEM foil bottom -5 µm

The simulated gain and transparency versus E_{TR} shown in Fig. 9.4 describes well the shape observed in Fig. 8.9. No error is displayed in this section due to the difficulty to compute the correlation between the different quantities.

To describe the results, these curves are divided in 3 regimes:

From 0 to 200 V/mm At very low E_{TR}, the electron transparency of the GEM is below 50% with a bad electronic transmission to the transfer gap. The number of charges extracted from the GEM foils is very low and the Micromegas good transparency has no effect on the gain. Gain is increasing with E_{TR}, as the gain of the GEM.

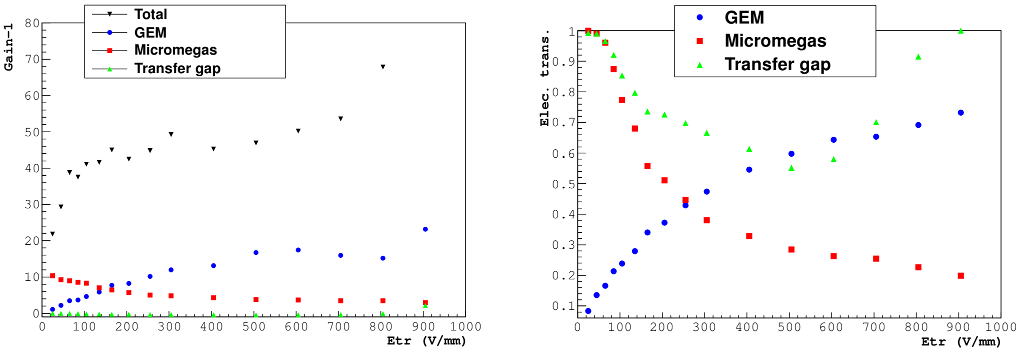

Figure 9.4: [Left] Gain and [Right] electron transparency simulation of the GEM-Micromegas detector.

From 200 to 700 V/mm In this regime the gain is pretty stable thanks to the compensation of the increase of the GEM electron extraction and the Micromegas loss of electron transparency. The detector has to be operated in this region to minimize the effect of the fluctuation of the transfer gap size.

From 700 to above 900 V/mm The transfer gap has a gain below 1 (Ar/CO$_2$ 90/10 is electro negative) until 700 V/mm. For larger field values, charges start to be created and the effective gain increases exponentially. Very high amplification could be reached with such a detector whereas it would suffer from at least the same discharge rate than a standard Micromegas. In addition the high ion backflow would be much more important than in a standard detector (see next section).

The stability of the gain for a transfer field between 200 to 700 V/mm reproduces well the gain measurement and shows how the Micromegas and GEM amplifications are compensating each other. Setting $E_{TR}$to rather high voltage has the advantages of increasing the velocity of electrons to improve timing performance and to reduce the Lorentz angle when the detector is operated in magnetic field.

9.2.3 Ion Transparency and Ion feedback

The gain of a gaseous detector in a intense beam is limited by the local decrease of the electric field by a high density of positive charges. This effect is one of the major drawback of wire detectors. The ion feedback, *i.e.* the number of ions that arrive in the drift volume per incoming electron (ϵ as defined in Sec. 2.6.3), directly limits the maximal rate that a detector can stand. Before studying the distribution of ions in the detector, the intrinsic ion feedback suppression mechanism of the micro-mesh and the GEM foil is detailed.

Ion feedback suppression : The GEM and Micromegas structures are used for their intrinsic ion backflow suppression. On Fig. 9.5, the black dots represent the end point of ions where positive charges are neutralized. The bottom part of the micro-mesh captures the ions as expected from the field configuration of a Micromegas (see Fig. 7.4). The bottom layer of the GEM foil stops ions that have been created in the transfer gap between holes extraction field lines. The top of the foil captures ions that have followed the field lines from the micro-mesh and the ones that have been created inside the holes by the GEM amplification.

It is important to note that some charges end up on the wall of polyimide, mainly near the edge of the internal ring. If the rate is sufficient, an equilibrium is created between charges that are captured

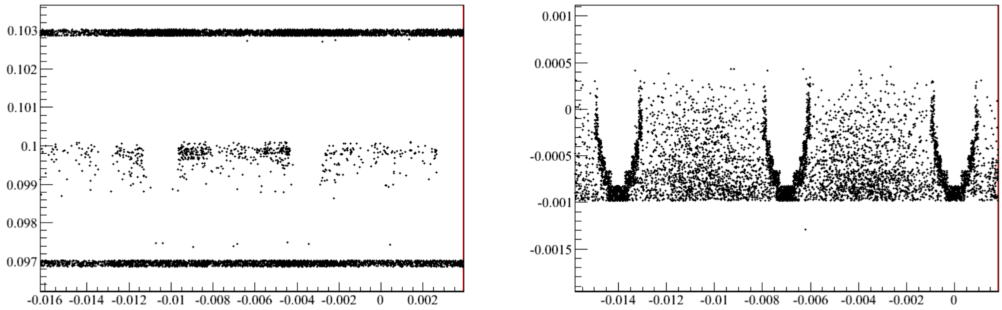

Figure 9.5: Detail of the GEM foil [Left] and micro-mesh [Right] simulation for ion capture at $E_{TR} = 900\,V/mm$. Each black dots represent an ion capture projected on the zx plane. 3 GEM double conical holes are shown in [Left], the two bold lines are the two $5\,\mu m$ copper layers of the foil that capture most of the ions. On the right, three $18\,\mu m$ diameter micro-mesh wires are shown, the background in between the wire is the projection of the other wires parallel to the picture. Axes units are in cm.

by the walls and the one that escape; the GEM is charging up. The resulting field modifies the GEM behavior depending on the hole geometry. Here the number of electrons that stop on the wall is greater than the number of ions compressing the field lines and improving the gain. A more complete picture of the GEM amplification is given in Fig. 3.1.

Ion transparency and ion feedback : The GEM-Micromegas structure implies that the ion feedback is the convolution of the Micromegas ion feedback and the GEM ion transparency in addition to the GEM ion feedback, see Fig. 9.6. For this particular micro-mesh geometry and field configuration, the Micromegas stage lets drift from 0.8 to 1.1 ion per incoming electron into the transfer gap. At low E_{TR}, the Micromegas ions follow the field lines through the GEM into the drift volume. For a transfer field larger than 300 V/mm the GEM starts to capture the ions but this effect is compensated by the increasing number of incoming ions. In addition to the Micromegas ions, the GEM releases its own ions, but the proportion is much lower since the number of incoming electrons (the primary electrons) is small. At the end 11 ions per primary electron are released into the drift volume at a gain of ~ 50.

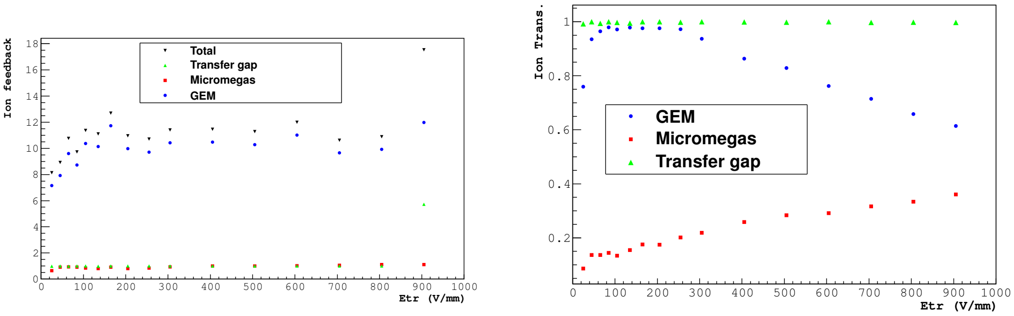

Figure 9.6: Ion feedback, ϵ, [Left] and ion transparency [Right] of the different stages of the GEM-Micromegas detector.

Current measurements on the Pixel Micromegas with an embedded GEM foil at Compass has shown currents of $I_{MM} = 1000\,nA$, $I_{GEM_{TOP}} = 90\,nA$ and $I_{DRIFT} = 40\,nA$ at $V_{MM} = 300\,V$, $V_{TR} = 280\,V$ and

$V_{\Delta\mathrm{GEM}} = 300\,\mathrm{V}$ in $\mathrm{Ne/C_2H_6/CF_4}$ 85/10/05. The ratio between I_{DRIFT} and I_{MM} gives an approximation of the ion backflow[1] of 4%. Similar measurements on standard COMPASS Micromegas give $\sim 2\%$. The condition of this measurements are far from the simulation but the significant increase of ion backflow compared to a standard Micromegas is confirmed.

The simulated ion backflow of the GEM-Micromegas detector is over $\sim 20\%$ in the presented field configuration. Even if this is not an issue for a tracking detector that has a 5 mm drift length, this high value is a major drawback for a long drift length. The GEM-Micromegas detector is an optimized high-gain detector for high-rate environment but not suitable for a TPC.

9.2.4 Diffusion

The transverse diffusion is expected to be the convolution of the different diffusions of each area of the detector. In this naive model, the projected diffusion σ_T on the readout plane is the quadratic sum of the width of the distributions σ_D at each stage. The different values of σ_D are summarized in Tab. 9.1.

Area	Z length $[\mu m]$	E $[V/cm]$	D $[\mu m/\sqrt{cm}]$	σ_D $[\mu m]$
DRIFT	150	800	340	43
GEM	50	60K	180	13
MM	128	21.9K	210	24
TRANS. GAP	1000	20	600	190
TRANS. GAP	1000	300	250	79
TRANS. GAP	1000	900	350	111

Table 9.1: Estimation of the transverse diffusion σ_D for each area of the detector, D is the transverse diffusion in $\mathrm{Ar/CO_2}$ 90/10 from [89].

The quadratic sum of the numbers given in Tab. 9.1 is $\sigma_{\mathrm{D}} = 94\,\mu\mathrm{m}$ at $E_{\mathrm{TR}} = 300\,\mathrm{V/mm}$. This value corresponds to the $\sim 100\,\mu\mathrm{m}$ of the simulation (see Fig. 9.7). However the diffusion should be larger at low field (<100 V) and at higher field (>500 V). This is not the case in simulation because the transverse diffusion is dominated by the non-linear diffusion effects at the exit of the GEM holes.

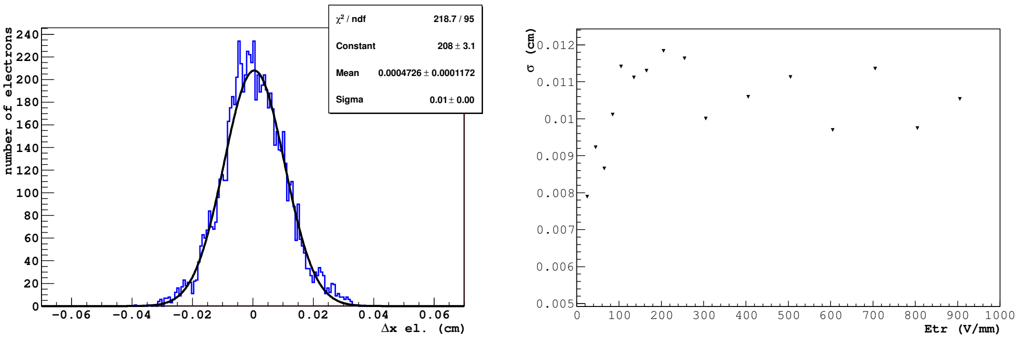

Figure 9.7: [Left] Distribution of the distance between the position of the primary electron and the position of the electrons in the readout plane. [Right] Evolution of the σ of the fitted Gaussian function of the [Left] distribution versus the transfer field.

---

[1] The ion backflow is not ϵ the ion *feedback* which is not measurable, see definitions in Sec. 2.6.3.

The increase of a factor of 2.5 of the diffusion thanks to the GEM foil is a clear advantage of such a detector compared to a simple Micromegas detector. Experimental measurements showing an increase of the cluster size from 1.7 to 3.8 strips confirm this simulation, see Sec.8.4.7.2. Since cluster of size one is the major limitation of Micromegas resolution, GEM-Micromegas detectors have better spatial resolution as measured with TF10 prototypes in Chap. 8.

The simulations have shown to be in a good agreement with the measurements, in terms of gain and diffusion. It explains the characteristics of the GEM-Micromegas concept. In addition to its lower discharge probability, this detector has a better diffusion that leads to an improved spatial resolution. Independence of the gain and E_{TR}, in a defined regime, relaxes constrains on mechanical design and introduces freedom in the choice of operating field configuration.

Building a model of the GEM-Micromegas detector has improved the understanding of the combination of the amplification mechanisms. Its great performances are characterized with a full scale prototype in COMPASS environment in the next chapter.

Chapter 10

The Pixel Micromegas Prototypes

10.1 Introduction

In the perspective of the COMPASS-II experiment, it has been decided to study the possibility to improve the large COMPASS Micromegas chambers. The new detectors would have to offer comparable performances over the full active area plus the beam area. This requires large tracking detectors, of $40 \times 40\ \ \mathrm{cm}^2$, fully active, with a spatial resolution better than $100\,\mu\mathrm{m}$ and a time resolution below 10 ns. A reduction of the discharge probability by a factor 10 to 100 is needed to prevent extensive dead-time, instability and ageing. These detectors should stand an increase of beam flux.

These requirements led to a detector with segmented electrodes in the beam area, a more integrated electronics based on the APV chip and a discharge reduction technology: the Pixel Micromegas. Several of these prototypes have been built and studied in the COMPASS environment, to confirm the design of such a detector and its compatibility with the APV readout electronics for a full characterization. After the description of the common Pixel Micromegas base, its electronics, and the different spark reduction technologies, results of the characterization are presented.

10.2 General Characteristics

Results presented here are based on the characterization of four prototypes. All these prototypes have been used to validate the PCB design, the segmentation of the electrodes in the central region, the bulk technology and the APV based FEE. In order to reduce the discharge rate and impact, two prototypes embedded a GEM foil as a pre-amplification stage and one embedded the buried resistance scheme presented in Chap. 8.
The base structure of these prototypes is a sandwich of 5 mm honeycomb and $100\,\mu\mathrm{m}$ FR4, stiffened by a 1 cm wide epoxy frame on the side. The readout circuit is printed on both side of a $200\,\mu\mathrm{m}$ PCB, which is glued on the honeycomb-based structure. The micro-mesh is embedded on the readout via the bulk process described in Sec. 10.2.2. Materials and their radiation length are detailed in Tab. 10.1.

10.2.1 Geometry

The Pixel Micromegas detectors have an active area of $40 \times 40\ \mathrm{cm}^2$ divided into two different types of strips in addition to a pixelized zone. The overall detector is based on a PCB of $64 \times 64\ \mathrm{cm}^2$, as shown in Fig. 10.1. The most external strips ((1) on Fig. 10.1) have a pitch of $480\,\mu\mathrm{m}$ and are 40 cm long. On the central area the strips are cut in two, with a lower pitch of $400\,\mu\mathrm{m}$ adapted to the larger particle flux ((2) on Fig. 10.1). The $400\,\mu\mathrm{m}$ pitch is conserved in the pixel area. The 2.5 mm long pixels in the

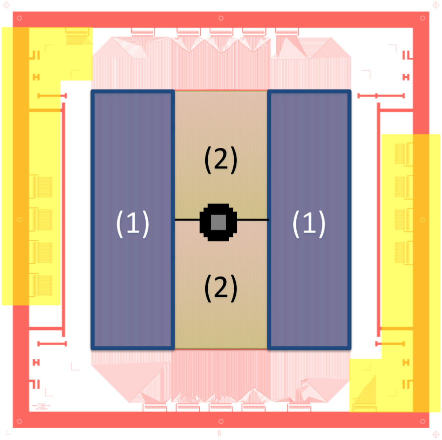

Figure 10.1: Schematics of the Pixel Micromegas detector. The zone labeled (1) is segmented into 40 cm long strips at a pitch of 480 µm, and (2) of 20 cm long strips at a pitch of 400 µm. The pixelized area in the center of the detector in divided between the 6.25 mm long pixels, in black, and the 2.5 mm long pixels in gray. Connectors highlighted in yellow are connected to the pixels, the others (in pink) to the strips.

central region are surrounded by 6.25 mm long pixels in the 5 cm diameter beam region. The 2560 channels are distributed into 512 40 cm long strips, 768 20 cm strips, 640 6.25 mm pixels and 640 2.5 mm pixels.

10.2.1.1 Pixel Micromegas with a GEM Pre-Amplification Stage

The GEM foil has the standard geometry described in Fig. 2.9. The 40×40 cm^2 active area of the foil is divided into 16 sectors separated by a 100 µm dead space. The sectors are connected in series by 1 MΩ resistors. This division limits the charge transferred during a discharge in the GEM foil. The foil is held at 2 mm above the micro-mesh by 16 pillars of 3 mm diameter.

10.2.1.2 Pixel Micromegas with Buried Resistors

The buried resistor scheme consists here in 2545×280 µm^2 resistive pads connected to the readout electrodes via buried resistors of few MΩ. A schematic view of the structure is shown in Fig. 8.2 and Fig. 2.7 [Right] shows a photograph of a similar detector.

10.2.2 The Bulk Fabrication

On the readout electrodes, a stainless steel laminated micro-mesh is held by pillars etched in a coverlay layer. The process is summarized in Fig. 10.2. The 0.2 mm diameter pillars are placed over the whole active area every 2 mm. The copper mesh used with the standard Compass Micromegas is too fragile to withhold the production process, a more solid woven stainless steel micro-mesh is needed. This micro-mesh has 18 µm diameter wires at a pitch of 45 µm that provides a good mechanical strength whereas the optical transparency is 49% (compared to 64% for the previous Compass nickel mesh and the 40% of the standard copper mesh).

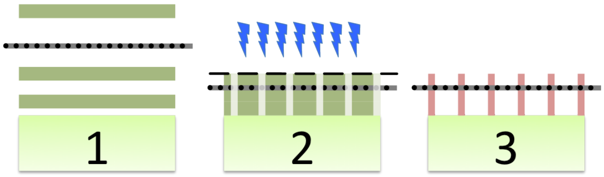

Figure 10.2: Schematic view of the Micromegas in a bulk process fabrication. First (1) the woven micro-mesh is laminated within 3 photo-sensible layers. In (2): UV-light irradiation polymerizes the pillars according to the pattern printed on the mask (in black here). Then the photo-sensible layers are removed by wet etching and the micro-mesh is held on the PCB by the holding pillars.

10.2.3 Material Budget

In hadronic experiments, material budget is a concern in order to avoid multiple scattering and photo conversion. Therefore the Pixel Micromegas detectors must have the minimum material budget. It is summarized in Tab. 10.1. Despite the fact that the bulk and discharge reduction technologies increase the radiation length, the pixel Micromegas detectors stays under $0.4\% X/X0$, which is acceptable for COMPASS-II. The PMM_BR_2011 prototype has a 3 mm PCB as mechanical support instead of the 5 mm honeycomb structure, due to a problem in production. That explain its 5 times larger $X/X0$. Further resistive prototypes will have a lower material budget than the prototypes that embedded a GEM foil. GEM foils, optimized for material budget with thinner copper layers of 2 µm instead of 5 µm, are available and have a radiation length of 0.035% $X/X0$ instead of 0.067% $X/X0$.

Layer	Thickness (cm)	fraction of area (%)	Material	Radiation length $X0$/cm	$X/X0$ %
Rear PCB	5×10^{-4}	100	Cu	1.43	0.035
	1×10^{-2}	100	FR4	19.4	0.05
Honey comb	5×10^{-1}	1.8	G10	19.4	0.05
Readout PCB	1×10^{-3}	20	Cu	1.43	0.014
	1×10^{-2}	100	FR4	19.4	0.05
	1×10^{-3}	80	Cu	1.43	0.056
Total board					0.255
Mesh	1.8×10^{-3}	49	Fe	1.72	0.05
Pillars	1.28×10^{-2}	2.3	Vacrel	44.4	0.001
Total Bulk					0.051
Drift	5×10^{-4}	77	Cu	1.43	0.027
Gas window	2.5×10^{-3}	100	Kapton	28.6	0.009
	2×10^{-4}	100	Cu	1.43	0.014
Total window					0.023
Total PMM					0.329
GEM	5×10^{-4}	77	Cu	1.43	0.027
	5×10^{-3}	77	Kapton	28.6	0.013
	5×10^{-4}	77	Cu	1.43	0.027
Total GEM					0.067
Resistive	5×10^{-3}	90	C	18.9	0.024
	5×10^{-3}	90	Vacrel	44.4	0.01
Total Res.					0.034
BR_2011 PCB	3×10^{-1}	100	FR4	19.4	1.54
Total PMM					0.329
Total PMM + GEM					0.396
Total PMM + resist.					0.363
Total BR_2011	at r>1.5 cm				1.90
Std. MM*					0.287
Pixel GEM**	at r<1.5 cm				0.4
Pixel GEM**	at r>1.5 cm				0.7

Table 10.1: Detail of the materials and their radiation length used in a Pixel Micromegas. * from [90] and ** from [61]

10.2.4 The APV based Readout Electronics

The APV25-s1[1] is an analog pipeline, amplifier and multiplexer ASIC built for the silicon tracker of the CMS experiment in 25 µm CMOS technology [38]. Each of the 128 channels is connected to a pre-amplifier/shaper followed by 192 memory cells forming an analog circular buffer. In order to read several different samples, the addresses in the memory has to be kept and only 160 cells can be used per channel. Written with 40 MHz, this memory allows to cover up to 4 µs between the event and the recorded signal. Upon a trigger signal, 3 samples are read-out as illustrated in Fig. 10.3. Once calibrated, amplitude ratios are computed to reconstruct the time of a signal with respect to the trigger signal.

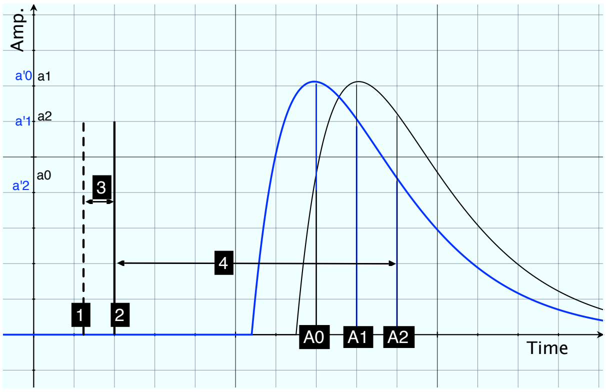

Figure 10.3: Two typical signals at the output of the APV amplifier/shaper. The numbers represent: **1**:Trigger signal, **2**: Synchronized trigger, **3**: TCS phase, **4**:Trigger latency, **A0 A1 A2**: Digitalization times of the 3 APV samples, **a'0 a'1 a'2** (in blue): amplitude of the 3 samples for the blue curve, **a0 a1a2**: amplitude of the 3 samples for the black curve. The amplitude of the signal is reconstructed from the amplitude measurements and the time from the amplitude ratios.

10.2.4.1 The Readout Chain

The bare APV chips are mounted on front-end cards with the sparks protection circuit. To read the 2560 channels of the Pixel Micromegas, 20 APV cards are needed. They are connected to 2 ADC cards via bus cards, both originally developed by the TUM-E18 electronics lab for the Pixel GEM detectors [91]. Each ADC card houses two ADC chips of 8 channels each, and a FPGA to perform online data processing. Common mode noise correction and zero suppression [40] algorithms reduce drastically the data volume. One data concentrator, the HGeSiCa module, concentrates the information coming from up to 8 ADC cards. The connection to the computers in charge of the COMPASS event reconstruction is done via an optical link using the SLINK standard [92]. All the parts are shown in Fig. 10.4.

10.2.4.2 Influence of Entry Capacitance on the APV Signal Shape

Preliminary measurements of the compatibility of the APV chip with the rather large capacitance of the Micromegas detector (compared to silicon detectors) have been performed.
First the different detector capacitances of the Pixel Micromegas have been measured. The absolute value is difficult to measure, because it is not possible to get rid of parasitic capacitors and because it depends on the concerned frequency domain. It has been measured using a large band-width capacitance meter, see Tab. 10.2.

---

[1] APV: Analog Pipeline Voltage

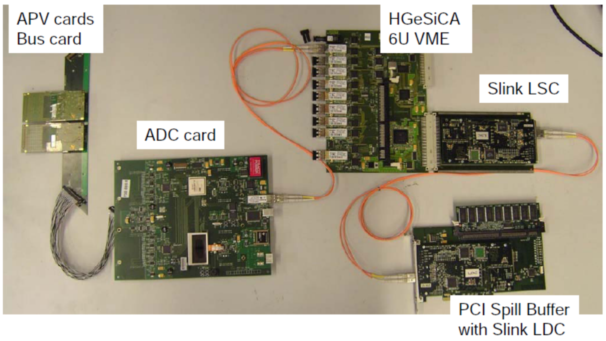

Figure 10.4: The front-end electronics chain connected to the Pixel Micromegas detector.

Type	0.5 MHz	1 MHz	20 MHz	40 MHz	100 MHz
0 cm	3.5 pF	3.5 pF	3.5 pF	3.5 pF	3.5 pF
Strip 20 cm	24 pF	24 pF	25 pF	28 pF	54 pF
Strip 40 cm	45 pF	45 pF	54 pF	49 pF	-30 pF
Pixels	23 pF	20 pF	21 pF	23 pF	47 pF

Table 10.2: Measured capacitance of the different electrodes of the Pixel Micromegas detector. “0 cm” corresponds to the connector alone.

To study the influence of this capacitance to the amplitude of signals and noise, a dedicated setup has been mounted. By injecting a pulse of 4.4 mV on the detector capacitor or a standard SMD[2] 1 pF capacitor, the output signal of the APV has been studied. In order to scan the full shape of the signal, the latency is changed between the trigger signal and a pulse generator by 25 ns steps. Using several tens of artificial spills, the response of the APV system is recorded and the influence of the detectors is studied, as shown in Fig. 10.5.

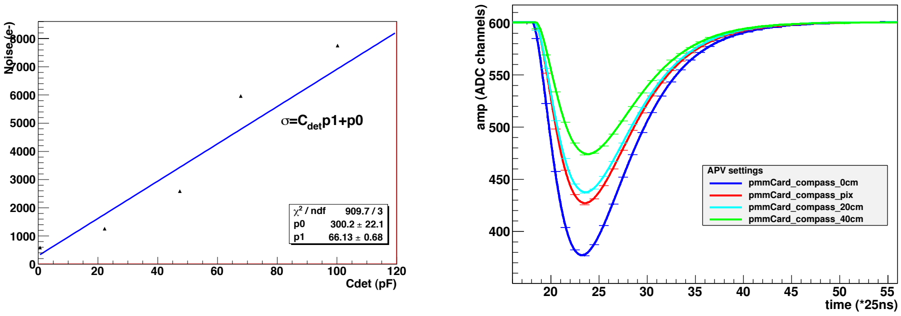

Figure 10.5: Evolution of the noise [Left] and the gain[Right] of the APV according to the detectors capacitance.

10.2.4.3 Shaping Optimization

To optimize the parameters of the APV [38] to the Micromegas signal, systematic studies on the influence of three of these parameters have been done. To be effective at high rate, the electronics signals have to be as short as possible, with the minimal undershoot possible. However the rising time must

---

[2] SMD: Surface Mount Device

cover the 100 ns of the Micromegas signal to avoid ballistic deficit (see Sec. 2.6.4.1). Moreover the signal shape has to be symmetric to optimize noise performances. The three parameters studied here are :

VFP controls the preamplifier feedback current

VFS controls the shaper feedback current, it influences the exponential decay of the signal tail

ISHA is the shaper powering current. It impacts the rising time which must cover the 100 ns of the Micromegas signal.

The effect of these 3 parameters have been measured and are shown in Fig. 10.6.

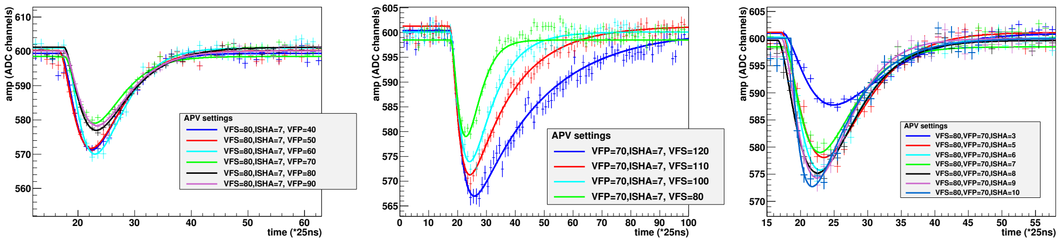

Figure 10.6: Influence of, from left to right, VFP, VFS and ISHA on the APV signal shape. VFS influences the decay length of the tail, ISHA the rising time and VFP the pre-amplifier gain which is hidden by the shaper that comes later in the APV processing chain.

This study concludes that a good compromise for the Pixel Micromegas detector is: ISHA=7, VFS=80 and VFP=70. This shaping has a signal duration, in response to a pulse, of 500 ns and is quite symmetric. It is optimized for a reduce electronics noise. A shorter version of this shaping with a signal length of 400 ns, less symmetric, has been later introduced to reduce electronics occupancy and improve time resolution, see Sec.10.3.6.

10.3 Characterization of Pixel Micromegas Prototypes at Compass

Using a dedicated position in the compass spectrometer (see Fig. 7.1), the four Pixel Micromegas prototypes of Tab. 10.3 have been characterized using the standard muon beam of the SPS[3]. The prototype support structure has been installed in 2010 in the forward spectrometer of Compass at 2.23 m of the center of the target. The Pixel Micromegas have been characterized using the data of Compass in 2010 and 2011. Tab. 10.4 describes the condition of data taking.

Detector	Type	Particularities
PMM_2010	Bulk MM	4 APVs missing
PMM_GEM_2011_1	Bulk + GEM	1 dead GEM sector
PMM_GEM_2011_2	Bulk + GEM	-
PMM_BR_2011	Buried resistor MM	unconnected channels

Table 10.3: Prototypes tested at Compass in 2010 and 2011.

10.3.1 Methodology

The offline software of Compass, CORAL [93], uses all the detection planes to reconstruct particle trajectories and velocities. This reconstruction does not include the data from the Pixel Micromegas prototypes therefore no bias is introduced. First, tracks are extrapolated to the estimated position of detector plane and several iterations are needed to obtain a good alignment of the prototype with respect to the spectrometer[4]. Then tracks extrapolations are compared to the hit position to characterize the detector in term of efficiency, spatial and time resolutions. The prototypes measure the X projection (horizontal axis, perpendicular to the beam axis) whereas the notation U and V are used in the figures to indicate when the figures are in detector coordinates.

10.3.2 Data Selection

In order to use tracks that are likely to be caused by particles, cuts on track quality have been applied. To obtain a good extrapolation at the detector plane, the tracks must contain hits before and after the plane along the track direction. The tracks have also to be detected by the other Micromegas detectors and drift chambers. The reconstructed particle must have a momentum *i.e.* a curvature in the bending magnet field. Finally a χ^2/NDF lower than 3 is requested.

10.3.3 Experimental Conditions

As shown in Tab. 10.4, the characterization is limited to a certain set of data corresponding to particular conditions. In Tab. 10.4, the standard shaping refers to the one described in Sec. 10.2.4.3 that lasts 500 ns. The short shaping has a length of 400 ns (but is more asymmetric). Systematic studies have been performed and further analysis will provide a complete picture before the technical choices for Compass-II are made. The results presented below have been produced with the close collaboration of F. Thibaud.

---

[3] SPS: Super Proton Synchrotron at CERN

[4] The alignment of Pixel Micromegas has been performed by Luigi Capozza

Detector	Beam	Shaping	HV settings	Gain	Run nb.
PMM_2010	$3.7 \times 10^{8} \mu/\text{spill}$	std.	420/700	3500	87870
PMM_GEM_2011_1	$9.3 \times 10^{7} \mu/\text{spill}$	std.	320/620/920/1220	4000	91666
PMM_GEM_2011_2	$2.2 \times 10^{8} \mu/\text{spill}$	short	300/620/940/1240	5500	94827
PMM_BR_2011	$2.0 \times 10^{8} \mu/\text{spill}$	short	470/700	8000	95988

Table 10.4: Experimental conditions of the data used for the Pixel Micromegas prototypes characterization. A spill lasts 9.8 s every $\sim$ 45 s.

10.3.3.1 Discharge Probability

The detector PMM_2010 has been hit by discharges on 32% of the spills. The other prototypes embedded a discharge reduction technology and no discharge has been recorded with the nominal COMPASS muon beam and a solid ^{6}LiD target [94] during the whole data taking period (∼1-2 months per detector). See Tab. 10.4 for the precise rate.

10.3.4 Efficiency Measurement

The efficiency, as defined in Sec. 2.7.5, is the probability that a detector detects a particle, corrected from the probability of a false positive detection (background correction). The road width is the zone around the track extrapolation at the detector plane where a hit is considered to belong to the track. The road width depends on the resolution of the detectors. A road width of 2 mm along the measured coordinate and 1.5 cm in the perpendicular direction has been chosen. Maximal apparent efficiency is reached for this road width, larger values increase only the background efficiency. Since the Pixel Micromegas detectors are sensitive in the beam area, they have to sustain high rate and the background becomes significant. The same method is used to calculate the background efficiency whereas instead of using cluster of an event k, hits of the event $k-1$ are considered. This method also corrects for the non homogeneity of the beam rate over the detector acceptance. Tab. 10.5 shows that background efficiencies over 50% are observed in the pixel area. However the resulting correction remains under 1% thanks to the high apparent efficiency of the detectors. This effect is illustrated in Fig. 10.7.

However background is a potential issue for track reconstruction and must be kept as low as possible. That is why a gate in time and a road width are applied to reject background signals.

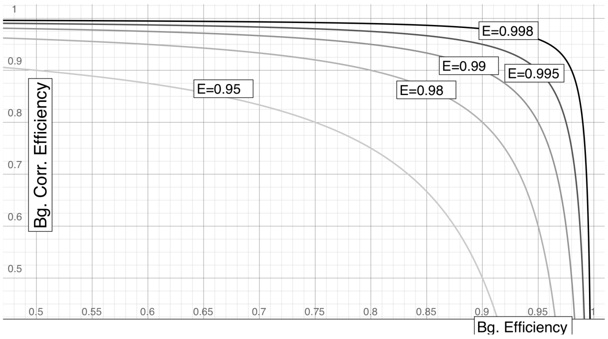

Figure 10.7: Evolution of the corrected efficiency with the background efficiency for different values of apparent efficiency. The evolution of the correction depends on the apparent efficiency E of the detector. A detector with a 99.8% uncorrected efficiency can sustain 60% background efficiency without significant loss.

In the pixelized area, piling-up signals due to the high rate is common. Therefore signal duration is important and an additional optimization of the APV shaping has led to the shortening of the signal from 700 to 500 ns between the “standard” and the “short” shaping (as mentioned in Tab. 10.4). An increase of the efficiency below 1% has been observed. A shaping time below 500 ns has been tried but it caused a ∼ 30% loss of efficiency due to signal undershoot.

Detector	Strips	Pixels	Integrated	Bg Eff. Strips	Bg Eff. Pixels
PMM_2010	78.0	63.2	92.5	9.1	51.3
PMM_GEM_2011_1	96.8	99.1	98.0	6.2	42.9
PMM_GEM_2011_2	98.1	99.5	98.6	12.1	67.7
PMM_BR_2011	97.7	99.1	98.5	10.1	49.9

Table 10.5: Efficiency of Pixel Micromegas prototypes in the Compass environment. Values are in %. Strips, Pixels and integrated efficiencies are corrected from the background.

The **PMM_2010** prototype was not fully equipped with APV cards. Among the 20 front-end cards, 2 were missing in the pixelized area and 2 on the 40 cm strips. This explains the white region in the pixels and the vertical discontinuities at ±7.2 cm in Fig. 10.8. The absence of an efficiency drop at the interface of small/large pixels and around the pixelized area has validated the design of the Pixel Micromegas design in term of electrode segmentation.

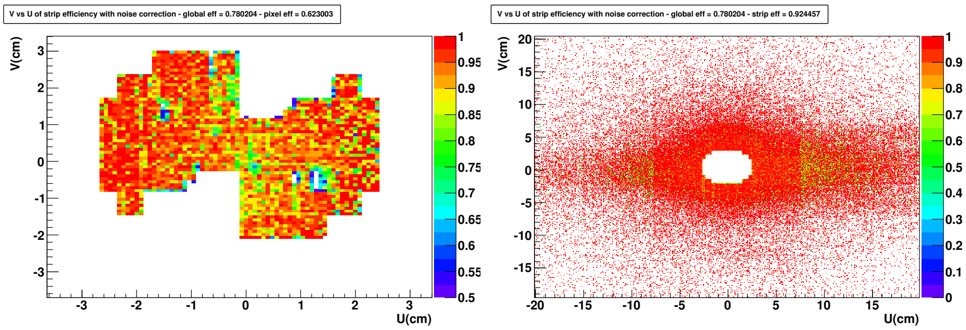

Figure 10.8: Map of the efficiency of the PMM_2010 prototype, [Left] pixelized area, [Right] strips.

The **PMM_GEM_2011** has its first GEM sector disconnected. The resulting un-efficiency is observed on the top of Fig. 10.9 [Right]. The overall efficiency is not much impacted due to the low occupation of this region. A loss of efficiency is measured in the lower left part of the pixels area. This was caused by an unstable readout chip.

Fig. 10.10 shows the fully working **PMM_GEM_2011_2**. One can observe the inactive areas due to the 3 mm diameter spacers that maintain the GEM foil at 2 mm above the micro-mesh. The difference of background efficiency with PMM_GEM_2011_1 (see Tab. 10.5) is explained by the shorter shaping time used with PMM_GEM_2011_2.

The **PMM_BR_2011** has also shown a high efficiency, above 99.4%, even-though this detector was the first buried resistor Micromegas of this size ever produced. Only one inefficient area is observed in the pixel area (Fig. 10.11 [Left]) and it was expected from the PCB production feedback since some channels had been cut.

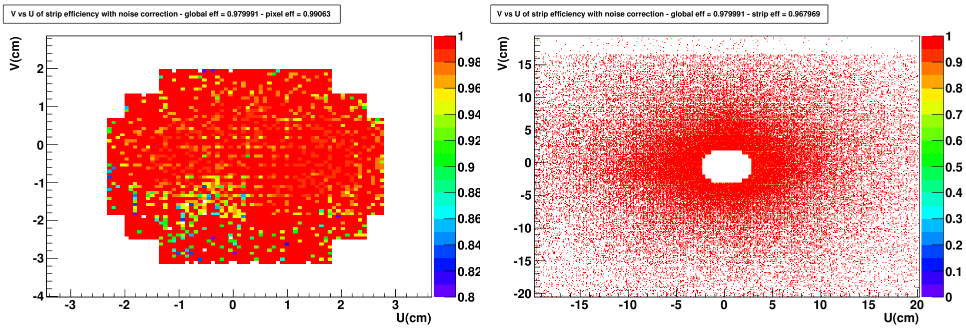

Figure 10.9: Map of the efficiency of the PMM_GEM_2011_1 prototype, [Left] pixelized area, [Right] strips.

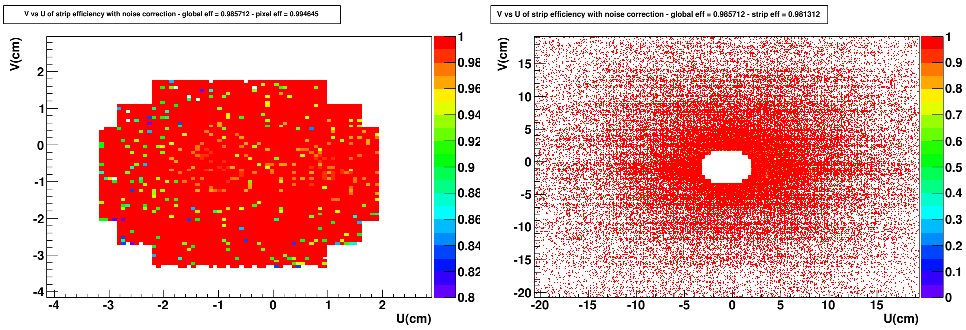

Figure 10.10: Map of the efficiency of the PMM_GEM_2011_2 prototype, [Left] pixelized area, [Right] strips.

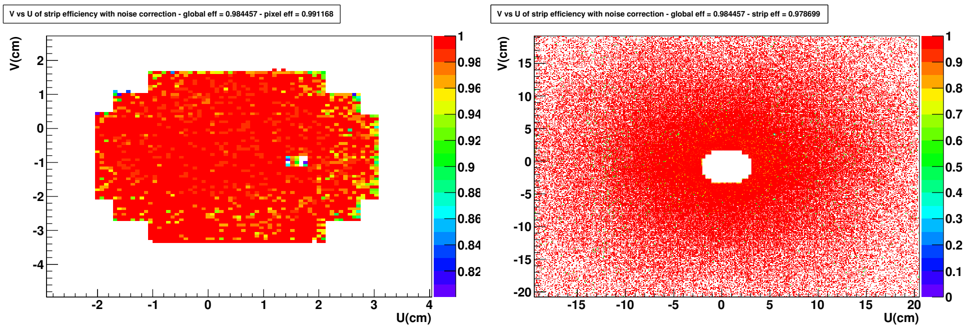

Figure 10.11: Map of the efficiency of the PMM_BR_2011 prototype, [Left] pixelized area, [Right] strips.

10.3.5 Spatial Resolution

The residual distribution of the detectors is obtained by histogramming the difference of position, projected on the measured coordinate, between detectors hits and selected tracks. The expected distribution is Gaussian with a constant background. The background is more important in the pixelized area due to higher occupancy. Therefore the number that will be retained to describe the pixel area residuals is the width of the Gaussian peak σ_{pix}. The function used to fit the pixelized area distribution is f_1:

$$f_1(x) = P_0 + A_{\text{pix}}.\exp(\frac{-(x-a)^2}{2\sigma^2_{\text{pix}}}) \tag{10.1}$$

with P_0 the amplitude of background, A_{pix} the height of the peak and a the center of the Gaussian distribution. To describe the residual distribution on the strips, another term is needed to fit the contribution of the two pitches of the strips. The function f_2 is used :

$$f_2(x) = P_1 + A_{\text{st1}}.\exp(\frac{-(x-a_1)^2}{2\sigma^2_{\text{st1}}}) + A_{\text{st2}}.\exp(\frac{-(x-a_2)^2}{2\sigma^2_{\text{st2}}}) \tag{10.2}$$

with A_{st1}, a_2 and σ_{st1} to describe the contribution of the 480 µm and A_{st2}, $a_2$and σ_{st2} for the 400 µm pitch. The number that is considered here as the width of residuals of the strips is the weighted mean of the two contributions:

$$\sigma_{\text{st}} = \frac{A_{\text{st1}}.\sigma_{\text{st1}} + A_{\text{st2}}.\sigma_{\text{st2}}}{A_{\text{st1}} + A_{\text{st2}}} \tag{10.3}$$

As explained in Sec. 2.7.6, the resolution of the characterized detector is obtained using the residual and the track error. Since the track resolution is not well known (it is estimated to be $\sim$ 70 µm in the strip area and $\sim$ 60 µm on pixels) for these recent data, only residuals will be presented. As a point of reference, we use the residuals of the Micromegas station 3 that is close to the prototype position. The standard Micromegas detectors are known [77] to have a spatial resolution better than 100 µm. In the same conditions, the MM03Y has a residual distribution of 158 µm. With a track resolution of 85 µm it gives a resolution of 134 µm. The MM03X that measures along the same coordinate than the prototypes has a 305 µm residual width [95]. This detector suffers from the fringe field of the spectrometer magnet (this effect does not affect the Y coordinate). It is expected that the Pixel Micromegas would have a residual width between the MM03X and MM03Y values. In pixelized area, the error on the track resolution is larger due to the lack of active tracking detector planes.

A local measurement of the resolution of the 20 cm strips, at 3 cm of the center of the detector, is done using the residual distribution over a 12 cm^2 area. This local measurement includes only one type of strips and does not suffer from the integration on the full active area. Several different positions have shown similar results. The difference in resolution between global and local includes the difference in pitch but mainly indicates the misalignment and/or non-flatness of the detectors.
Fig. 10.13 to 10.16 show the residuals distribution of the four prototypes, results are summarized in Tab. 10.6. Both **PMM_GEM_2011_1** and **PMM_GEM_2011_2** have shown $\sim$ 150 µm residuals equal or better than the standard COMPASS Micromegas (158 µm in the same conditions), even in the pixelized area.
Numerous dead zones of the **PMM_2010** deteriorate the resolution because of edge effects.
The **PMM_BR_2011** residual distribution is not fully understood. As with smaller prototypes (see Chap. 8), the spatial resolution of this detector seems to be 100 µm worse than for other prototypes. A different cluster algorithms, with a limitation on the cluster size to direct neighboring electrodes, lowered the residuals by 30 µm on pixels. This indicates that the classic weighted mean cluster algorithm is not optimal for these resistive technologies. Further investigation is needed, in particular on the measurement of the possible propagation of signals between resistive pads. The discrimination of signals induced by charge propagation in the resistive layers would drastically improve the

Detector	Strip global σ_{st}	Strip local σ_{st_loc}	Pixels σ_{pix}
PMM_2010	196.5	143.3	195.7
PMM_GEM_2011_1	149.0	110.5	153.5
PMM_GEM_2011_2	158.4	134.4	153.9
PMM_BR_2011	265.5	218.1	259.8

Table 10.6: Spatial residual of PMM, Values in microns from the fitted width of the residual distribution with $f_1(x)$, $f_2(x)$ from Eq. 10.1 and Eq. 10.2.

PMM_BR_2011 resolution.

Three effects have been identified that degrades this measurement:

Mechanical holding structure: The position of the detector plane is not well known inside the spectrometer, in particular because of the non-fixed support structure and the light non-flatness of the prototypes PCB board.

Clustering between strips and pixels: The clustering algorithm does not consider the information of both pixels and strips at the same time. If the charge created by a particle is shared between both zones, it will be reconstructed two times with missing information. A distortion of the residual appears at the interface of strips/pixels.

Cross-talk in time: Secondary peaks degrading the residual distribution are observed, see Fig. 10.12. These peaks correspond to a correlation of channels distant by several strips or pixels. The correlated channels are consecutive during the analog transmission between APVs and ADCs. Indeed the channels are multiplexed by the APV before being transmitted to the ADC. When the APVs and the ADCs are not perfectly synchronized, an influence of the amplitude of signal is observed from one channel to the next one. Therefore a correlation of non-consecutive channels on the PCB is observed.

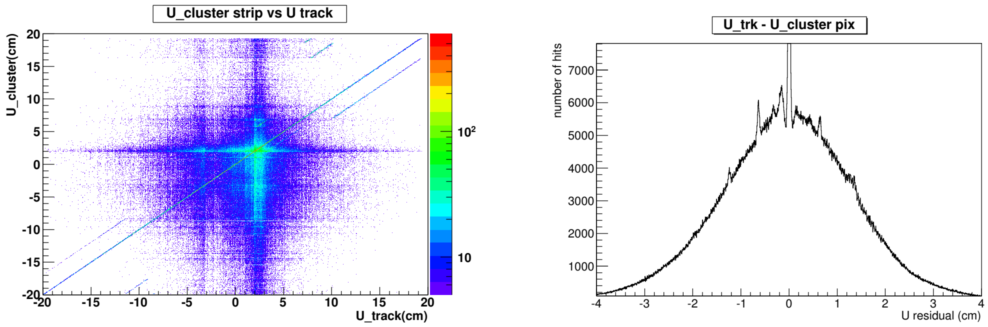

Figure 10.12: Effect of the cross-talk in time. [Left] Correlation of the position of the cluster and tracks. Non physical correlation appears on lines parallel to one to one correlation expected between cluster and tracks. [Right] Correlation peaks observed in the background of the residual distribution in the pixelized area.

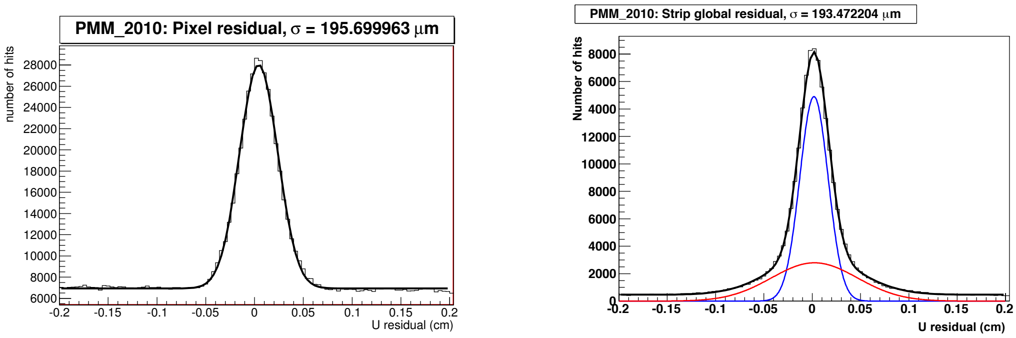

Figure 10.13: Spatial resolution of the PMM_2010 prototype, [Left] pixelized area, [Right] strips.

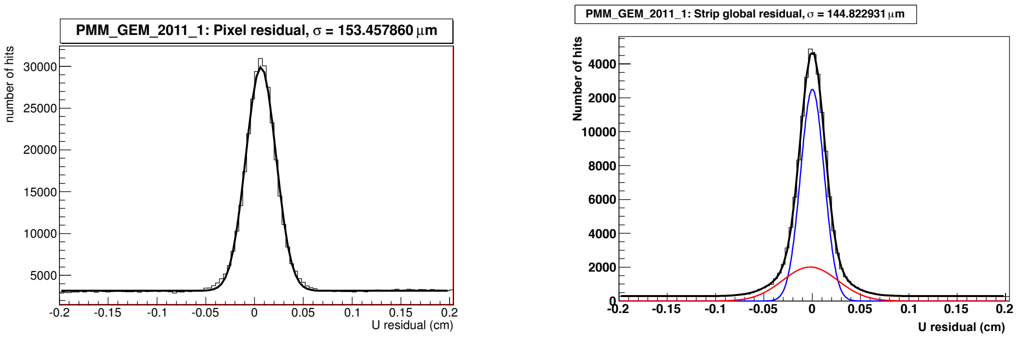

Figure 10.14: Spatial resolution of the PMM_GEM_2011_1 prototype, [Left] pixelized area, [Right] strips.

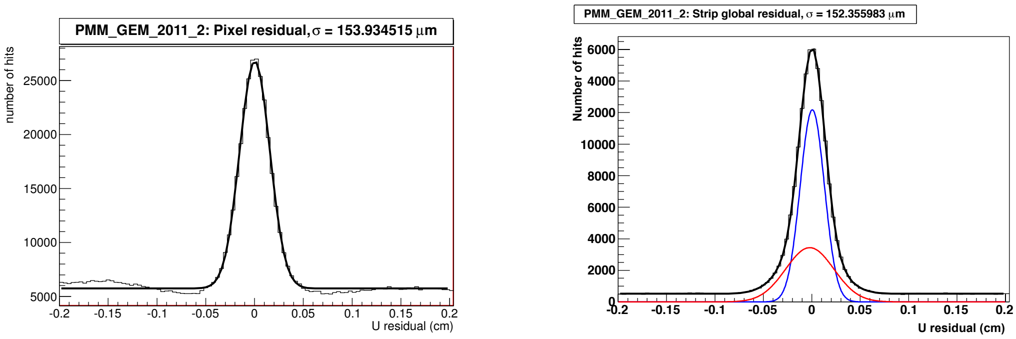

Figure 10.15: Spatial resolution of the PMM_GEM_2011_2 prototype, [Left] pixelized area, [Right] strips.

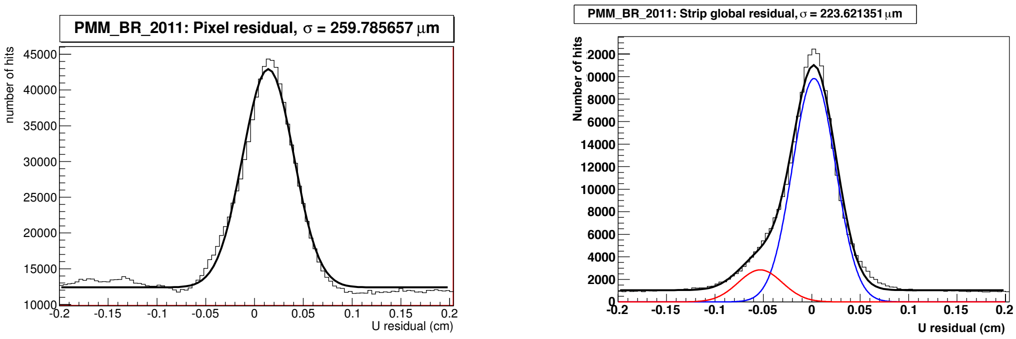

Figure 10.16: Spatial resolution of the PMM_BR_2011 prototype, [Left] pixelized area, [Right] strips.

10.3.6 Time Resolution

The time resolution of the Pixel Micromegas depends on the performances of the APV readout electronics. The trigger signal is synchronized on a 38.8 MHz global clock, produced by the COMPASS Trigger Control System (TCS). The APVs are also synchronized on the same clock. The time different between the trigger and the readout clock is called TCS phase, see Fig. 10.3. The timing information of signals is given by the ratio of the APV samples $r_{12} = a_1/a_2$. Indeed, for a given signal shape, r_{12} is known for a fixed time difference between a_1 and a_2, see Fig. 10.3. From the relation between this ratio and the TCS phase, one can calibrate the FEE in time, as in Fig. 10.17. The relation is supposed to be linear here.

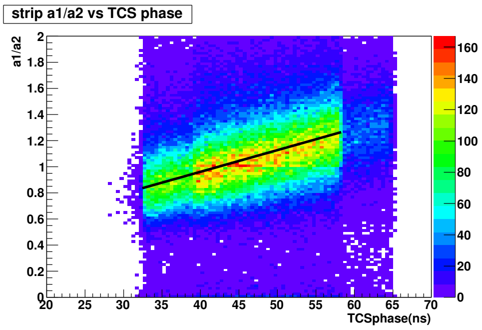

Figure 10.17: Time calibration of PMM_GEM_2011_2. The relation between the amplitude ratio of the APV samples a_1/a_2 and the trigger phase is fitted by the black line.

This calibration is not optimal and the presence of an important background makes the measurement difficult. Therefore several cuts are applied on the data to obtain the best defined tracks in time. Only tracks that are issued from a reconstructed primary vertex are selected. Their timing is well measured from the incoming particle. This is used to cancel the jitter on the trigger time introduced by the diversity of trigger related detectors. To reduce the background, only clusters in the road width around tracks, as in the efficiency computation, are considered. Since timing does not intervene in the track reconstruction, no bias is introduced by this mean, only background signals are rejected. These selections are illustrated in Fig. 10.18.

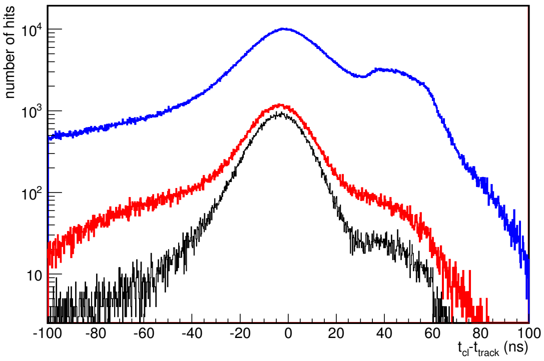

Figure 10.18: Effect of the different cuts on the time distribution of PMM_GEM_2011_2. The blue curve is the distribution with no selections on tracks. The red curve includes only the clusters inside the road width around the tracks. The black line corresponds to the same distribution when only tracks belonging to a primary vertex are considered.

The distributions are fitted with a Gaussian and the measured widths are summarized in Tab. 10.7. The shaping length is the APV signal duration in response to a pulse. In the same conditions, the standard Micromegas MM03Y and MM03X have a time residual of respectively 14.1 ns and 16.8 ns with a (negligible) track error below 1 ns [95].

Detector	Strips	Pixels	Shaping Length
PMM_GEM_2010	13.1	11.1	500 ns
PMM_GEM_2011_1	13.4	11.0	500 ns
PMM_GEM_2011_2	10.9	10.4	400 ns
PMM_BR_2011	22.6	21.0	400 ns

Table 10.7: Time residuals of PMM in ns.

Apart from PMM_BR_2011, these residuals, corresponding to the figures from Fig. 10.19 to 10.22, have better values for the standard Micromegas in the same conditions, and similar to Pixel GEM detectors [61] that have a more elaborate time reconstruction. In particular a secondary peak appears on the time distribution of the pixels. This is coming from background hits that are at the edge of the expected time window. The non linearity of the relation between r_{12} and the TCS phase, applied to these background hits, creates a fake peak in the distribution. A more complex calibration algorithm would improve these distributions and the correction of crosstalk in time (as mentioned in Sec. 10.3.5) could improve the time performances.

An improvement of 3 ns is obtained between **PMM_GEM_2011_1** and **PMM_GEM_2011_2** thanks to the influence of the shorter shaping length (400 ns instead of 500 ns).

The timing behavior of **PMM_BR_2011** is not fully understood and further analysis is needed to explain the worse time resolution of this technology. Again, this analysis suggests a possible time propagation of signals between resistive pads.

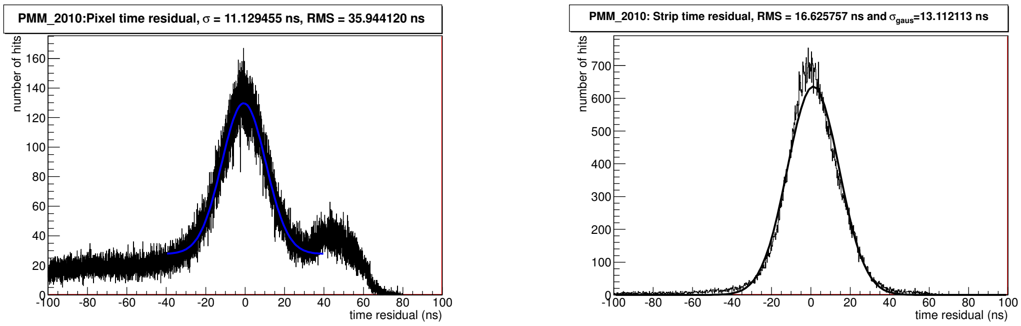

Figure 10.19: Time residual of the PMM_2010 prototype, [Left] pixelized area, [Right] strips. The APV shaping length is 500 ns.

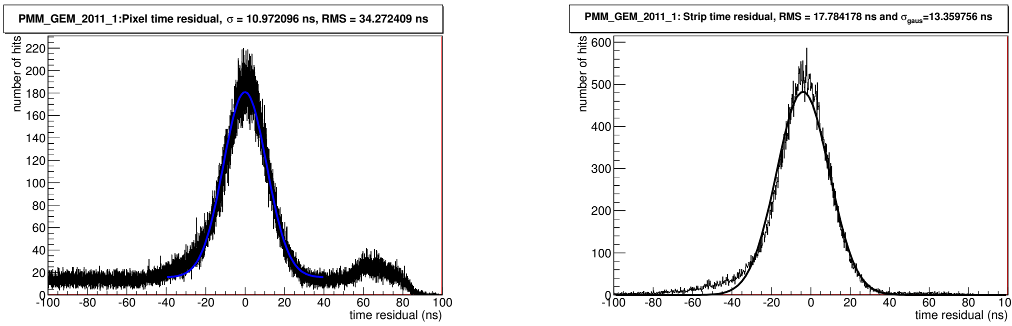

Figure 10.20: Time residual of the PMM_GEM_2011_1 prototype, [Left] pixelized area, [Right] strips. The APV shaping length is 500 ns.

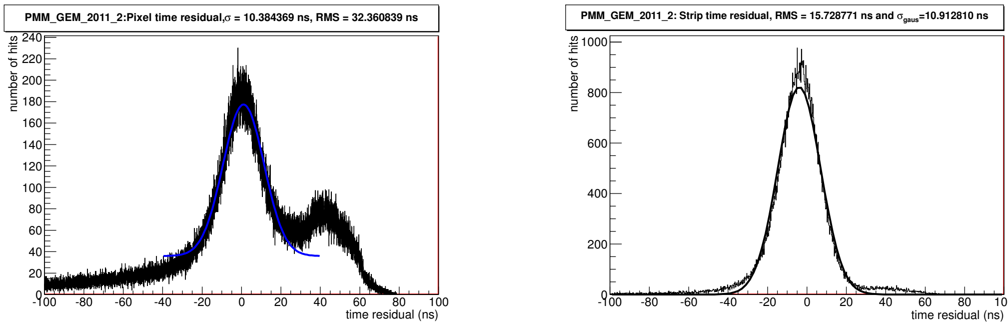

Figure 10.21: Time residual of the PMM_GEM_2011_2 prototype, [Left] pixelized area, [Right] strips. The APV shaping length is 400 ns.

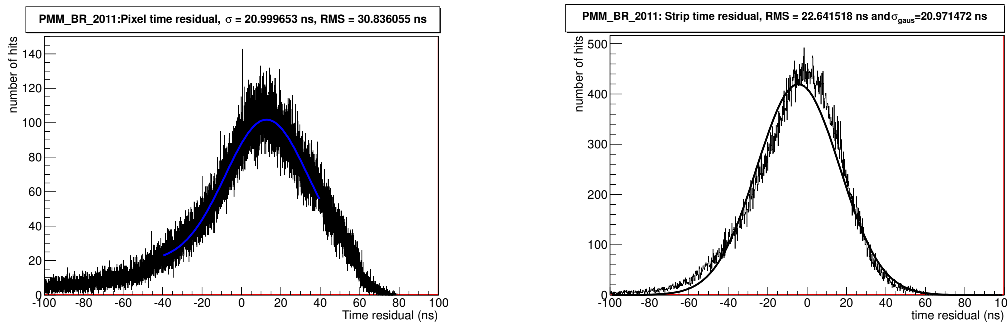

Figure 10.22: Time residual of the PMM_BR_2011 prototype, [Left] pixelized area, [Right] strips. The APV shaping length is 400 ns.

10.4 Outlook of the Development of the Pixel Micromegas

In 2010 the Pixel Micromegas tests began at COMPASS with a highly segmented bulk Micromegas operating with the APV front-end electronics. This electronics has been optimized to the large detector capacitance and the Micromegas protection circuit. The bulk technology greatly improves the detector solidity without degrading the performances. With the PMM_2010, the Pixel Micromegas design has proved to be adapted to the non-homogeneous particle flux distribution at COMPASS. Using this base, the discharge rate reduction technologies, which have emerged from the R&D described in Chap. 8, have been characterized with full scale prototypes in COMPASS environment.

Two Pixel Micromegas prototypes with GEM pre-amplification have demonstrated great rate capabilities. Efficiencies up to 99% in the pixel area has been observed within a beam of $2.2 \times 10^8 \mu$/spill. These detectors have shown better residual distributions of ~ 150 µm than standard chambers in the same conditions (~ 160 µm). This is explained by the diffusion induced by the GEM pre-amplification that enlarges the cluster size and eases the COG reconstruction. This has been confirmed with microscopic simulations of this detector in Chap. 9. This study has also explained how the electron extraction of the GEM and the electron transparency of the micro-mesh cancel each others for transfer field between 300 to 900 V/mm. This effect provides a safe operating field configuration where the gain of the detectors does not depend on the mechanical holding of the GEM foil. A time resolution of $\sim$ 11 ns and a material budget of 0.4% radiation length (optimizable in the final design) complete the requirements of COMPASS-II. The combination of Micromegas and GEM is a concept optimized for high-rate experiment with a discharge probability down to 10^{-7}, a moderate cluster size that allowed high segmentation, moderate thickness and low material budget. This concept has a great potential as a precise tracking detector for intense particle flux.

The first large resistive Micromegas embedding buried resistors has been built using the Pixel Micromegas design. This detector has shown to be fully efficient whereas its spatial and time residuals, of respectively ~ 250 µm and ~ 20 ns, do not reach the requirements. It is believed that further study on signal propagation could drastically improve these performances. Nevertheless this single stage amplification discharge free detector has a great potential. The evacuation of charges through the readout electrodes allows large design with pixels. Moreover the monolithic structure is very stable and compatible with PCB production processes. These advantages made of the Buried Resistor a simple reliable detector that could democratize Micromegas detectors outside of physics experiments.

The final choice of technology for the COMPASS-II Pixel Micromegas is still open. Either way this detector will match the requirements and improve the spectrometer resolution, in particular in the VSAT region.

Chapter 11

Conclusion

The work presented here shows the efforts in developing the next generation of Micro-Pattern Gas Detectors for charged particle tracking in high-rate experiments.

The replacement of MWPCs by GEMs for the gaseous amplification in a TPC has proved to be a promising option. A GEM-TPC test chamber with triple GEM readout of $10 \times 10\,\mathrm{cm}^2$ and hexagonal pad readout has been built. The AFTER front-end electronics, designed for MPGDs, has been optimized for GEM readout. Very good noise performance of 625 e^- has been obtained. A tracking telescope composed of 4 silicon planes and 2 GEM detectors has been installed on a test bench to characterize the chamber. The test bench with the TPC has first been commissioned using an electron beam of the ELSA facility. Then it has been relocated to CERN for precision measurement with highly energetic muons. The commissioning of this small experiment and the related analysis constitute a sizable part of this work. It has resulted in the measurement of un-bias spatial residuals of $\sim 210\,\mu\mathrm{m}$, both along the readout coordinate and along the drift coordinate. Using the internal tracking capability of the chamber, residuals of $170\,\mu\mathrm{m}$ were measured with hexagonal pads of 1.25 mm radius, and residuals of $200\,\mu\mathrm{m}$ with pads of 1.5 mm. Optimizations of the reconstruction algorithms improved the performances, in particular the energy resolution from 50% to 5.1% for the 41.5 KeV ray of krypton in a larger prototype. Algorithms for improving the time reconstruction have been proposed, but experimental data with the necessary time synchronization are needed to choose a method.

The symmetric shape of the pads associated with a powerful analysis framework allows the reconstruction of various of track topologies that qualifies the GEM-TPC as a general-purpose detector. As a result, a 60 cm drift length detector has been built and operated in the FOPI experiment at GSI with good performances. The installation of a second prototype is foreseen at Crystal Barrel experiment at ELSA for 2013. The success of the GEM-TPC will certainly continue since the ALICE collaboration has recently shown its interest for an upgrade of its TPC with GEMs, aiming at higher trigger rates.

The conditions at the future COMPASS-II experiment imposed to rethink the Micromegas tracking detectors, in particular in terms of rate capability and discharge probability. The fast APV based readout has been successfully integrated and adapted to the large capacitance of the Pixel Micromegas to stand rates of 50 $\mathrm{MHz/cm}^2$. With a beam of 1.5×10^7 hadrons/spill, a rate of 0.3 discharge/spill has been measured. An important effort in discharge impact reduction in Micromegas led to the construction and characterization of a dozen of $10 \times 6\,\mathrm{cm}^2$ strips detectors embedding a variety of new concepts. Two possible solutions emerged from the study of these detectors during two test beam periods at CERN.

The first one where a GEM foil is used as a pre-amplification stage combines the advantage of GEM and Micromegas. The combined effects of gain sharing and increased diffusion reduce the discharge rate by a factor of 100 in operating conditions. The larger diffusion improves the spatial resolution, down to 60 µm compared to the 90 µm of standard detectors. Simulations at the microscopic level based on GARFIELD and MAGBOLTZ have revealed the influence of the field between the GEM foil and the micro-mesh. Full scale COMPASS detectors of $40 \times 40\,\mathrm{cm}^2$ confirmed the potential of this concept with spatial residuals of $\sim 150\,\mu$m and time residuals of ~ 11 ns. The full efficiency of 99%, including the beam region, is reached. The modest material budget of less than 0.4% of radiation length completes the requirement for COMPASS-II. A doublet of PMM+GEM prototypes is already installed in the spectrometer for the 2012 run.

The second solution consists in the implementation on the readout of resistive structures that deeply reduce discharge amplitudes. The innovating Buried Resistor scheme has proved to be have an efficiency close to 100%. However the spatial resolution of 120 µm for small detectors and 250 µm residual for COMPASS format has still to be improved. Nevertheless this single stage amplification, discharge free, gaseous detector has the great advantage to be a monolithic detector and compatible with industrial PCB production. In addition its flexibility opens the door of a wide range of applications. The characterization of the first large scale prototype is an important step.

The choice for COMPASS-II is still opened and the Pixel Micromegas will fulfill the requirements and improve the spectrometer performances, in particular in the beam area.

Through the characterizations of numerous different MPGDs, this work has shown the great potential of these developing technologies. The MPGDs are now being considered in almost all new experiments, confirming the prediction of G. Charpak when he stated that the MPGDs would revolutionize experimental physics the same way the MWPCs did.

Bibliography

[1] E. Rutherford and H. Geiger, "An electrical method of counting the number of α-particles from radio-active substances," *Proceedings of the Royal Society of London. Series A, Containing Papers of a Mathematical and Physical Character*, vol. 81, no. 546, pp. 141 – 161, 1908.

cited on page 3.

[2] H. Geiger and O. Klemperer, "Beitrag zur Wirkungsweise des Spitzenzählers," *Zeitschrift für Physik A Hadrons and Nuclei*, vol. 49, pp. 753–760, 1928. 10.1007/BF01328628.

cited on page 3.

[3] P. Galison, *How Experiments End*. University Of Chicago Press; First edition (October 15, 1987), 2002.

cited on page 4.

[4] F. Sauli, *Seminal Papers by Georges Charpak*. Elsevier, Nuclear Instruments and Methods in Physics Research Section A: Accelerators, Spectrometers, Detectors and Associated Equipment, 2011.

cited on pages 4 and 5.

[5] H. Spieler, "Introduction to radiation detectors and electronics." `http://www-physics.lbl.gov/~spieler/physics_198_notes_1999/`, 1999.

cited on pages 4, 12, and 16.

[6] F. Angelini, R. Bellazzini, M. Bozzo, A. Brez, M. Massai, R. Raffo, G. Spandre, M. Spezziga, and A. Toropin, "A large area, high gain Micro Gap Chamber," *Nuclear Instruments and Methods in Physics Research Section A: Accelerators, Spectrometers, Detectors and Associated Equipment*, vol. 362, no. 2-3, pp. 273 – 276, 1995.

cited on pages 4 and 6.

[7] Y. Giomataris, P. Rebourgeard, J. Robert, and G. Charpak, "Micromegas: a high-granularity position-sensitive gaseous detector for high particle-flux environments," *Nuclear Instruments and Methods in Physics Research Section A: Accelerators, Spectrometers, Detectors and Associated Equipment*, vol. 376, no. 1, pp. 29 – 35, 1996.

cited on page 5.

[8] F. Sauli, "GEM: A new concept for electron amplification in gas detectors," *Nuclear Instruments and Methods in Physics Research Section A: Accelerators, Spectrometers, Detectors and Associated Equipment*, vol. 386, no. 2-3, pp. 531 – 534, 1997.

cited on page 5.

[9] "RD51 proposal - final version." `http://rd51-public.web.cern.ch/rd51-public/Documents/RD51Proposal_21082008.pdf`, 2008.

cited on page 5.

[10] "The continuing rise of micropattern detectors." `http://cerncourier.com/cws/article/cern/41011`, 2009.

cited on page 5.

[11] K. Bernier, "Étude du comportement de détecteurs gazeux à micro-pistes MSGC sous irradiation intense de neutrons rapides." `http://cp3.irmp.ucl.ac.be/upload/theses/phd/bernier.pdf`. PhD thesis, 2001. Université catholique de Louvain (UCL).

cited on page 6.

[12] V. Karimäki, *The CMS tracker system project: Technical Design Report.* Technical Design Report CMS, Geneva: CERN, 1997.

cited on page 6.

[13] A. Ochi, Y. Homma, T. Dohmae, H. Kanoh, T. Keika, S. Kobayashi, Y. Kojima, S. Matsuda, K. Moriya, A. Tanabe, and K. Yoshida, "A new MPGD design: Micro-mesh micro-pixel chamber," *Nuclear Instruments and Methods in Physics Research Section A: Accelerators, Spectrometers, Detectors and Associated Equipment*, vol. 604, no. 1-2, pp. 11 – 14, 2009. PSD8 Proceedings of the 8th International Conference on Position Sensitive Detectors.

cited on page 6.

[14] S. Biagi, J. Bordas, D. Duxbury, E. Gabathuler, T. Jones, and S. Kiourkos, "First experimental results from a microdot gas avalanche detector integrated onto a silicon wafer," *Nuclear Instruments and Methods in Physics Research Section A: Accelerators, Spectrometers, Detectors and Associated Equipment*, vol. 366, no. 1, pp. 76 – 78, 1995.

cited on page 6.

[15] A. Ochi, Y. Homma, M. Inoue, S. Kobayashi, K. Miyazaki, A. Tanabe, and Y. Takayama, "Development of Micro-Mesh Micro-Pixel Chamber," *Journal of Instrumentation*, vol. 4, no. 12, p. P12014, 2009.

cited on page 7.

[16] I. Giomataris, R. D. Oliveira, S. Andriamonje, S. Aune, G. Charpak, P. Colas, G. Fanourakis, E. Ferrer, A. Giganon, P. Rebourgeard, and P. Salin, "Micromegas in a bulk," *Nuclear Instruments and Methods in Physics Research Section A: Accelerators, Spectrometers, Detectors and Associated Equipment*, vol. 560, no. 2, pp. 405 – 408, 2006.

cited on page 7.

[17] A. Delbart, "Production and calibration of 9m^2 of bulk-micromegas detectors for the readout of the ND280/TPCs of the T2K experiment," *Nuclear Instruments and Methods in Physics Research Section A: Accelerators, Spectrometers, Detectors and Associated Equipment*, vol. 623, no. 1, pp. 105 – 107, 2010. 1st International Conference on Technology and Instrumentation in Particle Physics.

cited on page 7.

[18] H. van der Graaf, "GridPix: An integrated readout system for gaseous detectors with a pixel chip as anode," *Nuclear Instruments and Methods in Physics Research Section A: Accelerators, Spectrometers, Detectors and Associated Equipment*, vol. 580, no. 2, pp. 1023 – 1026, 2007. Imaging 2006 Proceedings of the 3rd International Conference on Imaging Techniques in Subatomic Physics, Astrophysics, Medicine, Biology and Industry.

cited on page 9.

[19] F. Sauli, "GASEOUS DETECTORS FUNDAMENTS, *EDIT School 2011*." `http://edit2011.web.cern.ch/edit2011/`, 2011.

cited on pages 9, 15, and 28.

[20] J. Maia, D. Mormann, A. Breskin, R. Chechik, J. Veloso, and J. dos Santos, “Progress in MHSP electron multiplier operation,” *Nuclear Science, IEEE Transactions on*, vol. 51, pp. 1503 – 1508, aug. 2004.

cited on page 10.

[21] A. Breskin, R. Alon, M. Cortesi, R. Chechik, J. Miyamoto, V. Dangendorf, J. Maia, and J. D. Santos, “A concise review on THGEM detectors,” *Nuclear Instruments and Methods in Physics Research Section A: Accelerators, Spectrometers, Detectors and Associated Equipment*, vol. 598, no. 1, pp. 107 – 111, 2009. Instrumentation for Collding Beam Physics Proceedings of the 10th International Conference on Instrumentation for Colliding Beam Physics.

cited on page 10.

[22] N. McConkey, G. Barker, A. Bennieston, P. Harrison, P. Lightfoot, B. Morgan, D. Stewart, N. Spooner, and Y. Ramachers, “Optical Readout Technology for Large Volume Liquid Argon Detectors,” *Nuclear Physics B - Proceedings Supplements*, vol. 215, no. 1, pp. 255 – 257, 2011. Proceedings of the 12th Topical Seminar on Innovative Particle and Radiation Detectors (IPRD10).

cited on page 10.

[23] A. Di Mauro, B. Lund-Jensen, P. Martinengo, E. Nappi, V. Peskov, L. Periale, P. Picchi, F. Pietropaolo, and I. Rodionov, “A new gem-like imaging detector with electrodes coated with resistive layers,” *Nuclear Science Symposium Conference Record, 2006. IEEE*, vol. 6, pp. 3852 – 3859, 29 2006-nov. 1 2006.

cited on page 10.

[24] G. Charpak, P. Benaben, P. Breuil, P. Martinengo, E. Nappi, and V. Peskov, “Progress in the development of a S-RETGEM-based detector for an early forest fire warning system,” *Journal of Instrumentation*, vol. 4, no. 12, p. P12007, 2009.

cited on page 10.

[25] W. Blum, W. Riegler, and L. Rolandi, *Particle Detection with Drift Chambers*. Particle Acceleration and Detection, Springer, 2008.

cited on page 12.

[26] W. R. Leo, *Techniques for nuclear and particle physics experiments: a how-to approach*. Springer, 1994.

cited on pages 12, 14, 18, 37, 39, and 93.

[27] A. Sharma, “Properties of some gas mixtures used in tracking detectors.” SLAC-J-ICFA-16-3.

cited on page 13.

[28] M. Titov, “Gaseous Detectors: recent developments and applications.” `http://adsabs.harvard.edu/abs/2010arXiv1008.3736T`, 2010. ArXiv e-prints.

cited on page 14.

[29] H. Raether, *Electron avalanches and breakdown in gases*. London: Butterworths, 1964.

cited on page 15.

[30] I. Giomataris, “Development and prospects of the new gaseous detector, “Micromegas”,” *Nuclear Instruments and Methods in Physics Research Section A: Accelerators, Spectrometers, Detectors and Associated Equipment*, vol. 419, no. 2-3, pp. 239 – 250, 1998.

cited on page 15.

[31] H. Genz, "Single electron detection in proportional gas counters," *Nuclear Instruments and Methods*, vol. 112, no. 1-2, pp. 83 – 90, 1973.

cited on page 15.

[32] S. Ramo, "Currents induced by electron motion," *Proceedings of the IRE*, vol. 27, pp. 584 – 585, Sept. 1939.

cited on page 15.

[33] R. Veenhof, "Garfield, recent developments," *Nuclear Instruments and Methods in Physics Research Section A: Accelerators, Spectrometers, Detectors and Associated Equipment*, vol. 419, no. 2-3, pp. 726 – 730, 1998.

cited on pages 15, 17, and 112.

[34] V. Radeka, "Low-noise techniques in detectors," *Annual Review of Nuclear and Particle Science*, vol. 38, no. 1, pp. 217–277, 1988.

cited on page 18.

[35] C. Grupen and B. Shwartz, *Particle Detector, Second Edition.* Cambridge University Press, 2008.

cited on pages 18, 22, 33, 34, 35, and 36.

[36] V. Radeka, "Detector signal processing, ieee short course on integrated circuit front-end electronics," 2009.

cited on pages 18 and 34.

[37] E. Delagnes, P. Abbon, Y. Bedfer, J. Faivre, F. Kunne, A. Magnon, S. Platchkov, P. Rebourgerad, and D. Thers, "SFE16, a low noise front-end integrated circuit dedicated to the read-out of large micromegas detectors," *Nuclear Science, IEEE Transactions on*, vol. 47, pp. 1447–1453, aug 2000.

cited on pages 18 and 20.

[38] M. French, L. Jones, Q. Morrissey, A. Neviani, R. Turchetta, J. Fulcher, G. Hall, E. Noah, M. Raymond, G. Cervelli, P. Moreira, and G. Marseguerra, "Design and results from the APV25, a deep sub-micron CMOS front-end chip for the cms tracker," *Nuclear Instruments and Methods in Physics Research Section A: Accelerators, Spectrometers, Detectors and Associated Equipment*, vol. 466, no. 2, pp. 359 – 365, 2001. 4th Int. Symp. on Development and Application of Semiconductor Tracking Detectors.

cited on pages 18, 21, 123, and 124.

[39] P. Baron, D. Calvet, E. Delagnes, X. de la Broise, A. Delbart, F. Druillole, E. Mazzucato, E. Monmarthe, F. Pierre, and M. Zito, "AFTER, an ASIC for the Readout of the Large T2K Time Projection Chambers," *Nuclear Science, IEEE Transactions*, vol. 55, pp. 1744 –1752, june 2008.

cited on pages 18, 20, 21, 47, and 52.

[40] B. Grube, "The trigger control system and the common GEM and silicon readout for the COMPASS experiment," Master's thesis, Technische Universität München, 2001.

cited on pages 19 and 123.

[41] L. L. Jones, M. J. French, Q. Morrissey, A. Neviani, M. Raymond, G. Hall, P. Moreira, and G. Cervelli, "The APV25 deep submicron readout chip for CMS detectors," *CCLRC ePublication Archive [http://epubs.cclrc.ac.uk/oai] (United Kingdom)*, 1999.

cited on page 20.

[42] E. Delagnes, "Recent front-end ASICs developments,," tech. rep., RIKEN, January 2011.

cited on page 21.

[43] R. Turchetta, “Spatial resolution of silicon microstrip detectors,” *Nuclear Instruments and Methods in Physics Research Section A: Accelerators, Spectrometers, Detectors and Associated Equipment*, vol. 335, no. 1-2, pp. 44 – 58, 1993.

cited on pages 25, 26, and 106.

[44] J. Manjarrés *et al.*, “Performances of anode-resistive Micromegas for HL-LHC environment, *MPGD 2011, Kobe, Japan*,” 2011.

cited on pages 26 and 95.

[45] P. Fonte, V. Peskov, and B. Ramsey, “The fundamental limitations of high-rate gaseous detectors,” *Nuclear Science, IEEE Transactions on*, vol. 46, pp. 321 –325, jun 1999.

cited on pages 27 and 28.

[46] P. Fonte and V. Peskov, “On the physics and technology of gaseous particle detectors,” *Plasma Sources Science and Technology*, vol. 19, no. 3, p. 034021, 2010.

cited on page 27.

[47] E. Marode, “The mechanism of spark breakdown in air at atmospheric pressure between a positive point and a plane. I. Experimental: Nature of the streamer track,” *JAPIAU*, vol. 46, no. 5, pp. 2005–2015, 1975.

cited on pages 27 and 28.

[48] K. Nakamura *et al.*, “Review of Particle Physics,” *Journal of Physics G*, vol. 37, pp. 1+, 2010.

cited on pages 28, 34, 35, and 65.

[49] F. Sauli, L. Ropelewski, and P. Everaerts, “Ion feedback suppression in time projection chambers,” *Nuclear Instruments and Methods in Physics Research Section A: Accelerators, Spectrometers, Detectors and Associated Equipment*, vol. 560, no. 2, pp. 269 – 277, 2006.

cited on pages 29 and 96.

[50] P. Colas, I. Giomataris, and V. Lepeltier, “Ion backflow in the micromegas tpc for the future linear collider,” *Nuclear Instruments and Methods in Physics Research Section A: Accelerators, Spectrometers, Detectors and Associated Equipment*, vol. 535, no. 1-2, pp. 226 – 230, 2004. Proceedings of the 10th International Vienna Conference on Instrumentation.

cited on page 29.

[51] C. Bernet, *Caractérisation des Micromégas et mesure de la polarisation des gluons sur COMPASS*. PhD thesis, Université Paris 7, 2004.

cited on page 32.

[52] J. Bouchez, D. Burke, C. Cavata, P. Colas, X. D. L. Broise, A. Delbart, A. Giganon, I. Giomataris, P. Graffin, J.-P. Mols, F. Pierre, J.-L. Ritou, A. Sarrat, E. Virique, M. Zito, E. Radicioni, R. D. Oliveira, J. Dumarchez, N. Abgrall, P. Bene, A. Blondel, A. Cervera, D. Ferrere, F. Maschiocchi, E. Perrin, J.-P. Richeux, R. Schroeter, G. Jover, T. Lux, A. Rodriguez, and F. Sanchez, “Bulk micromegas detectors for large TPC applications,” *Nuclear Instruments and Methods in Physics Research Section A: Accelerators, Spectrometers, Detectors and Associated Equipment*, vol. 574, no. 3, pp. 425 – 432, 2007.

cited on page 38.

[53] M. Ball *et al.*, “Development of a Large GEM TPC Prototype for the PANDA Central Tracker,” *Preprint submitted to Nuclear Instruments and Methods in Physics Research Section A*, 2011.

cited on page 40.

[54] P. Schade and J. Kaminski, "A large TPC prototype for a linear collider detector," *Nuclear Instruments and Methods in Physics Research Section A: Accelerators, Spectrometers, Detectors and Associated Equipment*, vol. 628, no. 1, pp. 128 – 132, 2011. Proceedings of the 12th International Vienna Conference on Instrumentation.

cited on page 41.

[55] F. Haas, "Design and Commissioning of a General Purpose Triple GEM and Installation of a GEM Tracking Detector at COMPASS," 2011. Diploma Thesis, Technische Universität München.

cited on pages 41 and 43.

[56] Q. Weitzel, F. Böhmer, C. Höppner, T. Huber, B. Ketzer, I. Konorov, A. Mann, S. Neubert, S. Paul, and C. Simonetto, "Development of a high-rate GEM-based TPC for PANDA," in *Nuclear Science Symposium Conference Record, 2007. NSS '07. IEEE*, vol. 1, pp. 227 –233, 26 2007-nov. 3 2007.

cited on page 42.

[57] C. Höppner, *First Measurement of the Cross Section for the Production of Hadrons with High Transverse Momenta at COMPASS, and Developments for Particle Tracking in High-Rate Experiments.* PhD thesis, Technische Universität München, 2012.

cited on pages 44 and 75.

[58] K. Abe *et al.*, "The T2K experiment," *Nuclear Instruments and Methods in Physics Research Section A: Accelerators, Spectrometers, Detectors and Associated Equipment*, vol. 659, no. 1, pp. 106 – 135, 2011.

cited on page 47.

[59] E. Delagnes, "Pulse Shapes of the AFTER ASIC," 2007. CEA internal note, SEDI.

cited on pages 48 and 49.

[60] P. Baron and E. Delagnes, "After data sheet version 1.1," 2008. CEA internal note, SEDI.

cited on page 53.

[61] S. Uhl, "Construction and commissioning of the PixelGEM tracking system for the COMPASS experiment." `http://www.e18.physik.tu-muenchen.de/publications/thesis/diploma_suhl.pdf`, 2008. Diploma Thesis, Technische Universität München.

cited on pages 53, 122, and 134.

[62] R. Schmitz, "Phd thesis in preparation." Rheinischen Friedrich-Wilhelms Universität Bonn.

cited on pages 57 and 58.

[63] C. A. D. group, "ALICE DATE User's Guide." `www.if.pw.edu.pl/~janik/documents/date_v3.7.pdf.gz`, 2007.

cited on page 63.

[64] A. Winnebeck, *Design Studies for a Tracking Upgrade of the Crystal Barrel Experiment at ELSA and Installation of a Tracking Test Bench.* PhD thesis, Rheinischen Friedrich-Wilhelms Universität Bonn, 2009.

cited on pages 63 and 64.

[65] S. Dørheim, "Track Reconstruction in a Setup for the Characterization of a GEM-TPC at ELSA," 2009. Diploma Thesis, Technische Universität München.

cited on pages 64 and 65.

[66] A. Lazzaro and L. Moneta, "MINUIT package parallelization and applications using the RooFit package," *Journal of Physics: Conference Series*, vol. 219, no. 4, p. 042044, 2010.

cited on pages 67 and 101.

[67] C. Höppner, S. Neubert, B. Ketzer, and S. Paul, "A novel generic framework for track fitting in complex detector systems," *Nuclear Instruments and Methods in Physics Research Section A: Accelerators, Spectrometers, Detectors and Associated Equipment*, vol. 620, no. 2-3, pp. 518 – 525, 2010.

cited on page 72.

[68] P. Abbon *et al.*, "The COMPASS experiment at CERN," *Nuclear Instruments and Methods in Physics Research Section A: Accelerators, Spectrometers, Detectors and Associated Equipment*, vol. 577, no. 3, pp. 455 – 518, 2007.

cited on pages 75 and 79.

[69] N. Makke, *Measurement of the polarization of strange quark in the nucleon and determination of quark fragmentation functions into hadrons.* PhD thesis, Université Paris SUD-XI, 2011.

cited on pages 75 and 77.

[70] F. Gautheron, "COMPASS-II proposal," Tech. Rep. CERN-SPSC-2010-014. SPSC-P-340, CERN, Geneva, May 2010.

cited on pages 76 and 85.

[71] P. Abbon *et al.*, "The COMPASS setup for physics with hadron beam." (To be published).

cited on pages 76, 77, and 79.

[72] B. Ketzer, A. Austregesilo, F. Haas, I. Konorov, M. Kramer, A. Mann, T. Nagel, and S. Paul, "A triple-GEM Detector with pixel readout for high-rate beam tracking in COMPASS," *Nuclear Science Symposium Conference Record, 2007. NSS '07. IEEE*, vol. 1, pp. 242 –244, 26 2007-nov. 3 2007.

cited on page 78.

[73] G. Barouch and G. Puill, "Garfield manual." `http://consult.cern.ch/writeup/garfield/examples/mm/Welcome.html`.

cited on page 81.

[74] G. Puill and B. Tamain, *Le developpement de Micromegas, un nouveau detecteur gazeux de position Ĺ microgrille. oai:cds.cern.ch:466540.* PhD thesis, Caen Univ., Saclay, 2000.

cited on page 81.

[75] V. B. Carballo, C. Salm, S. Smits, J. Schmitz, M. Chefdeville, H. van der Graaf, J. Timmermans, and J. Visschers, "On the geometrical design of integrated micromegas detectors," *Nuclear Instruments and Methods in Physics Research Section A: Accelerators, Spectrometers, Detectors and Associated Equipment*, vol. 576, no. 1, pp. 1 – 4, 2007.

cited on pages 81 and 112.

[76] I. Krajcar Bronic and B. Grosswendt, "Townsend ionization coefficients of some argon-based mixtures in strong nonuniform electric fields," *Journal of Applied Physics*, vol. 88, pp. 6192 – 6200, dec 2000.

cited on page 82.

[77] D. Thers, *Développement du détecteur gazeux Micromégas pour l'expérience COMPASS.* PhD thesis, Université Blaise-Pascal, 2000.

cited on pages 83, 99, and 130.

[78] F. Thibaud, "Développement de détecteurs à microstructure "MicroMeGas" pour les très hauts flux de particules," 2011. Rapport de Projet de Fin d'Études, Grenoble-INP Phelma.

cited on page 90.

[79] S. Bachmann, A. Bressan, M. Capens, M. Deutel, S. Kappler, B. Ketzer, A. Polouektov, L. Ropelewski, F. Sauli, E. Schulte, L. Shekhtman, and A. Sokolov, "Discharge studies and prevention in the gas electron multiplier (GEM)," *Nuclear Instruments and Methods in Physics Research Section A: Accelerators, Spectrometers, Detectors and Associated Equipment*, vol. 479, no. 213, pp. 294 – 308, 2002.

cited on page 90.

[80] D. Neyret, M. Anfreville, Y. Bedfer, E. Burtin, N. d'Hose, A. Giganon, B. Ketzer, I. Konorov, F. Kunne, A. Magnon, C. Marchand, B. Paul, S. Platchkov, and M. Vandenbroucke, "New pixelized micromegas detector for the COMPASS experiment," *Journal of Instrumentation*, vol. 4, no. 12, p. P12004, 2009.

cited on page 94.

[81] T. Alexopoulos, J. Burnens, R. de Oliveira, G. Glonti, O. Pizzirusso, V. Polychronakos, G. Sekhniaidze, G. Tsipolitis, and J. Wotschack, "A spark-resistant bulk-micromegas chamber for high-rate applications," *Nuclear Instruments and Methods in Physics Research Section A: Accelerators, Spectrometers, Detectors and Associated Equipment*, vol. 640, no. 1, pp. 110 – 118, 2011.

cited on page 95.

[82] K. Nikolopoulos, P. Bhattacharya, V. Chernyatin, and R. Veenhof, "Electron transparency of a micromegas mesh," *Journal of Instrumentation*, vol. 6, no. 06, p. P06011, 2011.

cited on page 96.

[83] C. Adloff, D. Attié, J. Blaha, S. Cap, M. Chefdeville, P. Colas, A. Dalmaz, C. Drancourt, A. Espargilière, R. Gaglione, R. Gallet, N. Geffroy, I. Giomataris, J. Jacquemier, Y. Karyotakis, F. Peltier, J. Prast, and G. Vouters, "Micromegas chambers for hadronic calorimetry at a future linear collider," *Journal of Instrumentation*, vol. 4, no. 11, p. P11023, 2009.

cited on page 97.

[84] G. Charles, M. Anfreville, S. Aune, J. Ball, Y. Bedfer, M. Boyer, P. Konczykowski, F. Kunne, C. Lahonde-Hamdoun, L. Cai, I. Mandjavidze, C. Marchand, O. Meunier, B. Moreno, H. Moutarde, D. Neyret, A. Obertelli, S. Procureur, F. Sabatié, and M. Vandenbroucke, "Discharge studies in Micromegas detectors in low energy hadron beams," *Nuclear Instruments and Methods in Physics Research Section A: Accelerators, Spectrometers, Detectors and Associated Equipment*, vol. 648, no. 1, pp. 174 – 179, 2011.

cited on pages 98 and 100.

[85] S. Procureur, S. Aune, J. Ball, Y. Bedfer, M. Boyer, H. Colas, A. Giganon, P. Konczykowski, F. Kunne, C. Lahonde-Hamdoun, N. Makke, C. Marchand, O. Meunier, A. Morreale, B. Moreno, H. Moutarde, D. Neyret, S. Platchkov, and F. Sabatie, "Discharge studies in Micromegas detectors in a 150 GeV/c pion beam," *Nuclear Instruments and Methods in Physics Research Section A: Accelerators, Spectrometers, Detectors and Associated Equipment*, 2011.

cited on pages 104 and 108.

[86] S. Biagi, "Phage lambda: description & restriction map." `http://cnlart.web.cern.ch/cnlart/2000/001/magboltz`.

cited on page 112.

[87] "ANSYS: Software products for engineering simulation." `http://www.ansys.com/`.

cited on page 112.

[88] S. Biagi, "Monte carlo simulation of electron drift and diffusion in counting gases under the influence of electric and magnetic fields," *Nuclear Instruments and Methods in Physics Research*

Section A: Accelerators, Spectrometers, Detectors and Associated Equipment, vol. 421, no. 12, pp. 234 – 240, 1999.

cited on page 113.

[89] A. Ishikawa, "Gas Study with MAGBOLTZ." `http://www-hep.phys.saga-u.ac.jp/ILC-TPC/gas`. ILC wiki.

cited on page 117.

[90] F. Kunne, P. Abbon, J. Ball, Y. Bedfer, C. Bernet, E. Burtin, T. Dafni, E. Delagnes, A. Giganon, N. d'Hose, J. Le Goff, A. Magnon, C. Marchand, J. Marroncle, D. Neyret, S. Panebianco, S. Platchkov, S. Procureur, F. Robinet, and P. Rebourgeard, "Micromegas: Large-Size High-Rate Trackers in the High Energy Experiment COMPASS," in *Nuclear Science Symposium Conference Record, 2006. IEEE*, vol. 6, pp. 3838 –3841, 29 2006-nov. 1 2006.

cited on page 122.

[91] A. B. Mann, I. Konorov, H. Angerer, M. Kramer, S. Huber, B. Grube, J. Friedrich, B. Ketzer, S. Uhl, F. Haas, *et al.*, "The universal sampling ADC readout system of the COMPASS experiment," *2009 IEEE Nuclear Science Symposium Conference Record NSSMIC*, pp. 2225–2228, 2009.

cited on page 123.

[92] H. C. van der Bij, R. A. McLaren, O. Boyle, and G. Rubin, "S-LINK, a data link interface specification for the LHC era," *IEEE Transactions on Nuclear Science*, vol. 44, pp. 398–402, June 1997.

cited on page 123.

[93] "CORAL: The COMPASS reconstruction program." `http://coral.web.cern.ch/coral/`.

cited on page 126.

[94] G. Mallot, "The COMPASS spectrometer at cern," *Nuclear Instruments and Methods in Physics Research Section A: Accelerators, Spectrometers, Detectors and Associated Equipment*, vol. 518, no. 1-2, pp. 121 – 124, 2004.

cited on page 127.

[95] Y. Bedfer, "Compass internal document." `http://wwwcompass.cern.ch/twiki/bin/view/Detectors/MMDetectorStudies`, 2011.

cited on pages 130 and 134.

Abstract :

This thesis work is dedicated to the design, development and characterization of Micro-Pattern Gas Detectors. The performances of a Time Projection Chamber (TPC) equipped with a triple Gas Electron Multiplier (GEM) amplification structure are reported. The intrinsic ion backflow suppression of GEM foils drastically reduces the space charge produced by wire readout in traditional TPC. The GEM solution allows the operation of a TPC at much higher event rate. The second part of this thesis describes the development of a 40 × 40 cm^2 Micromegas detector with a highly segmented central area. A reduction of discharges compared to conventional Micromegas detectors is needed for stable operation in intense beams of hadrons. Spark reduction technologies have been successfully studied and results are presented.

Keywords: Particle Detectors, Micro-Pattern Gas Detectors, Time Projection Chamber, Hadron Physics, GEM, Micromegas, Front-End Electronics

Résumé :

Le présent travail porte sur la conception, le développement et la caractérisation des Détecteurs Gazeux à Micro Motifs (“Micro Pattern Gaseous Detectors”, MPGD). Les performances d’une Chambre à Projection Temporelle (TPC pour “Time Projection Chamber”) équipée d’une amplification à base de GEM (Gas Electron Multiplier) sont rapportées. La neutralisation intrinsèque des ions par la structure GEM réduit la densité de charges dans l’espace de dérive par rapport au cas d’une lecture à base de chambre à fils. Cette solution permet de supporter des taux de comptage plus élevés. La seconde partie de cette thèse décrit le développement de détecteurs Micromegas de 40 × 40 cm^2 dont le centre est fortement segmenté. Une réduction du taux de décharges par rapport aux détecteurs Micromegas conventionnels est nécessaire pour garantir un fonctionnement stable en faisceau intense de hadrons. Des solutions ont été testées avec succès et sont présentées dans ce travail.

Mots-clés: Détecteurs de Particules, Micro-Pattern Gas Detectors, Chamber à Projection Temporelle, Physique Hadronique, GEM, Micromegas, Électronique Frontale

Zusammenfassung :

Diese Arbeit beschäftigt sich mit Entwurf, Entwicklung und Charakterisierung auf mikroskopisch kleinen Strukturen basierender Gasdetektoren (Micro-Pattern Gas Detectors). Zuerst werden die Eigenschaften einer durch Gas-Electron-Multipliers (GEMs) verstärkten Zeitprojektionskammer beschrieben. Die intrinsische Unterdrückung des Ionenrückflusses aus der Verstärkungsebene in das Driftvolumen reduziert die Auswirkungen von “Space Charge” verglichen mit der üblicherweise benutzen Vieldrahttechnologie und erlaubt damit eine deutlich höhere Ereignisrate. Im zweiten Teil wird von der Entwicklung eines 40 × 40 cm^2 großen Micromegas-Detektors mit einer im Zentralbereich sehr fein unterteilten Auslesestruktur berichtet. Verglichen mit bisherigen Micromegas-Detektoren sind einige Maßnahmen zur Reduzierung von Entladungen bei hadronischen Strahlen hoher Intensität notwendig. Dazu wurden verschiedene mögliche Technologien getestet. Die Ergebnisse dieser Tests werden hier präsentiert.

Schlüsselwörter: Teilchendetektoren, Micro-Pattern Gas Detectors, Zeitprojektionskammer, Hadronphysik, GEM, Micromegas, Front-End-Elektronik